General Disclaimer

One or more of the Following Statements may affect this Document

- This document has been reproduced from the best copy furnished by the organizational source. It is being released in the interest of making available as much information as possible.

- This document may contain data, which exceeds the sheet parameters. It was furnished in this condition by the organizational source and is the best copy available.

- This document may contain tone-on-tone or color graphs, charts and/or pictures, which have been reproduced in black and white.

- This document is paginated as submitted by the original source.

- Portions of this document are not fully legible due to the historical nature of some of the material. However, it is the best reproduction available from the original submission.

Produced by the NASA Center for Aerospace Information (CASI)

NASA CR-143846

DESIGN AND DEVELOPMENT OF A STRUCTURAL MODE CONTROL SYSTEM

Rockwell International Corporation
5701 West Imperial Highway
Los Angeles, California 90009

October 1977

Distribution limited to
U.S. Government Agencies and Contractors

(NASA-CR-143846) DESIGN AND DEVELOPMENT OF A STRUCTURAL MODE CONTROL SYSTEM (Rockwell International Corp., Los Angeles) 184 p
HC A09/MF A01 CSCL 01C

N77-33201

Unclas
G3/08 50761

Prepared for

NATIONAL AERONAUTICS AND SPACE ADMINISTRATION
Dryden Flight Research Center
Edwards, Calif. 93523

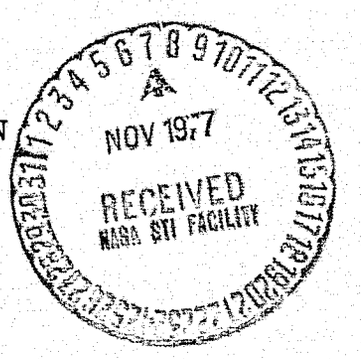

PRECEDING PAGE BLANK NOT FILMED

TABLE OF CONTENTS

	Page
SUMMARY	
INTRODUCTION	
SMCS RATIONALE	4
Ride Quality Criteria	4
Weight Savings	5
KEY SMCS DESIGN CONSIDERATIONS	8
SMCS Concepts	8
Control Surface Selections	15
SMCS Mechanization	20
SMCS Vane Wind Tunnel Test Results	25
SMCS Performance	49
SMCS Vane Load and Hinge Moment Requirements	58
SMCS Stiffness Requirements	67
SMCS DESIGN DETAILS	72
SMCS Vane Construction	72
SMCS Bearing Design	72
SMCS Actuation Design	79
SMCS Vane/Actuation Installation	86
LABORATORY TESTING OF SMCS ACTUATOR	86
Endurance Tests	89
Free-Play Tests	92
Steady-State Actuator Rate Test	98
Dynamic Spring Rate	98
FLIGHT CONTROL SIMULATOR TESTS OF SMCS	101
SMCS Logic Controller Frequency Responses	106
SMCS Actuator Frequency Response	111
Transient Responses	114

Page

SMCS VANE EFFECT ON INLET/ENGINE CHARACTERISTICS 118

Test Description 118
Test Results 127
Summary Remarks 144

RECOMMENDED FUTURE EFFORT 146

APPENDIX A NOMENCLATURE 148

APPENDIX B DESCRIPTION OF DATCOM METHOD AND SMCS VANE PLANFORM OPTIMIZATION STUDY 158

APPENDIX C DISTRIBUTED VANE FORCE CHARACTERISTICS 165

APPENDIX D SMCS VANE MASS AND STIFFNESS PROPERTIES 167

REFERENCES 174

LIST OF ILLUSTRATIONS

Figure	Title	Page
1	B-1 aircraft with wings swept aft.	3
2	Crew sensitivity index for ride quality.	6
3	Fuselage vertical bending stiffness requirements for vertical ride quality.	7
4	Control surfaces used for ride quality improvement, proposal configuration	9
5	Simplified illustration of ILAF structural mode control system concept	12
6	Sensor scheme forseparation of sensed structural motion from rigid-body motion, longitudinal-symmetric modes	12
7	Typical ILAF system root loci.	14
8	Location of XB-70 ILAF system sensors and control surfaces for longitudinal-symmetric mode control.	14
9	Controllability of structural modes contributing to crew station motion	16
10	Vane configuration for vertical and lateral bending control.	18
11	Vane control forces.	18
12	Original structural mode control vane geometric characteristics.	19
13	Modified structural mode control vane geometric characteristics.	21
14	Theoretical vane normal force characteristics versus α, M = 0.85	22
15	Structural mode control system block diagram	23
16	Vane-fuselage interference downwash angle versus vehicle angle of attack, M = 0.85.	28
17	Original vane normal force effectiveness, M = 0.85	29
18	Original vane normal force characteristics versus vane local angle of attack, M = 0.85.	30
19	Original vane side force effectiveness, M = 0.85	31
20	Modified vane normal force effectiveness, M = 0.85	33
21	Modified vane normal force characteristics versus local angle of attack, M = 0.85.	34
22	Modified vane side force effectiveness, M = 0.85	35
23	Modified vane normal force and pitching moment coupling due to antisymmetric deflections, M = 0.85	36
24	Modified vane normal force coupling due to asymmetric deflections, M = 0.85.	37

Figure	Title	Page
25	Nonlinear vane effectiveness comparison of test versus calculated data.	39
26	Interference flow from structural mode control vane, low speed, δ = +20°.	41
27	Interference flow from structural mode control vane, low speed, δ = -20°.	42
28	Original vane pitching moment effectiveness interference effects, M = 0.85.	43
29	Modified vane pitching moment effectiveness interference effects, M = 0.85.	45
30	Schematic of lateral interference phenomenon on forebody . .	46
31	Modified single vane panel side force effectiveness, M = 0.85	47
32	Modified comparison of vane side force effectiveness for two panels from test and constructed from single panel data, M = 0.85	48
33	Original vane side force as affected by aircraft components, M = 0.85	50
34	Modified vane side force as affected by aircraft components, M = 0.85	53
35	Power spectral density associated with vertical crew sensitivity index, $\bar{H}_z$, M = 0.85, h_p = 762m (2500 ft), Λ_w = 65°, medium weight.	56
36	Power spectral density associated with lateral crew sensitivity index, $\bar{H}_y$, M = 0.85, h_p = 762m (2500 ft), Λ_w= 65°, medium weight	57
37	Effect of SMCS on normal load factor response along the fuselage due to turbulence, M = 0.85, h_p = 762 (2500 ft), Λ_w= 65°, medium weight.	59
38	Effect of SMCS on lateral load factor response along the fuselage due to turbulence, M = 0.85, h_p = 762m (2500 ft), Λ_w= 65°, medium weight.	60
39	Stability analysis using frequency evaluation of characteristic determinant, longitudinal - symmetric case, SCAS + SMCS operating, M = 0.85, h_p = 762m (2500 ft), Λ_w= 65°, medium weight.	61
40	Stability analysis using frequency evaluation of characteristic determinant lateral-directional-anti-symmetric case, SCAS + SMCS operating, M = 0.85, h_p = 762m (2500 ft), Λ_w= 65°, medium weight.	62

Figure	Title	Page
41	Combined vertical and lateral SMCS vane exceedances, SCAS + SMCS.	66
42	SMCS flutter characteristics with aft actuator failed.	70
43	SMCS vane flutter velocity versus actuator pitch frequency, M = 1.05	71
44	SMCS vane construction details	73
45	SMCS vane pivot bearings	76
46	SMCS hydraulic system.	80
47	SMCS control valve and actuator operation.	81
48	Functional schematic of hydraulic flow through aft SMCS actuator	83
49	Functional schematic of hydraulic flow through forward SMCS actuator.	84
50	SMCS vane pivot bearing support structure.	87
51	Installation of SMCS actuators	88
52	Schematic of SMCS actuator endurance test setup.	90
53	SMCS actuator load-stroke requirements for endurance test.	91
54	Frequency-amplitude distribution for SMCS actuator endurance tests.	93
55	Thermal profile for SMCS actuator endurance tests.	94
56	SMCS actuator freeplay test setup.	96
57	Typical SMCS actuator freeplay test results.	97
58	No-load test fixture installation for rate tests	99
59	Typical actuator rate test results	100
60	Results of dynamic spring rate tests, normal actuator.	103
61	Results of dynamic spring rate tests, actuator failed to minimum stiffness	104
62	SMCS right side vane actuators as installed on flight control simulator.	105
63	Frequency response of actuator input to forward vertical SMCS accelerometer input	107
64	Frequency response of actuator input to forward lateral SMCS accelerometer input	108
65	Frequency response of model output to forward vertical SMCS accelerometer input	109
66	Frequency response of model output to forward lateral SMCS accelerometer input	110
67	Frequency response of SMCS actuator with a 0.01-second lag in actuator demodulator ripple filter.	112
68	Frequency response of SMCS actuator with a 0.001-second lag in actuator demodulator ripple filter.	113
69	Frequency response of SMCS actuator as a function of amplitude.	115

Figure	Title	Page
70	SMCS response to a step input at forward accelerometer input.	116
71	SMCS anomaly due to operational amplifier characteristics. .	119
72	B-1 air induction system	120
73	B-1 duct flow area distribution ECI-7.	121
74	B-1 air induction system, boundary layer control features. .	123
75	B-1 inlet development wind tunnel model with SMCS vanes. . .	124
76	Engine face instrumentation.	125
77	Photo of vortex generators on B-1 full-scale inlet/engine model installed in Transonic Propulsion Wind Tunnel at AEDC.	126
78	Test matrix, 0.2 scale inlet model with SMCS vane deflection	129
79	Yaw angle sweep with constant inlet weight flow and variable SMCS vane angle, outboard inlet, W2CORR = 156.5 kg/sec (345 lb/sec)	130
80	Steady-state total pressure contours, outboard inlet with constant inlet flow and variable SMCS vane deflection, α = 3°, ψ = -6°.	131
81	Dynamic total pressure contours, outboard inlet, with constant inlet flow and variable SMCS vane deflection, α = 3°, ψ = -6°.	132
82	Yaw angle sweep with constant inlet weight flow and variable SMCS vane angle, inboard inlet, W2CORR = 156.5 kg/sec (345 lb/sec)	133
83	Dynamic total pressure contours, inboard inlet, with constant inlet airflow and variable SMCS vane deflection, α = 3°, ψ = -5°.	134
84	Dynamic total pressure contours, inboard inlet with constant instant airflow during variations in yaw, SMCS vane deflection = 20°	135
85	Dynamic distortion during SMCS vane transient, 0.2 scale model, M = 0.85, α = 3°, ψ = -5°, W2CORR = 156.5 kg/sec (345 lb/sec)	136
86	Influence of SMC vane angle on performance α = 2.5, ψ = -0.0, M = 2.20, inboard inlet.	138
87	Effect of vortex generator vane angle on dynamic distortion characteristics, M = 0.85, full scale (engine), W2CORR = 138.3 kg/sec (305 lb/sec)	139
88	Effect of vortex generator angle on dynamic engine face total pressure contours, M = 0.85, full scale (engine), W2CORR = 138.3 kg/sec (305 lb/sec)	140

Figure	Title	Page
89	Effect of vortex generators on dynamic distortion characteristics, M = 0.85, full scale (engine) and 0.2 scale maneuver point	141
90	Effect of SMCS vane on dynamic engine face total pressure contours, M - 0.85, full scale (engine) and 0.2 scale, W2CORR = 138.3 kg/sec (305 lb/sec)	142
91	Dynamic distortion characteristics during engine transient with vortex generators, M = 0.85	143
92	Predicted envelope of SMCS vane wake ingestion by inlet	145
93	Angle of attack (α) and sideslip (β) definitions	152
94	Sign convention for coefficients and control surface deflections	153
95	Vane normal force coefficient versus angle of attack curves for various sweep angles at M - 0.85, AR = 2.5, λ = 0.2	159
96	Vane normal force coefficients versus angle of attack curves for various sweep angles at M = 0.85, AR = 2.5, λ = 0.1	160
97	Vane normal force coefficient versus angle of attack curves for various sweep angles at M = 0.85, AR = 3.0, λ = 0.1	161
98	Vane normal force coefficient versus angle of attack curves for various sweep angles at M = 0.85, AR = 3.0, λ = 0.2	162
99	Vane normal force coefficient versus angle of attack curves for various sweep angles at M = 0.85, AR = 2.0, λ = 0.1	163
100	Vane normal force coefficients versus angle of attack curves for various sweep angles at M = 0.85, AR = 2.0, λ = 0.2	164
101	Aerodynamic characteristics of Λ_V = 60° vane, M = 0.85	166
102	SMCS vane mass properties sections	168
103	SMCS vane elastic axis location	170
104	SMCS vane spanwise variation of EI and GJ	171
105	SMCS vane actuators and backup structure symmetric flexibility influence coefficients	172

LIST OF TABLES

Table	Title	Page
I	Structural Mode Control Weight Summary	10
II	Analytic Fatigue Load Spectrum For The SMCS Vane Flight-By-Flight Composite Mission	68
III	Teflon Bearing Test Results.	77
IV	SMCS Vane-Installed Free-Play Teat Results	95
V	SMCS Actuator Dynamic Spring Rate Test Schedule.	102
VI	Continuity Sense Check	117
VII	Transient Responses to Shaper On SMCS CG Accelerometers	117
VIII	Summary of Wind Tunnel Tests Investigation SMCS Vane Effects On Engine/Inlet Characteristics.	127
IX	SMCS Vane Strip Mass Properties - One Panel.	169

STRUCTURAL MODE CONTROL SYSTEM STUDY

John H. Wykes, Christopher J. Borland, Martin J. Klepl,
and Cary J. MacMiller
Rockwell International, B-1 Division

SUMMARY

A 10-month program was conducted to compile and document for publication some of the existing information about the conceptual design, development, and tests of the B-1 structural mode control system (SMCS) and its impact on ride quality. Since the B-1 is the first aircraft to have a system such as the SMCS designed for production and long service use, it is expected that this report will add to the technology base for the design of future large military or civil aircraft. This report covers the following topics:

(1) Rationale of selection of SMCS to meet ride quality criteria versus basic aircraft stiffening.

(2) Key considerations in designing an SMCS, including vane geometry, rate and deflection requirements, power required, compensation network design, and fail-safe requirements.

(3) Summary of key results of SMCS vane wind tunnel tests.

(4) SMCS performance.

(5) SMCS design details including materials, bearings, and actuators.

(6) Results of qualification testing of SMCS on the "Iron Bird" flight control simulator, and lab qualification testing of the actuators.

(7) Impact of SMCS vanes on engine inlet characteristics from wind tunnel tests.

INTRODUCTION

The B-1 aircraft is one of the first vehicles to include a control configured vehicle (CCV) concept in the early design phases. The aircraft has a requirement to provide a specified level of ride quality for the crew. This

requirement has been met on the B-1 through the use of an automatic control system called a structural mode control system (SMCS) whose main external feature is a set of vanes near the crew station which are canted down 30° from the horizontal, as shown in figure 1. A substantial savings in weight was achieved with this approach as compared to direct material stiffening. The details of system requirements had to be determined from a production (long-life) point of view, which has not been done before for a system of this type. Extensive wind tunnel tests of the vane characteristics were conducted. Analytical models of the flexible aircraft and control systems were developed to analyze requirements and to investigate stability and performance. Component parts were tested to the requirements in the laboratory. Flight test of the SMCS is continuing, and comparisons with analytical predictions are being made. Because of all of this, it has been recognized that the B-1 offers an excellent opportunity for much needed further evaluation of such a system as the SMCS to insure the optimum use of these systems for future applications.

The overall objective of this research area is to compile and document information about the conceptual design, development, and flight tests of the B-1 SMCS and its impact on ride quality. Since the B-1 is the first aircraft to have a system such as the SMCS designed for production and long service use, it is expected that the reports prepared will add to the technology base for the design of future large military or civil aircraft. The specific objectives are to:

(1) Investigate the improvements in total dynamic response of a flexible aircraft and the potential benefits to ride qualities, handling qualities, crew efficiency, and reduced dynamic loads on the primary structures.

(2) Evaluate the effectiveness and performance of the SMCS, which uses small aerodynamic surfaces at the vehicle nose to provide damping to the structural modes.

The major effort of the present study was to compile, edit, and prepare for publication as a NASA contractor report the existing information on the B-1 SMCS conceptual design and development. No additional analyses were performed during this initial effort. However, additional analyses that would be of value to the overall research objectives have been identified for consideration in future study efforts.

Symbols used in the text of this report may be found in appendix A.

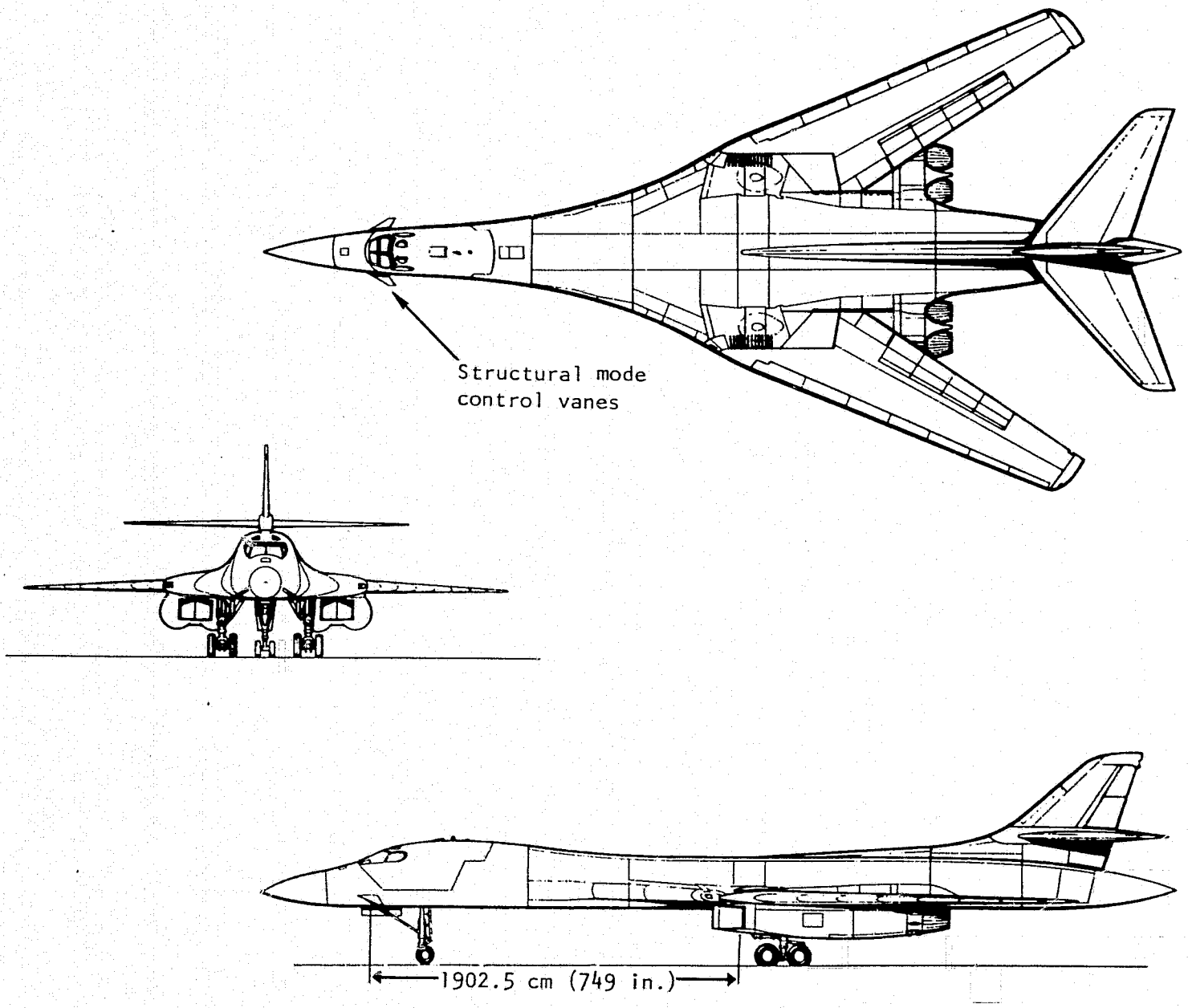

Figure 1. - B-1 aircraft with wings swept aft.

SMCS RATIONALE

One of the principal missions of the B-1 strategic bomber involves flying for long periods of time in close proximity to the terrain. B-1 design requirements have produced a relatively flexible aircraft. This vehicle flexibility combined with the ever-present low-altitude atmospheric turbulence can produce an acceleration environment at the crew station which can degrade handling qualities and general crew efficiency with a consequent degradation of mission success. Ref. 1 reviews this ride quality problem and offers design criteria which, when complied with, tend to alleviate the problems described. These criteria have been formally included in the B-1 design specifications. This report discusses Rockwell International's design approach to comply with these requirements.

The B-1 (figure 1) employs a variable sweep wing which is swept aft when flying the low-altitude mission. The wing is swept primarily to improve the vehicle drag characteristics; however, this is fortunately favorable to improving the vehicle ride qualities also. The aft-swept wing has a low lift curve slope and thus is less susceptible to turbulence-induced angles of attack and the consequent excitation loads. Despite sweeping the wing, the level of turbulence excitation susceptibility on the flexible B-1 was still too high to meet the ride quality requirements. Two basic design choices remained in order to comply: (1) add material (and weight) to stiffen the structure over that needed for strength and flutter requirements; or (2) use automatic control systems. A choice was made in favor of the latter approach because of a potential savings in weight and because of the existing depth of analytical and flight test experience available (refs. 2 through 6) on these types of systems.

The SMCS has been designed to the fail-safe rather than the fail-operate, fail-safe concept. This approach has been taken because the system is intended strictly for improving ride quality; thus the B-1 will have full structural integrity with or without the SMCS operating. Should the system fail for any reason, it will be centered and held and the mission continued; admittedly at a worsened level of ride quality.

Ride Quality Criteria

The SMCS's performance ability to improve ride quality is evaluated against a parameter called the crew sensitivity index, $\bar{H}$. The parameter $\bar{H}_z$ is associated with vertical motion and the $\bar{H}_y$ is associated with lateral motion. The development of the $\bar{H}$ concept of ride quality evaluation can be found in ref. 1.

In order to illustrate the component considerations entering the definition of $\bar{H}$, the vertical parameter $\bar{H}_Z$ will be examined. The three main components of $\bar{H}_Z$ are shown in figure 2. The gust power spectral density shown at the top of the figure is a measure of excitation energy in the atmosphere as a function of the wave number, Ω; or once the speed of the aircraft is defined, the wave number can be viewed as a frequency parameter ($\Omega = \omega/Vo$).

The middle curve is a typical flexible airplane normal load factor due to a unit vertical gust velocity frequency response plot for the crew station. Correlating against the gust power spectral density curve, it can be seen that the energy in the atmosphere can excite the rigid-body (whole-vehicle) motion and a number of the lower frequency structural modes.

The third curve may be viewed as a weighting of the response motion at various frequencies depending on the dynamic response characteristics of the human body and how the human feels about them. As shown at the bottom of the figure, all of these data are brought together in what is a weighted root mean square (rms) normal load factor due to a unit gust intensity. If T_D were left out of the calculation, the rms load factor, $\bar{A}$, would be obtained.

The lateral parameter $\bar{H}_Y$ is developed similarly with the gust spectrum remaining the same but with lateral load factor frequency response and the human response function reflecting different characteristics.

The level of $\bar{H}_Z$ and $\bar{H}_Y$ accepted as design criteria are influenced by a number of factors including mission time; these are discussed and evaluated against response characteristics of a number of typical military aircraft in ref. 1.

The only element of the parameter that can be changed by a control system is the contribution of the structural response to the normal and lateral load factors.

Weight Savings

The weight savings attributable to use of the SMCS was evaluated by determining the stiffnesses required to meet the ride quality with and without the use of the SMCS. Only the fuselage stiffnesses were affected by the trade-offs made; the lifting surface stiffness levels were set by strength and flutter considerations. Experience from several other design studies showed that the vertical stiffness was the one requiring the main adjustment. Figure 3 shows two levels of stiffnesses determined from the comparative study. As indicated, the lower level curve met all requirements for strength, stability and control, and flutter, but fell short of providing stiffness enough for

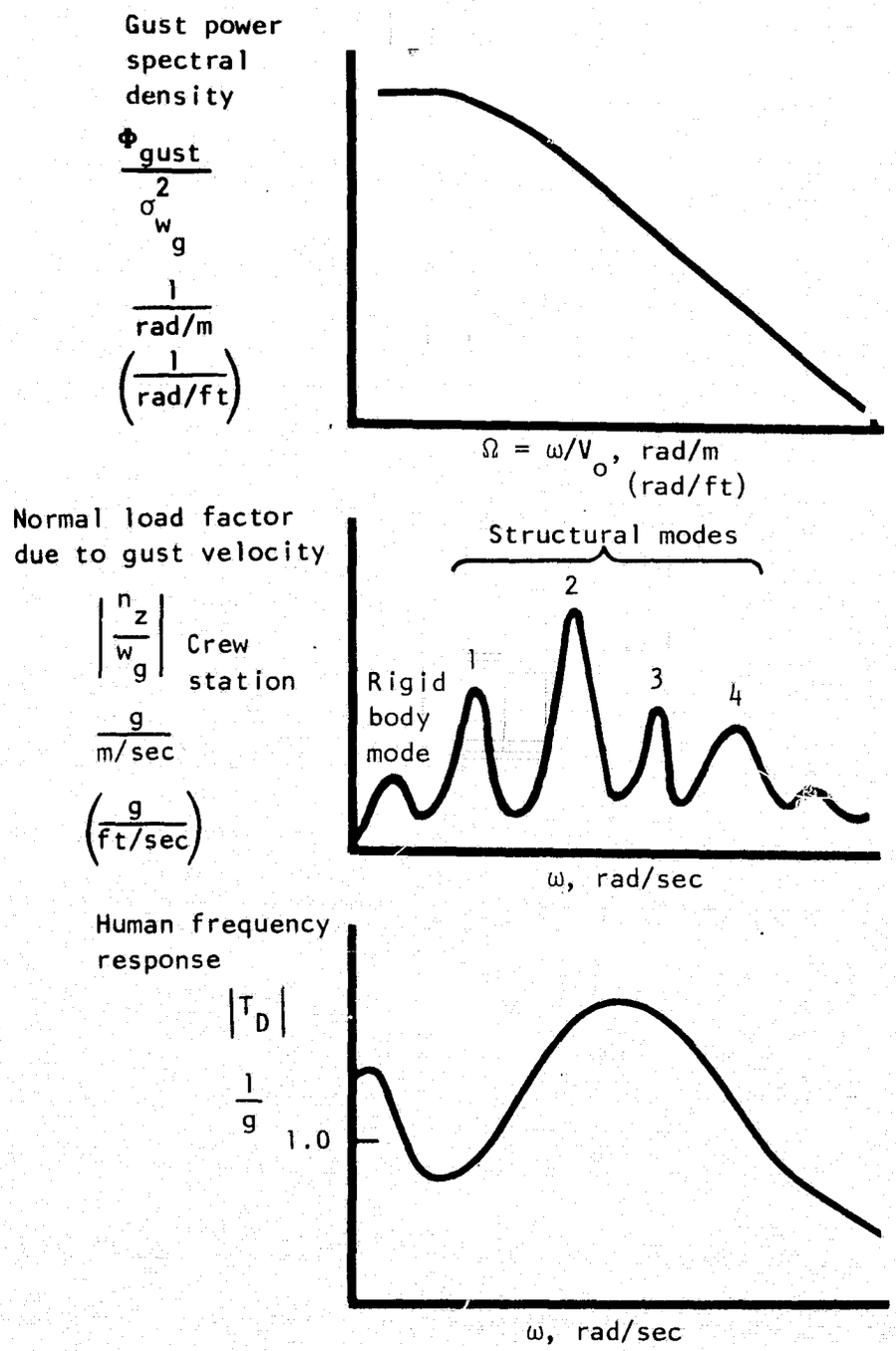

$$\overline{H}_Z = \left[\int_0^\infty |T_D|^2 \left|\frac{n_z}{w_g}\right|^2 \frac{\Phi_{gust}}{\sigma^2_{w_g}} \, d\omega \right]^{\frac{1}{2}} \frac{1}{m/sec} \left(\frac{1}{ft/sec}\right)$$

Figure 2. - Crew sensitivity index for ride quality.

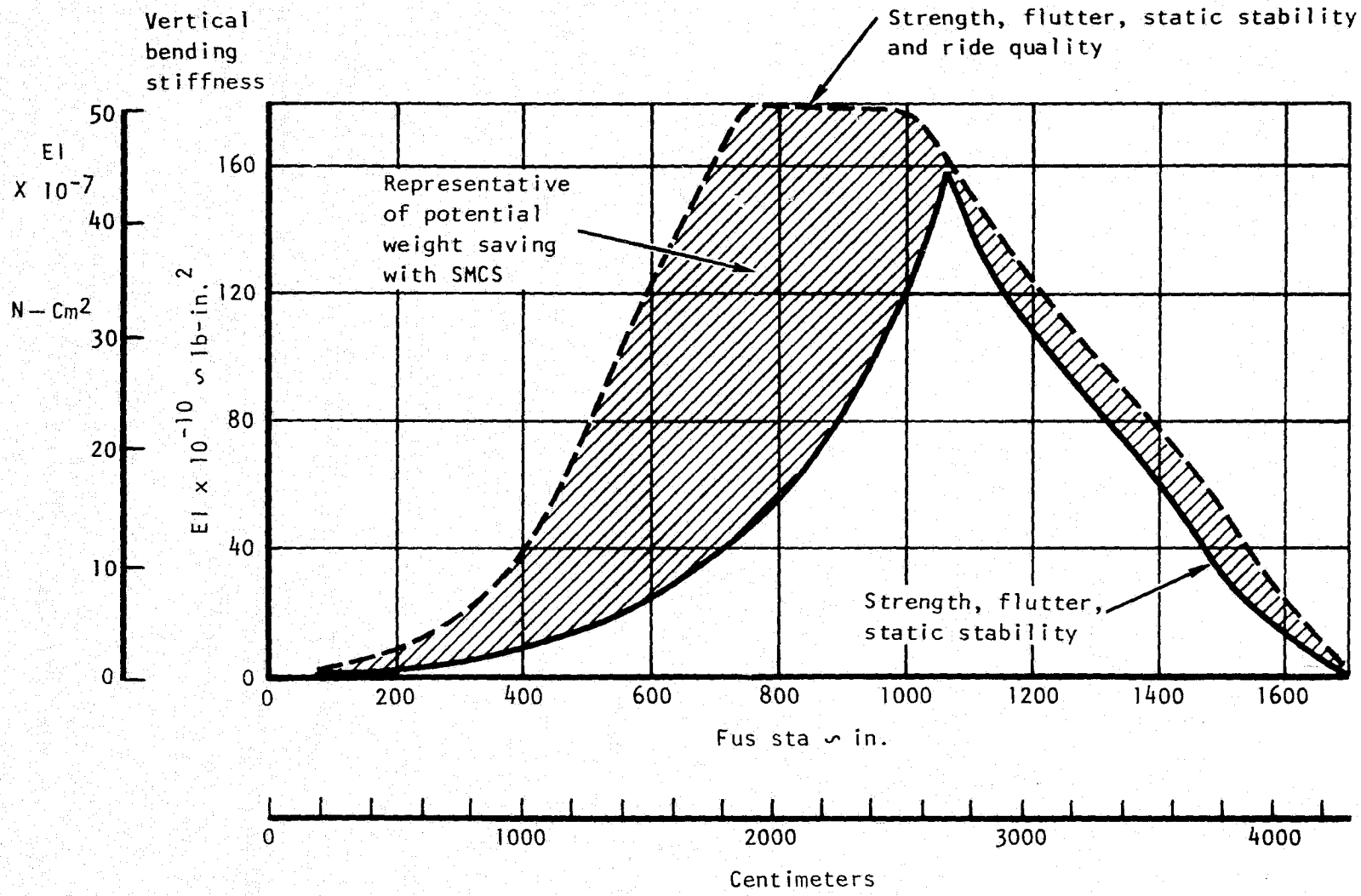

Figure 3. - Fuselage vertical bending stiffness requirements for vertical ride quality.

ride quality compliance. The higher level curve provides the required level of stiffness to meet the ride quality requirement. The initial level of this latter stiffness was set by establishing a frequency requirement for the first fuselage mode of about 2 Hz; this had been established as a criterion as the result of several earlier design iterations which showed that when used in detailed computations, ride quality criteria could be met. The weight associated with the difference between the two curves was evaluated as the weight savings attributable to the SMCS.

To establish the basis for determining what was paid in SMCS weight for the stiffness savings, a brief description of the proposed system is required The external features of the SMCS as originally proposed are shown in figure 4; a small 0.697 m^2 (7.5 ft^2) (total area) pair of horizontal vanes was located at the nose to control vertical structural motion, while the lower rudder panel was used to control lateral structural motion. The lower rudder panel also was used by the yaw stability and control augmentation system (SCAS).

Table I summarizes weight elements of the trade-off study made. It indicated that a total of 4482 kg (9880 lb) of stiffening weight would have had to be added to the fuselage to meet ride quality requirements without the SMCS. Also shown are the component weights and the total of 182 kg (400 lb) which was estimated for the proposed SMCS. Thus it was estimated that a weight savings of approximately 4300 kg (9480 lb) could be realized in meeting the ride quality requirements using an SMCS. As will be discussed in subsequent sections, the details of the SMCS have changed during development, but these changes have not invalidated the order of magnitude of the estimated weight savings. A continual tracking of the weight savings has not been made on as detailed a basis as discussed here. The fact that the SMCS continued to be required to meet specification ride quality levels served as proof of a continuing weight savings through its use.

KEY SMCS DESIGN CONSIDERATIONS

SMCS Concepts

A successful design for structural mode control embodies control of lower structural modes, up to 10 Hz, for a wide range of vehicle weight, configuration, and flight condition changes; and control of structural modes without interference with basic handling qualities. Solutions to these requirements were defined during the Air Force-sponsored research documented in refs. 2, 3, and 4. From these studies, a concept of implementation called identical location of accelerometer and force (ILAF) was developed and verified. This concept was used on the B-1.

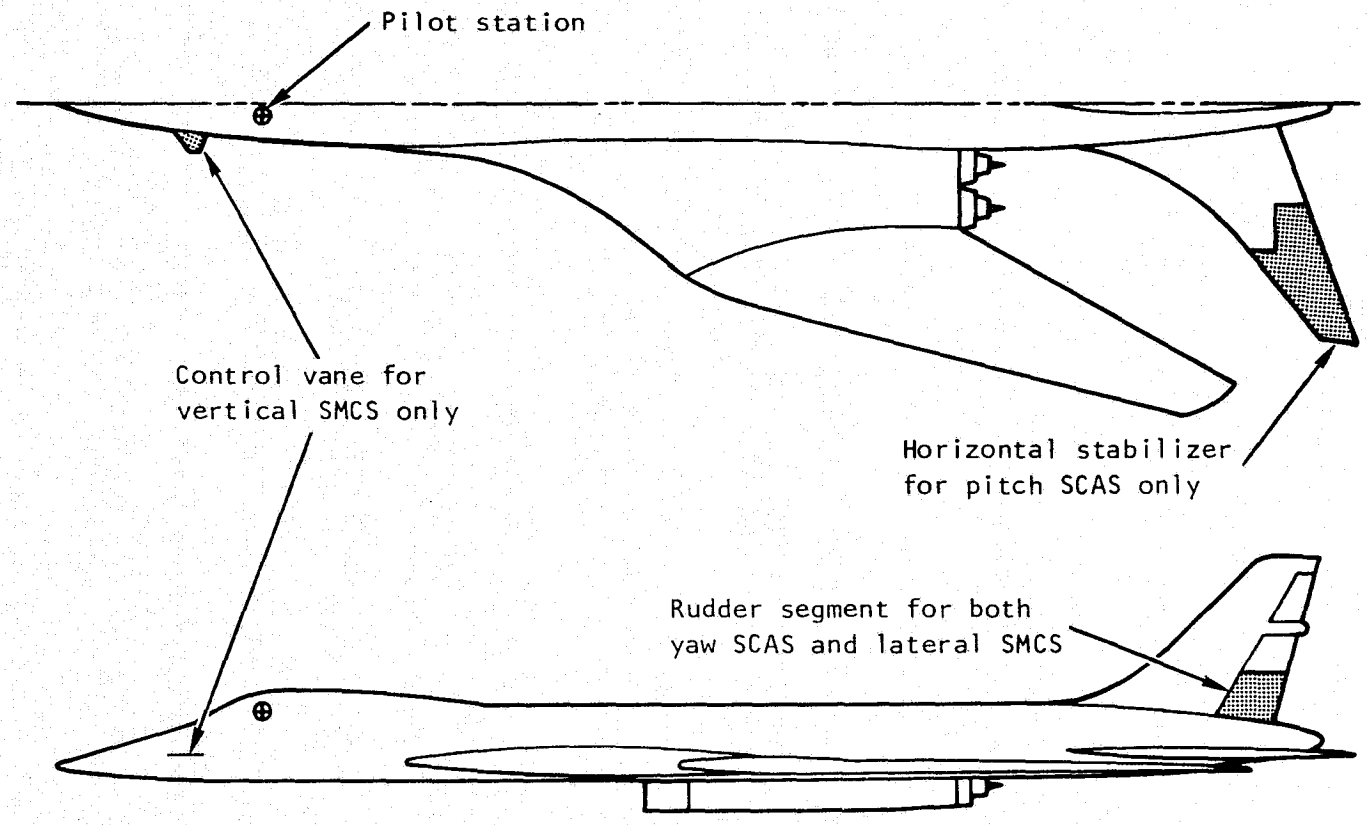

Figure 4. - Control surfaces used for ride quality improvement, proposal configuration.

TABLE I. — STRUCTURAL MODE CONTROL WEIGHT SUMMARY

Item	Without SMCS	With SMCS	Weight Δ
Fuselage stiffness increment	4482 kg (9880 lb)	0	-4482 kg (-9880 lb)
Structural mode control			
SMCS fin, support, and bearings		40.82 (90)	
Support frame and backup		36.39 (80)	
Actuator and controls		11.34 (25)	
Accelerometer		2.27 (5)	
Servo		4.54 (10)	
Hydraulic system change		38.56 (85)	
Rudder actuation and controls		15.88 (35)	
Servo		9.54 (10)	
Accelerometer		2.27 (5)	
Hydraulic system		11.34 (25)	
Miscellaneous		13.61 (30)	
Subtotal structural mode		+182 (+400)	+182 (+400)
Total weight saving			-4300 (-9480)

A simplified explanation of the ILAF system technique is diagrammed in figure 5. The controlling force on a particular structural mode is called the generalized force. This force is the product of the ith normalized natural vibration mode shape, ϕ_i^F, at the force application point and the force magnitude, F; that is, $F\phi_i^F$. The structural acceleration at a given point on the vehicle is the product of the normalized mode shape, ϕ_i^A, at a given point on the vehicle and the generalized coordinate acceleration $\ddot{\eta}_i$; that is, $\phi_i^A \ddot{\eta}_i$. For the control system to be stable at effective gain levels, K, of a fixed sense, the sense of ϕ_i^F and ϕ_i^A must always be the same. One way of insuring this requirement for all modes, i, simultaneously, is to place the sensing element and accelerometer at the force application point; thus, $\phi_i^F = \phi_i^A$. With this arrangement, both the magnitude and sense of ϕ_i^F and ϕ_i^A may change as fuel or vehicle geometry varies during flight without changing the net effect on the sense of the feedback loop. More detailed explanations may be found in ref. 2. This sensing scheme solves the basic problem of designing for changing vehicle and flight condition combinations. Many systems can be conceived that work well at one design point, but it is more difficult to produce a design that will accommodate the wide range of vehicle and flight conditions normally experienced.

Another key element of the ILAF system is the approximate integration of the accelerometer signal to obtain the required velocity signal to activate the damping force. This approximate integration makes use of existing lags in the actuator and other system components, thus simplifying network shaping.

Unless an attempt is made to isolate sensed structural motion from rigid-body motion, the ILAF scheme can affect the short-period or Dutch-roll characteristics. The scheme that employs the difference signal of two linear accelerometers (figure 6) can satisfactorily perform the desired motion-sensing separation. One accelerometer is located near, but not on, the control surface, while the other is located near the vehicle center of gravity. These sensors pick up three components of acceleration - that experienced at the center of gravity when the vehicle as a whole accelerates, n_{zCG}; that due to rotary acceleration, $\dot{q}$, about the center of gravity, which appears as linear acceleration at a distance off the center of gravity, $\frac{\ell}{g}\dot{q}$; and that due to structural acceleration at a particular point on the vehicle, $\sum_{i=1}^{n} \frac{\phi_i}{g} \ddot{\eta}_i$. Experience gained from working on several flexible vehicles shows that when the signal from the sensor near the center of gravity is subtracted from the other sensor signal, the result is essentially a reinforced structural signal, $\frac{\Delta\phi_i}{g}\ddot{\eta}$; for the lower frequency modes, and some small pitch acceleration $\frac{\Delta\ell}{g}\dot{q}$. The whole-vehicle translation acceleration signal of the center of gravity is completely canceled. A low-pass filter can be used to avoid potentially interfering signals from higher frequency modes.

Key features:

- o Identical location of accelerometer and force (ILAF)
- o Approximate integration of acceleration to obtain velocity signal

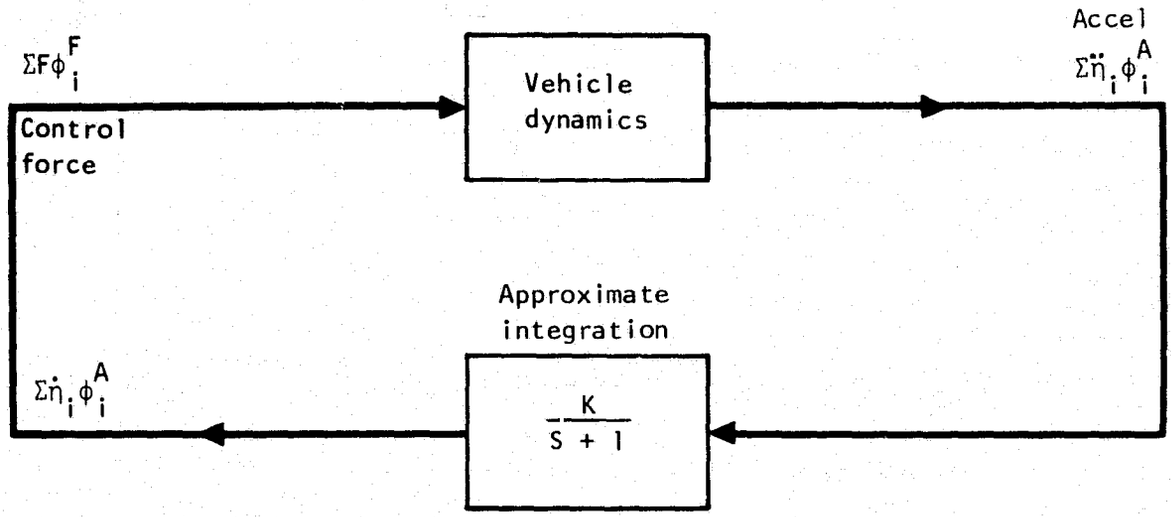

Figure 5. - Simplified illustration of ILAF structural mode control system concept.

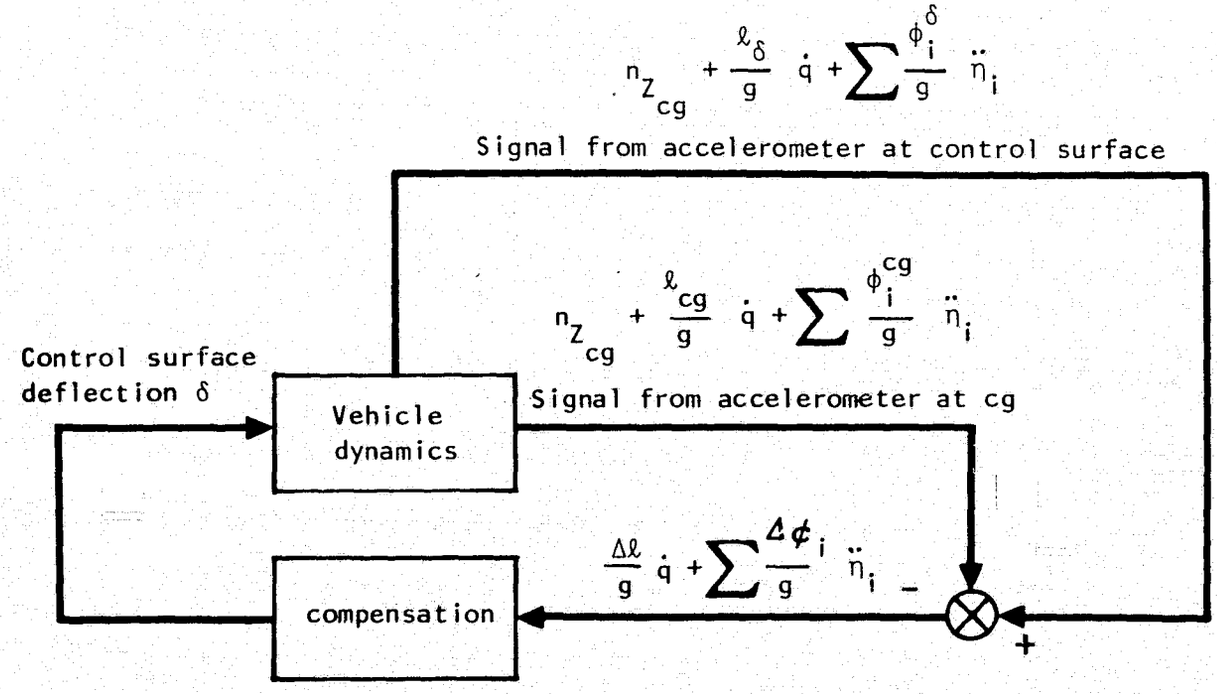

Figure 6. - Sensor scheme for separation of sensed structural motion from rigid-body motion, longitudinal-symmetric modes.

Figure 7 shows typical root loci of an ILAF system. The illustration includes the longitudinal short-period, or rigid-body mode, and four symmetric modes for the XB-70, and illustrates the ILAF sensor-force scheme and separation of sensed rigid-body and structural motion. The loci of the poles-to-zeroes are typical of an ILAF system. Where there is movement with increasing gain, as shown for modes 1 and 2, the movement is out into the left plane, which is a stable direction. The interlacing of poles and zeroes set up by the ILAF scheme produces this effect. Damping is increased significantly in modes 1 and 2, while modes 3 and 4 are little affected but remain stable.

The short-period characteristics set by the regular stability augmentation system (SAS) are little affected. The ramification of this is that the ILAF system can operate satisfactorily without the SAS and that the SAS can operate without the ILAF system.

Extensive analytical verifications of the concepts described are reported in refs. 2 through 5. During the joint Air Force - NASA flight test program for the XB-70, experimental proof was obtained of the validity of the ILAF SMCS concept. The system installation was an exploratory device, not an optimum system, and was constrained to use of existing control surfaces and actuation components. Figure 8 shows the location of the ILAF system sensors and control surfaces for the longitudinal-symmetric SMCS. This sensor arrangement employed the principles explained in figures 5 and 6. The details of the system design effort were reported in ref. 5.

When the SMCS was tested in turbulence, the pilots reported a definite reduction in crew compartment acceleration with the ILAF system operating. These flight test results are reported in ref. 6. In addition to this physical demonstration, the program provided important detailed design information on compensation, sensing, control surface size, and actuation, as well as experience with general system installation and checkout. This progress was reflected in the B-1 SMCS design.

Also during the XB-70 flight test program, Rockwell designed and installed a small pair of shaker vanes forward of the cockpit, as indicated in figure 8. These vanes were used to force structural motion in flight, as described in ref. 7. The proposed SMCS control vane installation in the B-1 was similar to the shaker vane installation. The XB-70 vane had 0.372 m^2 (4 ft^2) of total exposed surface area, while the B-1 control vane had 0.697 m^2 (7.5 ft^2). A study design to turn the XB-70 shaker vanes into an SMCS had been completed, and implementation had begun, but the XB-70 flight program was canceled before flight testing could be accomplished.

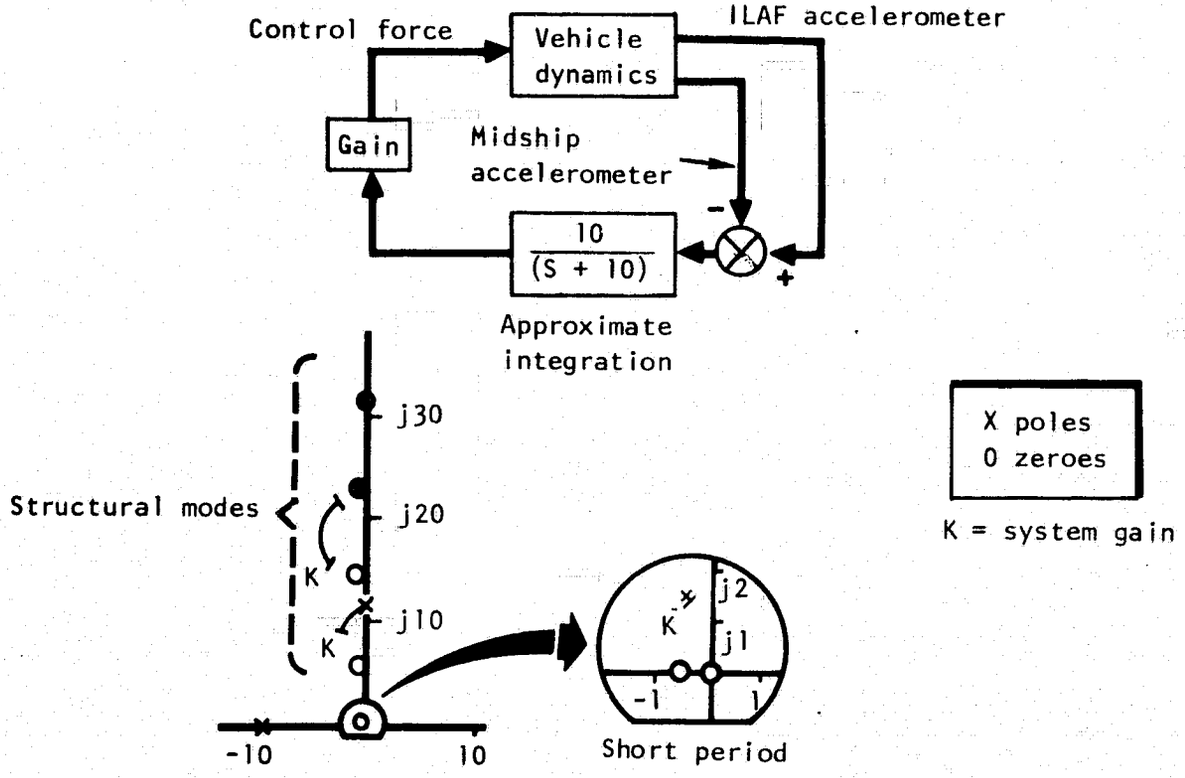

Figure 7. - Typical ILAF system root loci.

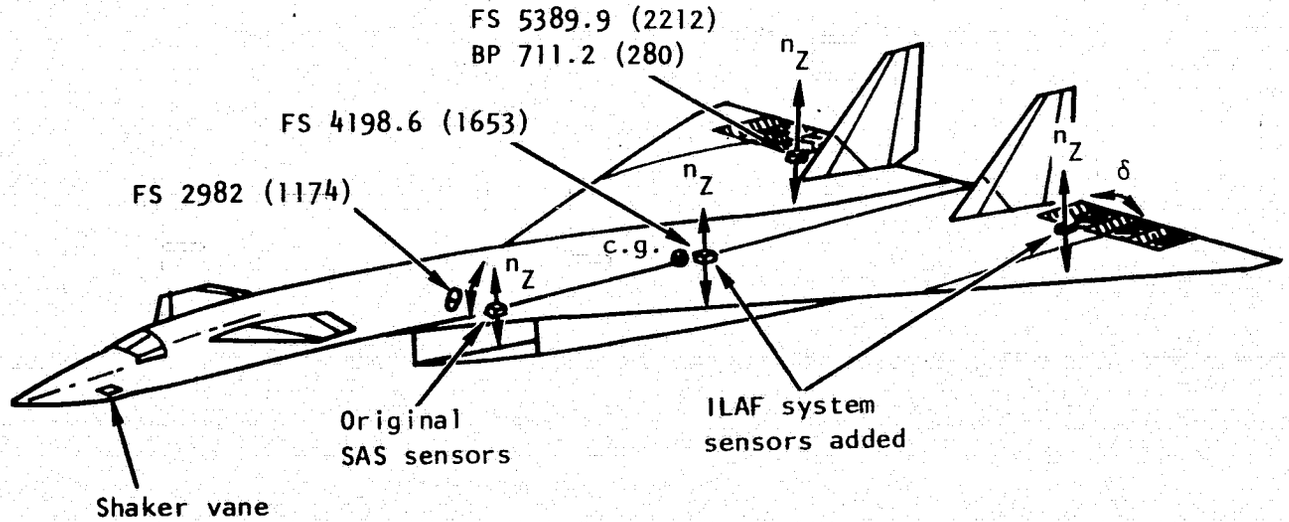

Figure 8. - Location of XB-70 ILAF system sensors and control surfaces for longitudinal-symmetric mode control.

Control Surface Selections

A forward-located control vane is an optimum force generator for structural mode control to improve ride quality. This can be seen in figure 9a, which displays the fuselage component of two whole-vehicle-free vibration modes that are composed primarily of first and second fuselage bending. A measure of control for a given structural mode is expressed as a generalized force defined as the force (F) multiplied by the mode shape at the point of force application, ϕ_i^F; that is, $F\phi_i^F$. The figure demonstrates that for the maximum control of a mode for a given force magnitude, the force should be placed on a vehicle extremity. However, because the goal is to improve ride quality, the force should be constrained to a forward location near the crew station. Therefore, if a mode is contributing to pilot motion, the force generator can control it. If the crew station is on a node line, there is no crew motion from that mode, and the force generator cannot (and need not) be effective.

The initially proposed location of the horizontal control vane forward of the crew station at the fuselage maximum breadth permitted use of the smallest surface possible for the degree of vertical ride quality control required. Small size was desirable to reduce drag, minimize destabilizing effects on static stability, and minimize fail safety effects of hardover failures. Results of low-speed wind tunnel tests of the proposed horizontal control vane indicated that the vane drag increment was so small as not to be identifiable in the measured data, while the pitch destabilization was insignificant. Additional wind tunnel results are the subject of more complete discussions in a following section of this report.

In addition to reasons of aerodynamic drag and stability, a small vane was desirable for control implementation. A small surface can be moved faster, power needs are lower, and nonlinear effects of control surface threshold and hysteresis are minimized relative to total surface maximum deflections. The vertical location of the vane was selected so as not to obscure pilot vision or distort the engine inlet flow.

While the logic for placing a vertical vane for lateral control near the crew station could have been developed in the same way as that for the horizontal control vane, it was not practical to place a forward vertical vane on the aircraft because conflicts would have resulted with internal equipment arrangements. An optional location for a structural mode control at the rear of the vehicle was selected, and the lower-segment rudder used as a control force generator. As can be seen in figure 9b, the control force would be effective on the whole-vehicle antisymmetric modes that are made up mainly of fuselage first and second bending mode components. One primary disadvantage of the rudder was the possibility of obtaining a higher frequency mode of significance to pilot ride quality with a large mode deflection at the pilot station (ϕ_i^P)

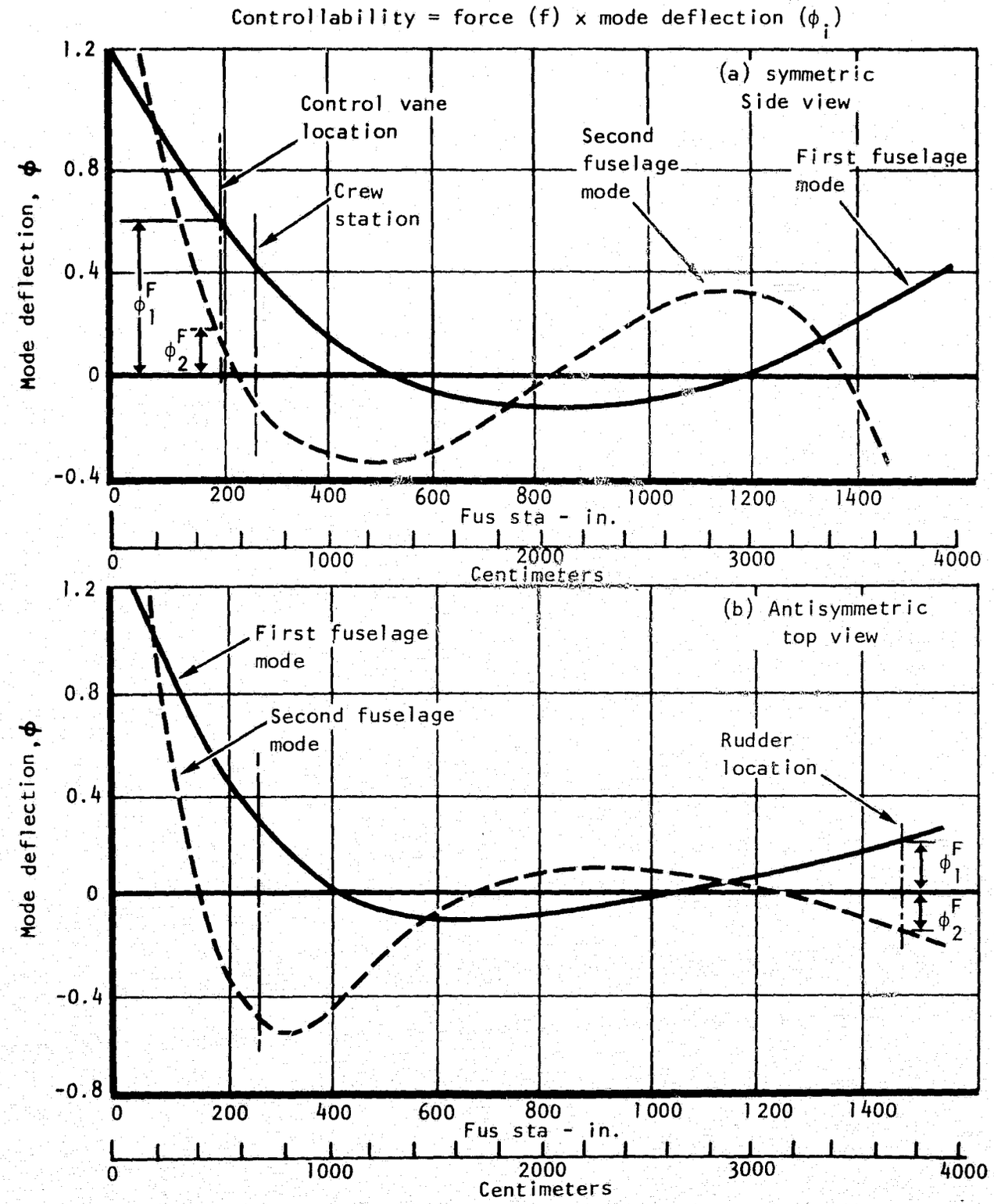

Figure 9. - Controllability of structural modes contributing to crew station motion.

but a node line at the control force application point so that controllability would be lost, $F\phi_i^R = 0$.

As noted, the structural mode control force generators just described were as originally proposed. Subsequent development work dictated a reevaluation of these initial choices. Characteristics of the lower frequency fuselage modes changed in a manner that left the rudder ineffective in controlling the pilot station motion. When this fact became apparent, the need to consider lateral force sources at the forward end of the aircraft became mandatory.

As previously mentioned, control surfaces in the vertical plane at the forward end of the aircraft had been considered but eliminated from consideration due to interference with other design requirements. At this point it was decided to cant the vanes down 30^o from the horizontal as illustrated in figure 10 and use symmetric deflections to produce vertical forces and differential deflections to produce lateral deflections as shown in figure 11. Analyses of ride quality of the vehicle at that stage of development showed that sufficient control existed in both the vertical and lateral axis to meet ride quality requirements.

The fore and aft location on the fuselage, the planform geometry, and the vane area have changed during the development phase of the system. The proposal configuration had the vane (pivot) located at fuselage station 482.6 (190) as shown in figure 9a. As internal structure and equipment arrangements were better defined, the vane was moved to fuselage station 581.7 (229). Figure 9a shows that at this second location, a vane of fixed area would have less control ($F\phi_i^F$) of the first symmetric fuselage mode since ϕ_i^F was reduced while F stayed fixed. To compensate for the smaller ϕ_i^F, the planform total area was increased by the ratio of $\phi_i^{old}/\phi_i^{new}$ from the original 0.697 m^2 (7.5 ft^2) to 0.929 m^2 (10 ft^2). Then when the decision was made to cant the vanes to 30^o for lateral control, the total vane area was increased to 1.068 m^2 (11.5 ft^2) or 0.929 $m^2/\cos 30^o$ (10 $ft^2/\cos 30^o$) in order to hold the vertical force component constant.

The planform characteristics of the vane, at this point in the design process, appeared as shown in figure 12. The planform was selected to have a low-aspect ratio of moderate sweep and taper ratio in order to permit building as stiff and light a surface as possible and yet have linear force characteristics over the range of design deflections. Wind tunnel tests were conducted on the 1.068 m^2 (11.5 ft^2), $\Lambda = 35^o$ configuration to determine the force characteristics over the design range of deflections and angles of attack. The specific data will be reviewed in depth in subsequent sections; suffice it here to say that these tests showed that the force characteristics were highly nonlinear and not satisfactory for the proposed design.

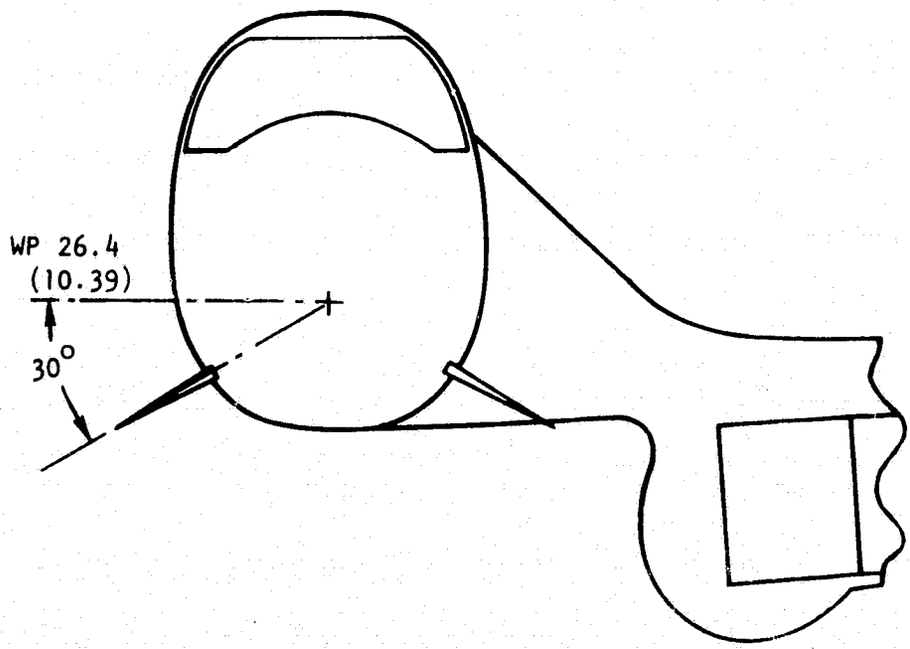

Figure 10. - Vane configuration for vertical and lateral bending control.

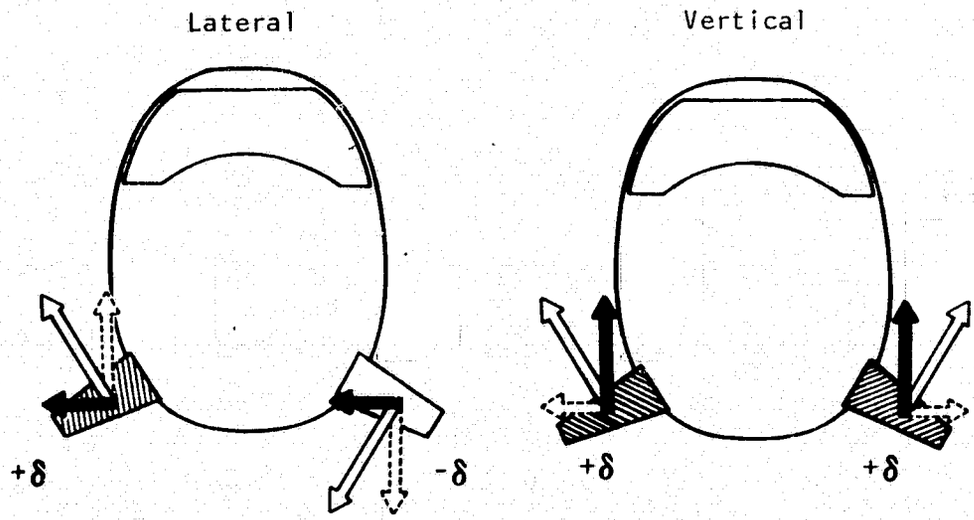

Figure 11. - Vane control forces.

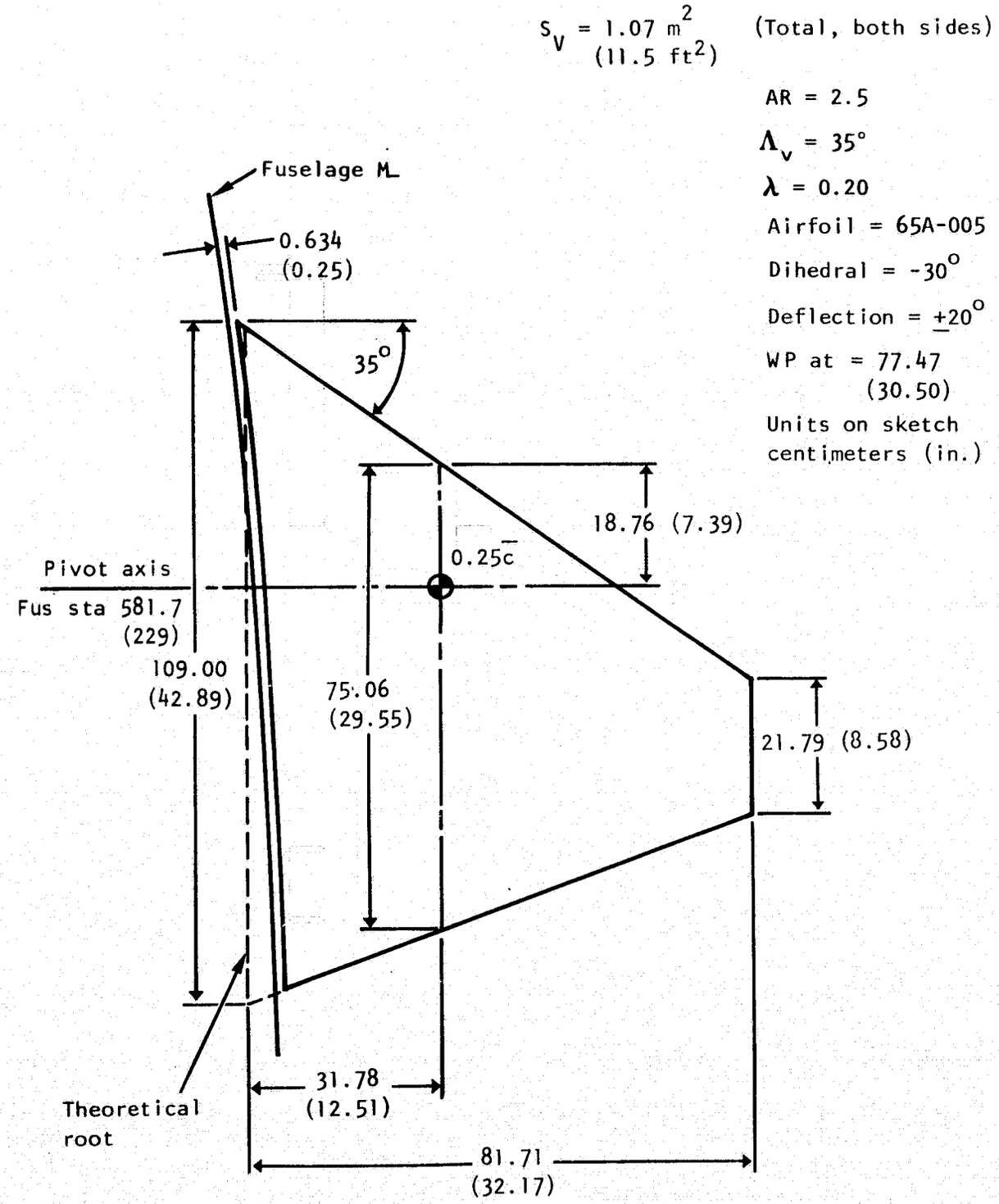

Figure 12. - Original structural mode control vane geometric characteristics.

When these degraded force characteristics were discovered, analytical methods were used to select a new planform configuration. The USAF Stability and Control Methods Handbook (DATCOM) technique, described in appendix B, was programmed for the IBM S/360 and used to perform a parametric study of the C_N (vane body axis reference) versus α characteristics of various planforms. The leading edge sweep angle was varied from 35^o to 65^o, the aspect ratio from 2 to 3, and the taper ratio from 0.1 to 0.2. Different thickness airfoil sections were also included. Results of the parametric study are given in appendix B.

It was found that a planform with 60^o leading edge sweep, but with the same aspect ratio (2.5) and taper ratio (0.2), and thickness (5 percent) as the original vane gave far more favorable normal force characteristics, and still seemed to be within the realm of practical construction. A 65^o swept vane with 0.1 taper gave the most favorable characteristics, but would in all probability have had unsatisfactory stiffness characteristics. Accordingly, the 60^o swept vane was identified as the primary candidate for a "modified" SMCS vane. The modified SMCS vane is shown in figure 13. The total and distributed force characteristics based on linear theory are given in appendixes B and C. The predicted normal force curves for the original and modified SMCS vanes are shown in figure 14. Although some reduction in linear normal force curve slope is evidenced by the modified vane, this is largely counteracted by the slightly nonlinear increase due to leading edge vortex suction at small to moderate angles of attack. For large angles of attack, the advantage for the modified vane is clear.

SMCS Mechanization

The mechanization of the SMCS is presented in figure 15. Some of the numerical values associated with elements of the block diagram shown have changed during the system development, but the mechanization has remained essentially as shown from proposal through fabrication and test. The system consists of two basic functional parts; one is associated with operating the vane panels in unison to control symmetric structural motion (vertical system), and the other is associated with operating them differentially to control antisymmetric side bending structural motion (lateral system).

The implementation of the basic ILAF concept can be seen in the placement of the vertical and lateral accelerometers at the same general location as the control vanes. To augment this principle by eliminating most of the rigid-body motion, a second set of accelerometers is placed near the center of gravity. Because the rigid-body motion content and lower structural modes only are desired from the signal of the center-of-gravity accelerometer, the signal is passed through a simple lag which eliminates higher frequency structural mode content.

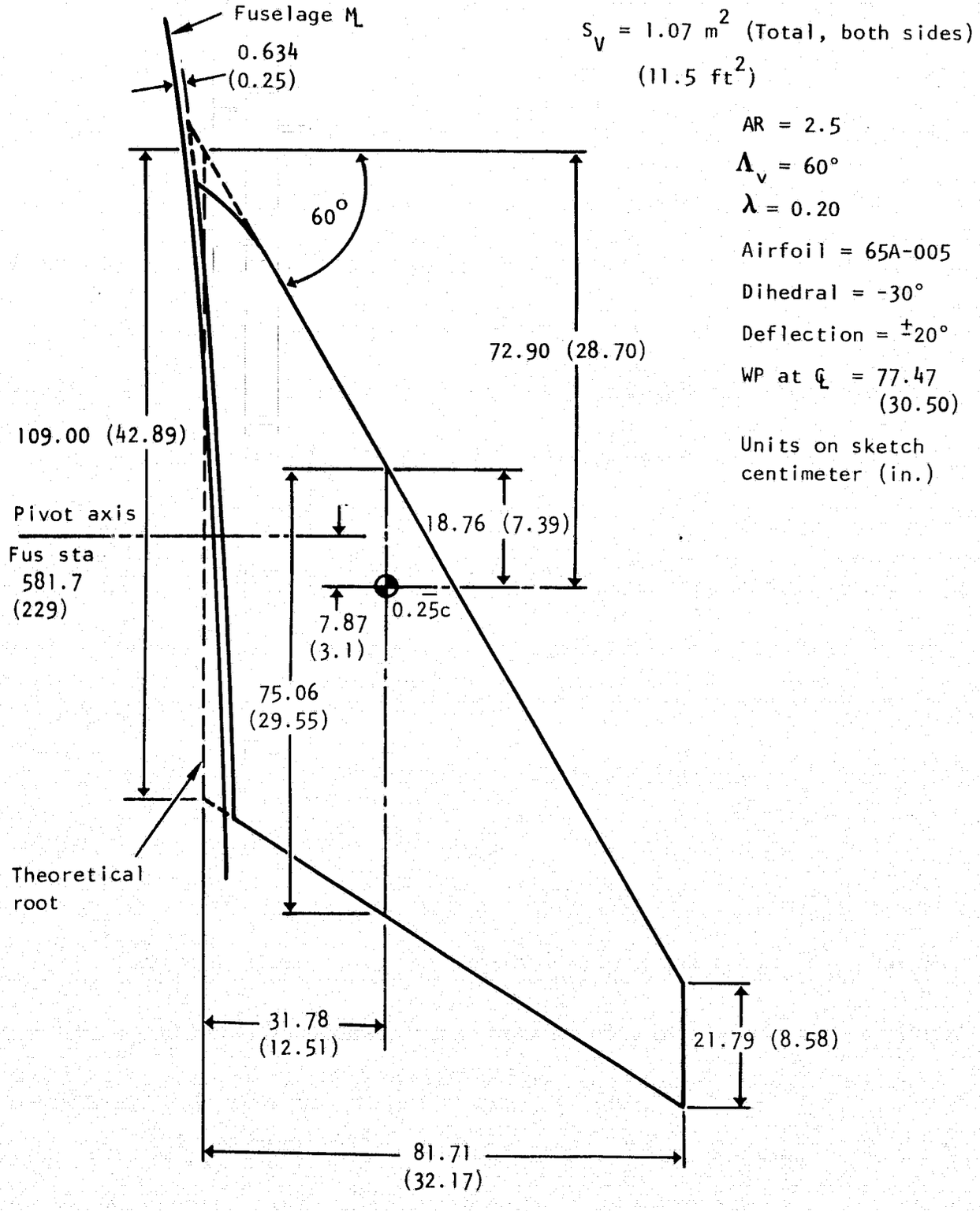

Figure 13. - Modified structural mode control vane geometric characteristics.

Note: C_{N_V} based on vane area and referenced to vane body axis.

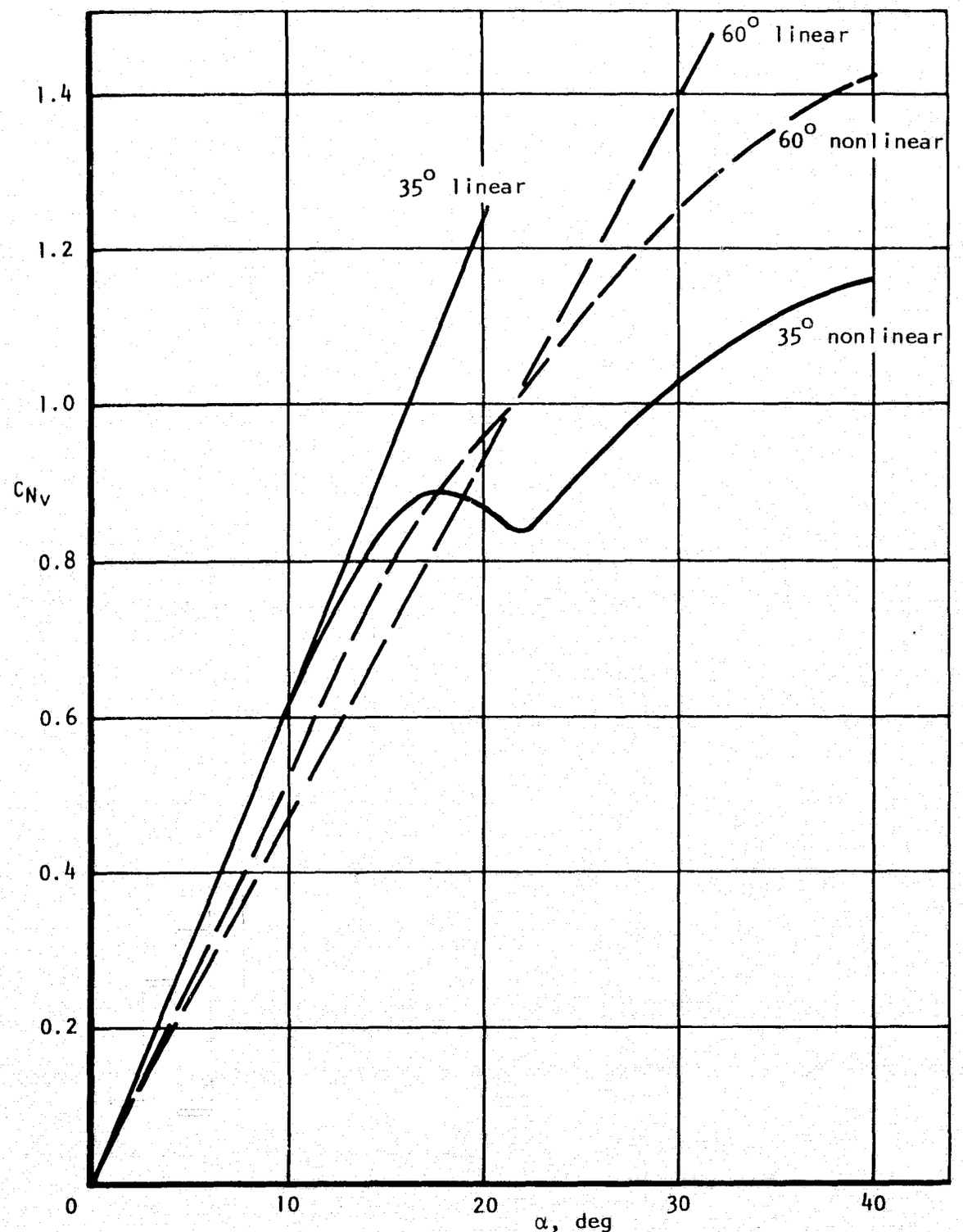

Figure 14. - Theoretical vane normal force characteristics versus α, M = 0.85.

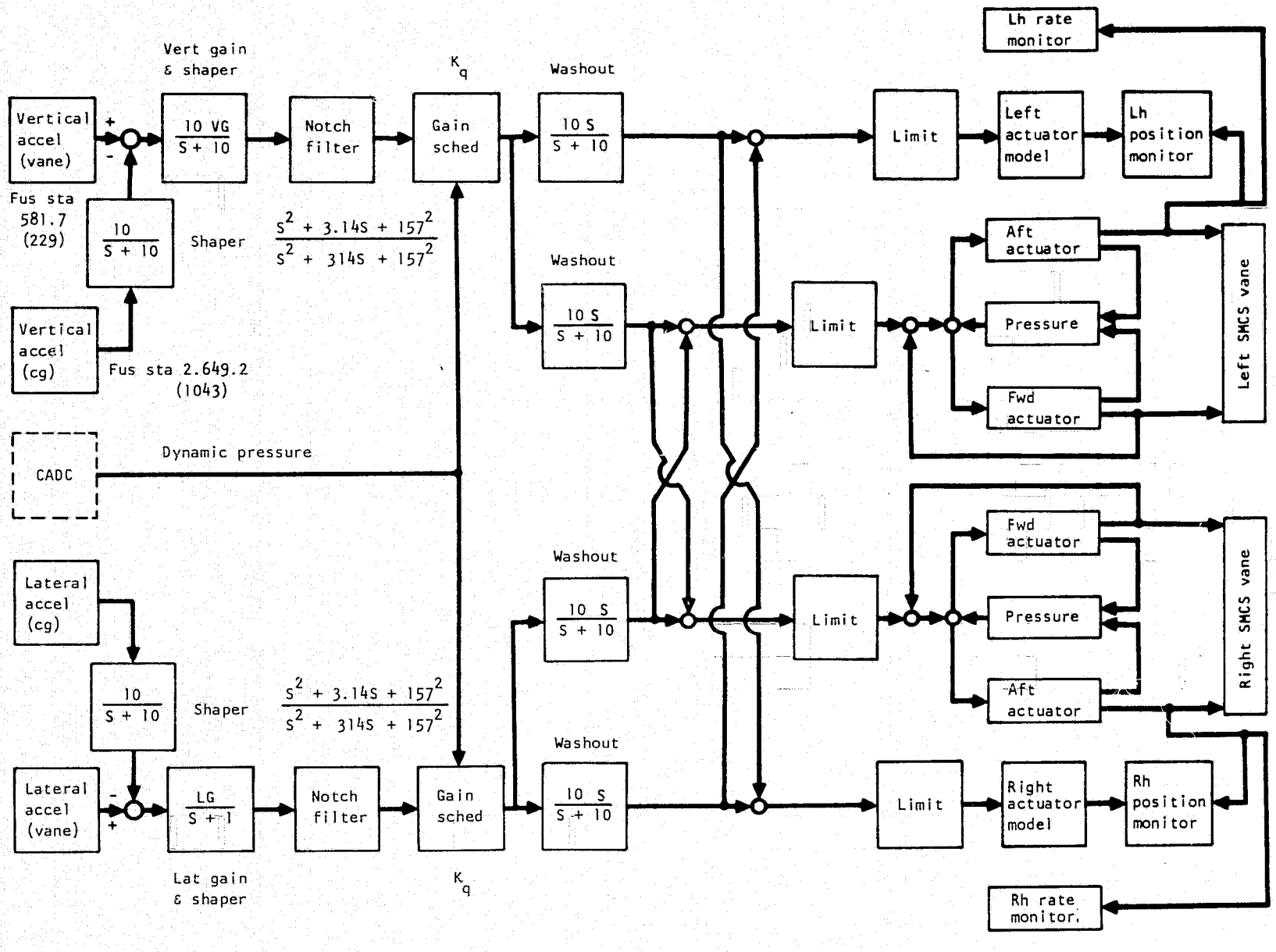

Figure 15. - Structural mode control system block diagram.

After the difference signal from the accelerometers at the vane and at the center of gravity is obtained, it is passed through shaping and a notch filter designed to eliminate the primary natural frequencies of the vane-actuator installation. The signal then passes through a gain which is scheduled by dynamic pressure from the central air data system. The primary utilization of the SMCS will be during low-altitude high-speed flight. The speed and altitude, however, will vary over a limited range; thus dynamic pressure gain scheduling was selected to maintain control force effectiveness.

The functional intent of the system is to produce structural damping; therefore, the signal to the force actuation devices must be proportional to structural velocity. This velocity signal is obtained by appropriate gains and shaping networks. Selections of the gains and shaping networks are a function of the structural, aerodynamic, and actuator dynamic characteristics. Basically, simple lags are used to approximate integration of the structural acceleration signals to obtain the required velocity signals.

Washout networks are used to effectively disengage the vertical or lateral functional parts of the system in event of hardover failures. In addition to isolating hardover failures, the washout networks attenuate rigid-body (whole-vehicle) response acceleration signals that cannot be canceled by the accelerometer signal differencing.

After the washout circuits, the signals are divided and proceed to the independent left and right vane-actuator assemblies. Before reaching the actuators, however, the signals pass through electronic limiters in the circuits. These electronic limiters prevent the vane actuators from making hard contact with the physical actuator throw stops.

Depending upon whether the signals come from the vertical or lateral motion sensing part of the system, the actuators move the left and right vanes in unison or differentially to produce the required aerodynamic control forces. The system will also respond to mixed signals from the vertical and lateral sensor systems. Pressure sensors coordinate the force output between the forward and aft actuators.

There are two actuators associated with each vane so that a free floating vane can be avoided in event of a malfunction. Use of the dual hydromechanical components insures that the vanes can be returned to neutral position, and held when disengaged manually by the pilot or automatically by the SMCS monitors. The monitors use vane deflection and maximum vane rate information

to detect malfunctions. The part of the monitor that uses vane deflection information consists of a duplicate of the electronics from the shaping network output to the actuator input and an electronic model of the actuator. Thus, differences between the command vane position and the actual vane position exceeding certain values for a specified time interval are used to automatically disengage the SMCS. The part of the monitor that uses vane maximum rate information disengages the SMCS when maximum rate is sustained for more than an accumulated number of seconds during a specified time interval. This latter monitor is designed to handle dynamic instability possibilities such as limit cycling.

In the early design phases it was thought prudent to design the SMCS so that it would operate only in conjunction with the SCAS. Thus, any unforseen hardover vane failure effects on rigid-body motion would be attenuated. In retrospect, it appears that this design approach is overly conservative because of the SMCS vane small size.

The SMCS is not designed to operate continuously. There is a cockpit switch enabling the crew to turn the system on prior to low-level flight and turn it off afterwards. Also, while not specifically noted on the block diagram, there is a switch mechanized so that the system is disabled automatically as the landing gear is lowered and enabled as the gear is raised. This feature is necessary to preclude the vane from inducing inertia reaction forces in the absence of aerodynamic forces which will cause instabilities (the so-called "tail wags dog" phenomenon) if the switch is accidently left on or during ground testing.

SMCS Vane Wind Tunnel Test Results

The original aerodynamic characteristics of the vane were estimated using a lifting surface theory which assumed the fuselage to act as an infinite end plate. These data sufficed for preliminary design analyses; but as more refined analyses were needed to support detailed design, wind tunnel testing was required to define the actual effectiveness of the SMCS vane and its interference effects on other aircraft components. Two different models were used in these tests: (1) a 0.036-scale force model, and (2) a 0.1-scale forebody force model. Tests were run on both models in the North American Aerodynamics Laboratory (NAAL) Tunnel at M = 0.23 and in the Trisonic Wind Tunnel (TWT) at M = 0.85. The low-speed tests were run to provide physical understanding of the various flow phenomena and indicate trends to be used in the development of the SMCS vane configuration. The high-speed tests were run to provide design verification and information for the B-1 ride quality analyses. Emphasis in this report will be placed on displaying the M = 0.85 data.

It is of interest to note that an extensive literature search revealed that little or no aerodynamic data have been generated on the type of configuration being discussed here, particularly with respect to the relatively large deflections and the differential deflection feature.

Determination of vane local flow angle. - Before proceeding, it is desirable to establish an important basis for comparisons of test data. pertinent to this is the definition of the local angle of attack of the aerodynamic surface. The basic vane panels are situated on the nose of the aircraft and project perpendicular to the mold line at a dihedral angle of -30°. Thus the local angle of attack on a vane panel is composed of the component of the vehicle angle of attack resolved into a plane perpendicular to the plane of the panel; the local downwash angle, induced by the fuselage nose, in the plane perpendicular to the plane of the panel; and the angle of attack caused by deflection of the vane panel about its axis of rotation from a reference plane parallel to the fuselage reference line (FRL).

The local angle of attack, then, defined in terms of these components is:

$$\alpha_V = \alpha\cos\Gamma - \varepsilon + \delta$$

where

α_V Angle of attack of vane panel, in plane perpendicular to vane surface ($+\alpha_V$ produces + normal force)

α Angle of attack relative to fuselage reference line

Γ Vane dihedral angle

ε Angle of downwash in plane perpendicular to vane panel surface (opposite sense of α)

δ Control vane deflection (same sense as α)

The effective downwash angle at the vane location has been determined by the following method:

(1) The variation of airplane pitching moment with angle of attack was measured with the vane off and with the vane on at various deflections.

(2) The incremental pitching moment between vane off and vane on and deflected were plotted against geometric angles of attack at the vane ($\alpha\cos\Gamma + \delta$) for various airplane angles of attack.

(3) For any given airplane angle-of-attack curve, the value of ($\alpha\cos\Gamma + \delta$) at which the incremental pitching moment was zero was taken to be equal to the downwash angle.

The downwash angles determined by this method from the test data at M = 0.85 are given in figure 16. The estimated accuracy of this method for determining ε is $\pm 1/2$ degree.

Original vane characteristics ($\Lambda_V = 35^\circ$). - Figure 17 displays the vane normal force effectiveness data for the original vane ($\Lambda_V = 35^\circ$). As shown, the data are the normal forces (in coefficient form) produced by moving the vanes symmetrically through the range of available deflections. It was the character of these data that led to the previously discussed study of the local flow angle at the vane. It was observed that the normal force produced by a $+20^\circ$ deflection at $\alpha = 0^\circ$, was far greater than the normal force produced by a $+13^\circ$ deflection at $\alpha = 8^\circ$, where it was assumed that the local angle of attack on the vane was composed of the aircraft angle of attack times cos Γ plus the vane deflection ($\alpha_V = \alpha\cos\Gamma + \delta$).

The data of figure 17 were the deciding factors in seeking a new vane configuration. The loss of normal force effectiveness at $\alpha = 4^\circ$ was judged to be too severe for positive vane deflections.

Plotting the normal force data against the vane local angle of attack, α_V, gave additional valuable insight into the flow phenomenon around the vane. (The reader is reminded that C_N is in the aircraft axis system, while α_V is in a plane perpendicular to the plane of the vane.) As demonstrated in figure 18, the data plotted in this manner define a single normal force curve. The characteristics of the curve on the negative attitude side were evaluated as quite satisfactory, but the rolloff of the force characteristics above $\alpha_V = +10^\circ$ was judged unsatisfactory.

The side force effectiveness data resulting from differential deflection of the vanes are shown in figure 19. Here, as in the case of the normal force effectiveness data, there was concern for the fact that the effectiveness dropped off markedly with angle of attack.

Modified vane characteristics ($\Lambda_V = 60^\circ$). - The reader has been exposed earlier to the analytical effort that was initiated to define a new planform

Note: ε is measured in plane perpendicular to control surface, sense opposite to sense of α.

α is measured in vertical plane of symmetry relative to FRL.

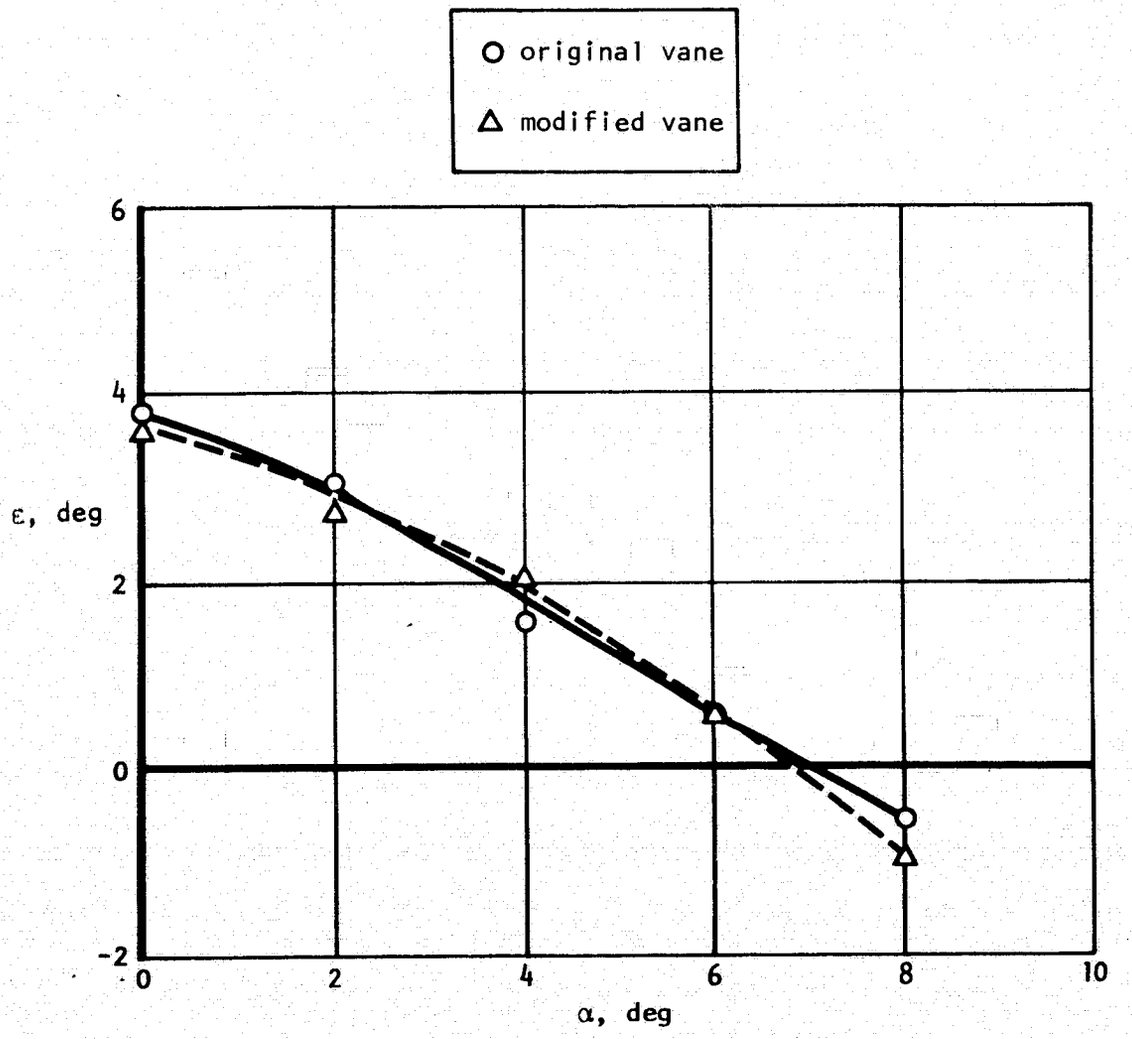

Figure 16. - Vane-fuselage interference downwash angle versus vehicle angle of attack, M = 0.85.

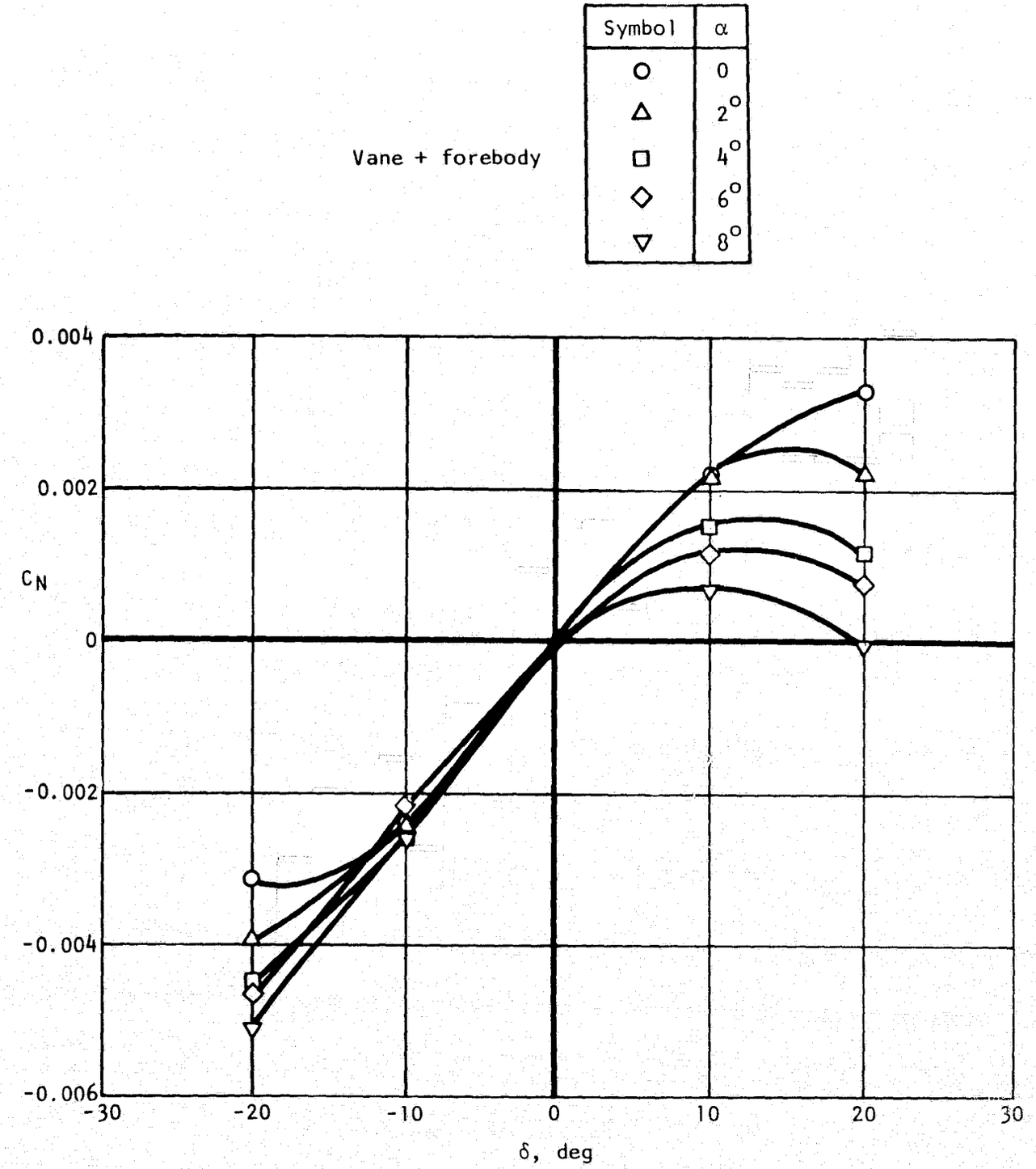

Figure 17. -Original vane normal force effectiveness, M = 0.85.

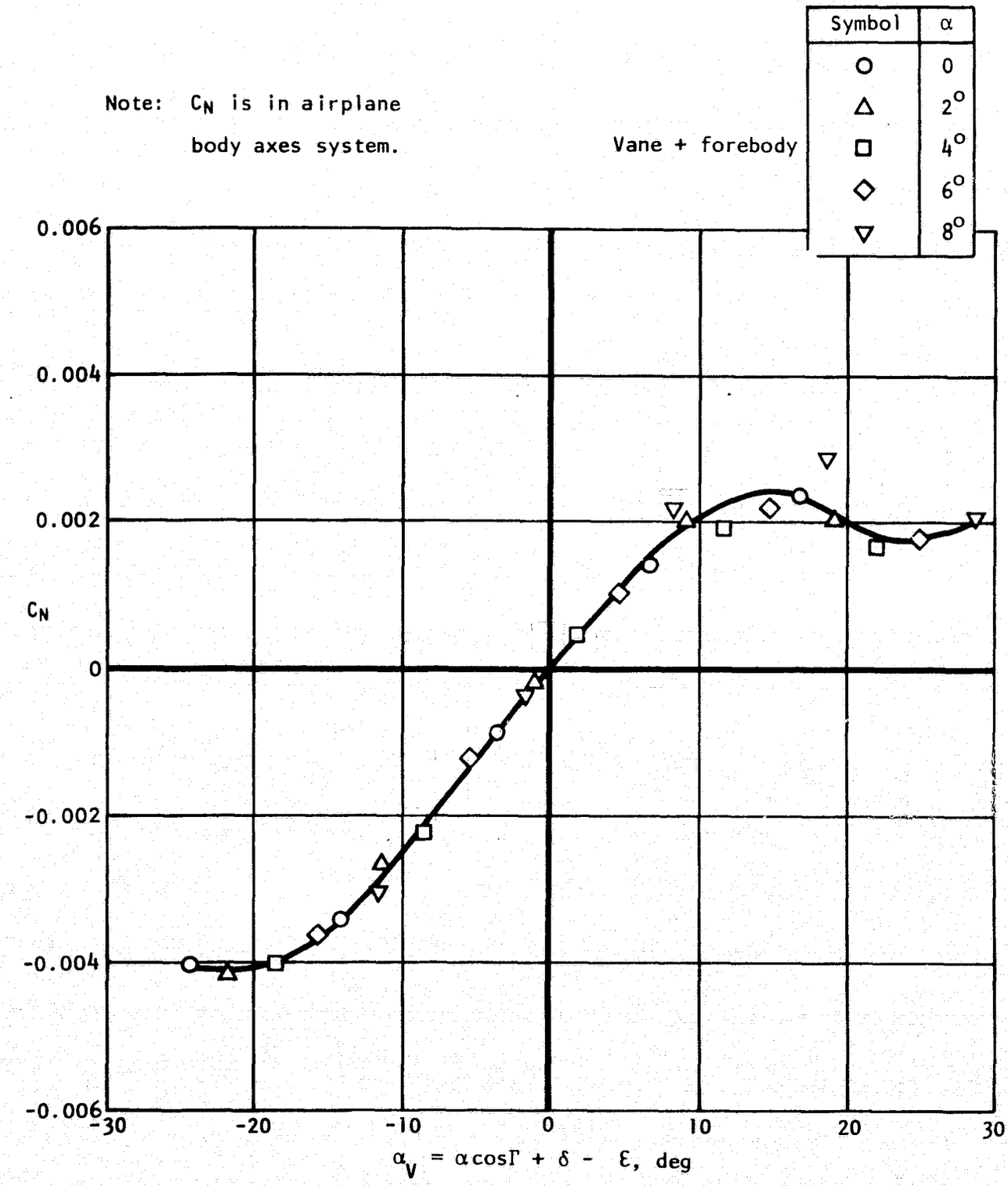

Figure 18. - Modified vane normal force characteristics versus vane local angle of attack, M = 0.85.

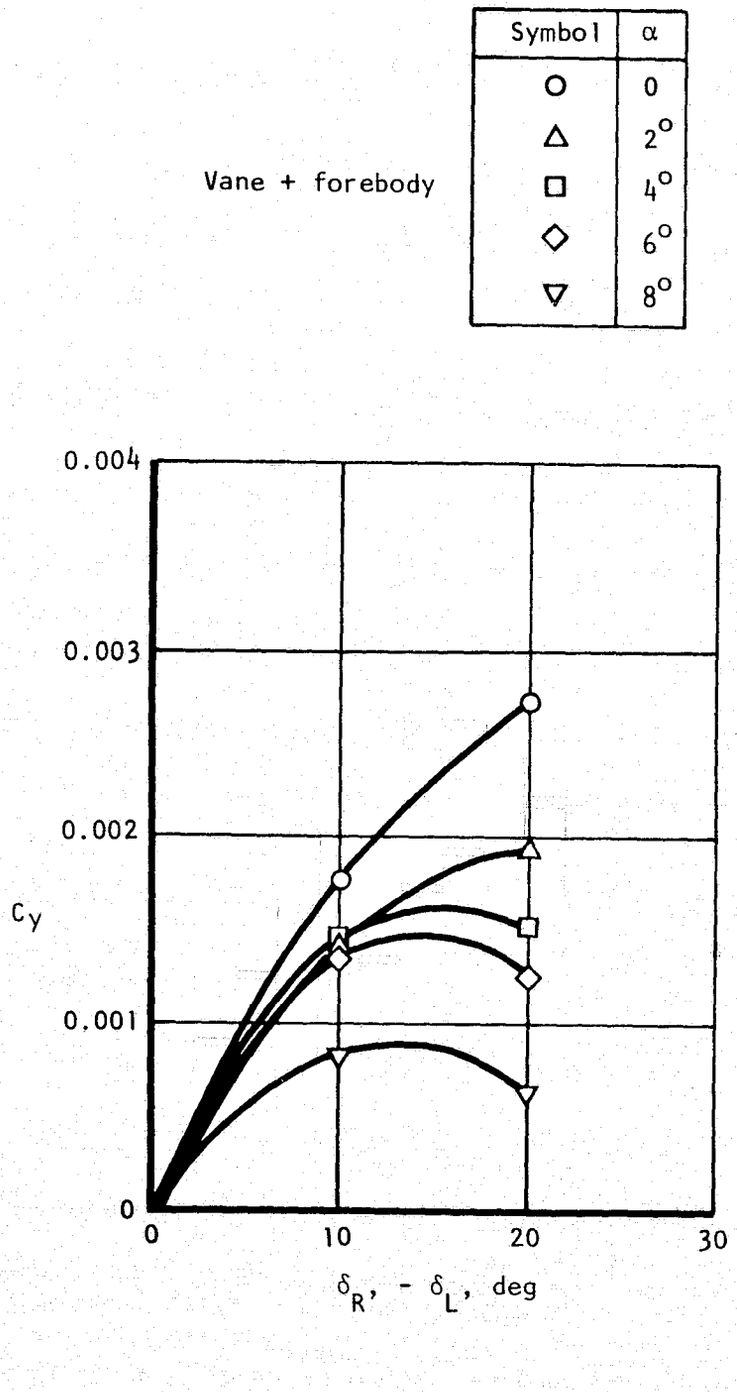

Figure 19. - Original vane side force effectiveness, M = 0.85.

which would hold both normal force and side force effectiveness to an acceptable level over the required range of vane deflections and angles of attack of the aircraft. All basic geometric characteristics of the original vane were retained in the modified vane with the exception of the leading edge sweep angle which was changed from 35° to 60°.

As can be seen by comparing the normal force effectiveness data of the $\Lambda_V = 60°$ vane in figure 20 with the similar data for the $\Lambda_V = 35°$ vane in figure 17, a significant improvement over the whole angle-of-attack region was obtained with the modified configuration.

The normal force curve for the modified vane shown in figure 21 has linear characteristics for the critical positive α_V to over +15°, while for the negative α_V the curve is linear to over -25°, the maximum angle investigated. A detailed comparison of the $\Lambda_V = 60°$ curve of figure 21 with the $\Lambda_V = 35°$ curve of figure 18 will reveal that the slight loss of normal force curve slope predicted by the analytical data of figure 14 did not occur. The asymmetry of the large angle data is attributed to induced loads on the fuselage.

The side force effectiveness for the modified vane was considerably improved in linearity, as well as in magnitude, over that for the basic vane as comparison of figure 22 and figure 19 demonstrates.

It was obvious that symmetric deflections of the vane would not produce coupling forces into the side force axis. It was not obvious, however, that antisymmetric (or differential) deflections would not produce coupling forces into the normal force axis. In fact, the asymmetry of the normal force curve gave a clue to the possibility of coupling. Normal force data recorded at the same time as the side force data, which produced the effectiveness data of figure 22, provided the coupling information displayed in figure 23. Up through 10° differential deflection, no coupling is induced. At anticipated flight attitudes between $\alpha = 0$ to +4°, the coupling is light to moderate at maximum differential deflection of 20°.

In operation, the SMCS commands both symmetric and differential deflections simultaneously. To obtain some insight into coupling induced in these circumstances, tests were run where a symmetric deflection of first -10° and then +10° was set and differential deflections of ±10° were superimposed. The results of these tests are shown in figures 24a and 24b, respectively. Under these rather severe conditions, the coupling is slight to moderate over the angle-of-attack range.

The impact of this coupling it was felt, would be minimized in a practical SMCS operational context by the fact that the normal axis feedback loops would quickly damp out these potential excitations.

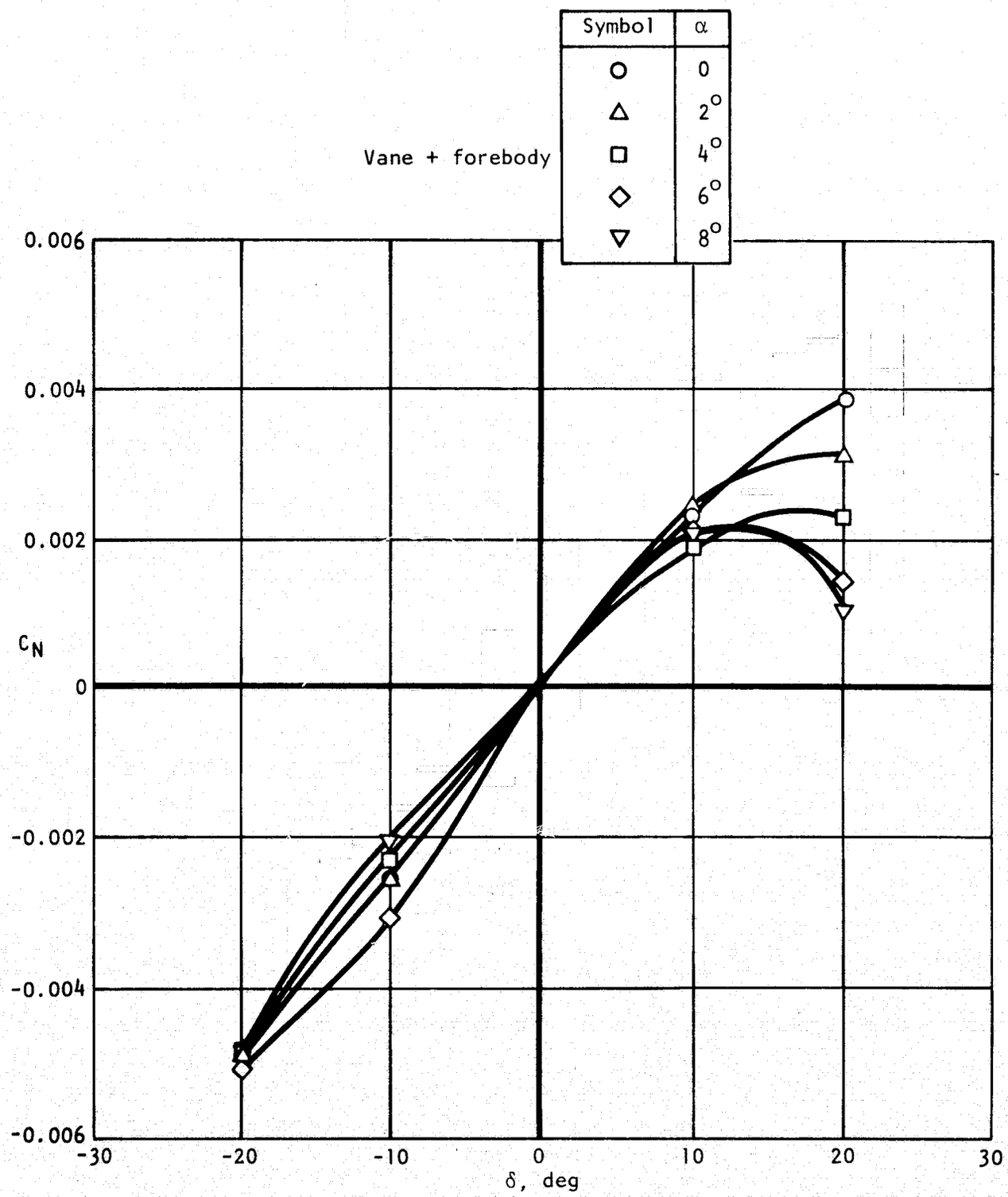

Figure 20. - Modified vane normal force effectiveness, M = 0.85.

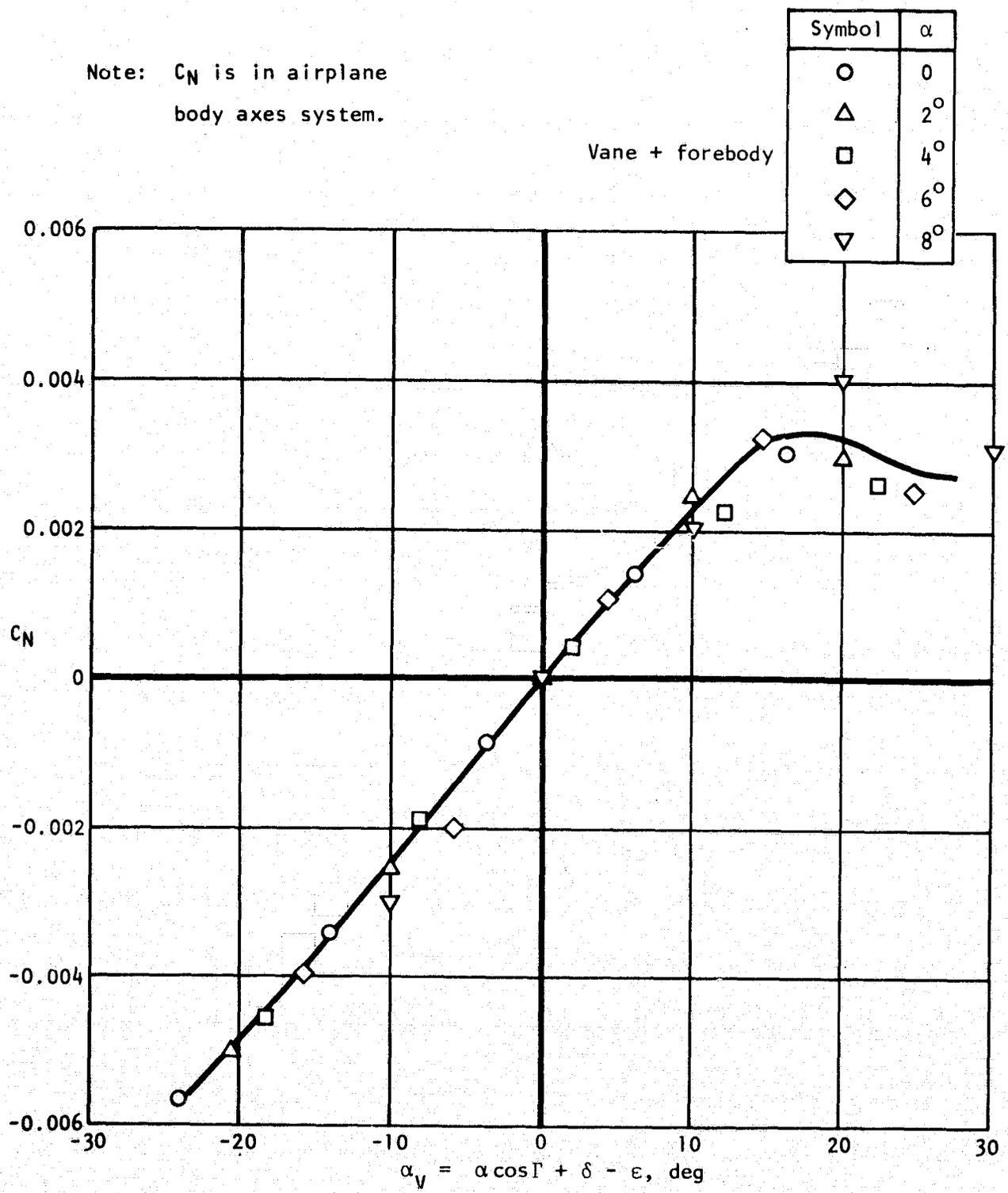

Figure 21. - Modified vane normal force characteristics versus local angle of attack, M = 0.85.

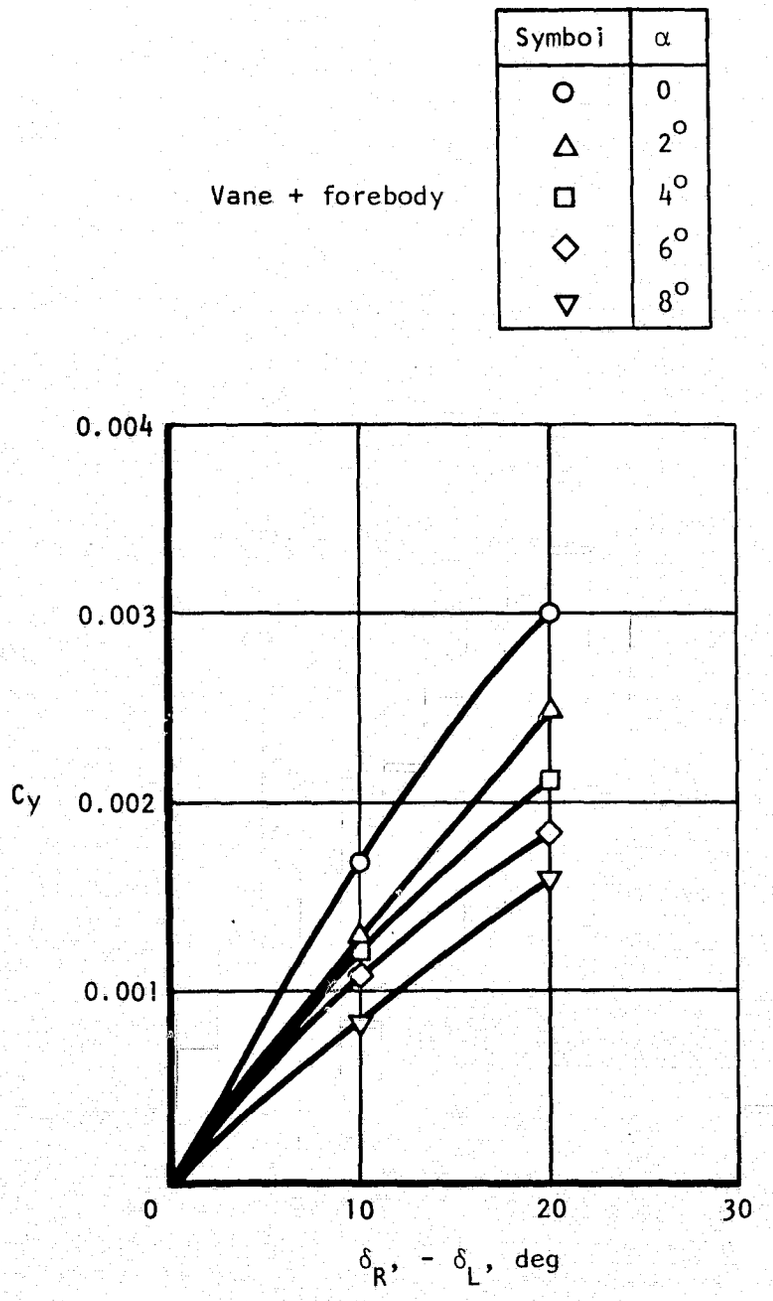

Figure 22. - Modified vane side force effectiveness, M = 0.85.

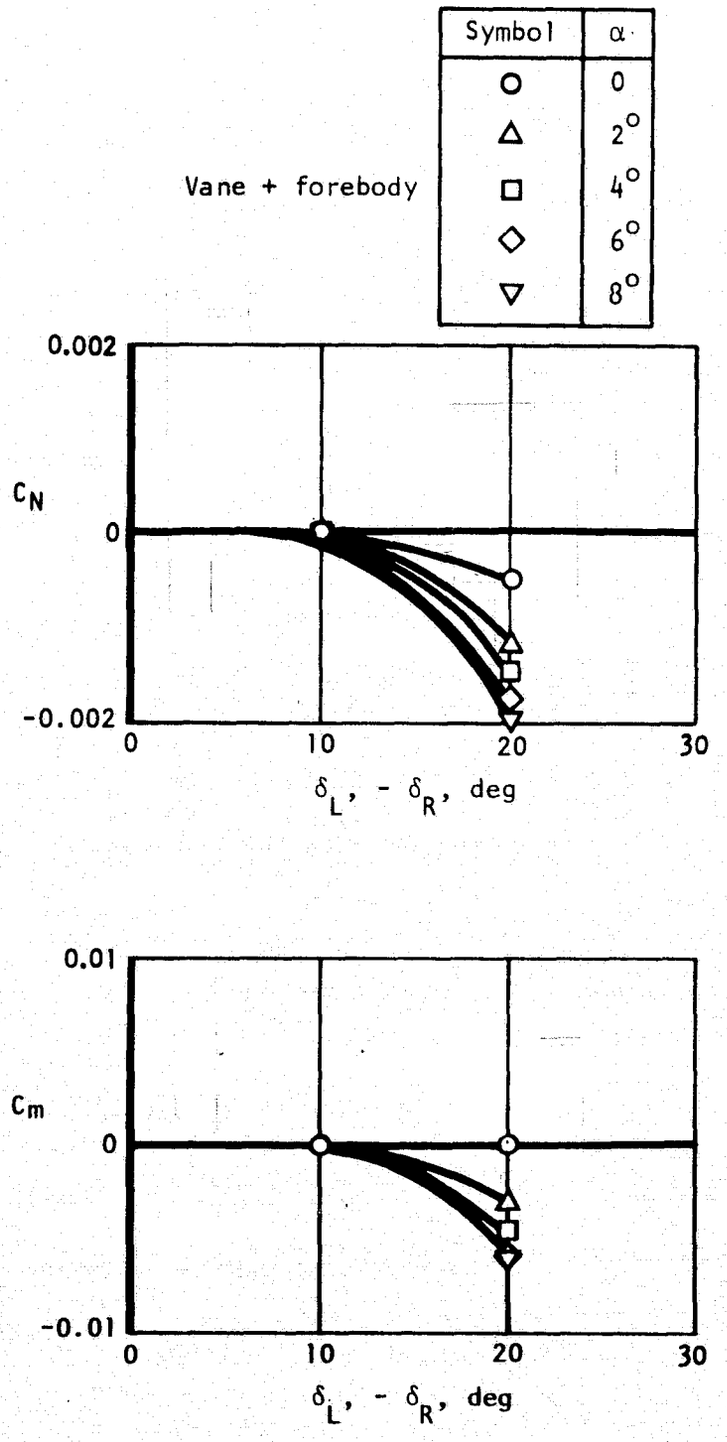

Figure 23. - Modified vane normal force and pitching moment coupling due to antisymmetric deflections, M = 0.85.

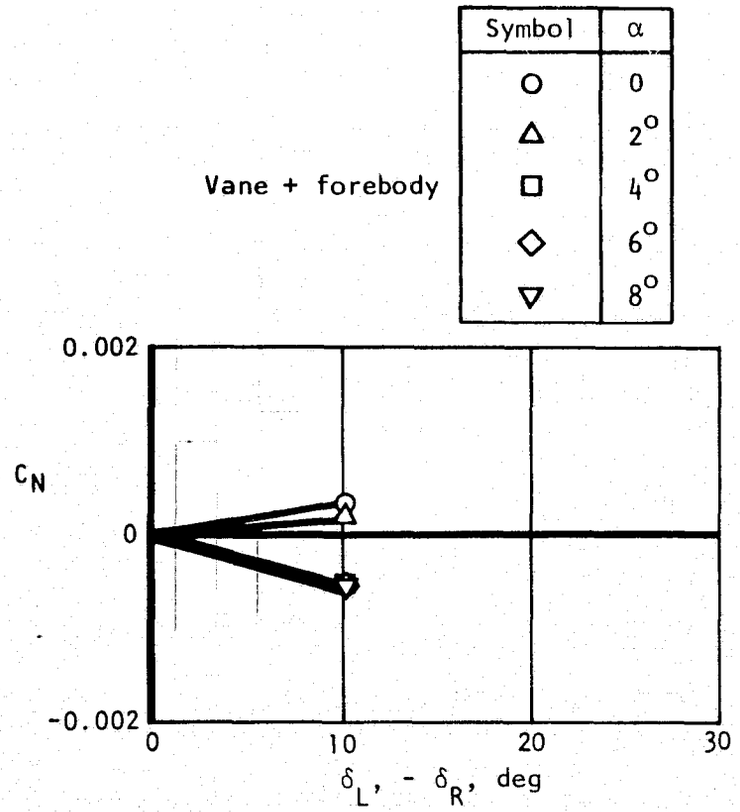

(a) -10° Mean symmetric deflection

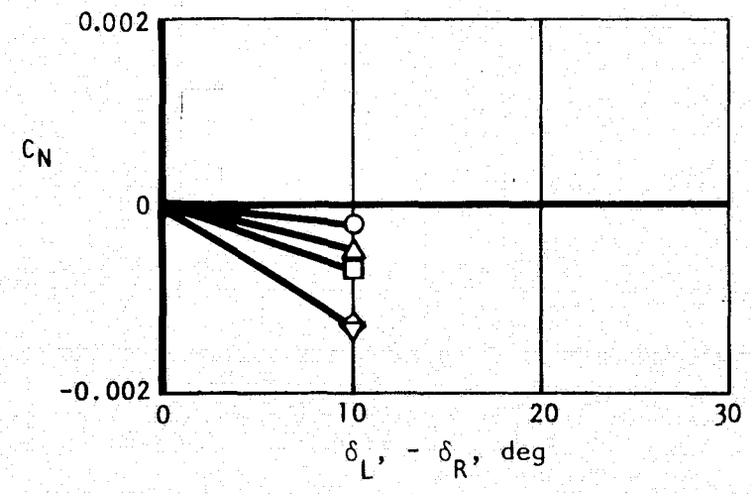

(b) +10° Mean symmetric deflection

Figure 24. - Modified vane normal force coupling due to asymmetric deflections, M = 0.85.

Vane interference effects. - When the SMCS vane panels are deflected, either symmetrically or antisymmetrically, the increase in normal force is accomplished by the development of circulation around the vane panel. This circulation is shed from the trailing edge of the vane in the form of trailing vortices. These vortices, which quickly roll up into distinct vortex cores and are convected downstream, cause regions of interference flow to be developed over the other components of the aircraft such as the body, wings, and empennage. These interference flows induce pressure fields, and hence net forces, on these components which may be significant when compared with the forces applied to the aircraft by the vane panels themselves.

The purpose of this section is to describe the interference effects that have been observed during wind tunnel tests of the SMCS vanes in conjunction with various combinations of aircraft components. The interference contributions to vertical and lateral effectiveness will be discussed separately; first vertical then lateral interference effects will be covered. Data for both the original (35^{o} sweep) and modified (60^{o} sweep) vanes will be reviewed.

The interference between the vane and the forebody may be seen in the asymmetry of the normal force curves of figures 18 and 21. This asymmetry arises because of (1) the location of the vane on the lower part of the fuselage cross section; and (2) the asymmetric shape of the forebody about a horizontal plane. The interaction between the upwash or downwash (depending on the sign of the vane deflection) field emanating from the vane panels and the pressure distribution on the body is a complicated one. It appears that the vane induces a downward load on the forward part of the body, irrespective of the sign of the vane deflection. Thus, the magnitude of the vane contribution to the body is reinforced for negative vane deflections, but degraded for positive vane deflections. The source of the downward load may be the local pressure interaction between the vane and the body surface, or the low-pressure regions induced on the body surface by the vortex emanating from the vane, or a combination of these two effects. At least some of the downward load appears to act on the body aft of the vane, since the effect is more pronounced in the total normal force than in the pitching moment, indicating an aftward shift in the center of pressure.

An indication of the magnitude of this interference may be seen by comparing the predicted effectiveness curve for the modified vane with the actual effectiveness derived from wind tunnel data. Such a comparison is made in figure 25 on the basis of absolute values of pitching movement versus deflection.

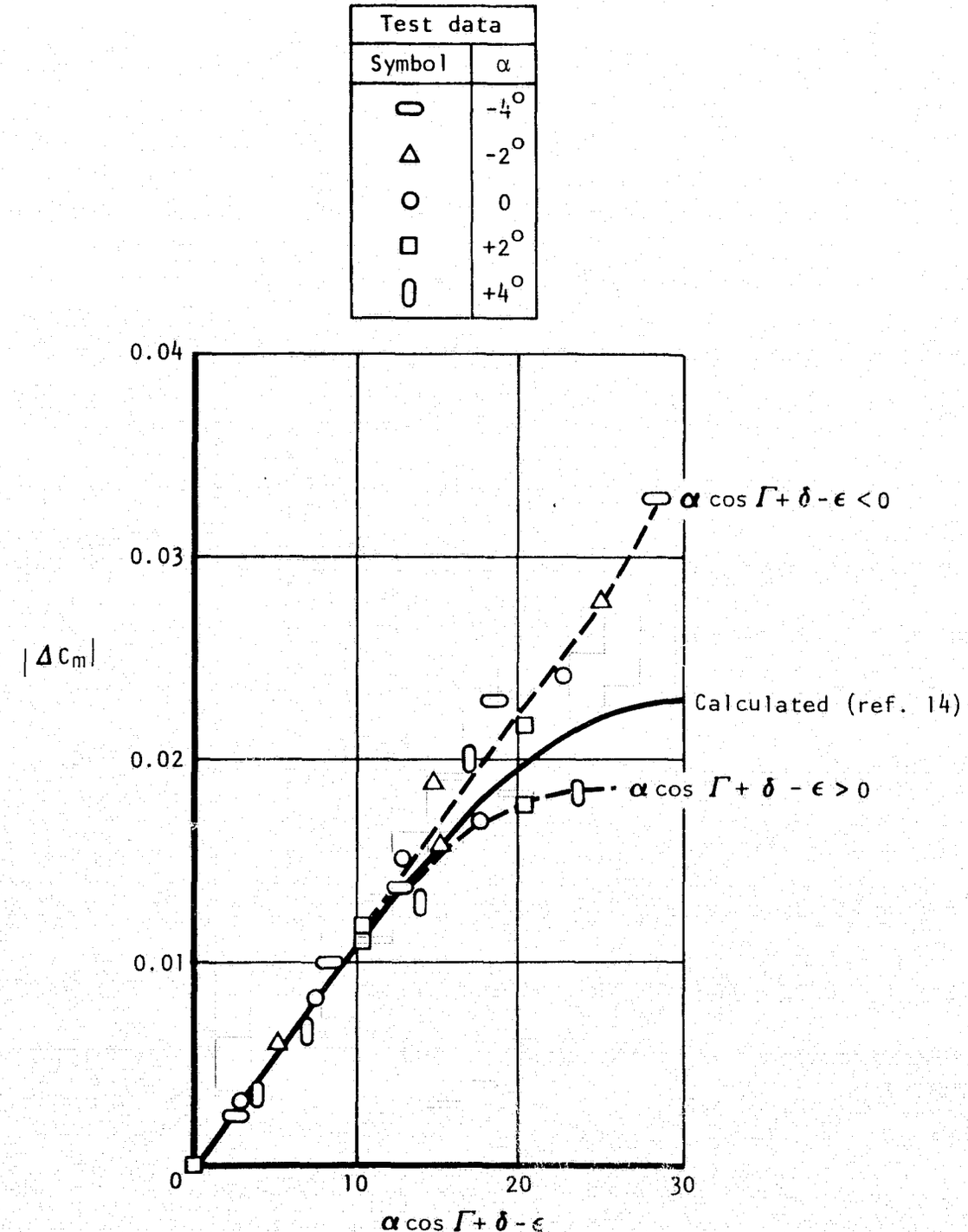

Figure 25. - Nonlinear vane effectiveness comparison of test versus calculated data.

The path of the vortices leaving the tip regions of the vane is highly dependent on both airplane angle of attack and vane deflection. In order to obtain a qualitative understanding of the flow-field behavior, smoke flow photographs were obtained during low-speed wind tunnel tests. Smoke released by a probe positioned ahead of the tip of the vane is entrained in the vortex flow, which is a low-pressure region. Figures 26 and 27 are sketches made from typical smoke flow photographs. In figure 26, the vane deflection is $+20^{o}$, and the airplane angle of attack varies from $+4^{o}$ to -4^{o}. At $+4^{o}$, the tip vortex trails back from the vane until it is strongly affected by the flow about the wing glove region. The vortex then splits into two separate wake regions, passing under and over the wing. At 0^{o}, the entire vortex region passes below the airplane, between the nacelles, but close to the surface of the body. At -4^{o}, the vortex region passes down and away from the airplane, being about a full diameter below the fuselage at the aft end.

In figure 27 the vane deflection is -20^{o}, and the vortex path is quite different for the same angles of attack. At $+4^{o}$, the vortex passes up and over the wing and the fuselage, and passes very near the horizontal tail close to the centerline of the body. At 0^{o}, the vortex is split by the wing glove region, while at -4^{o}, the vortex passes underneath the wing and fuselage, but close to the surface. The exact location of the smoke in the photographs is sensitive to the probe location, and thus should be used only for a qualitative indication of the interference effects.

It should be noted here that the normal force and pitching moment data for the built-up configuration may be used to provide quantitive measurement of the forces generated on the various components by steady-state deflection of the vane. They cannot, however, be used directly to describe the aerodynamic input of the SMCS to vehicle dynamic response. To adequately predict the effects of the SMCS operating in response to turbulence, these incremental loads must be applied with proper phasing due to flow disturbance transport time lags. It will be recalled that the controlling input to a mode was called a generalized force which is made up of a point force at location "q" (in the simplified approach) multiplied by the local deflection of a particular mode $\left(\sum_{q=1}^{m} F^{q} \phi_{i}^{q} \right)$.

Figure 28 shows pitching moment data for a buildup of aircraft components taken for the original vane at M = 0.85 at 2^{o} angle of attack, approximating the normal trim angle. Pitching moment data are used here because the magnitude of normal force measurements were not accurate enough to obtain incremental

Note: Sketches made from actual smoke probe test photographs.

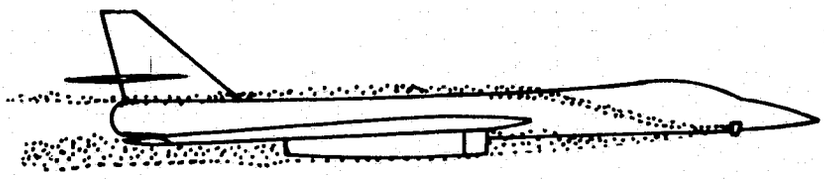

(a) $\alpha = +4^{o}$

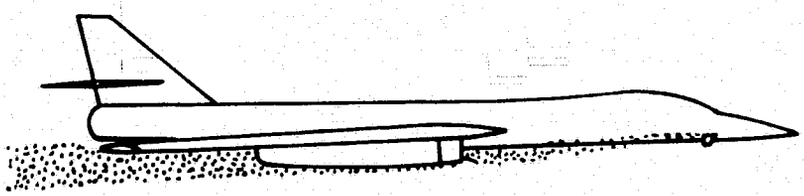

(b) $\alpha = 0$

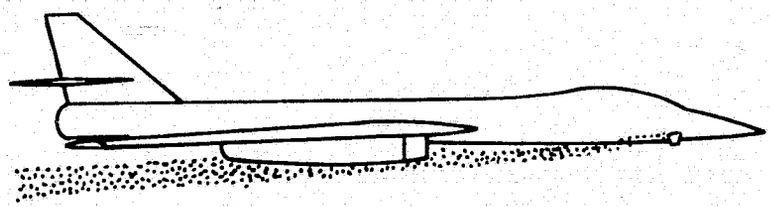

(c) $\alpha = -4^{o}$

Figure 26. - Interference flow from structural mode control vane, low speed, $\delta = +20°$.

Note: Sketches made from actual smoke probe test photographs.

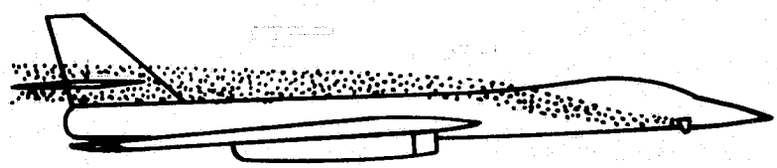

(a) $\alpha = +4^{o}$

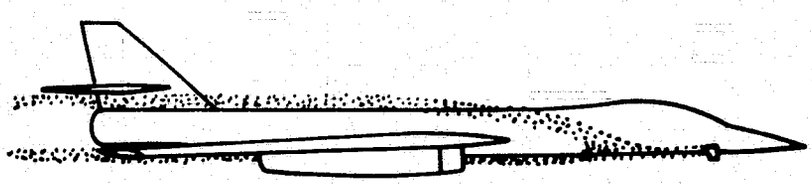

(b) $\alpha = 0$

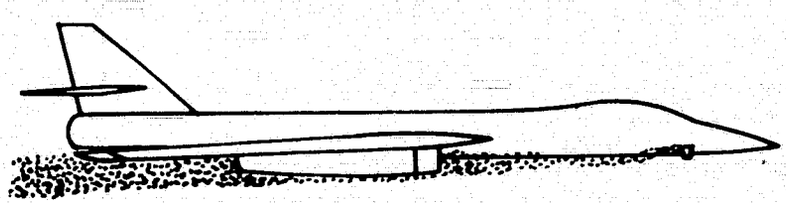

(c) $\alpha = -4^{o}$

Figure 27. - Interference flow from structural mode control vane, low speed, $\delta = -20°$.

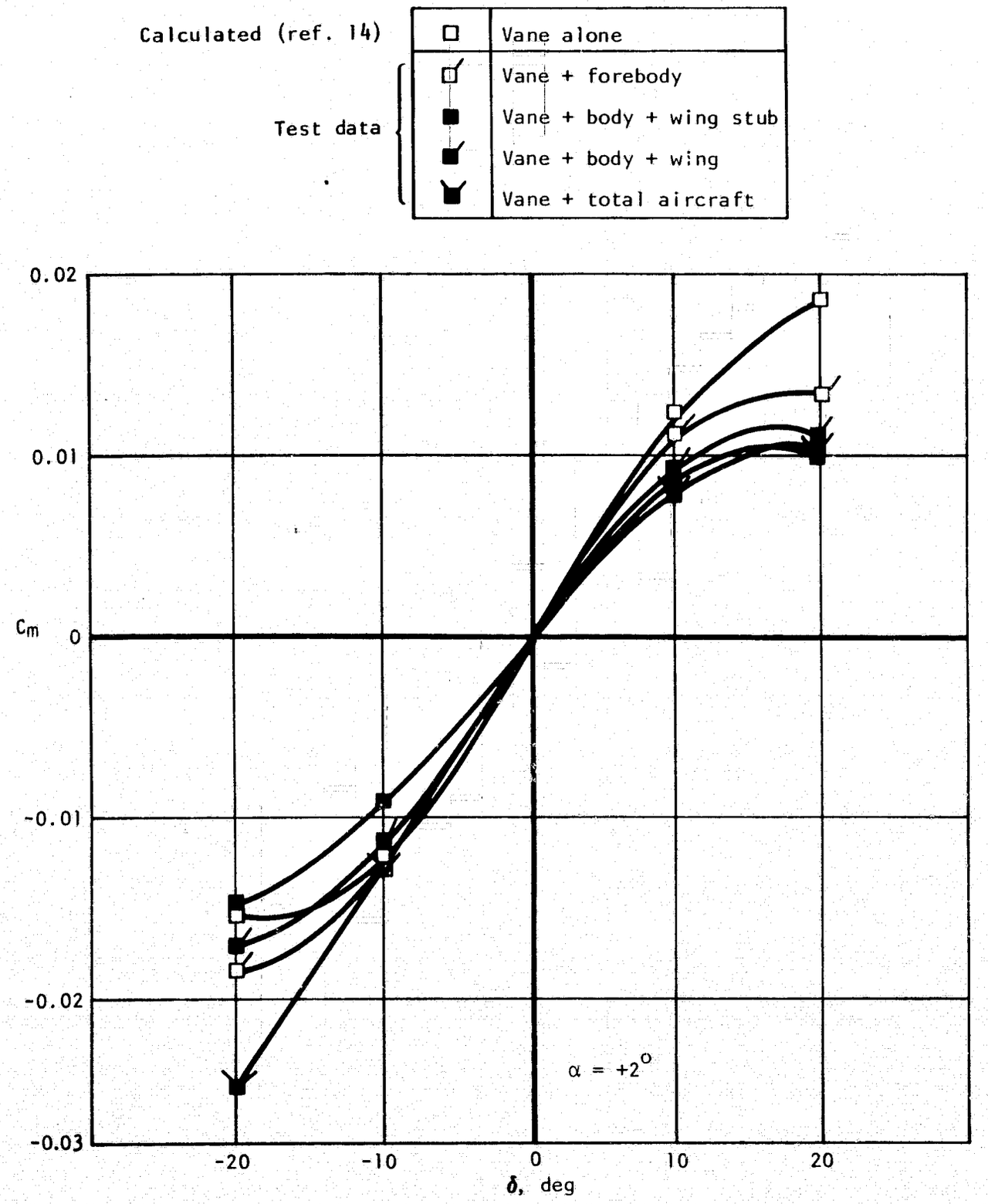

Figure 28. - Original vane pitching moment effectiveness interference effects, M = 0.85.

vane data for the small scale (0.036) buildup models tested. The significant interference load seems to be that of the forebody, but data for negative vane deflections show an additional effect on the horizontal tail. Buildup pitching moment data for the modified vane are shown in figure 29. For this configuration, forebody interference loads are greatly reduced, but there are additional interference effects on the wing stub and afterbody. For large negative vane deflections, there is still a large horizontal tail load.

Interference effects of a similar nature to those described in previous paragraphs have also appeared in the lateral effectiveness data. The lateral interferences, however, have proven to be a more difficult phenomena to understand due to the necessity of considering each vane panel and its interaction with the body separately. A schematic of explanation of the vane-forebody interference phenomenon is given in figure 30. In figure 30a, the vanes are deflected symmetrically in the positive direction. The trailing vortex behind each vane induces a low-pressure (suction) region as it passes the side of the body. The lateral components of the vane forces will cancel, as will the induced pressure forces on the body aft of the vane. In the case of antisymmetric deflection, as shown in figure 30b, the lateral components of the vane forces will add. The induced pressure forces on the body will tend to cancel, but may not cancel exactly, due to the sensitivity of the vortex position to vane deflection. Furthermore, the amount of induced pressure force is sensitive to angle of attack.

It appears that the canceling pressure load induced by the negatively deflected vane panel has a greater effect than the reinforcing pressure load induced by the positively deflected vane panel (figure 30c). This difference becomes more pronounced as the angle of attack increases; that is, as more of the vortex core sweeps up along the side of the body, as shown in figures 26 and 27.

In order to confirm the aforementioned hypothesis about the observed characteristics of the side force data, a single vane panel (right) of the modified vane configuration was tested at various combinations of surface deflection and body angle of attack. Figure 31 displays the data. The data for the vane off and at 0^{o} indicate a sizeable asymmetric lateral force for this model.

Using these data, side force data for two vane panels deflected antisymmetrically was constructed, and are compared in figure 32 with two panel data. This figure shows that the majority of the observed side force characteristics can be explained by use of the single panel data, and the interaction between left and right panels is negligible when compared with the single vane-body interaction.

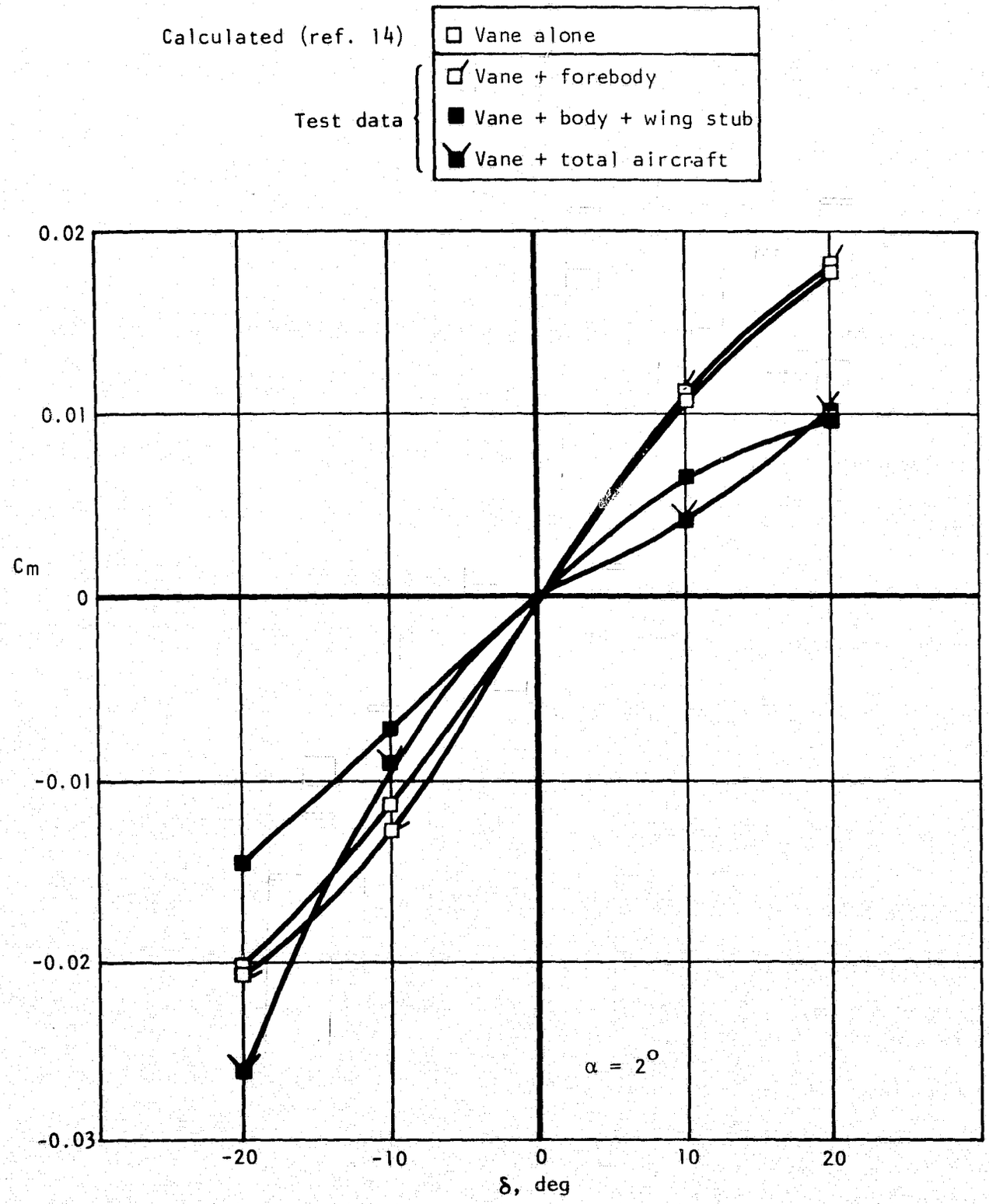

Figure 29. - Modified vane pitching moment effectiveness interference effects, M = 0.85.

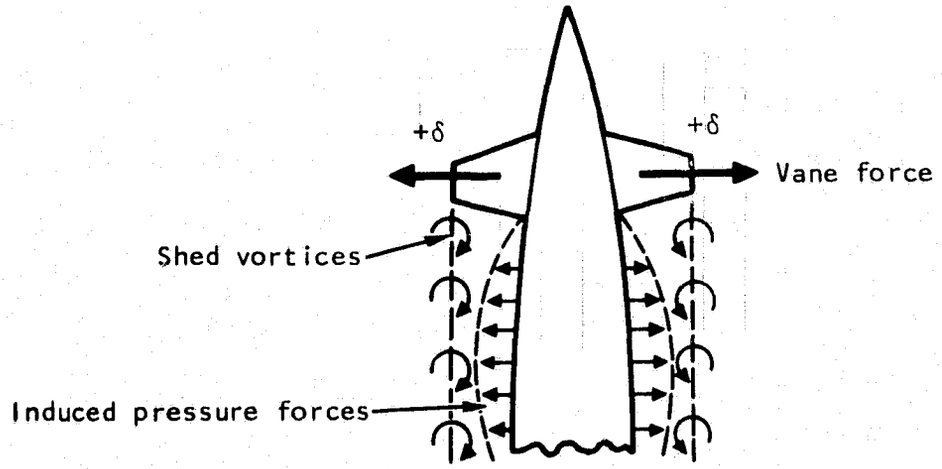

(a) Symmetric vane deflection

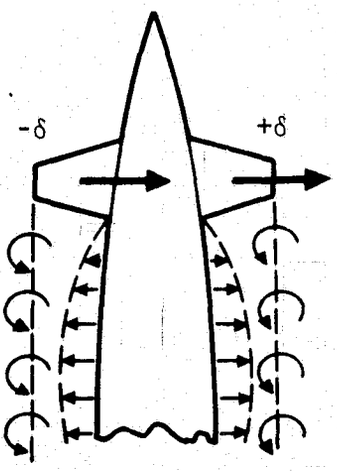

(b) Antisymmetric vane deflection

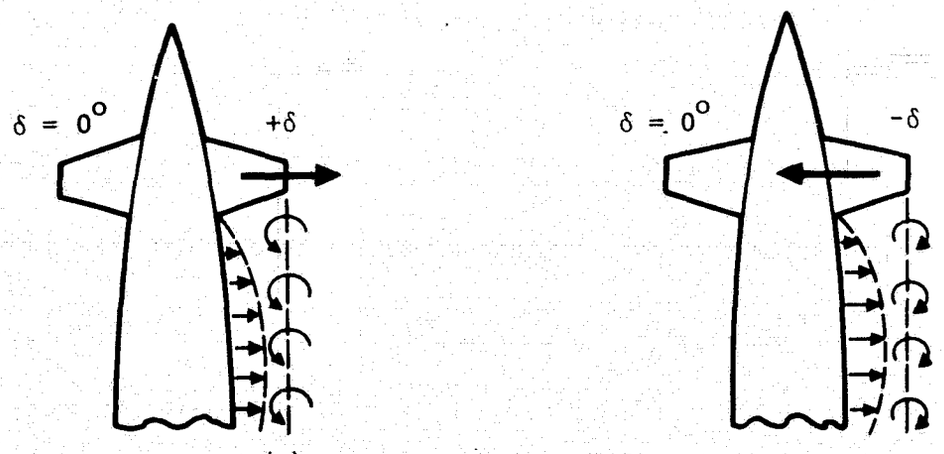

(c) Asymmetric vane deflection

Figure 30. - Schematic of lateral interference phenomenon on forebody.

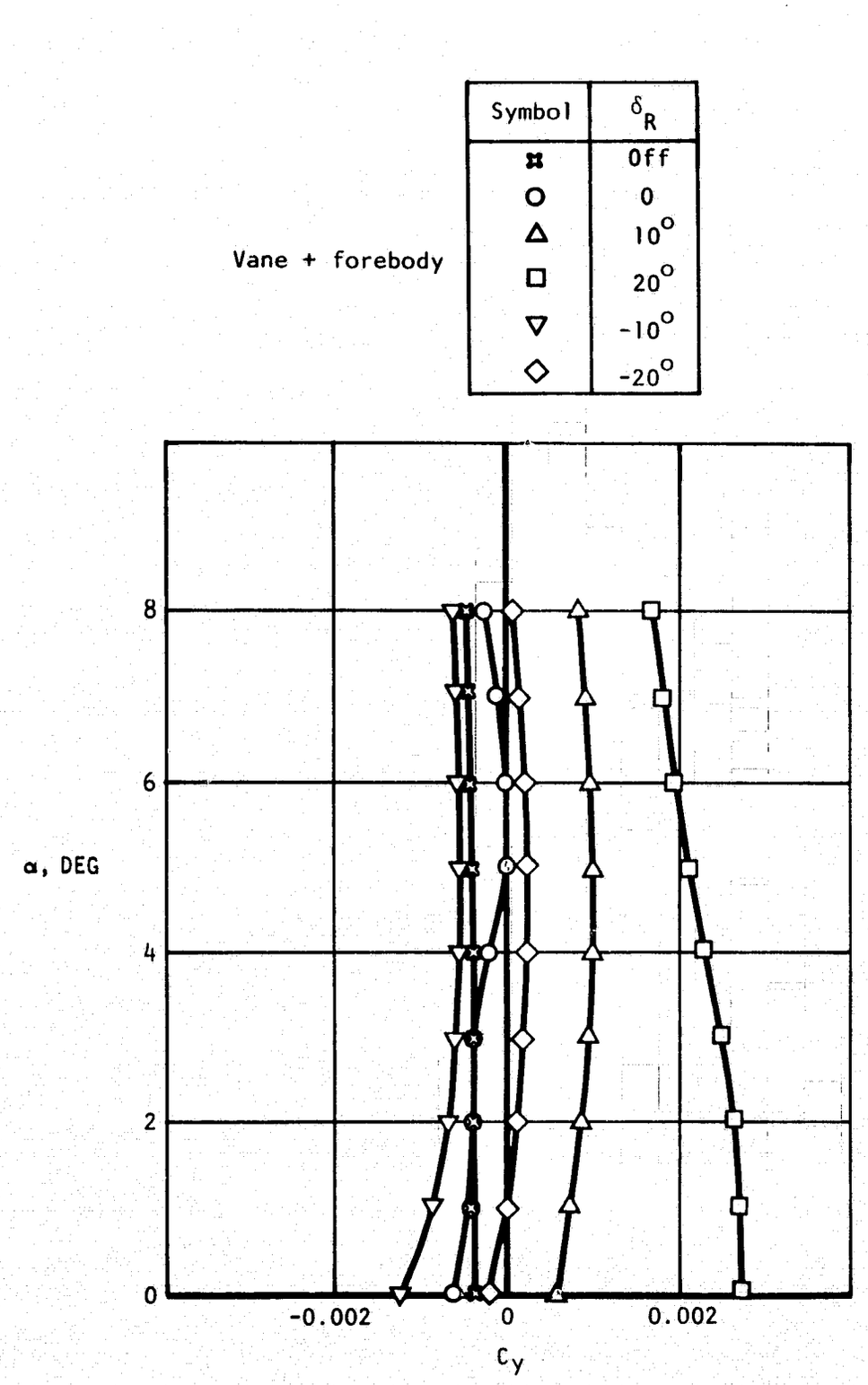

Figure 31. - Modified single vane panel side force effectiveness, M = 0.85.

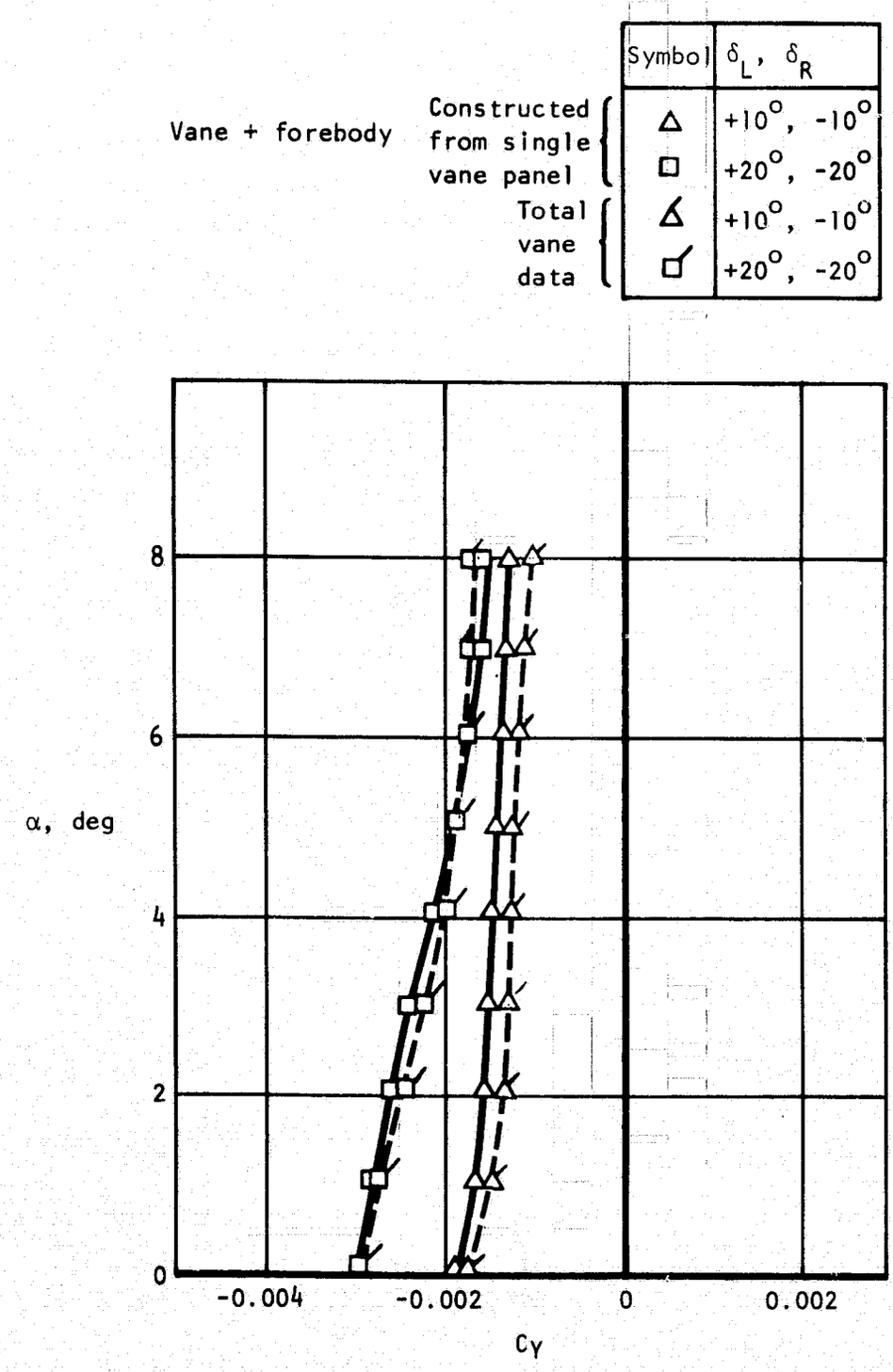

Figure 32. - Comparison of modified vane side force effectiveness for two panels from test and constructed from single panel data, M = 0.85.

As the vortices from the vanes pass by the wings, nacelles, empennage, and aft end of the body, additional side forces and yawing moments are induced. These are, like the vertical interference effects, dependent on airplane angle of attack, vane deflection, and mach number. Variations of side force with angle of attack are given in figures 33a through 33c for the original vane, and in figures 34a and 34b for the modified vane. Here separate data are given for the vane + body + wing stub (glove region present, but outer wing panel removed), vane + body + wing (original vane only), and vane + total aircraft. It may be noted that (1) the lateral interference effects are significant; (2) there is noticeable interference load due to the presence of the outer wing panel, which must be an additional induced body load since the wing has almost no effective lateral area; (3) some reverse total side force is possible at high angles of attack; and (4) the lateral interference effects are not significantly reduced for the modified vane configuration when compared with the original vane.

It should be noted that all of the wind tunnel tests run to determine vane interference effects were static tests. The vane on the actual aircraft, however, operates in a dynamic turbulent environment. Analysis conducted with the previously discussed interference effects, both included and excluded, show an impact of interference effects on vane performance. However, it is hypothesized that the atmospheric turbulence probably tends to break up the shed vane vortices and thus causes them to be ineffective in producing the interference effects on aircraft components some distance away from the vane. Interference effects on the nearby forebody should still be present. This will be difficult to prove. Analyses, though, are planned of flight conditions actually flown where accelerations are measured when the SMCS is operating. The degree to which flight test response data are matched with analytical data will provide some clue to vane effectiveness in a dynamic environment.

SMCS Performance

During the development of both the airplane and the SMCS, analyses were made on a continuing basis to monitor the SMCS performance relative to improving ride quality. One such cycle of analyses is discussed in this section.

The analytical models of the flexible aircraft used in these design studies employed modal (in contrast to direct structural influence coefficient) techniques. The mass characteristics and stiffness data were continually upgraded to reflect the airplane development; the stiffness and mass reflected in the data presented herein include ground vibration test results. Ten symmetric and 12 antisymmetric structural modes have been included in the analyses.

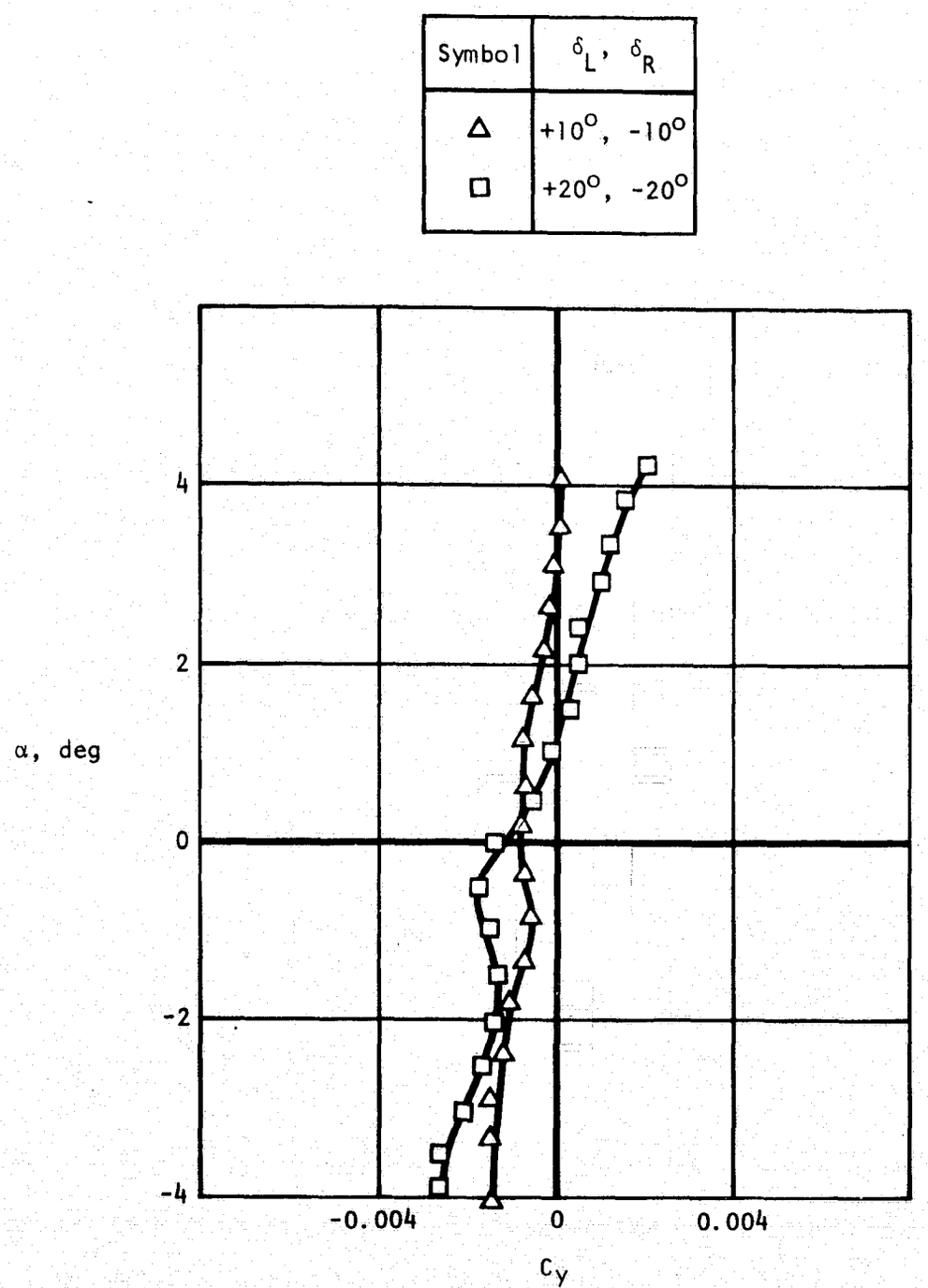

(a) Vane + body + wing stub

Figure 33. - Original vane side force as affected by aircraft components, M = 0.85.

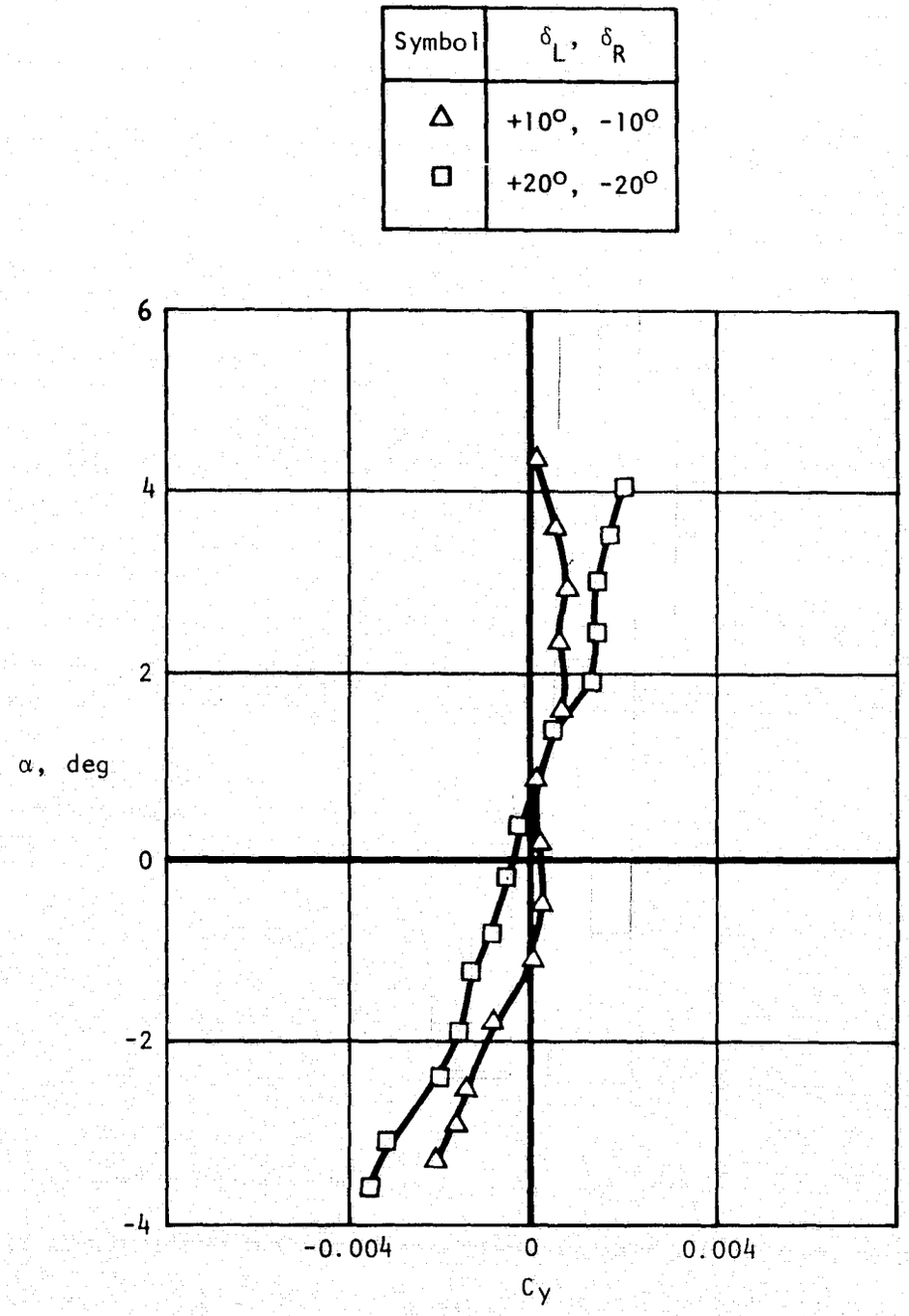

(b) Vane + body + wing

Figure 33. - Continued.

Symbol	δ_L, δ_R
△	+10°, -10°
□	+20°, -20°

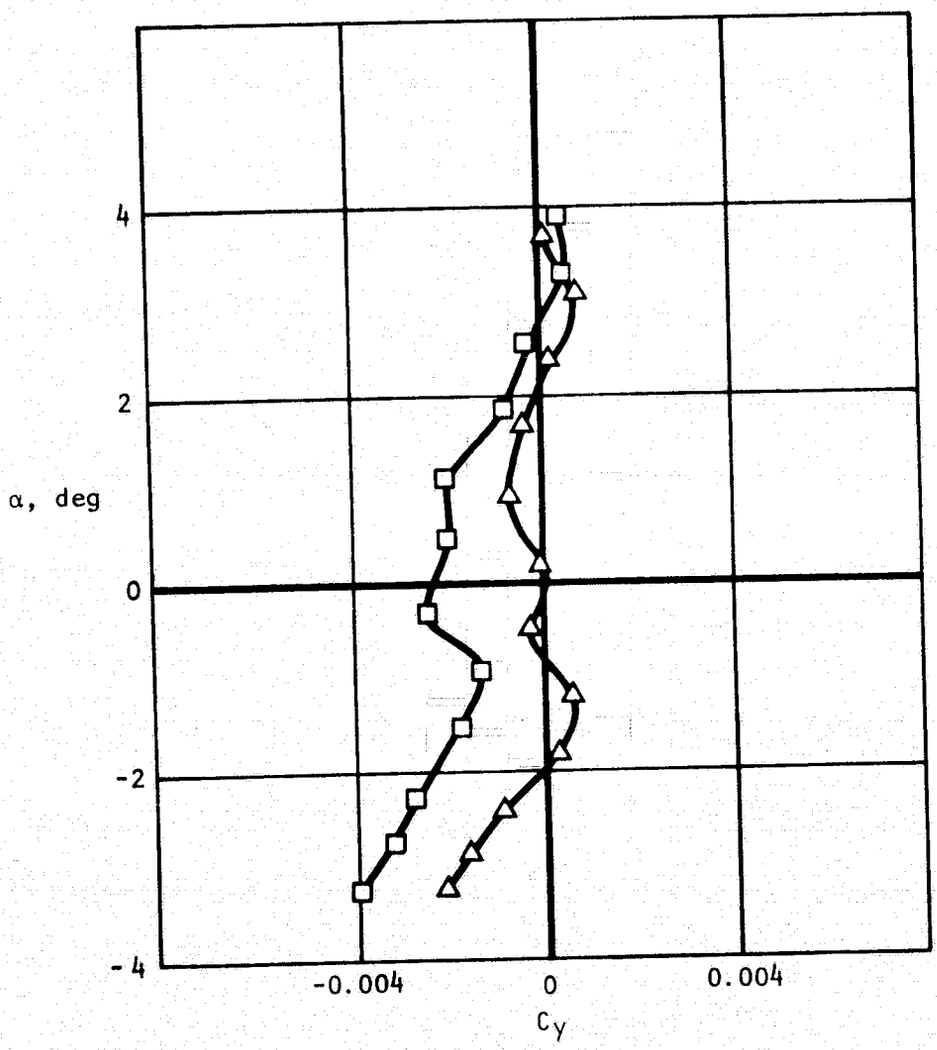

(c) Vane + total aircraft

Figure 33. - Concluded.

Symbol	δ_L, δ_R
△	+10°, -10°
□	+20°, -20°

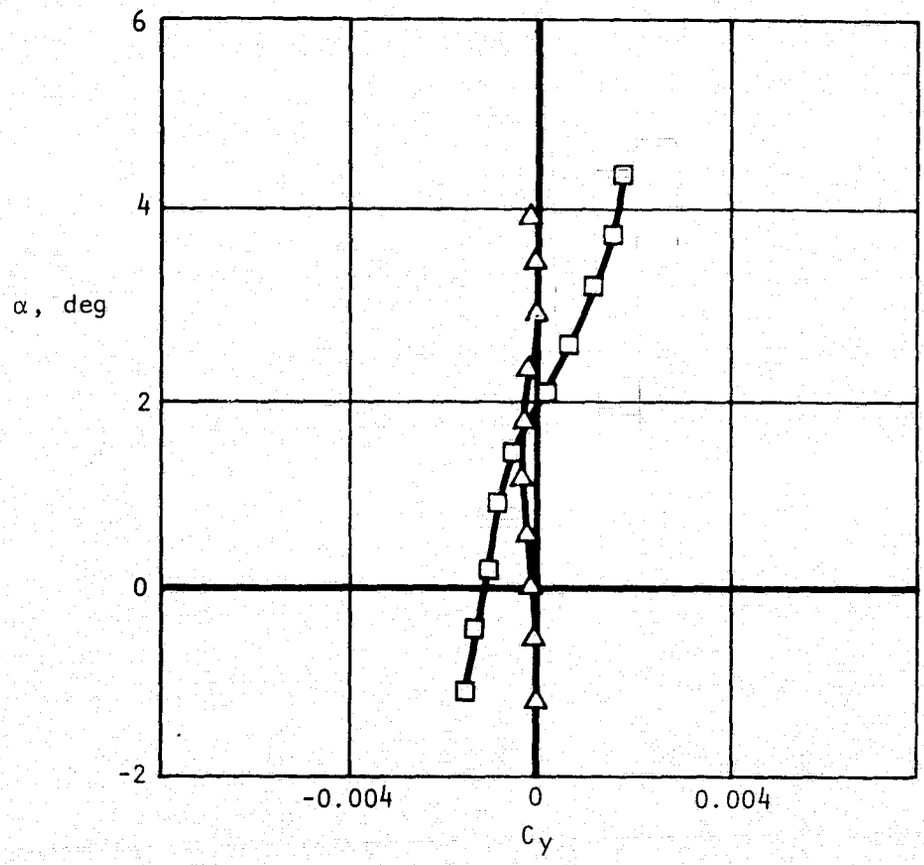

(a) Vane + body + wing stub

Figure 34. - Modified vane side force as affected by aircraft components, M = 0.85.

Symbol	δ_L, δ_R
△	$+10^o$, -10^o
□	$+20^o$, -20^o

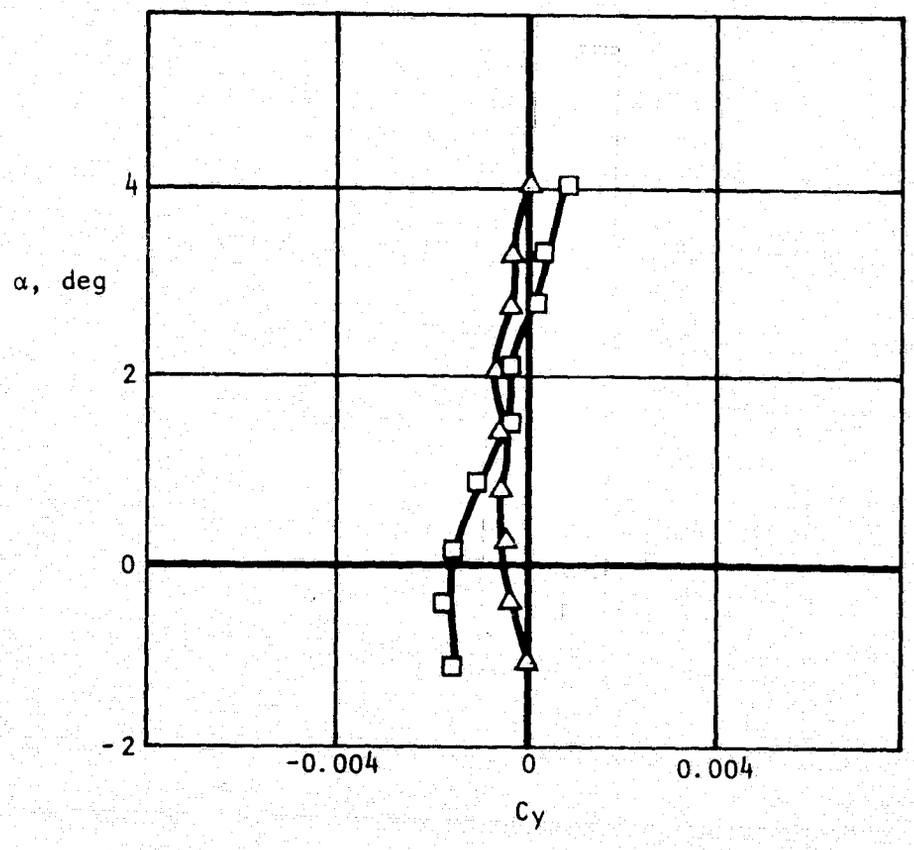

(b) Vane + total aircraft

Figure 34. - Concluded.

The aerodynamics associated with rigid aircraft shape reflect wind tunnel test data. The longitudinal-symmetric aerodynamics associated with symmetric structural bending and vertical gusts have been determined using unsteady subsonic doublet lattice lifting surface theory correlated with wind tunnel test results. The fuselage gust effects were determined using a modified slender body technique. The horizontal tail control data were obtained using the unsteady doublet lattice theory. The SMCS vane aerodynamics were quasi-steady and based on theory and correlated wind tunnel tests for both the longitudinal-symmetric and lateral-directional-antisymmetric cases. The lateral-directional rigid-body aerodynamics were from wind tunnel test data, while similar data for the antisymmetric structural bending modes have been determined using doublet lattice lifting surface quasi-steady aerodynamics; the rudder control effectiveness was determined using doublet lattice unsteady aerodynamics theory. The side gust loads on the fuselage were obtained using a modified slender body theory; while the gust loads on the vertical tail were calculated using unsteady doublet lattice theory.

The Von Karman gust power spectral density curve was used in calculations of the ride quality (crew sensitivity indexes, $\bar{H}_z$ and $\bar{H}_y$), and the rms accelerations due to turbulence, $\bar{A}_z$ and $\bar{A}_y$. The scale length, L, was 152.4 m (500 ft).

Crew sensitivity index data for the vertical axis, both $\bar{H}_z$ and the $\bar{H}_z$ power spectral density curve, are presented in figure 35. Data are shown for the basic aircraft, the SCAS operating, and the SCAS + SMCS operating. The peak at low frequency is the short period response and the large structural response at about 18 rad/sec frequency is a mode consisting primarily of first fuselage vertical bending mode motion. As can be seen, the SCAS does its intended job of damping the short period motion, but slightly excites the primary mode contributing to vertical motion. The specification level for $\bar{H}_z$ is ≤ 0.028. The data presented show that operation of the SMCS substantially reduces the structural motion (while not interfering with the short period) and does, in fact, show capability for meeting the specification $\bar{H}_z$.

The lateral crew sensitivity index, $\bar{H}_y$, and the power spectral density associated with $\bar{H}_y$ are presented in figure 36. Comparable data shown for the vertical case are shown for the lateral; that is, basic aircraft response, and the effects of SCAS and SCAS + SMCS operating on that response. The low-frequency responses are related to the Dutch roll mode and the two responses at 27 and 34 rad/sec are structural responses of aircraft modes which have large first fuselage side bending mode components. The SCAS is shown to modify the Dutch roll response but leaves the structural motion unchanged. Operation of the lateral SMCS does not have as dramatic an impact on the structural mode responses as does the vertical SMCS; however, the specification level of $\bar{H}_y$ ≤ 0.007 is met.

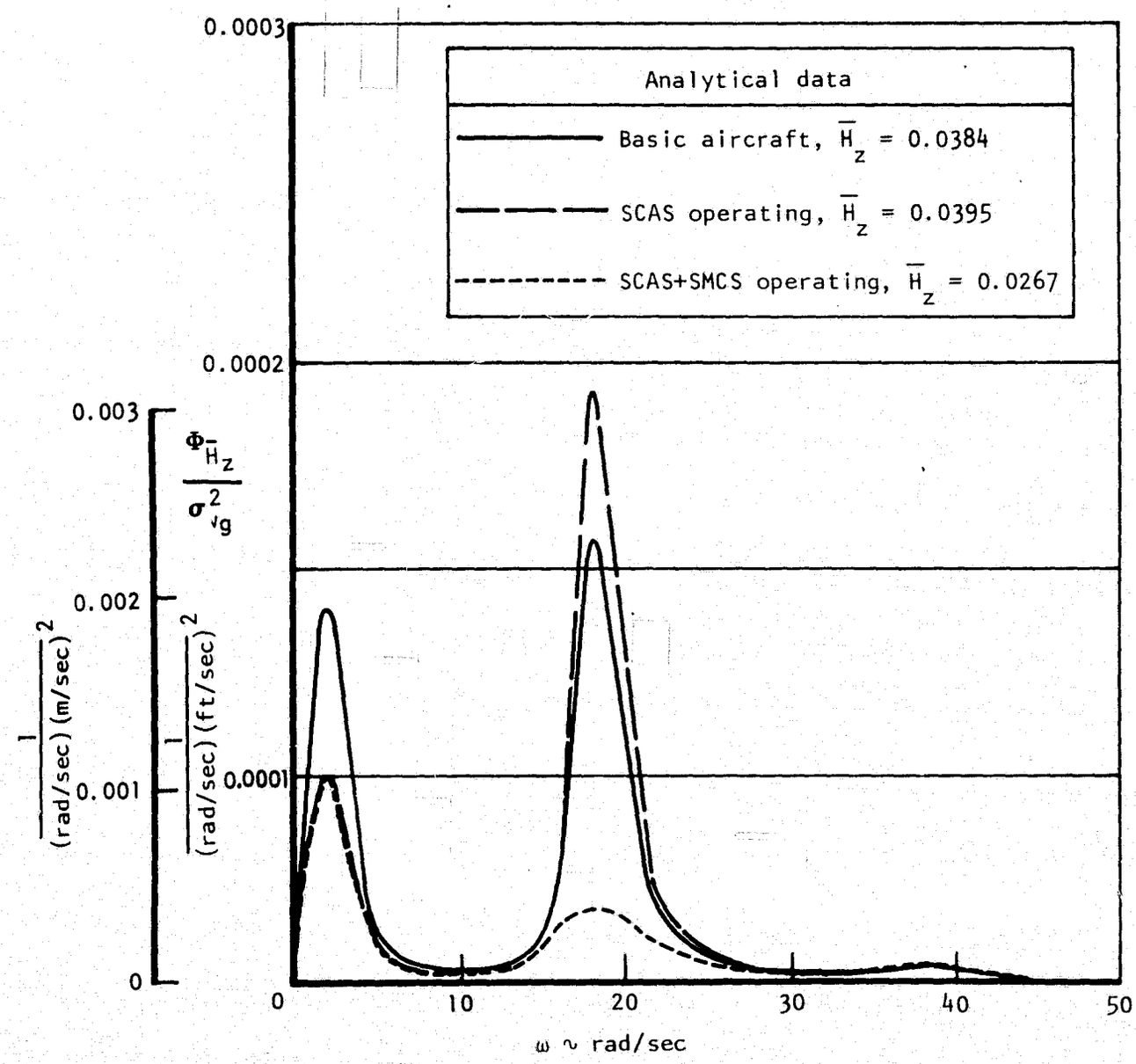

Figure 35. - Power spectral density associated with vertical crew sensitivity index, $\overline{H}_z$, M = 0.85, h_p = 762m (2500 ft), Λ_w = 65°, medium weight.

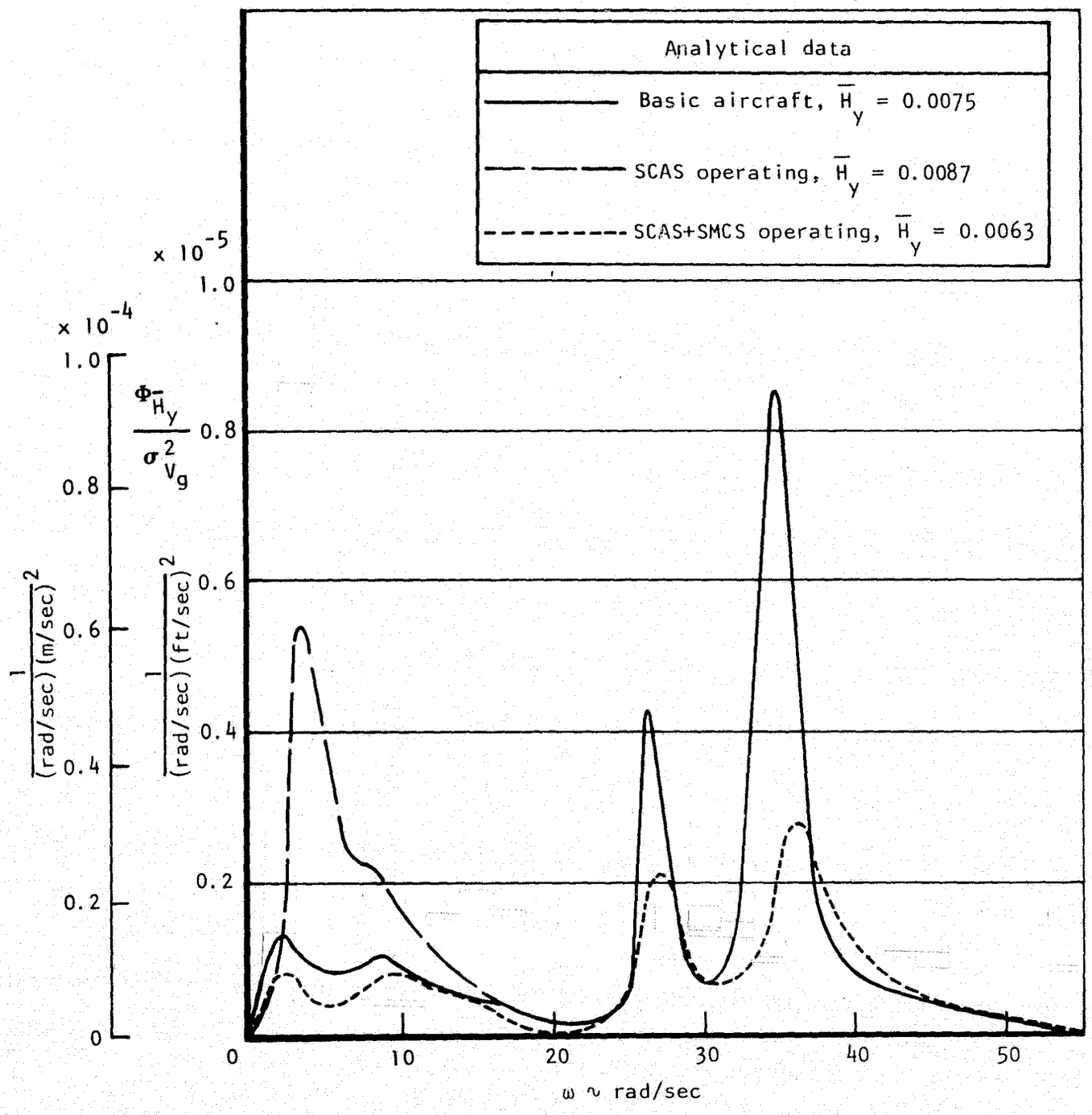

Figure 36. - Power spectral density associated with lateral crew sensitivity index, $\bar{H}_y$, M = 0.85, h_p = 762m (2500 ft), Λ_w = 65°, medium weight.

While the primary goal of the SMCS is to meet the ride quality requirement at the crew station, it is also of interest to see if the system reduces (or excites) loads at other fuselage locations. Figure 37 shows the effect of SCAS and SCAS + SMCS on the normal rms load factor, $\bar{A}_z$, along the fuselage; and figure 38 shows similar data for the lateral rms load factor, $\bar{A}_y$. On both figures it is shown that the SMCS reduces acceleration levels at all fuselage stations below that for either the basic aircraft or SCAS operating.

Figures 39 and 40 demonstrate that the configuration with SCAS + SMCS operating is indeed stable in both the vertical and lateral axes. This type of stability analysis has proven efficient and reliable in the past, but may be unfamiliar to some; refs. 6 and 7 are recommended for additional details of this stability approach.

SMCS Vane Load and Hinge Moment Requirements

Load and hinge moment requirements for the SMCS vanes were set by considering:

(1) Maximum deflection capability of the vane actuation system

(2) Additional vane relative angle of attack due to aircraft motion

(3) Vane planform and airfoil section

For the original vane configuration (35° leading edge sweep), the center of pressure was assumed to lie at 0.35 of the mean aerodynamic chord (MAC). The hinge line was placed at 0.20 MAC for flutter considerations; the most forward location practical with a standard vane airfoil section. This gave a hinge moment requirement for sea-level operations at M = 0.85, of 326 526 centimeters-newtons (cm-N)(28 900 inches-pounds)(in.-lb) for each vane panel.

The actuators designed to this requirement actually produced a 350 253 cm-N (31,000 in.-lb) hinge moment capability. Furthermore, the system was designed to have fully redundant hydraulics, so two complete actuation systems were specified. Thus, the available hinge moment capability of the system, in its operating condition was 700 506 cm-N (62 000 in.-lb) per vane panel.

When the change to the 60° leading edge sweep vane was proposed, one of the ground rules was that there would be no changes inboard of the fuselage mold line necessitated by the change in planform.

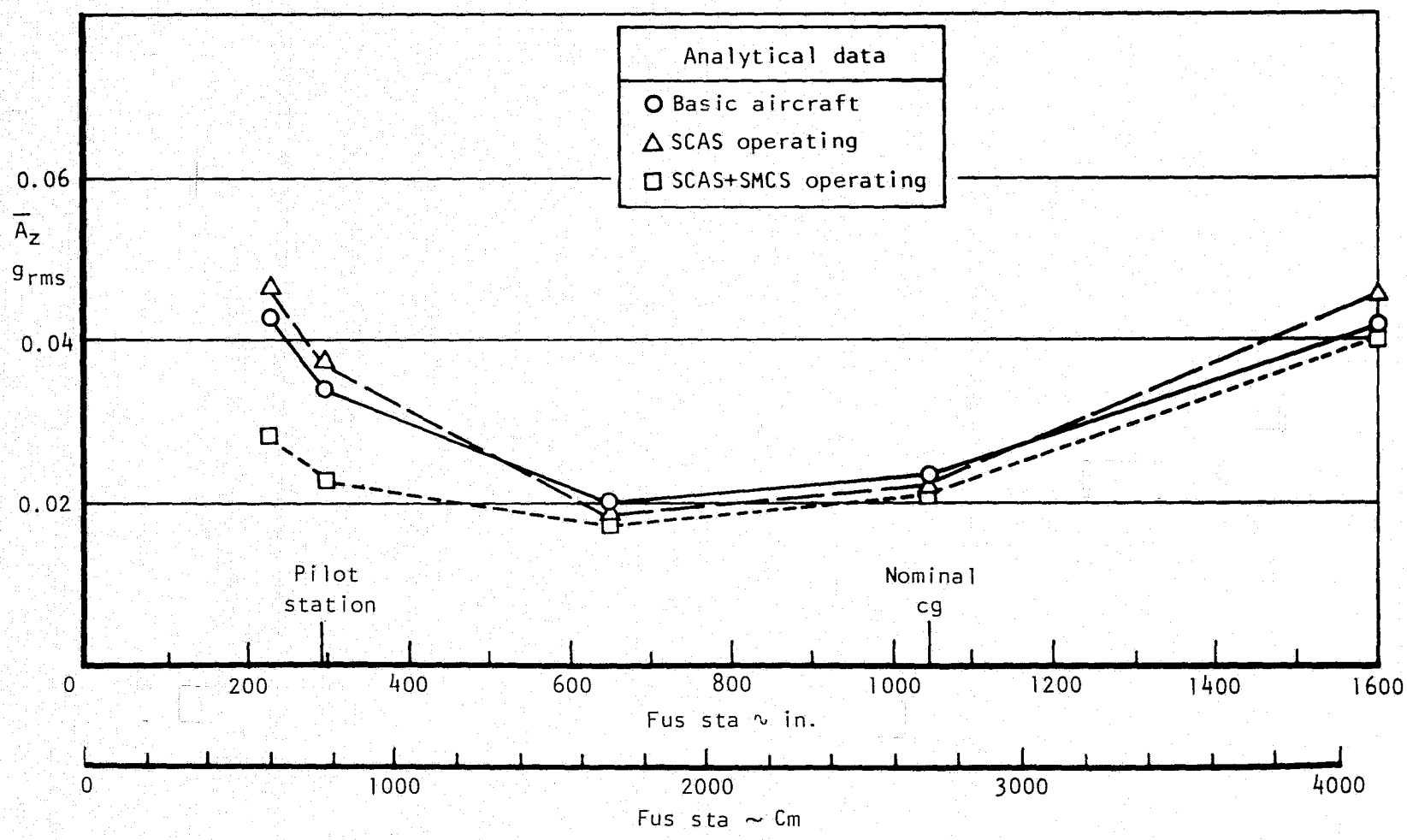

Figure 37. - Effect of SMCS on normal load factor response along the fuselage due to turbulence, M = 0.85, h_p = 762 (2500 ft), Λ_w = 65°, medium weight.

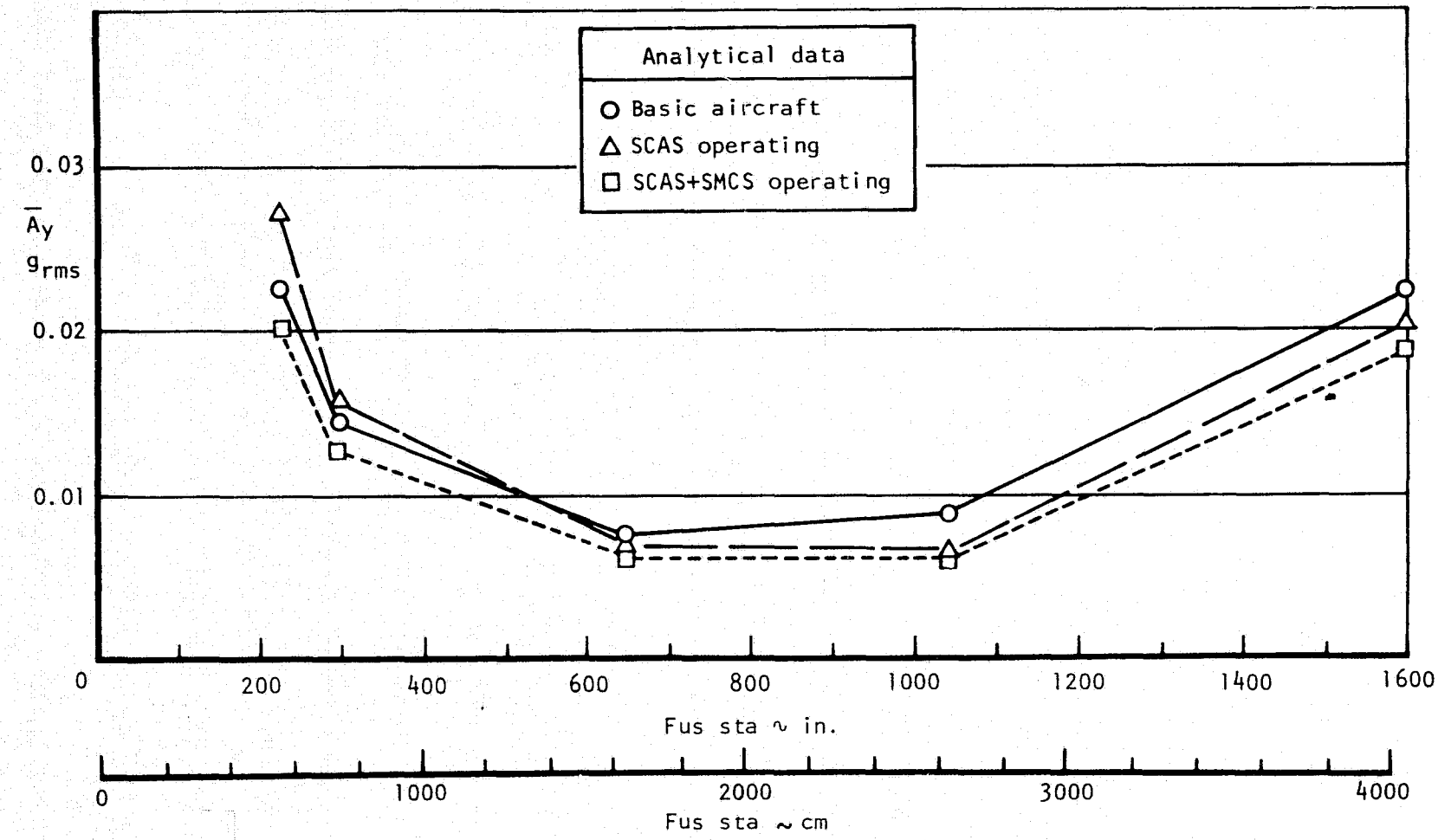

Figure 38. - Effect of SMCS on lateral load factor response along the fuselage due to turbulence, M = 0.85, h_p = 762m (2500 ft), Λ_w = 65°, medium weight.

Note: stability indicated by continuously increasing phase angle; an instability would show a slope change in sign at the unstable mode frequency.

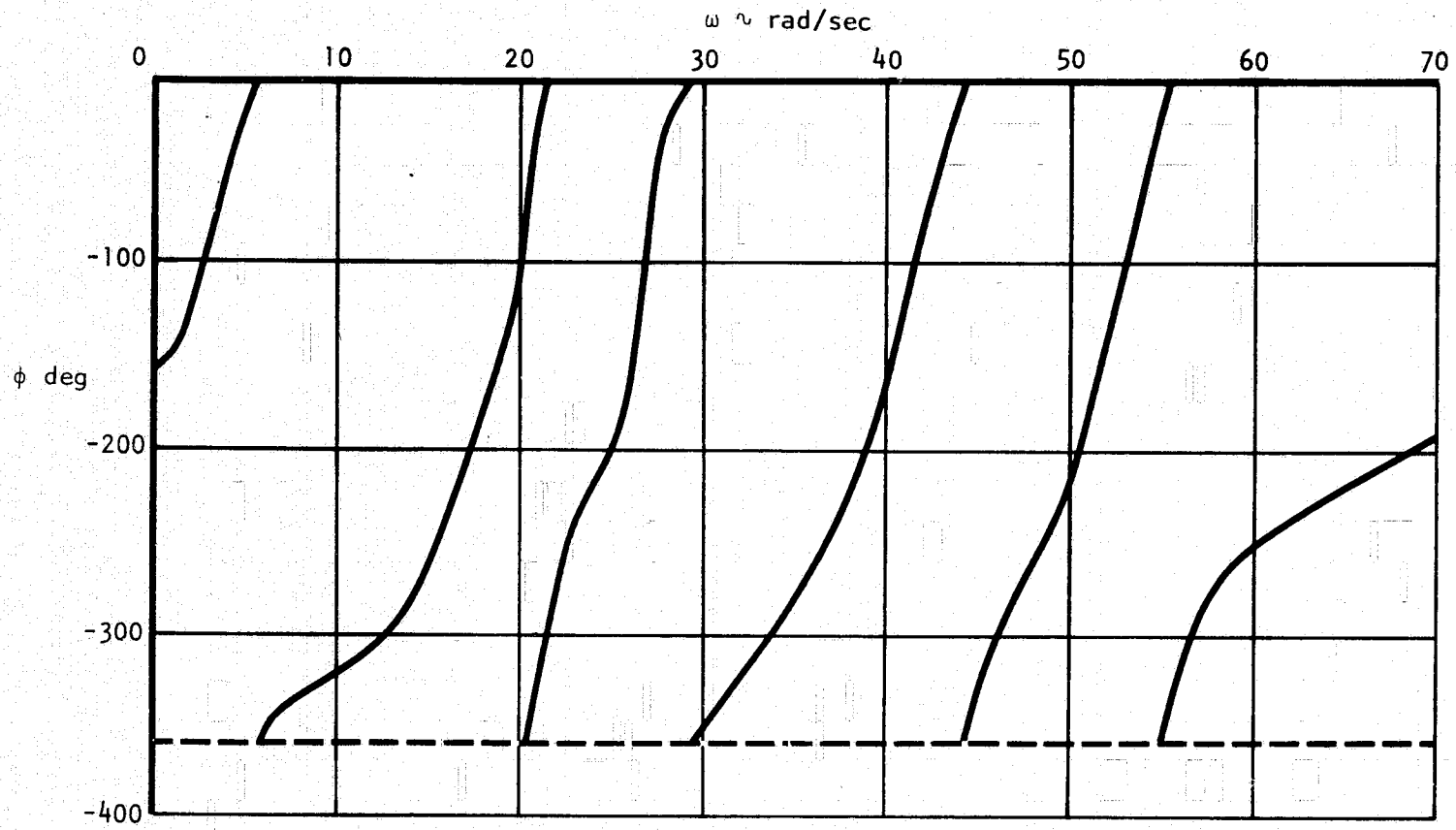

Figure 39. - Stability analysis using frequency evaluation of characteristic determinant, longitudinal - symmetric case, SCAS + SMCS operating, M = 0.85, h_p = 762m (2500 ft), Λ_w = 65°, medium weight.

Note: stability indicated by continuously increasing phase angle; an instability would show a slope change in sign at the unstable mode frequency.

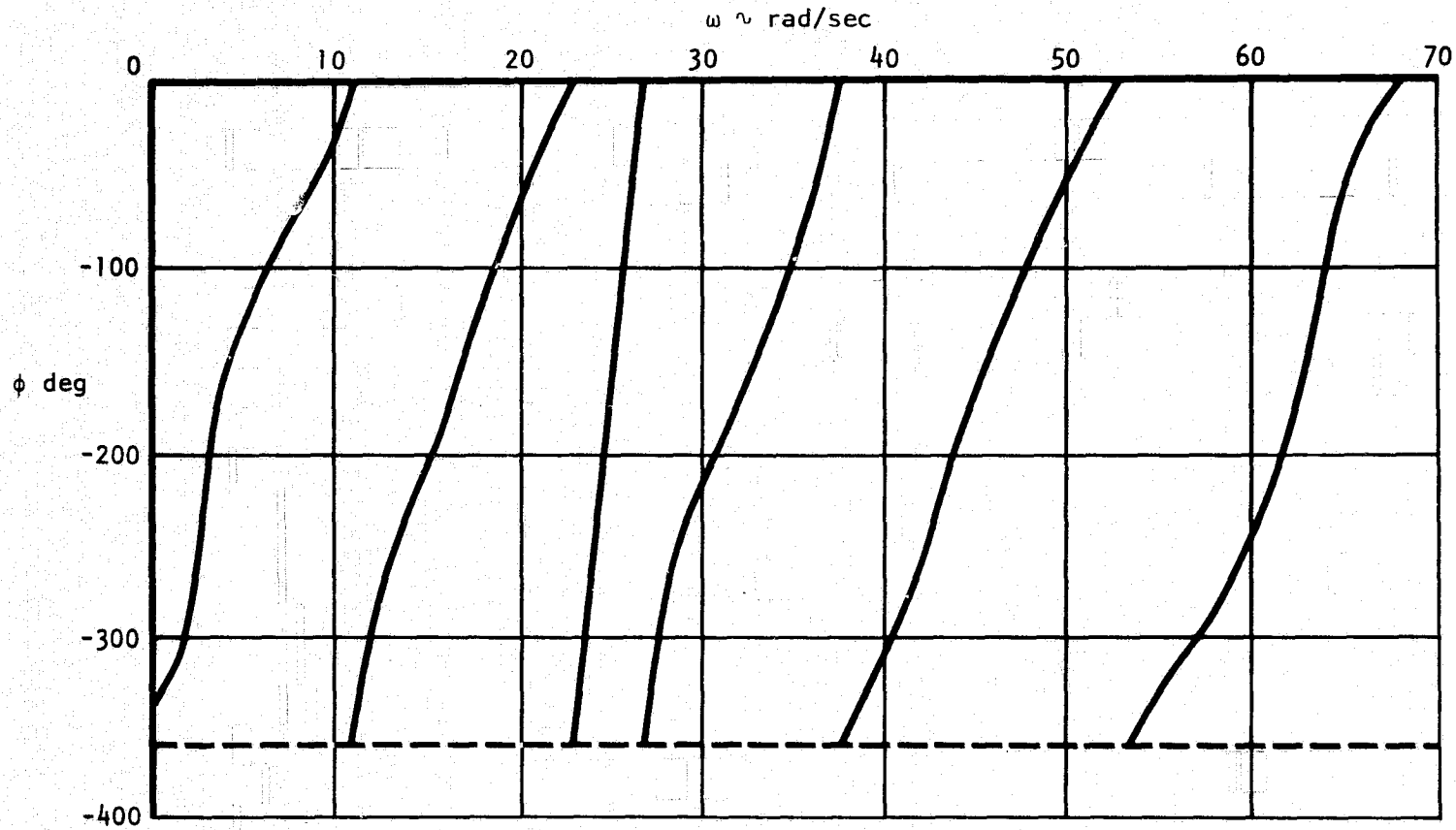

Figure 40. - Stability analysis using frequency evaluation of characteristic determinant, lateral-directional-antisymmetric case, SCAS + SMCS operating, M = 0.85, h_p = 762m (2500 ft), Λ_w = 65°, medium weight.

Review of the operational requirements dictated that the maximum vane angle of attack to the local free stream could be about 30^{o} as determined by the following relationship (upwash, ε, ignored):

$$\alpha_V = \delta + \alpha \cos\Gamma$$

where

Γ is the dihedral angle of the vane (-30^{o})

α_V is the effective angle of attack of the vane

α is the instantaneous aircraft angle of attack

δ is the vane deflection due to the SMCS vane actuation system

For sea-level operations at maximum speed, the maximum aircraft angle of attack could be as much as 12^{o} resulting from an escape pullup load factor commanded by the terrain-following (TF) system in the event of a TF system malfunction or penetration of a minimum clearance altitude. For a maximum vane deflection of 20^{o}, the effective angle of attack of the vane would be then approximately 30^{o}. Using the DATCOM-estimated nonlinear normal force curve, a normal force coefficient of 1.25 was estimated for $\alpha_V = 30^{o}$. This yielded a maximum load on each vane of 42 507 N (9559 lb), which was specified as the maximum possible operational load.

Hinge moment requirements were initially set by the more normal operational TF requirement, rather than the maximum speed escape requirement. For normal operations, the TF system commands a maximum pullup under sea-level operations at M = 0.85 which results in a maximum load of 31 863 N (7163 lb) per vane panel. For the 60^{o} vane, then, the hinge line location was specified such that the hinge moment corresponding to this load could be met by the existing requirement of 700 506 cm-N (62 000 in.-lb). (It had been determined that a fully redundant hydraulic system was not required, if the centering requirements could be met by a single actuator.) Using a doublet lattice aerodynamics program, a chordwise center-of-pressure location of 0.42 MAC was estimated rather than the 0.35 MAC previously used. With the SMCS vane hinge line placed at 0.145 MAC, the hinge moment required for full-vane deflection under normal load factor pullup conditions is 651 538 cm-N (57 666 in.-lb), well within the 700 506 cm-N (62 000 in.-lb) available from the two actuators per vane panel. The assumption was that this was the required hinge moment for operational capability, and the vane could be permitted to blow back if a higher hinge moment was encountered.

In the event of an SMCS failure, the system commands the vane to the center position where it is held by a mechanical centering valve. It is necessary to have an independent centering capability for each actuator. Since the center of pressure is located aft of the hinge line, the centering capability required is to hold the vane against the load due to aircraft angle of attack. For sea-level operations at maximum speed, a maximum holding moment of 431 399 cm-N (38 182 in.-lb) is required. This requirement, which was established after the vane hinge line had been fixed, caused a resizing of the actuation system to a 903 878 cm-N (80 000 in.-lb) capability. Thus, the maximum load of 42 521 N (9559 lb) and corresponding maximum hinge moment of 869 440 cm-N (76 952 in.-lb) could be obtained under the specified conditions; and blow back on this final design is not likely.

SMCS Fatigue Spectrum Development

There are two primary aspects of the problem of developing fatigue spectra for a control configured vehicle:

(1) Predicting the cyclic load spectra of the control surface itself together with associated mountings, actuation systems, and backup structure

(2) Predicting the effect of the CCV system on the overall spectrum of the aircraft

The process of predicting the spectrum for the SMCS itself is a relatively straightforward one consisting of the following steps:

(1) From a ride quality analysis of the aircraft in a low altitude, high-speed flight condition, with the SMCS operating, statistical parameters of vane deflection are obtained. They are:

$\bar{A}_\delta$ the rms value of vane deflection for a gust level of 0.3048 m/sec rms (1 ft/sec rms)

$N_{o\delta}$ the characteristic frequency of vane motion, i.e., the average number of zero crossings per unit time

Separate values of these parameters are obtained for longitudinal-symmetric (vertical gust) analyses and for lateral-directional-antisymmetric (lateral gust) analyses.

(2) The $\bar{A}_\delta$ and $N_{o\delta}$ values from vertical and lateral gust analyses are combined to give effective values for combined turbulence, since the SMCS vane

deflections are a linear superposition of commands from the vertical and lateral systems:

$$\bar{A}_\delta = \left[\bar{A}^2_{\delta_{wg}} + \bar{A}^2_{\delta_{vg}} \right]^{1/2}$$

$$N_{o_\delta} = \left[\frac{\bar{A}^2_{\delta_{wg}} N^2_{o_{\delta_{wg}}} + \bar{A}^2_{\delta_{vg}} N^2_{o_{\delta_{vg}}}}{\bar{A}^2_\delta} \right]^{1/2}$$

(3) An exceedance curve of magnitude of δ versus exceedances per hour is obtained by the following method:

$$N_{(\delta)} = N_{o_\delta} \left[P_1 \exp\left(-\frac{\delta}{b_1 \bar{A}_\delta}\right) + P_2 \exp\left(-\frac{\delta}{b_2 \bar{A}_\delta}\right) \right]$$

where P_1, P_2, b_1, and b_2 are properties of atmospheric turbulence, dependent only on altitude (ref. 8)

For low-altitude combined vertical and lateral turbulence:

$p_1 = 1.0$ $\qquad$ $p_2 = 10^{-5}$

$b_1 = 2.9$ $\qquad$ $b_2 = 12.4$

assuming $p_2 << p_1$

$$N(\delta) = N_{o_\delta} \exp\left(-\frac{\delta}{2.9 \bar{A}_\delta}\right)$$

For a typical low-altitude high-speed flight condition, the following parameters were obtained from a ride quality analysis:

$\bar{A}_\delta = 0.01219$ rad

$N_{o_\delta} = 1.8259$ per sec

Figure 41 shows the exceedance curve for vane deflection obtained.

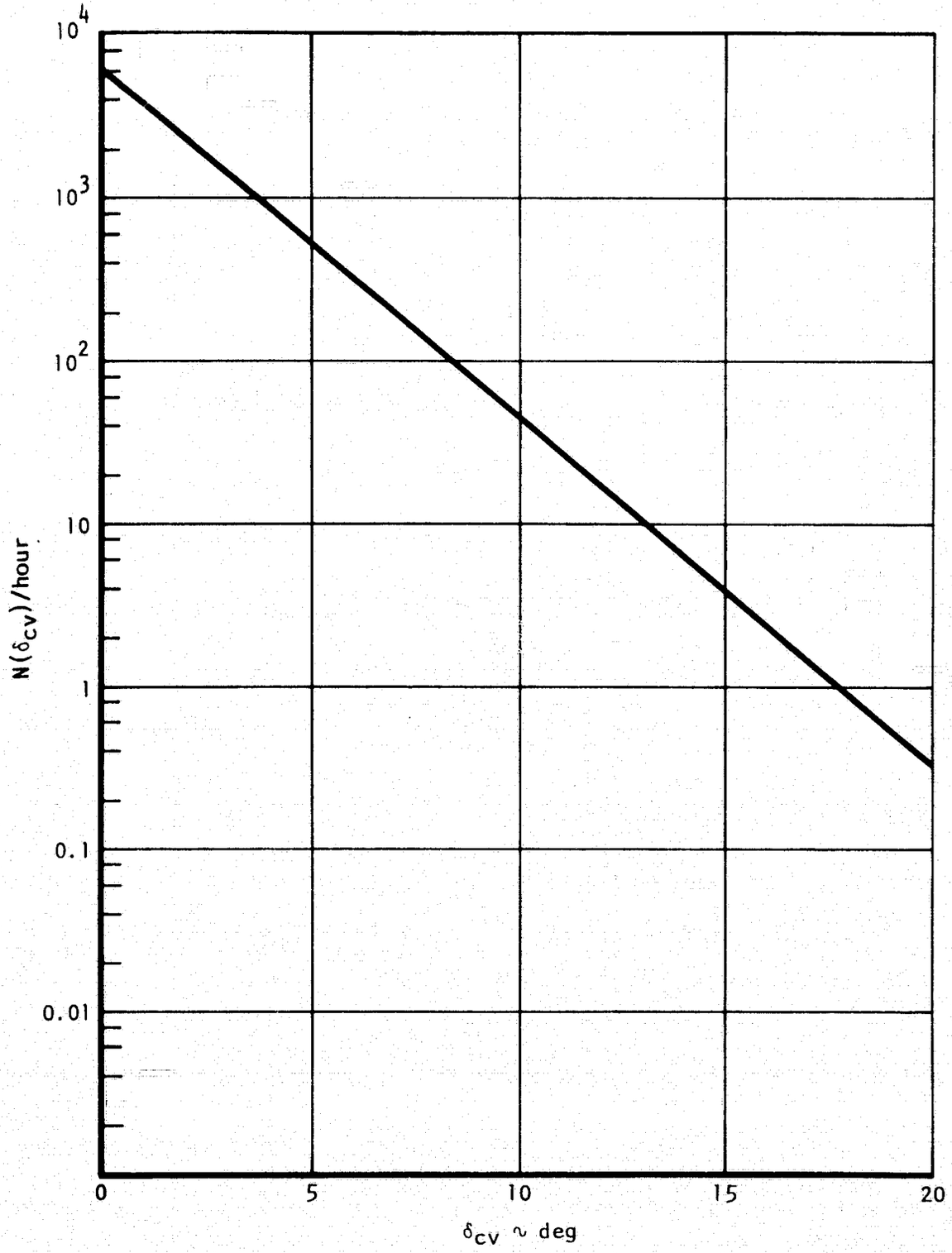

Figure 41. - Combined vertical and lateral SMCS vane exceedances, SCAS + SMCS.

(4) The exceedance curve is used to determine the total number of cycles above each load level for each flight condition where operation of the SMCS is planned, assuming the SMCS to be operating 100 percent of the time at that flight condition.

(5) The loads on the vane for specified deflections are determined from the normal force curve of figure 14, with a ratio of dynamic pressure applied for various flight conditions. The occurrences of the various loads are then summarized and expressed as a percentage of maximum design load. The resulting load spectrum is given in Table II, which expresses the total load history for the SMCS vanes over the life of the aircraft. The loads on the vane due to the established spectra of airplane angle-of-attack variations due to gust and maneuver, but with the SMCS not operating, were found to be a negligible increment to the SMCS operational load spectrum.

(6) This load spectrum is then used in a stress analysis, and using established stress versus number of load cycles (S-N) curves for the various materials, the fatigue life of the various components of the SMCS vane and the backup structure are estimated. The criterion that is used for proof-of-conformance testing on the B-1 is that the expected fatigue life shall exceed four times the expected operational life.

A second area of concern is the effect of the SMCS on the cyclic load spectrum to the other components of the aircraft. Although the B-1 was designed to have complete structural integrity without the SMCS operating, it has been predicted that there will be some beneficial effects of SMCS operations on the fatigue loading spectrum, particularly on the forward portions of the aircraft. The flight-by-flight load spectrum being used to demonstrate acceptable fatigue characteristics, therefore, includes the effect of SMCS for those portions of the flight where it is expected that the SMCS will be operational.

SMCS Stiffness Requirements

SMCS vane flexible-to-rigid-ratio. - As has been described earlier in the report, the vane planform geometry was determined by the requirement to have the force characteristics to be as linear as possible with angle of attack. The resulting highly swept planform precipitated some concern about the possibility of losing force generating capability through flexibility of the surface. In order to check this, a flexible-to-rigid ratio for the vane's normal force curve was determined using the stiffness characteristics of the vane presented in appendix D.

TABLE II. — ANALYTIC FATIGUE LOAD SPECTRUM FOR THE SMCS VANE FLIGHT-BY-FLIGHT COMPOSITE MISSION

Load Step	Mission segment	Spectrum load in terms of percent of design limit load		Occurrences per mission
		Maximum	Minimum	
1	Terrain following	80.0	-72.0	1 occurrence every 10 missions
2		72.5	-62.2	1
3		57.0	-48.0	10
4		41.5	-34.2	100
5		25.5	-14.0	1000
6		13.5	-2.2	4883

NOTES: 1. There are 1280 such missions per lifetime.

2. This spectrum represents 1932 hours of terrain following.

The flexible-to-rigid ratio for the vane surface as-built was 0.90 for the design condition of M = 0.85 at sea level. When the root flexibility encompassing the actuators and backup structure was also considered, this ratio dropped to 0.86. Based initially on judgment and later on flight test results, this level of SMCS vane stiffness was accepted as sufficient.

It should be emphasized that the need for a high flexible-to-rigid ratio for the surface became the prime stiffness requirement.

Flutter characteristics. - A single SMCS vane panel is moved by two actuators (one located forward of the pivot and one aft). Each actuator is fed by a separate hydraulic system. In the event of a hydraulic system failure, the good actuator moves to neutral and holds the vane in this position. This one-actuator-failed case was assumed to be a critical case with respect to flutter, although not the most critical (this will be discussed subsequently). The stiffness lost in one actuator is small as the first bending mode vibration frequency indicates; the frequency changes but little from 22.8 Hz for the normal case to 22.7 Hz for the failed case.

The SMCS vane panel stiffness, actuator and backup structure stiffness and mass characteristics are presented in appendix D.

After generating vibration mode characteristics using the information in appendix D, the generalized aerodynamic forces were computed for M = 1.2, 1.7, and 2.1 using mach box theory. Using these generalized forces, flutter analyses were conducted for each case at five altitudes - sea level, 3048 m (10 000 ft), 6096 m (20 000 ft), 10 668 m (35 000 ft), and 15 240 m (50 000 ft). It was found that no flutter will occur for all cases at speeds of M = 1.2 and higher.

Using similar methods, flutter analyses for M = 1.05 were also performed. Figure 42 presents the results of these analyses. Only the damping versus velocity and frequency versus velocity curves for the critical first bending flutter mode (single-degree-of-freedom) at sea-level conditions are presented. The flutter velocity and frequency at other altitudes are listed. The vane does not flutter at the true speed associated with M = 1.05 and shows adequate flutter speed margins with respect to this speed.

For the SMCS vane, the worst flutter case is both hydraulic systems out that supply the SMCS actuators. In this situation the vane dynamic spring constant drops to 70 051 N/cm (40 000 lb/in.) where the stiffness is supplied by fluid trapped in an accumulator. To evaluate this case, figure 43 was drawn showing flutter speed versus pitch actuator frequency at M = 1.05 for a number of altitudes. The previously described flutter analysis at M = 1.05 provided the data points at the actuator frequency of 22.7 Hz. The flutter velocity

Altitude meters (ft)	V_F meters/sec (knots)	f_F (Hz)
0 (0)	442.42 (860)	30
3,048 (10,000)	447.57 (870)	28
6,096 (20,000)	445.51 (866)	27
10,668 (35,000)	437.28 (850)	25
15,240 (50,000)	426.99 (830)	24

M = 1.05 aerodynamics
7 structural modes

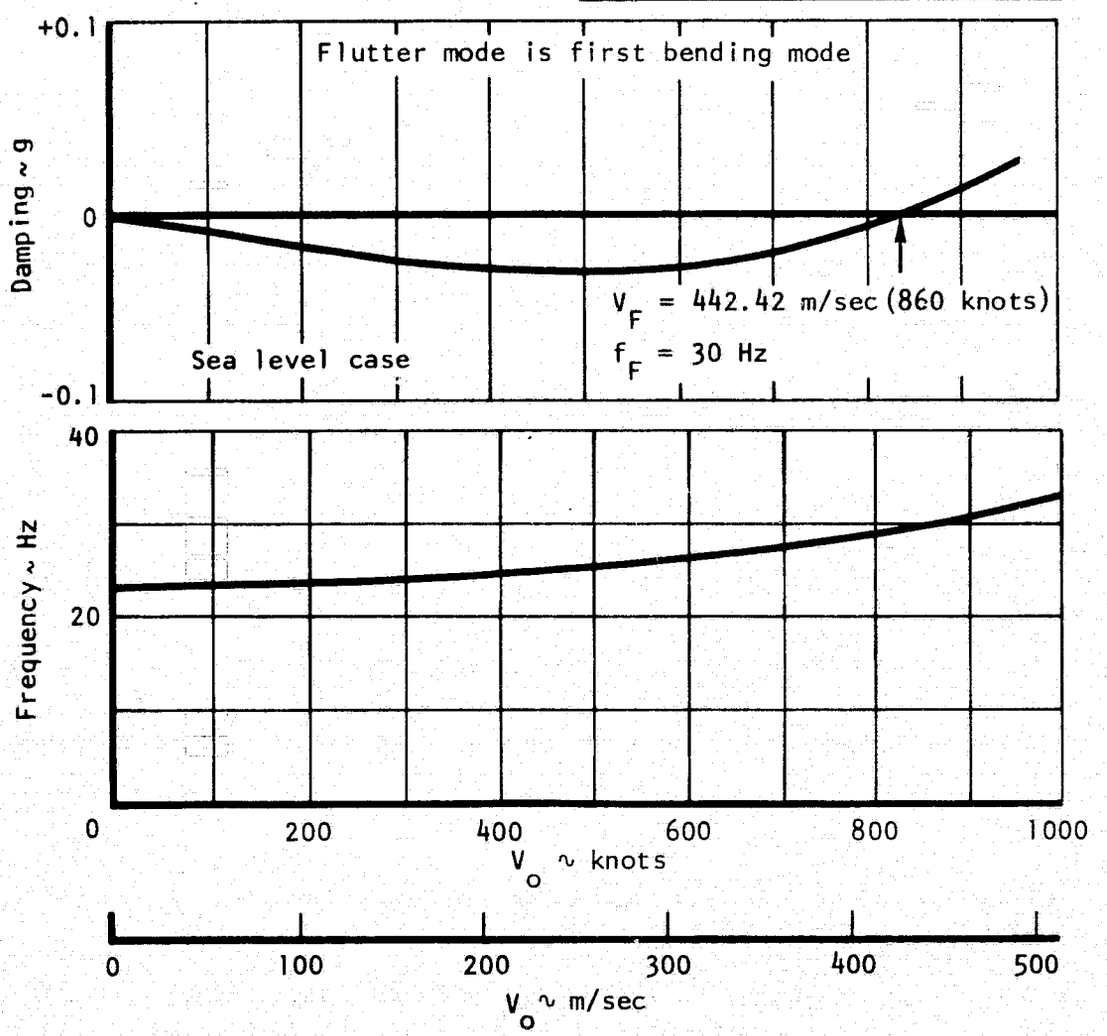

Figure 42.- SMCS flutter characteristics with aft actuator failed.

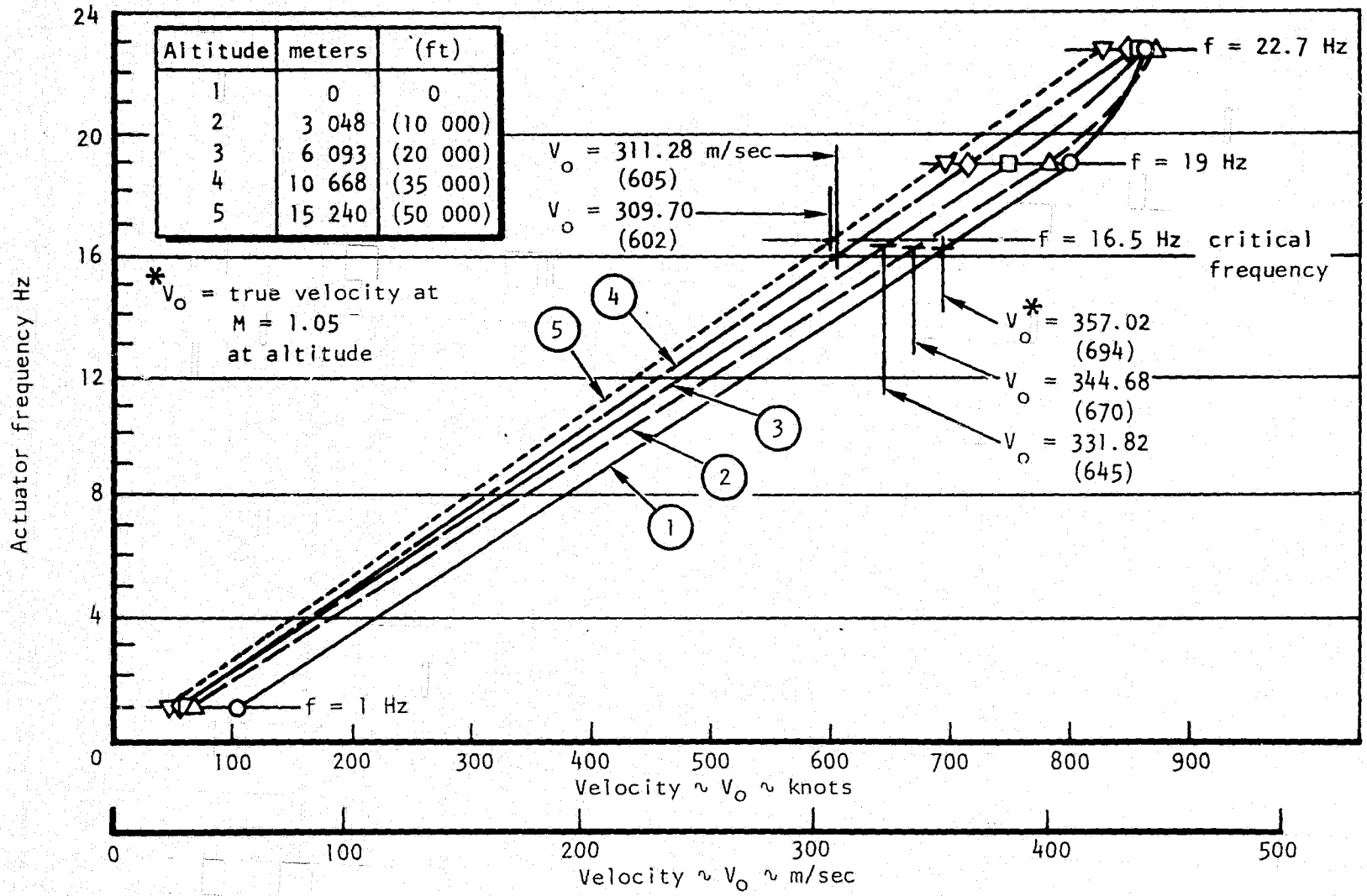

Figure 43. - SMCS vane flutter velocity versus actuator pitch frequency, M = 1.05.

data points at actuator frequencies of 19 and 1 Hz were obtained from flutter analyses incorporating arbitrary reductions in frequencies to the values mentioned. By connecting the points for a given altitude, it was possible to identify a point on that curve at the true velocity for M = 1.05 at that altitude. Considering all altitudes, a critical flutter frequency of 16.5 Hz was identified for the system. A vibration analysis of the SMCS vane, actuator, and backup structure where the 70 051 N/cm (40 000 lb/in.) pitch stiffness was incorporated for the actuator revealed a first mode frequency of 16.8 Hz. As seen from figure 43, this produces only a 3-percent margin in speed.

In light of this inadequate flutter margin and the fact that using mach box theory at M = 1.05 is stretching the theory some, a wind tunnel flutter test of a full-scale SMCS vane having zero pitch restraint is planned but not completed at this writing. Flight procedures presently require that flights be restricted to subsonic speeds with a single hydraulic failure and thus precludes encountering this second-hydraulic-system-failed possible flutter difficulty.

SMCS DESIGN DETAILS

SMCS Vane Construction

The key features of the SMCS vane construction details and materials used are shown in figure 44. The trunnion and main box skins are made of steel. The box main spars and ribs are titanium. The material forward and aft of the main structural box is fiberglass honeycomb and skins. The leading and trailing edge closeout strips are aluminum.

SMCS Bearing Design

Each SMCS vane is supported by two pivot bearings, mounted in trunion plates inboard and outboard of the actuator attach fitting (horn). Initial design studies indicated that spindle-mounted needle bearings would probably be the best approach to support the vane surfaces. Initial design selections included Series NBC Torrington aircraft needle bearings with needle thrust bearings, based on static-load requirements. Detail design on the bearing housings and associated parts for this application was begun. This detail design indicated problems in mounting of the bearings and also raised overall concern as to the adequacy of needle bearings in the SMCS. Specific problems were as follows.

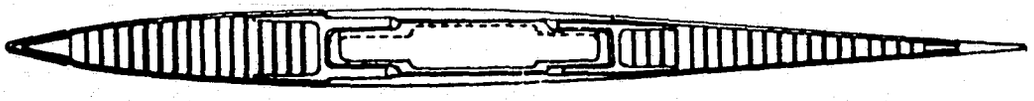

Typical cross section
perpendicular to 58% chord
(not to scale)

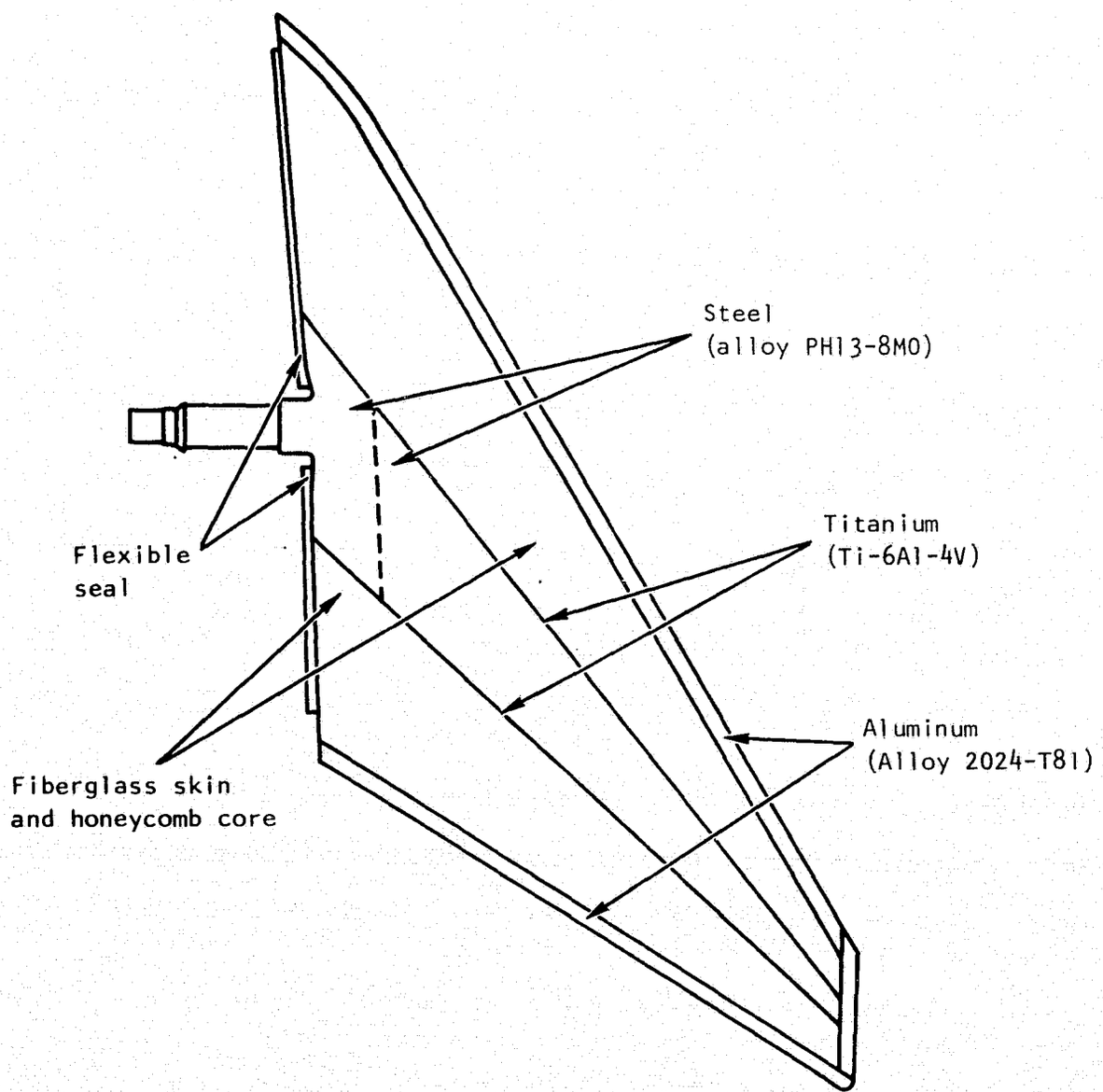

Figure 44. - SMCS vane construction details.

(1) Marginal oscillating (dynamic) load capacity

(2) Inability to control thread torque on spindle nut so as to prevent brinelling of the needle thrust bearings

(3) Concern over small amplitude motions that could cause severe fretting of the needle bearing races

(4) No practical way to provide relubrication of the needle thrust bearings.

As a result of these problems, alternate bearing designs were investigated. The only practical alternate design appeared to be the use of teflon (TFE) lined, plain spherical bearings to carry both the radial and thrust loads. This type of bearing, however, has certain drawbacks for use in such an installation. They are:

(1) Sustained rapid motion will produce significant frictional heating that is not as readily dissipated as in a grease-lubricated-type needle bearing. Such heating could produce failure in the TFE liner.

(2) The maximum coefficient of friction with this type bearing is approximately 10 times greater than with a needle bearing (0.10 compared to 0.01) and must be considered in relation to the available actuator power.

(3) TFE-lined bearings operate normally through a slow wear process of the liner so that free play will increase during the useful life of the bearing. A wear value of approximately 0.0102 to 0.0152 cm (0.004 to 0.006 in.) per bearing is considered a practical amount to use for design purposes.

(4) The TFE liner has a finite wear life and prediction of the probable life in terms of flight hours under these unusual operating conditions is very difficult. The use of TFE-lined bearings in other more normal B-1 airframe applications is based on the assumption that the bearings are good for the total life of the aircraft.

In spite of these drawbacks, TFE-lined bearings offered the best compromise for this application. It was necessary, though, to explore the frictional heating aspect and verify that power requirements were adequate using TFE-lined bearings.

A test was conducted on a TFE-lined plain spherical bearing typical of the type contemplated for use in the SMCS. Test conditions were chosen to simulate the most severe sustained operating condition in this application within the capabilities of the test equipment. The analysis of the basic

operating conditions indicated that the bearings must operate continuously at an average rate of 60°/sec at an angle of ±10°. (Rates as high as 200°/sec can occur but for only brief periods of time.) The total duration during a lifetime at this condition is approximately 2000 hours. The bearing tested was a Kahr KNDB16CR. This bearing has a bore of 2.540 cm (1.000 in.) and a spherical ball outside diameter of 3.968 cm (1.562 in.) with the TFE liner bonded to the spherical inside diameter of the outer race. The TFE liner used in this bearing is one of the two approved for B-1 use. The bearings used in the actual pivot points have bores of 6.350 cm (2.500 in.)(outboard) and 5.080 cm (2.000 in.) (inboard) with corresponding spherical outside diameters of 9.042 cm (3.560 in.) and 7.277 cm (2.865 in.) as shown in figure 45. The limit load for the outboard bearing is 157 912 N (35 500 lb) and for the inboard bearing 114 764 N (25 800 lb). In terms of loading at the TFE liner surface, the approximate values are 6894.8 N/cm^2 (10 000 psi) for the outboard bearing and 8135.8 N/cm^2 (11 800 psi) for the inboard bearing. At a rate of 60°/sec, the outboard bearing has an average surface velocity at the spherical TFE-lined surface of 2.844 meters per minute (mpm) (9.33 feet per minute)(fpm); and the inboard, an average surface velocity of 2.286 mpm (7.50 fpm). With the bearing tested, a load of 66 723 N (15 000 lb) would give a unit stress of 8 894.23 N/cm^2 (12 900 psi) and this load was well within the capabilities of the test equipment. However, in order to obtain a surface velocity of 2.844 mpm (9.33 fpm) at a motion of ±10°, a speed of 180 cycles per minute (cpm) would be required and this was not possible with the available test equipment. By increasing the angle of oscillation, however, the surface velocity could be increased. At the maximum angle of oscillation (±30°) and the maximum speed (60 cpm), the average surface velocity with this test bearing was 2.493 mpm (8.18 fpm), approximately 12-percent below the desired surface velocity for the outboard bearing.

Loads, speeds, and degree of motion were varied to determine the effects on frictional heating. Thermocouples were attached to the outer race of the bearing and were continuously monitored. Frictional heating is a function of both surface velocity and load and the results showed this relationship. Following this series of varied test conditions where it was determined that frictional heating was not excessive even at the most severe conditions, the bearing was cycled 1 000 000 times (298 hours) at a unit stress of 8894.2 N/cm^2 (12 900 psi) and a surface velocity of ±1.24 mpm (±4.08 fpm) to verify that early liner failure should not be anticipated. Posttest examination of the bearing disclosed that it was still preloaded, indicating negligible wear. The liner appearance was excellent with only a very small amount of sluffing (wear debris).

On the basis of these test results summarized in table III and an analysis of this application, the following conclusions were made relative to the use of TFE-lined plain spherical bearings in the structural mode control pivot points.

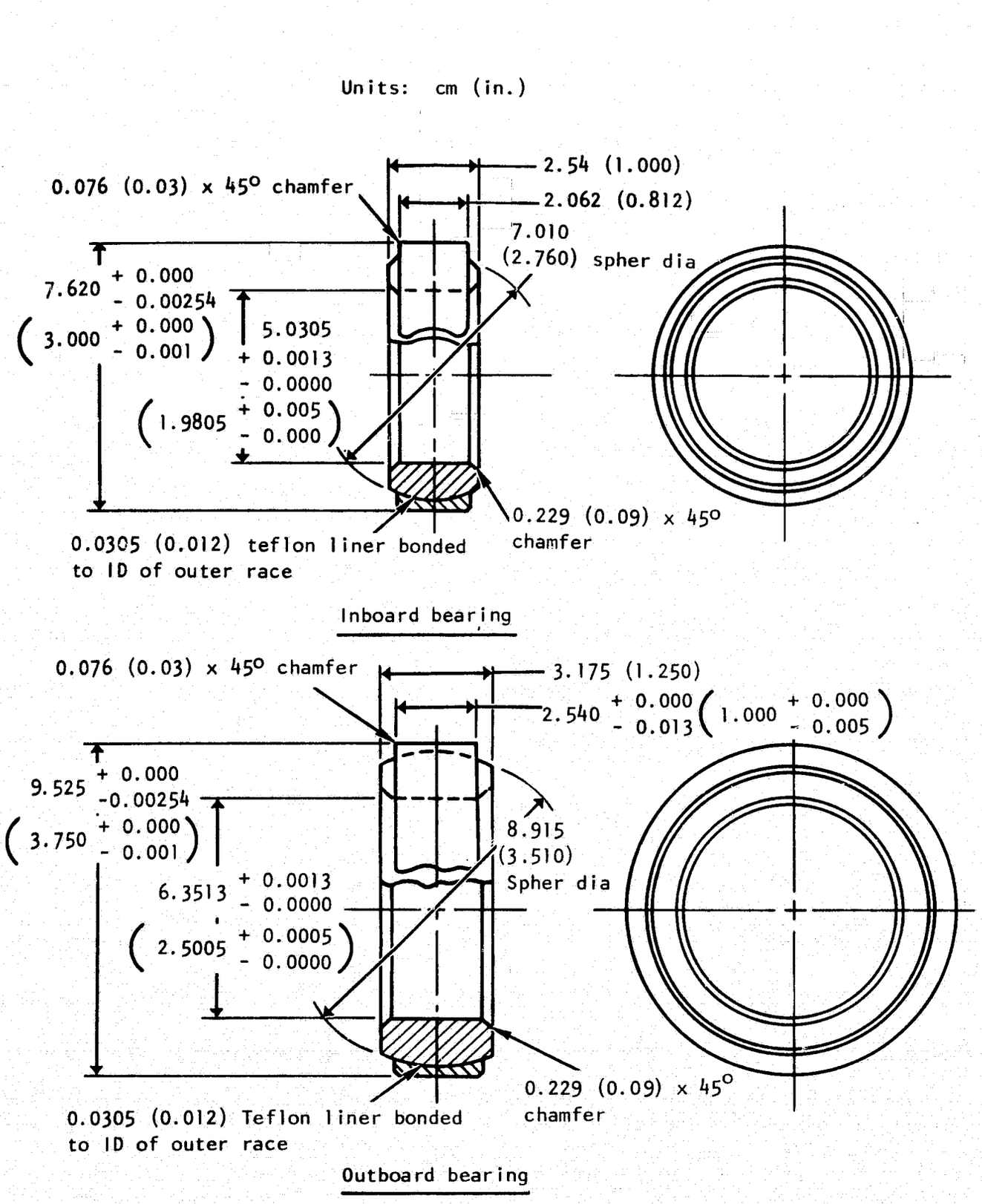

Figure 45. - SMCS vane pivot bearings.

TABLE III. - TEFLON BEARING TEST RESULTS

Cycle No.	Load		Oscil motion	Speed cpm	Deg cycle	m/min (ft/min)	Coef of friction	Temp °C (°F)
	Newtons (lb)	Newtons/cm^2 (psi)						
1	44,482 (10 000)	5 902 (8 560)	±15°	30	60°	0.622 (2.04)	0.061	29.44 (85)
200	↓	↓	↓	↓	↓	↓	0.051	38.89 (102)
300	↓	↓	↓	↓	↓	↓	0.051	40.56 (105)
301	↓	↓	↓	60	↓	1.244 (4.08)		
500	↓	↓	↓	↓	↓	↓	0.036	48.39 (120)
600	↓	↓	↓	↓	↓	↓	0.036	50.56 (123)
601	55 723 (15 000)	8 894 (12 900)	↓	30	↓	0.622 (2.040)	0.046	
800	↓	↓	↓	↓	↓	↓	0.041	46.67 (116)
900	↓	↓	↓	↓	↓	↓	0.041	47.22 (117)
901	↓	↓	↓	60	↓	1.244 (4.08)		
1 100	↓	↓	↓	↓	↓	↓	0.029	56.67 (134)
1 200	66 723 (15 000)	↓	↓	↓	↓	↓	0.029	57.22 (135)
1 201	88 964 (20 000)	11 859 (17 200)	↓	30	↓	0.622 (2.04)	0.041	
1 400	↓	↓	↓	↓	↓	↓	0.039	52.22 (126)
1 500	↓	↓	↓	↓	↓	↓	0.039	52.78 (127)
1 501	↓	↓	↓	60	↓	1.244 (4.08)		
1 800	↓	↓	↓	↓	↓	↓	0.028	62.78 (145)
2 100	↓	↓	↓	↓	↓	↓	0.029	63.89 (147)
2 101	111 206 (25 000)	14 755 (21 400)	↓	↓	↓	↓	0.034	
2 300	↓	↓	↓	↓	↓	↓	0.029	65.56 (150)
2 400	↓	↓	↓	↓	↓	↓	0.029	67.78 (154)
2 401	66 723 (15 000)	9 894 (12 900)	↓	30	↓	0.622 (2.04)	0.029	
5 000	↓	↓	↓	↓	↓	↓	0.034	48.33 (119)
33 000	↓	↓	↓	↓	↓	↓	0.024	40.56 (105)
33 001	88 964 (20 000)	11 859 (17 200)	↓	60	↓	1.244 (4.08)	0.024	
33 200	↓	↓	↓	↓	↓	↓	0.019	46.11 (115)
33 300	↓	↓	↓	↓	↓	↓	0.019	46.11 (115)

TABLE III. - Concluded

Cycle No.	Load		Oscil motion	Speed cpm	Deg cycle	m/min (ft/min)	Coef of friction	Temp °C (°F)
	Newtons (lb)	Newtons/cm^2 (psi)						
33 301	111 206 (25 000)	14 755 (21 400)	±15°	60	60°	1.244 (4.08)	0.021	
33 500	↓	↓	↓	↓	↓	↓	0.021	48.89 (120)
33 600	↓	↓	↓	↓	↓	↓	0.021	50.00 (122)
33 601	66 723 (15 000)	8 894 (12 900)	±30°	30	120°	↓	0.024	
33 800	↓	↓	↓	↓	↓	↓	0.021	45.56 (114)
33 900	↓	↓	↓	↓	↓	↓	0.021	46.11 (115)
33 901	↓	↓	↓	60	↓	2.488 (8.16)	0.15	
34 200	↓	↓	↓	↓	↓	↓	0.15	57.22 (135)
35 900	↓	↓	↓	↓	↓	↓	0.013	63.89 (147)
35 901	↓	↓	±15°	↓	60	1.244 (4.08)	0.018	
36 900	↓	↓	↓	↓	↓	↓	0.018	51.67 (125)
60 000	↓	↓	↓	↓	↓	↓	0.021	51.67 (125)
134 000	↓	↓	↓	↓	↓	↓	0.021	51.67 (125)
378 000	↓	↓	↓	↓	↓	↓	0.015	51.67 (125)
488 000	↓	↓	↓	↓	↓	↓	0.015	51.67 (125)
574 000	↓	↓	↓	↓	↓	↓	0.015	54.44 (130)
660 800	↓	↓	↓	↓	↓	↓	0.018	52.78 (127)
747 200	↓	↓	↓	↓	↓	↓	0.018	52.78 (127)
1 000 000	↓	↓	↓	↓	↓	↓	0.024	53.89 (129)

(1) Frictional heating sufficient to cause premature failure of the TFE bearing liner should not be a problem under the presently known operating conditions.

(2) The projected endurance life of these bearings cannot be predicted because of the limited amount of test data available under these abnormal conditions. Very short life, however, is not anticipated based on the test. Through periodic inspections, it should be possible to establish replacement periods if this becomes necessary.

(3) The higher coefficient of friction for this type of bearing is not a limitating factor on the basis of information from the actuator design group.

(4) Wear (free play) of the bearings will continue to increase during the aircraft life and cannot be eliminated with this type of bearing. This fact must be considered in determining the feasibility of applying this type of bearing to a SMCS.

SMCS Actuation Design

The pressure of the basic hydraulic system at its source is 2757.9 N/cm^2 (4000 psi); at the end of the lines to the SMCS actuators it has been assumed that a static pressure of 1723.7 N/cm^2 (2500 psi) will be available under maximum rate conditions. The other important actuation design requirements of vane maximum deflection, maximum rate, and maximum hinge moment have been discussed in foregoing sections. The fail-safety philosophy for the SMCS was also a significant actuation system design driver. The SMCS was to be a fail-safe system and be free from flutter potential in any failure state. This requirement led to the following implementation. Two servo cylinders actuate each of the two SMCS vane panels; one extends while the opposite retracts as shown in figure 46. Each servo cylinder actuating a given vane panel is supplied from one of two separate independent hydraulic systems. The airplane has a total of four separate hydraulic systems numbered one through four. The No. 2 hydraulic system feeds both the right forward actuator and the left aft actuator, while hydraulic system No. 3 feeds the right aft actuator and the left forward actuator. Thus, in the event of a failure in one of the hydraulic systems, sufficient power is available to center and hold both vane panels. Then, in the event of a failure of the second hydraulic system powering the SMCS actuators, a reservoir system holds pressure on the actuators to prevent flutter. Additional amplification of these design features is given in the following paragraphs.

Figure 46 shows the SMCS hydraulic system schematic while figure 47 presents the SMCS control valve and actuator operation schematic. For those

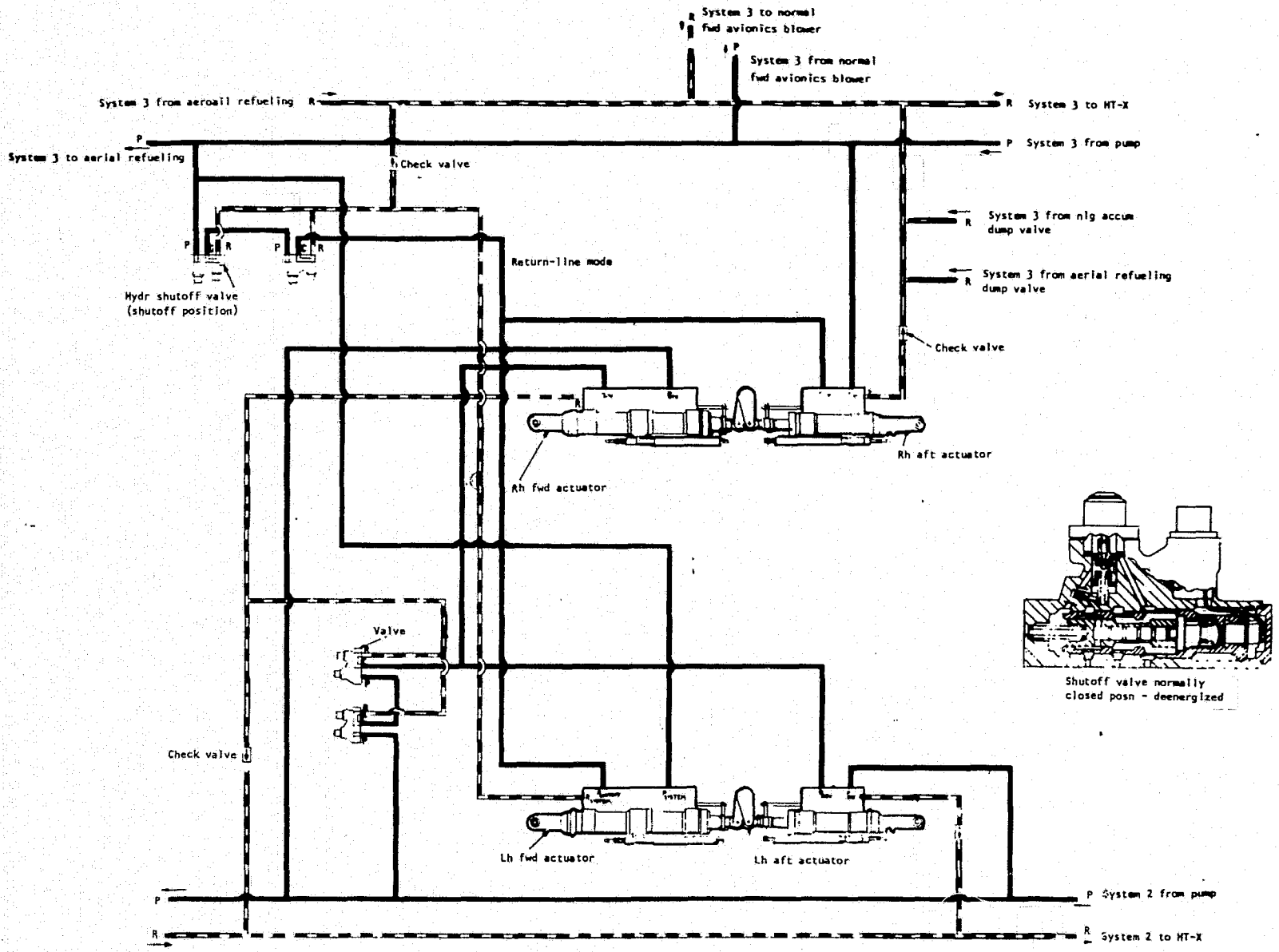

Figure 46. - SMCS hydraulic system.

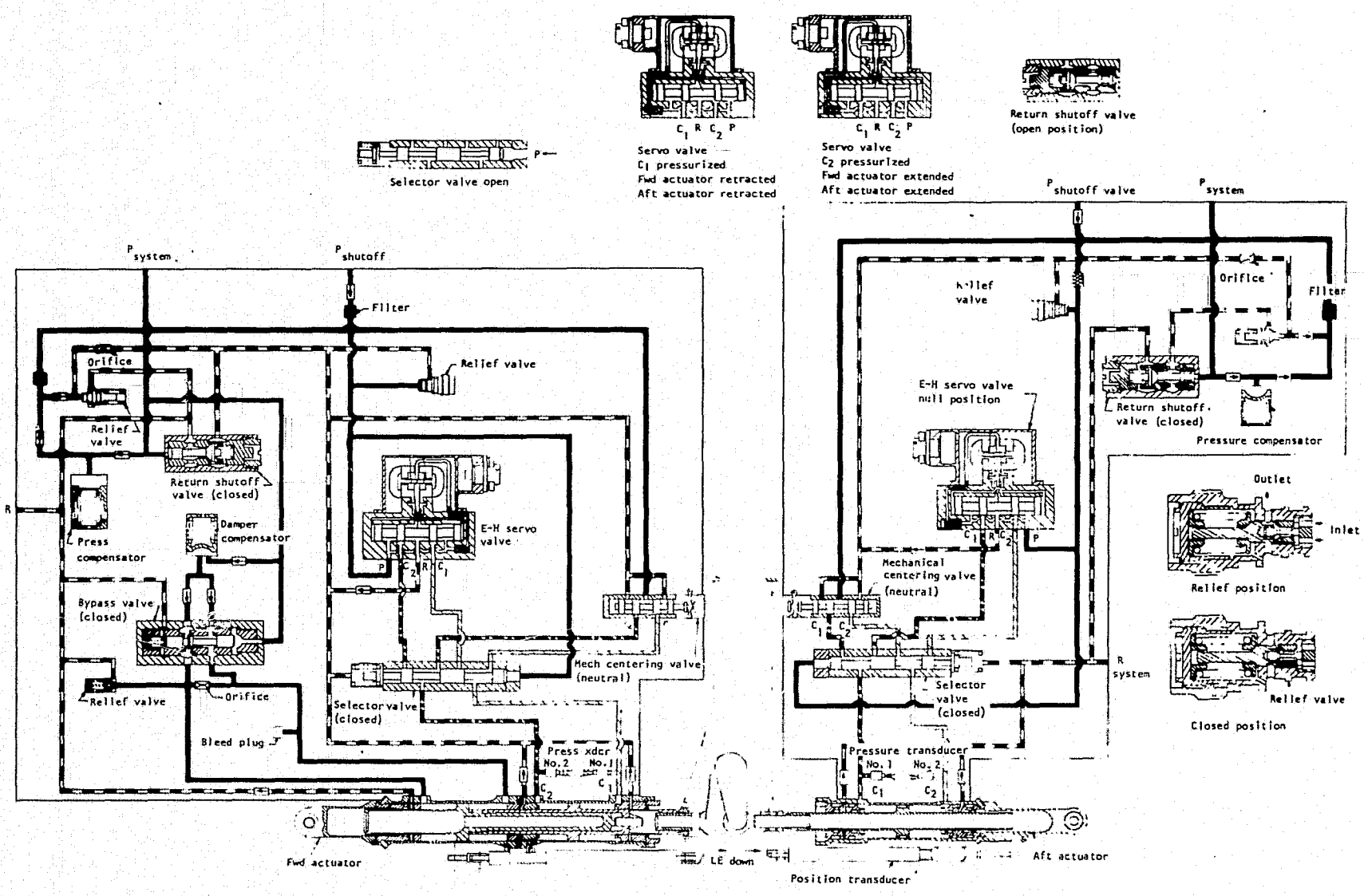

Figure 47. - SMCS control valve and actuator operation.

ORIGINAL PAGE IS
OF POOR QUALITY

minitiated in reading these more traditional forms of hydraulic operational diagrams, figures 48 and 49 are presented. These latter two figures have been assembled to illustrate a basic functional difference between the forward and the aft actuators. In order to mechanize the actuation system for the worst case of both hydraulic systems feeding the SMCS out, yet have sufficient flutter integrity, the forward servo cylinder is different and more complex than the aft servo cylinder to insure minimum stiffness.

There are three modes of operation which will be discussed and illustrated with the aid of figures 48 and 49. They are (1) SMCS engaged; (2) SMCS disengaged either because SMCS operation is not desired or because of a system failure of some kind; and (3) both hydraulic systems feeding SMCS failed.

Consider, first, figure 48. The SMCS can be engaged or disengaged by the pilot from the switch in the cockpit; but once the system is engaged, it can be disengaged by a system failure of some kind. Both the engage and disengage operation is accomplished by the hydraulic shutoff valve on the primary fluid flow path to the left on the schematic. If the hydraulic system is operating normally, the high-system pressure is sensed and causes the selector valve to operate to permit fluid flow along the primary path only. This selector valve is positioned by system pressure working against a spring-loaded spool. The primary fluid flow is actively controlled by the electrohydraulic servo valve according to the difference between the commanded actuator position and the actuator position feedback. From the actuator, the hydraulic fluid returns to the hydraulic power source through the return shutoff valve. This is the primary active mode of operation for the SMCS.

Secondary hydraulic fluid flow permits the passive control of the SMCS actuator. This flow is always available unless there is a hydraulic power source failure. The flow through the secondary path is activated by disengagement of the SMCS through pilot action or a system failure. With the primary fluid flow path cut off by the hydraulic shutoff valve, the system pressure drops and causes the selector valve to move in a manner so as to select secondary fluid flow. The pressure accumulator maintains pressure along the secondary flow path for over 2 hours even if the hydraulic power source should fail (check valves prevent reverse flow). The flow to the actuator is now controlled by the passive walking-beam arrangement of the hydromechanical centering valve. This control path does nothing more than center the actuator and hold it in this position. From the actuator, the hydraulic fluid returns to the power source through the return shutoff valve. If the secondary flow pressure is low because of hydraulic source failure, the unbalanced return shutoff valve closes this return path in order to maintain minimum stiffness requirements through the pressure accumulator.

The functions just described for the aft actuators can be identified in figure 49 for the forward actuators. The main difference between the forward

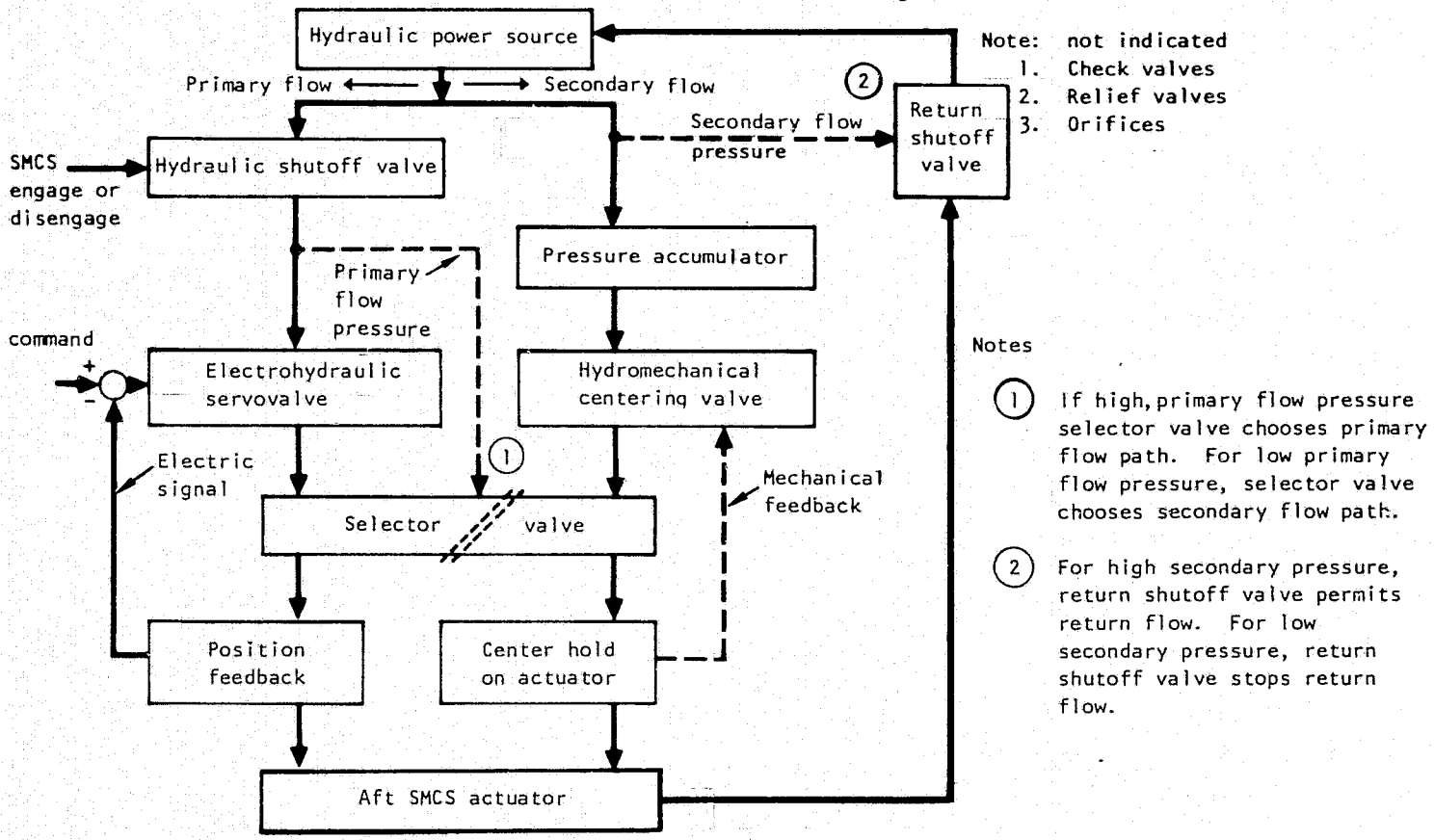

Figure 48. - Functional schematic of hydraulic flow through aft SMCS actuator.

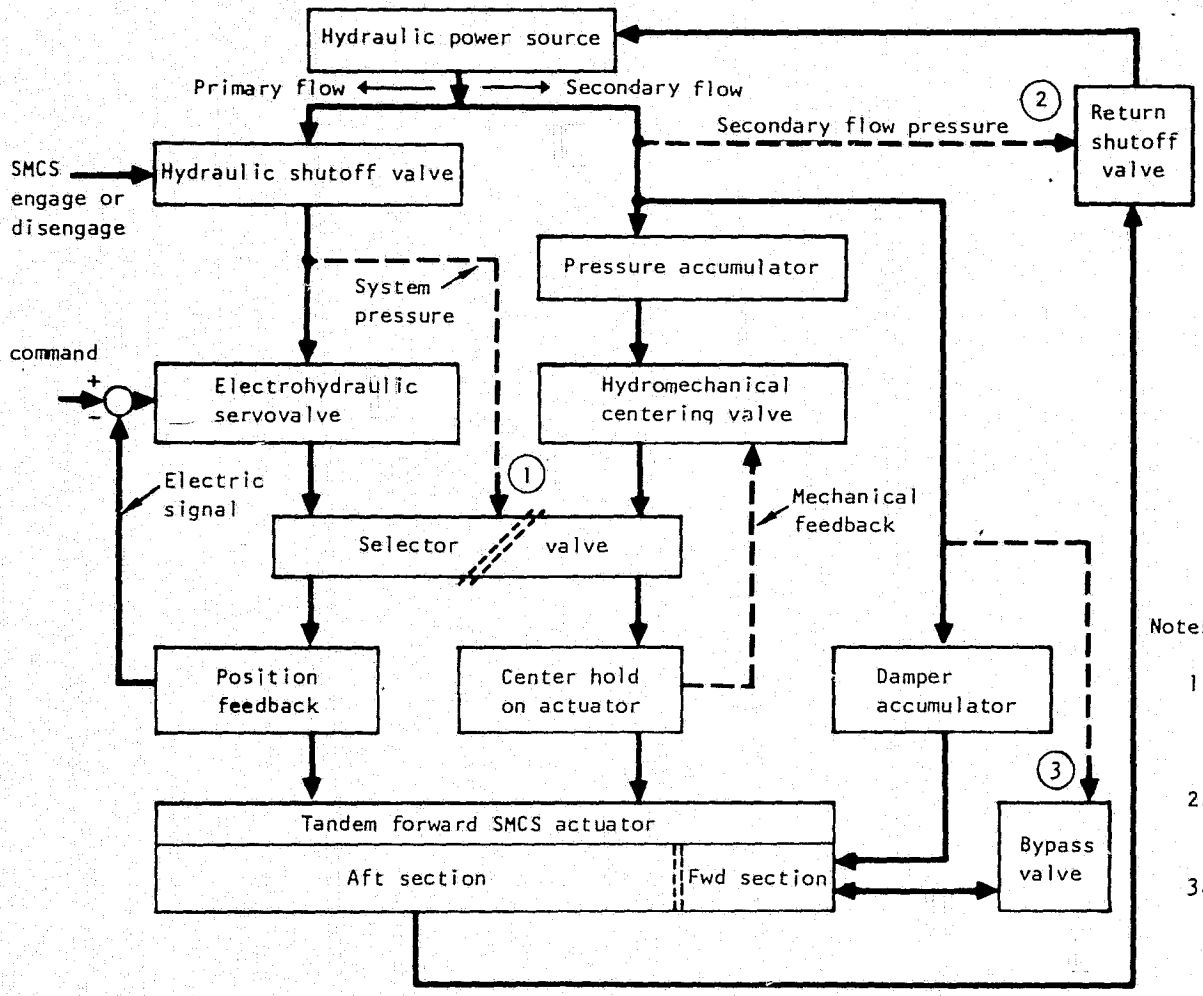

Note: not indicated
1. Check valves
2. Relief valves
3. Orifices

Notes

1. If high primary flow pressure selector value, chooses primary flow path.
2. If secondary pressure is down, return valve is closed.
3. If secondary pressure is down, bypass valve is closed trapping fluid in forward section of tandem actuator.

Figure 49. - Functional schematic of hydraulic flow through forward SMCS actuator.

and aft actuators can be seen in the lower part of figure 49. The forward actuator is a tandem actuator where the forward section is connected to a damper accummulator. If the secondary flow pressure is down, the bypass valve is closed in addition to the return shutoff valve. Thus, minimum-stiffness pressure is available for 2 hours from two sources in the forward actuator secondary flow (1) in the pressure accumulator, and (2) the damper accumulator. The significant feature of this arrangement is that the damper accumulator of the forward section could still function even if the secondary flow path through the pressure accumulator were destroyed.

For simplicity, figures 48 and 49 do not reflect the check valves, relief valves, and orifices as do figures 46 and 47. However, the check valves prevent flow from backing up and the relief valves allow fluid to return to the hydraulic power source when line pressure becomes too large from either load or temperature increases.

Another feature should be mentioned, but is not illustrated in figures 48 and 49. This is the actuator pressure sensing feature which coordinates the push-pull of the forward and aft actuators.

Because the forward and aft hydraulic servo actuators have different peripheral functions as described, they have different physical characteristics. They are described as follows:

Forward Hydraulic Servo Actuator

Bore diameter	5.380 cm (2.118 in.) maximum
Rod diameter	3.487 (1.373 in.) maximum
Stroke	8.941 (3.520 in.) maximum
Area to extend/retract	13.174 cm^2 (2.042 $in.^2$) maximum
Volume to extend/retract	117.790 cm^3 (7.188 $in.^3$) maximum

Aft Hydraulic Servo Actuator

Bore diameter	4.717 cm (1.867 in.) maximum
Rod diameter	2.535 cm (0.998 in.) maximum
Stroke	8.941 cm (3.520 in.) maximum
Area to extend/retract	12.619 cm^2 (1.956 $in.^2$) maximum
Volume to extend/retract	101.354 cm^3 (6.185 $in.^3$) maximum

Design hydraulic flow rate is 0.03532 m^3/min (9.33 gpm) for one actuator.

SMCS Vane/Actuation Installation

Figure 50 shows how the pivot bearings are supported and how this support structure ties into other structural elements. Figure 51 presents the details of how the actuators are installed relative to pivot attachment and backup structure.

LABORATORY TESTING OF SMCS ACTUATOR

The servo cylinder tested was one of the forward SMCS tandem hydraulic actuating cylinders and was supplied hydraulic power from one independent hydraulic system at two places. One side of the tandem actuator is bypassing until shutoff valves are deenergized, causing fluid to be trapped and act as a damper. The input was an electrical input to the servo valve, which in turn meters fluid to the servo cylinder.

A feedback system using a linear variable displacement transducer (LVDT) to close the electrical loop was employed to maintain the servo cylinder piston position. The servo cylinder was a single entity and consisted of the following components:

(1) Tandem hydraulic cylinder (including attachment fittings)

(2) Check valves

(3) Relief valves

(4) Hydraulic fluid filters

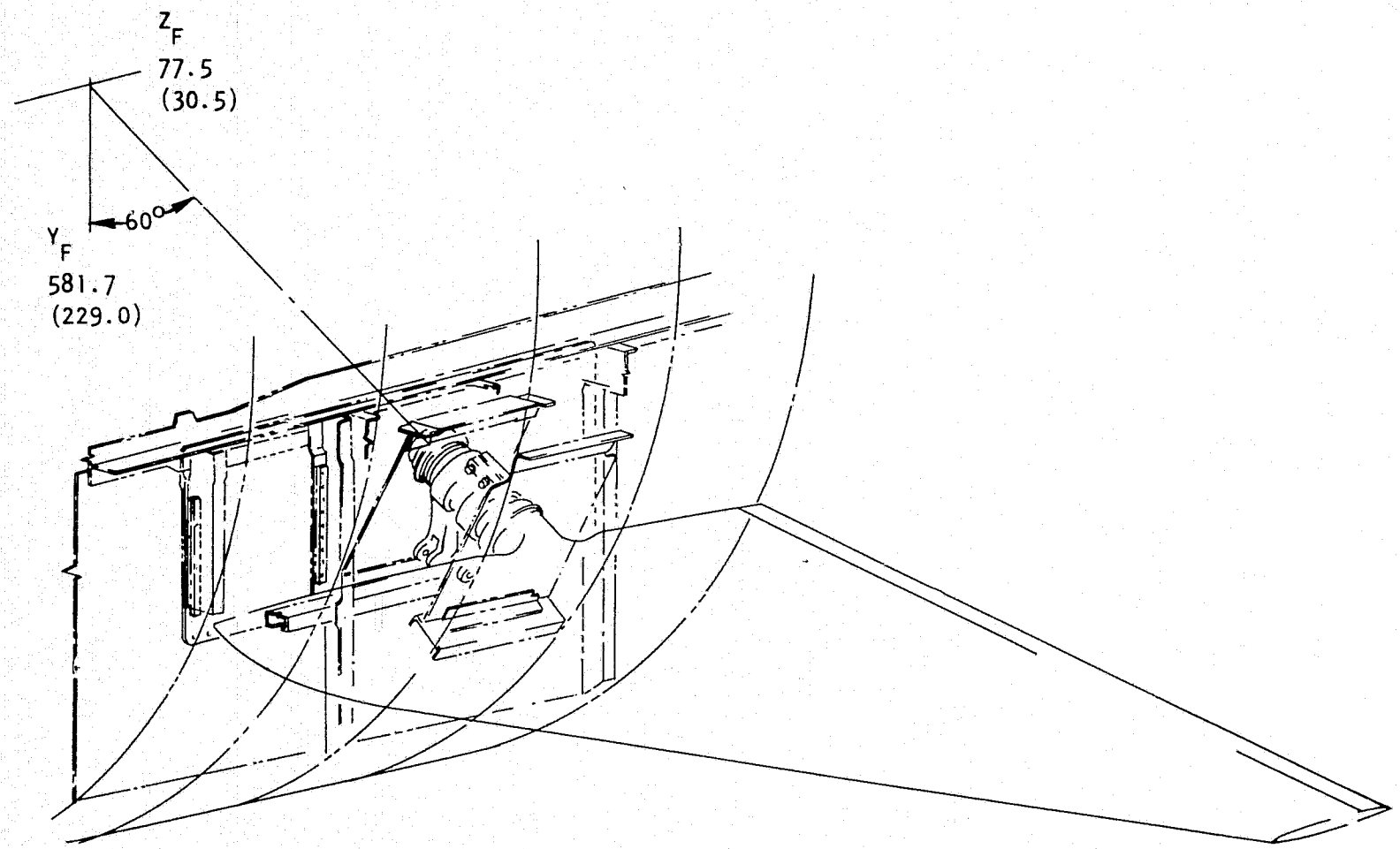

Figure 50. - SMCS vane pivot bearing support structure.

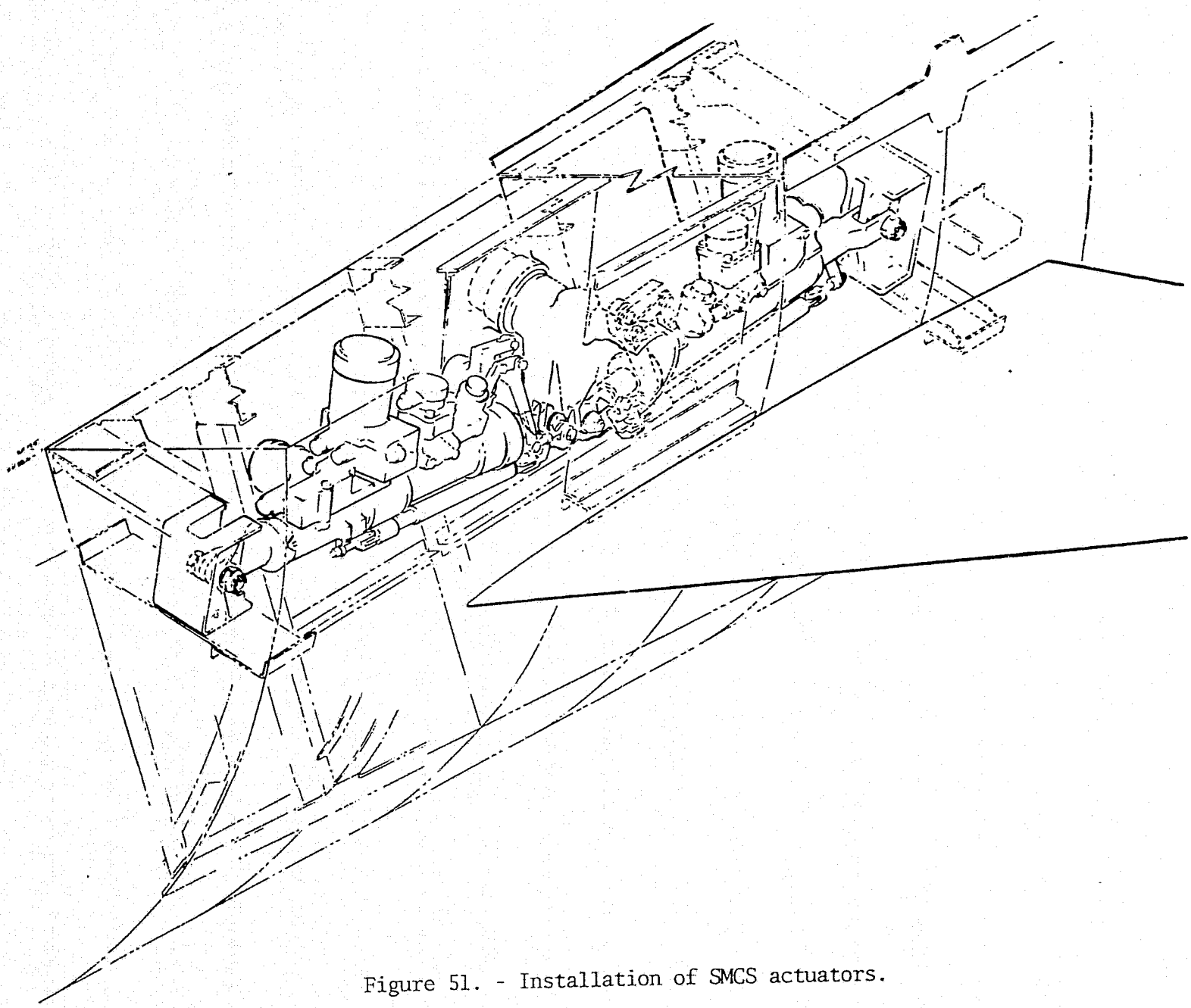

Figure 51. - Installation of SMCS actuators.

(5) Two hydraulic pressure transducers

(6) LVDT

(7) Electrohydraulic servo valve

During the endurance and vibration tests, the servo cylinder, with aircraft mounting bolts and hydraulic fluid supply lines, was installed in the fixtures to simulate installation in the B-1 aircraft.

The purpose of these tests was to verify conformance to specifications. For dynamic performance, a minimum vane angular rate and work torque (hinge moment) capability are specified. For flutter integrity, actuator spring rates and free-play requirements are specified. For hydraulic life, leakage and fluid filtering requirements are specified. For endurance tests of the system, the actuator was exercised for 10 percent of its designed life, under various environmental conditions. Applicable military specification requirements are covered in refs. 9, 10, and 11. Additional requirements are covered by refs. 12 and 13.

Endurance Tests

The endurance cycling test consisted of flight representative operation cycles with external loading for 10 percent of the designed duty life. Rather than cycle with a single amplitude and frequency, the actuators were cycled with the summation of four amplitudes and frequencies. The result of such an approach best simulated the actuator in its actual life cycle.

A schematic of the test configuration is shown in figure 52. The actuator worked through a bellcrank to the load system servo actuator. The load-stroke requirements are shown in figure 53.

The actuator was mounted in an endurance test fixture and placed in an environmental chamber. Hydraulic fluid was supplied from a hydraulic test stand and flowed through coiled tube heat exchangers in the environmental chamber for temperature conditioning before entering the test actuator. Thermocouples were installed in the actuator fluid supply and return lines for monitoring and control. Restrictors producing the required pressure drop to simulate aircraft line loss were installed in the lines to the actuator pressure and return ports.

C-2

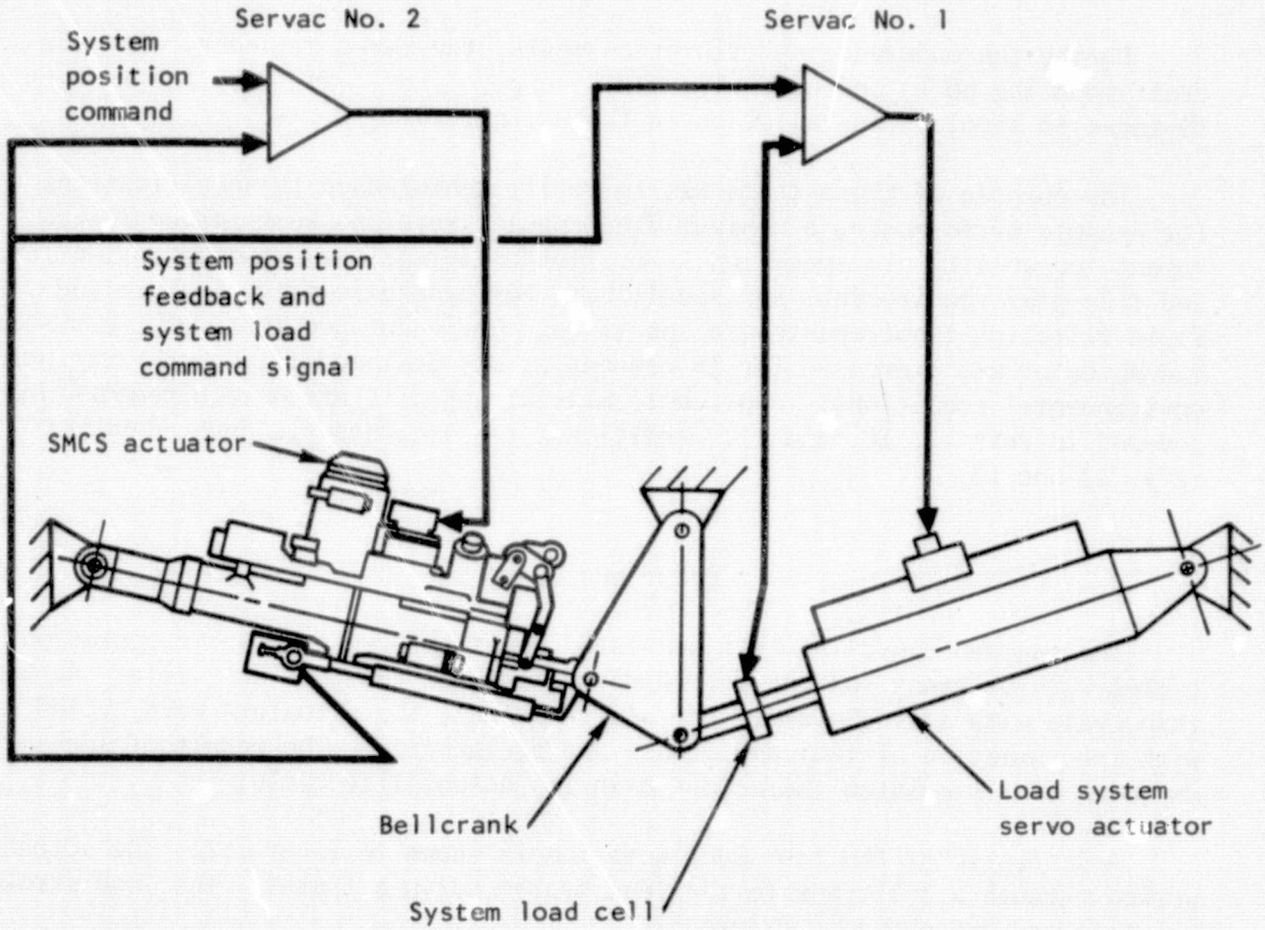

Figure 52. Schematic of SMCS actuator endurance test setup.

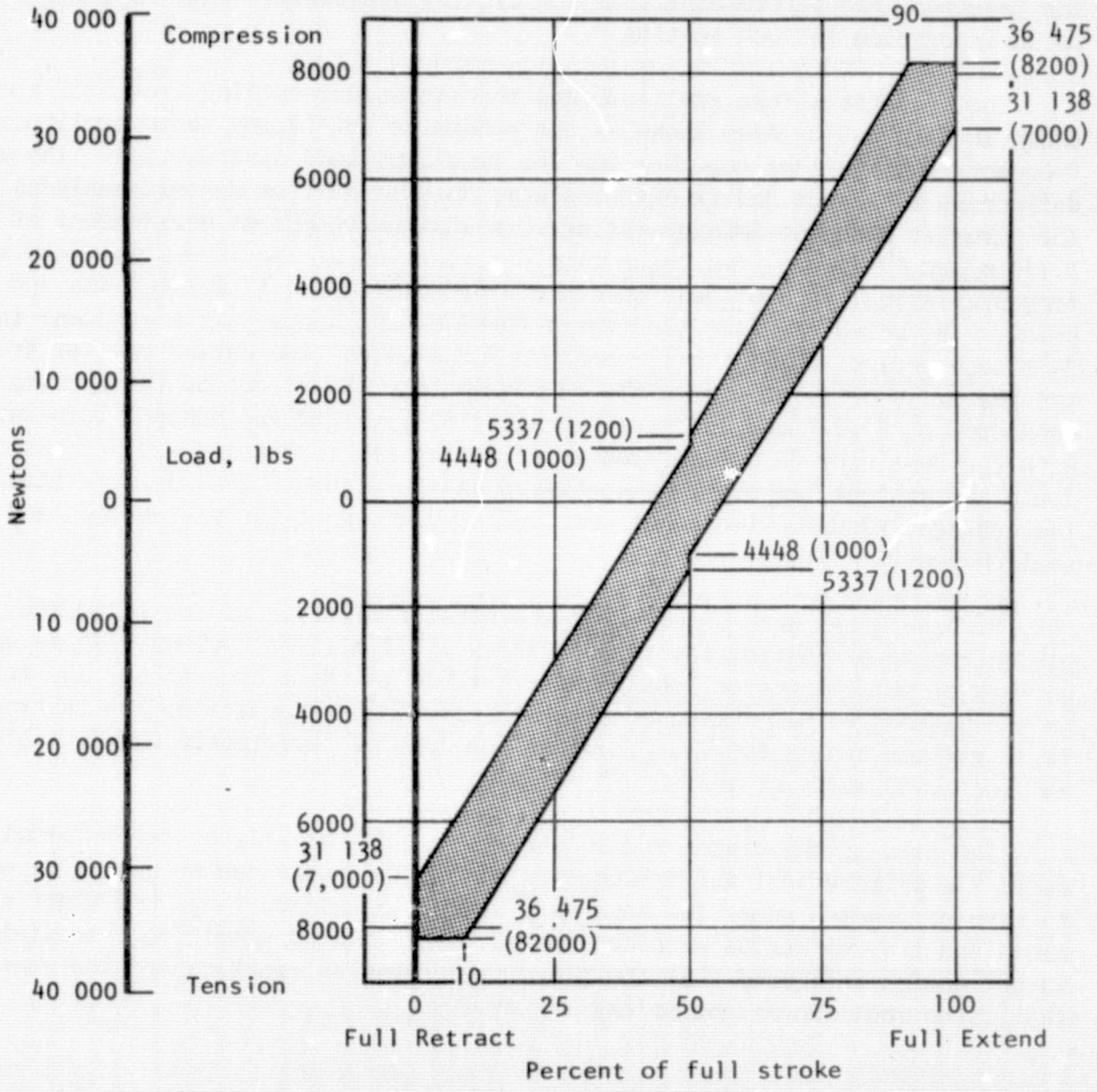

Figure 53. - SMCS actuator load-stroke requirements for endurance test.

The actuator stroke amplitudes and cycling frequencies were a simultaneous summation of four sinusoidal command signals. This produced a random cycle that closely duplicated the aerodynamic cycling loads to be encountered by the aircraft as predicted by analytical studies. Four frequency generators were coupled with a frequency summing amplifier and a control console that produced the required load-stroke amplitude and cycling frequency. This is believed to be an innovation in such testing.

The actuator stroke amplitude and the sinusoidal cycling frequency are shown in figure 54. Also shown is the schematic for adding these amplitude-frequency combinations together and the time-amplitude distribution. The vane deflection amplitude and frequencies were determined from dynamic analyses of the aircraft with the SMCS operating in a maximum turbulent environment of 2.134 m/sec (7 ft/sec) rms. The time distribution of amplitudes was determined from statistical data of gust encounters of 2.134 m/sec (7 ft/sec) rms and below. The actuator was cycled for a total of 193 hours. This was done in 30-minute periods where the temperature for a given time period was set from the thermal profile of figure 55. Approximately 75 percent of the cycling was conducted at 87.88° and 135° C (190° and 275° F) fluid and ambient temperatures with the remaining 25 percent conducted during the increasing and decreasing fluid and ambient temperatures specified on the figure. Records were made of the leakage, visual evidence of wear and/or galling of the piston rod, and all seal changes.

Scratch marks were observed on the outside diameter of the fixed end piston rod after testing for airworthiness (1.31 million cycles). There was no loss of performance or leakage attributable to these scratches. The marks on the piston rod had increased after the preliminary qualification testing (4.67 million cycles total). There was no loss of performance attributable to the increased marks or wear.

The area of the piston rod in question slides axially by two internal seals - a primary seal and a secondary seal. The marks and burnishing appeared to have originated under the secondary seal. The backup rings had minor extrusions and the cap strips were considered to be in good condition. Initial investigation indicated that the glass-filled backup rings caused the wear on the piston rod. No flight safety is involved.

Free-Play Tests

For free-play tests, the actuator was installed in the endurance test fixture (see figure 52) and a displacement transducer (LVDT) was mounted between the fixed and attach clevis and the rod and end attach clevis, as shown in

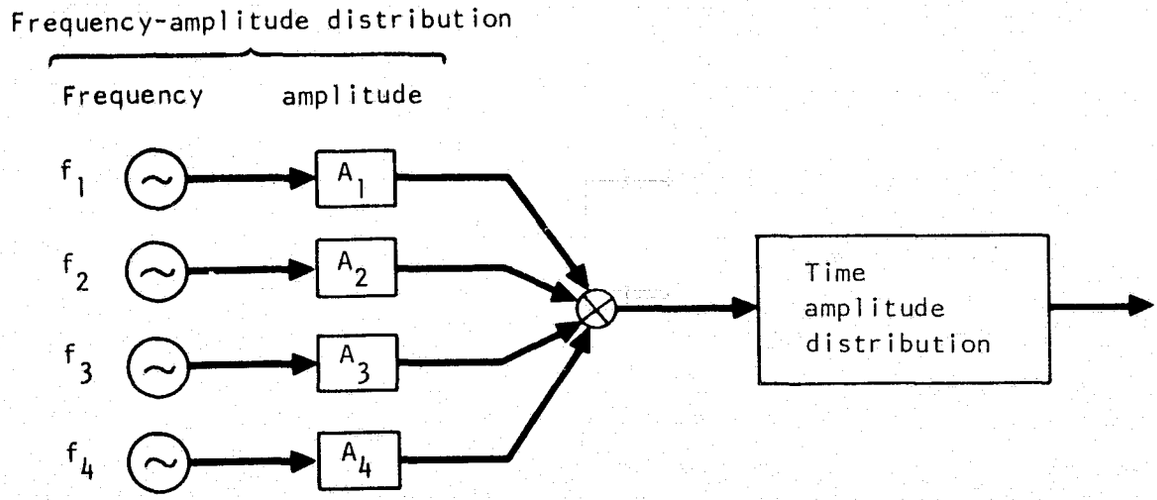

Frequency - amplitude distribution

Frequency Hz	Amplitude ± deg	
$f_1 = 0.636$	$A_1 = 4.15$	For gust maximum intensity of 2.134 m/sec (7 ft/sec) rms
$f_2 = 2.06$	$A_2 = 5.74$	
$f_3 = 4.77$	$A_3 = 1.87$	
$f_4 = 7.32$	$A_4 = 1.65$	

Combined signal = $\sum_{i=1}^{4} A_i \sin 2\pi f_i t$

Time - amplitude distribution (100% test duration = 193 hours)

Time % test duration	Amplitude % maximum
2.5	15
17.5	30
25.0	45
32.5	60
13.0	75
5.0	90
2.0	100

Figure 54. - Frequency-amplitude distribution for SMCS actuator endurance tests.

Tolerances:	
Inlet fluid temperature:	$^{+\ 0}_{-\ 8.3^{\circ}\ C}$ $\left(^{+\ 0}_{-\ 15^{\circ}\ F}\right)$
Ambient temperature:	$\pm$ 5.6° C ($\pm$ 10° F)

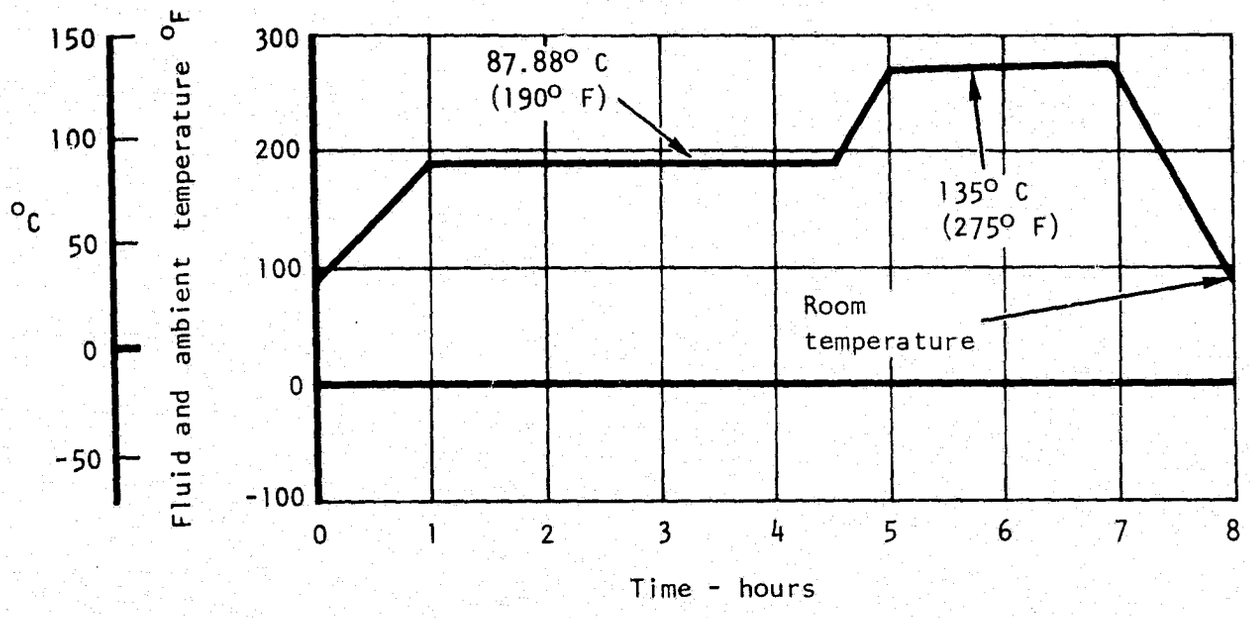

Notes:

1. Stabilize fluid and ambient temperature at 32.2° $\pm$ 11.1° C (90° $\pm$ 20° F) prior to start of cycling.

2. Time to and from maximum fluid and ambient temperatures may vary providing maximum temperatures are maintained for at least 75% of each thermal profile.

Figure 55. - Thermal profile for SMCS actuator endurance tests.

figure 56. The cyclic load, to the test actuator was applied through a bellcrank by a servo cylinder in the load system. Equivalent load on the test actuator was read from the output of a load cell installed between the loading cylinder and test fixture bell crank.

Free play is designated as the motion lost in a device when a load of 8896 ±2224 N (2000 ±500 lb) across the device is reversed and appears as a break in a load-deflection curve. Total free play for the servo cylinder included all free play between the attach fitting at one end of the servo cylinder and the attach fitting at the other end.

The free play requirement for maximum allowable is 0.00508 cm (0.002 in.). The actuator was tested at three positions: fully extended, midstroke, and fully retracted. Figure 57 contains results for the fully retracted case and is typical of those for this series of tests. As indicated, the free play is 0.00254 (0.001) and 0.00381 cm (0.0015 in.).

To put these results into perspective from a flutter analysis point of view, the free play of the SMCS vane as installed on the airplane and read as angular rotation of the pivot is displayed in table IV.

TABLE IV. - SMCS VANE-INSTALLED FREE-PLAY TEST RESULTS

Test type	Surface	Configuration	Free play, radians
Hand-load	LH	Aft act. pressurized	0.00017
Hand-load	LH	Fwd act. pressurized	0.00028
Hand-load	RH	Aft act. pressurized	0.00043
Hand-load	RH	Fwd act. pressurized	0.00021
Load-deflection	RH	Aft act. pressurized	0.00020
Load-deflection	RH	Fwd act. pressurized	0.00037

Specified free play $\leq$ 0.0006 radians

An LVDT position transducer was mounted to measure the test cylinder freeplay between the fixed end bolt and the rod end bolt, as shown.

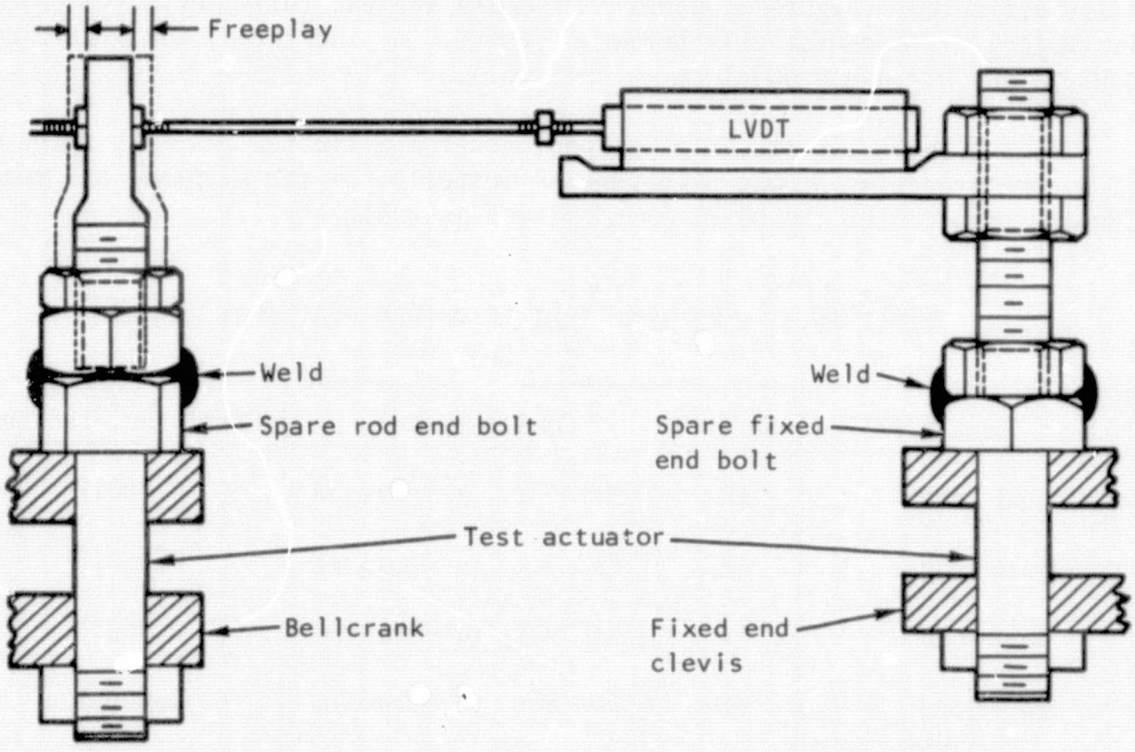

Figure 56. - SMCS actuator freeplay test setup.

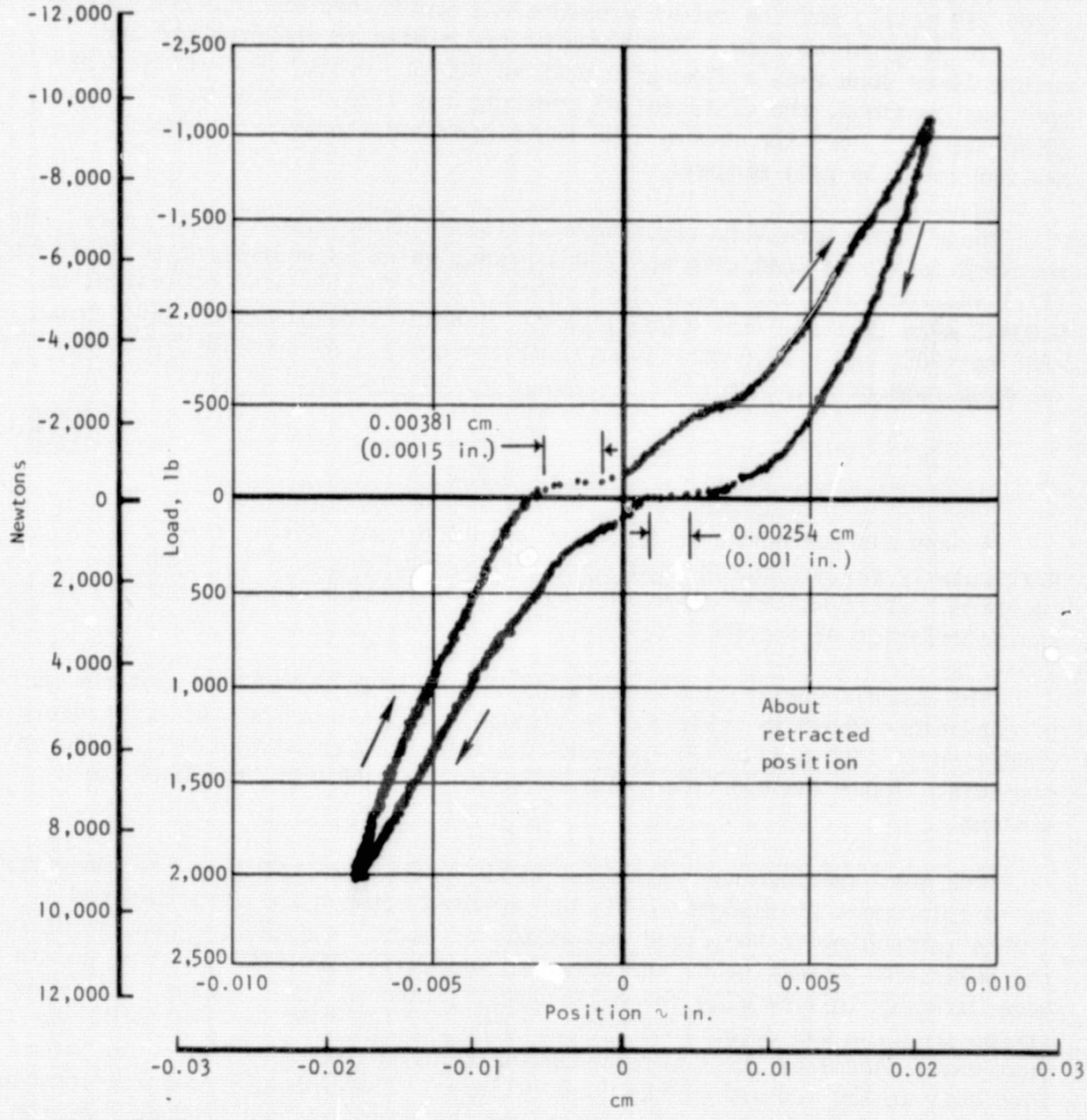

Figure 57. - Typical SMCS actuator freeplay test results.

Steady-State Actuator Rate Test

This test was conducted using the no-load test setup shown in figure 58. The supply pressure for these tests was maintained at 2826.8 ±34.5 N/cm^2 (4100 ±50 psig), and the return pressure was maintained at 103.4 ±6.9 N/cm^2 (150 ±10 psig) at no flow. Restrictors were placed in the pressure and return lines such that a flow of 0.0345 +0.00076, -0.0 m^3 (9.1 +0.2, -0.0 gpm) was obtained, the differential pressure was 1723.7 ±34.5 N/cm^2 (2500 ±50 psi), and the return line restrictor had a pressure loss of 344.7 N/cm^2 (500 psi) minimum.

These rate capability tests were performed using almost full stroke. The required design no-load rate was 200 deg/sec, which is equivalent to 43.43 cm/sec (17.1 in./sec) on a 12.7 cm (5 in.) moment arm. This is also equivalent to 0.03445 m^3/m (9.1 gpm) for a 117.8 cm^3 (7.188 $in.^3$) displacement (40° throw, -20° to +20°, and a 12.9 cm^2 (2 $in.^2$) piston area). As seen in figure 59, the required rate of 43.43 cm/sec (17.1 in./sec) was exceeded slightly.

Dynamic Spring Rate

A test was conducted to determine actual dynamic spring rates, particularly the minimum dynamic spring rate and frequency at which it occurred. These minimum characteristics are important in determining flutter characteristics of the SMCS.

The dynamic spring rate tests were performed in accordance with the matrix of conditions shown in table V. The tests were performed at the temperature condition of 135° C (275° F) for both the ambient air and the inlet fluid temperature. These maximum temperatures reduce the hydraulic stiffness to a minimum.

The test specimen was installed in the endurance test fixture. An external displacement transducer (LVDT) was mounted between the structure-end clevis (attaching to the fixed end of the actuator) and the rod-end clevis on the bellcrank (attaching to the actuator rod end). The LVDT mounting points were directly in-line with the bolts passing through the clevises. Actuator stroke position was determined by the output of the LVDT integral with the test unit. Actuator loads were indicated and controlled by the output of a load cell at the rod-end of the load cylinder. The hydraulic control console and associated feedback system controlled the magnitude and frequency of the applied loads. That portion of the fixture in which the test specimen was mounted was placed in an environmental temperature chamber. To assist in

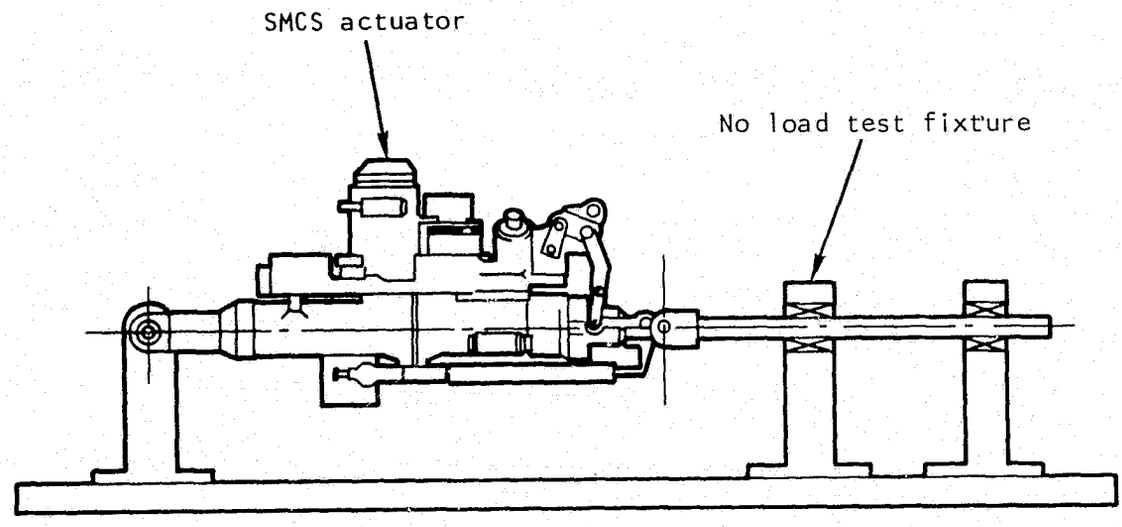

Figure 58. - No-load test fixture installation for rate tests.

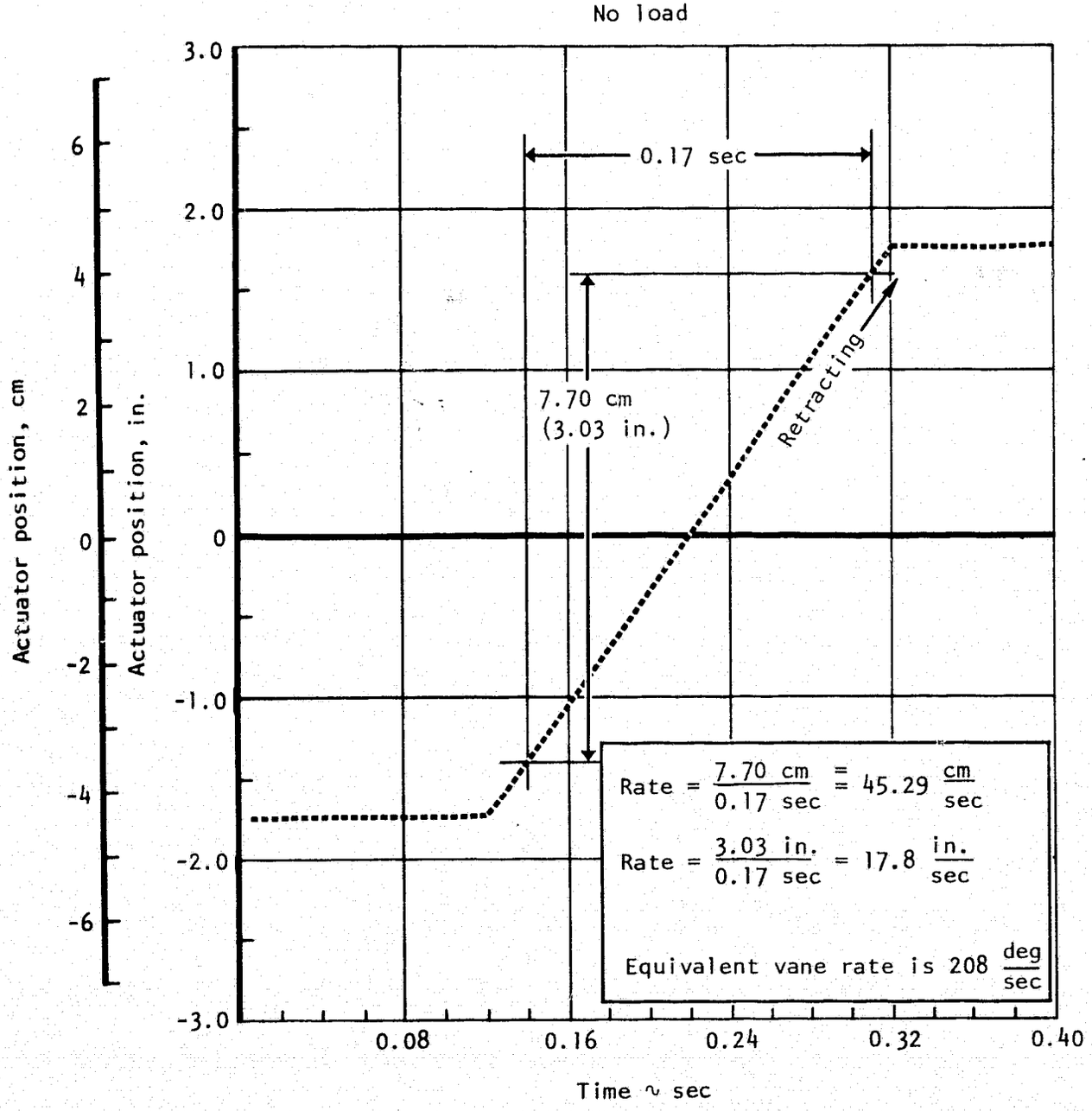

Figure 59. - Typical actuator rate test results.

maintaining fluid temperatures at the required environmental temperatures, fluid was circulated through large tubing coils within the chamber, prior to entering the test specimen. Thermocouples were inserted in the fluid lines adjacent to the test specimen to indicate the temperature of fluid entering and discharging from the actuator.

The conditioned output signals from the load cell (force) and the external LVDT (displacement) were plotted as frequency versus the complex amplitude ratio (force/displacement), or spring rate, and the phase angle (between applied load and resultant displacement). Figure 60 is an example of such a plot for test 1 (normal system operation) of table V. From these data, a minimum spring rate of 166 370 N/cm (95 000 lb/in.) at 8 Hz and above was specified for design purposes for this normal actuator.

Figure 61 shows the test data for the case of no fluid flow to the actuator, but with fluid trapped and pressure maintained by a compensator (minimum stiffness case), test 13 in table V. From these data, a minimum stiffness of 70 051 N/cm (40 000 lb/in.) at 10 Hz and above was specified for design purposes. This is the value used in minimum stiffness flutter analyses.

FLIGHT CONTROL SIMULATOR TESTS OF SMCS

SMCS tests were performed on the flight control simulator (the "Iron Bird"). A schematic view of the B-1 flight control simulator is shown in figure 62. An enlarged view of the structural mode control actuation installation on the B-1 flight control simulator is shown in this same figure. The SMCS, as tested on the flight control simulator, was functionally identical to that installed in the aircraft with the exception that the two actuators for the vane on the right side only of the aircraft were used. The control vane mass and inertia were simulated by a horizontal bar with the correct moment of inertia and fore and aft center of gravity; aerodynamic loads on the vane were not simulated. Also, actual system accelerometers were not used; signals from these sensors were represented by outputs from a sinusoidal signal generator or aircraft model simulation.

The B-1 development program included flight control simulator tests for individual systems checkout and total control system integration and performance tests. Specific SMCS test program objectives included the following:

(1) Verification of design compliance of the SMCS controller and actuator hardware with design specifications. These tests were part of the SMCS prequalification prior to flight test and provided validation of the analysis models used for performance evaluation.

TABLE V. - SMCS ACTUATOR DYNAMIC SPRING RATE TEST SCHEDULE

Test	Parameters				
	Frequency Hz	Preload newtons (lb)	Applied load newtons (lb)	Stroke %	Configuration
1	0.1 to 15	-17 793 (-4000)	± 8 896 (±2000)	50	1
2	↓	0	± 4 448 (±1000)	↓	1
3	↓	↓	±13 345 (±3000)	↓	1
4	↓	↓	±26 690 (±6000)	↓	1
5	↓	↓	± 4 448 (±1000)	↓	2
6	↓	↓	± 8 896 (±2000)	↓	2
7	↓	↓	±13 345 (±3000)	↓	2
8	↓	↓	±26 690 (±6000)	↓	2
9	↓	↓	± 4 448 (±1000)	↓	3
10	↓	↓	± 8 896 (±2000)	↓	3
11	↓	↓	±13 345 (±3000)	↓	3
12	↓	↓	±26 690 (±6000)	↓	3
13	↓	↓	± 4 448 (±1000)	↓	4
14	↓	↓	± 8 896 (±2000)	↓	4
15	↓	↓	±13 345 (±3000)	↓	4
16	0.1 to 15	0	±26 690 (±6000)	50	4
17	1 to 15	-17 793 (-4000)	± 8 896 (±2000)	5	1
18	15	0	±26 690 (±6000)	5	1
19	1 to 15	-17 793 (-4000)	± 8 896 (±2000)	20	1
20	15	0	±26 690 (±6000)	20	1
21	1 to 15	-17 793 (-4000)	± 8 896 (±2000)	40	1
22	15	0	±26 690 (±6000)	40	1
23	1 to 15	-17 793 (-4000)	± 8 896 (±2000)	80	1
24	15	0	±26 690 (±6000)	80	1
25	0.1 to 15	0	± 4 448 (±1000)	50	5
26	↓	↓	± 8 896 (±2000)	↓	5
27	↓	↓	±13 345 (±3000)	↓	5
28	0.1 to 15	0	±26 690 (±6000)	50	5

Configuration	Remarks
1	System pressure shall be normal operating.
2	System pressure shall be 0.
3	System pressure shall be 0. Bleeder plug removed.
4	System pressure shall be 0. Pressure transducer removed.
5	System pressure shall be normal operating. P_{so} port pressure shall be same as return pressure.

NOTE: Zero percent output position denotes piston bottomed at full retract position.

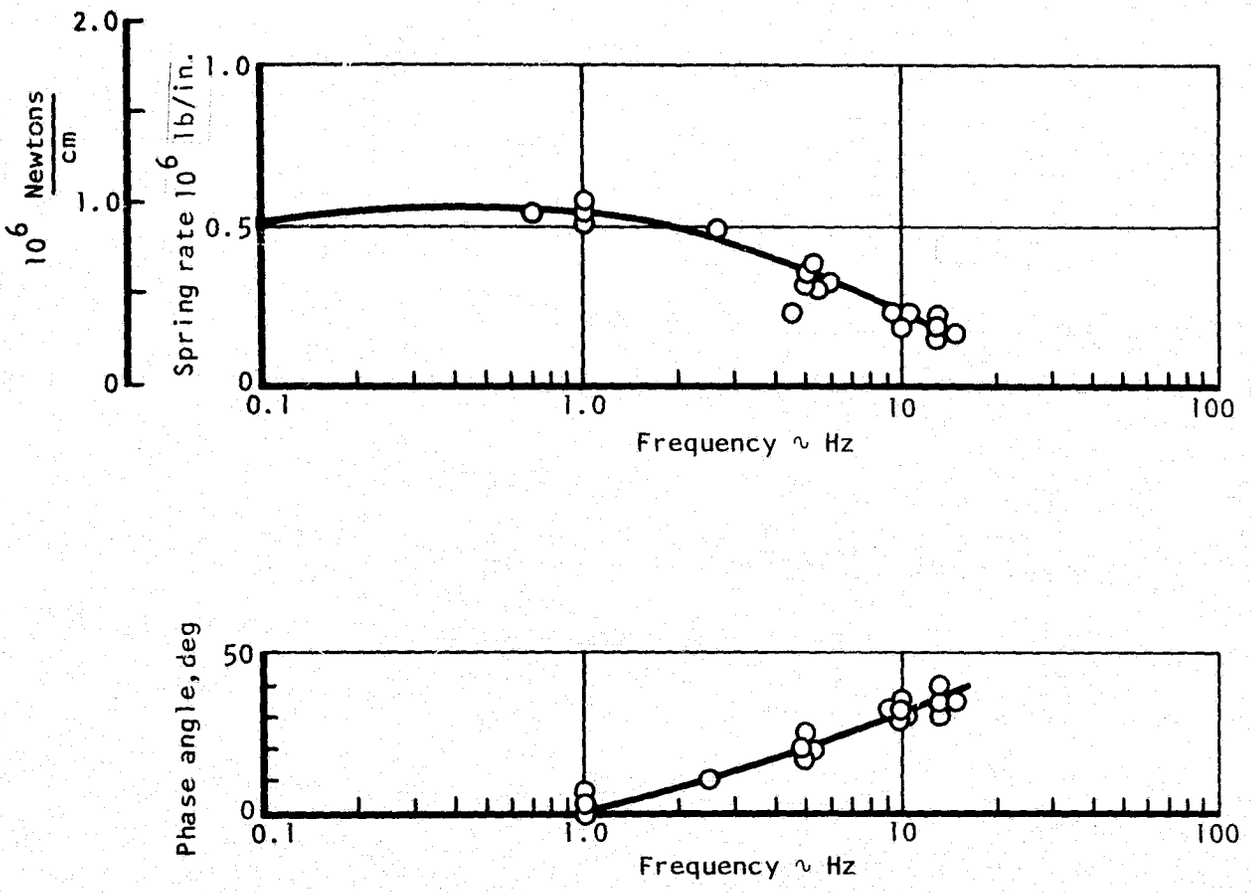

Test No. 1
Configuration: 1
Preload: -17 793 Newtons (-4000 lb)
Cyclic load: ±8896 Newtons (±2000 lb)

Figure 60. - Results of dynamic spring rate tests, normal actuator.

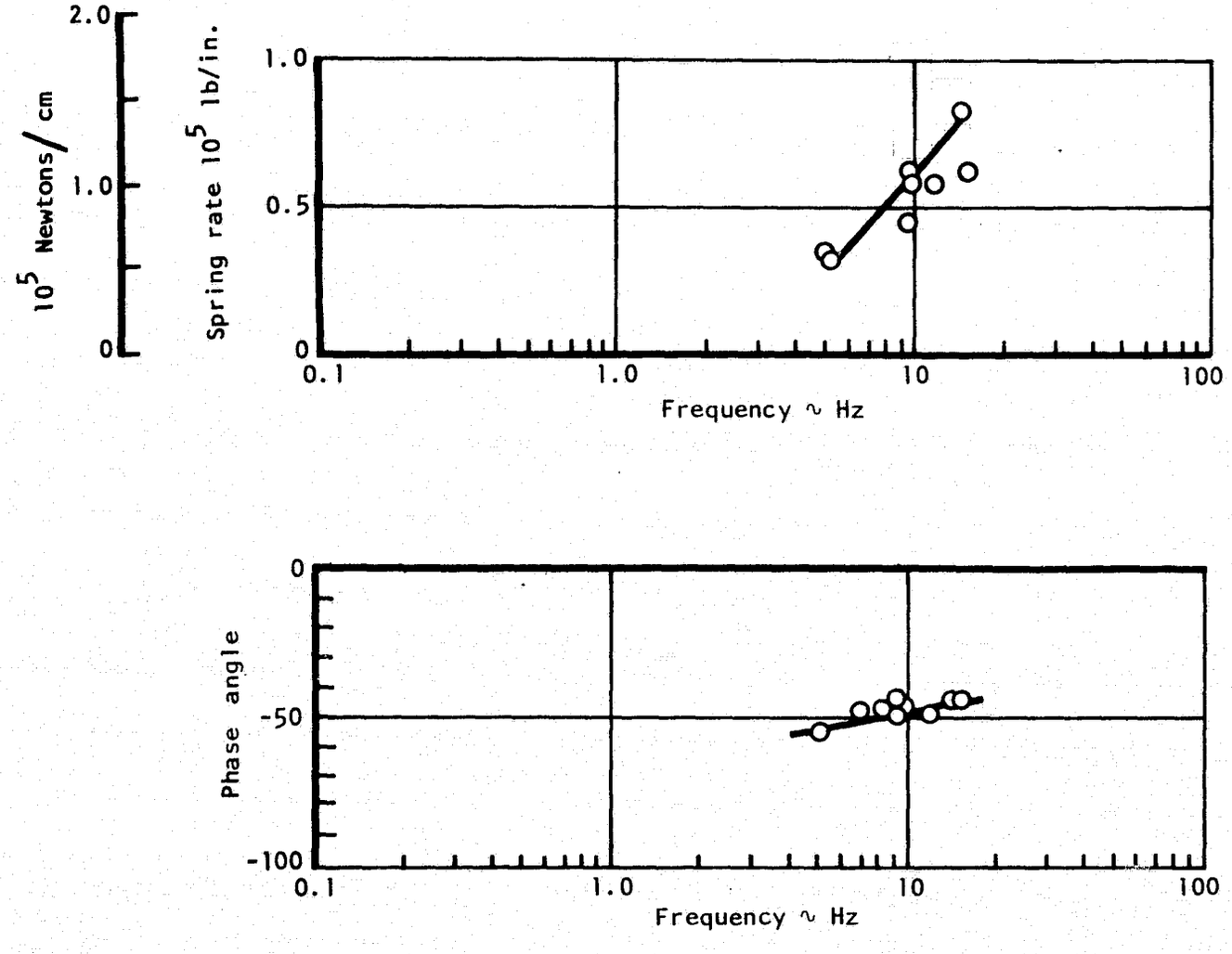

Test No. 13
Configuration: 4
Preload: 0
Cyclic load: ±4448 Newtons (±1,000 lb)

0 psi system pressure, 86.2 Newtons/cm^2 (125 psi) in compensator
135° C (275° F) fluid temperature

Figure 61. - Results of dynamic spring rate tests, actuator failed to minimum stiffness.

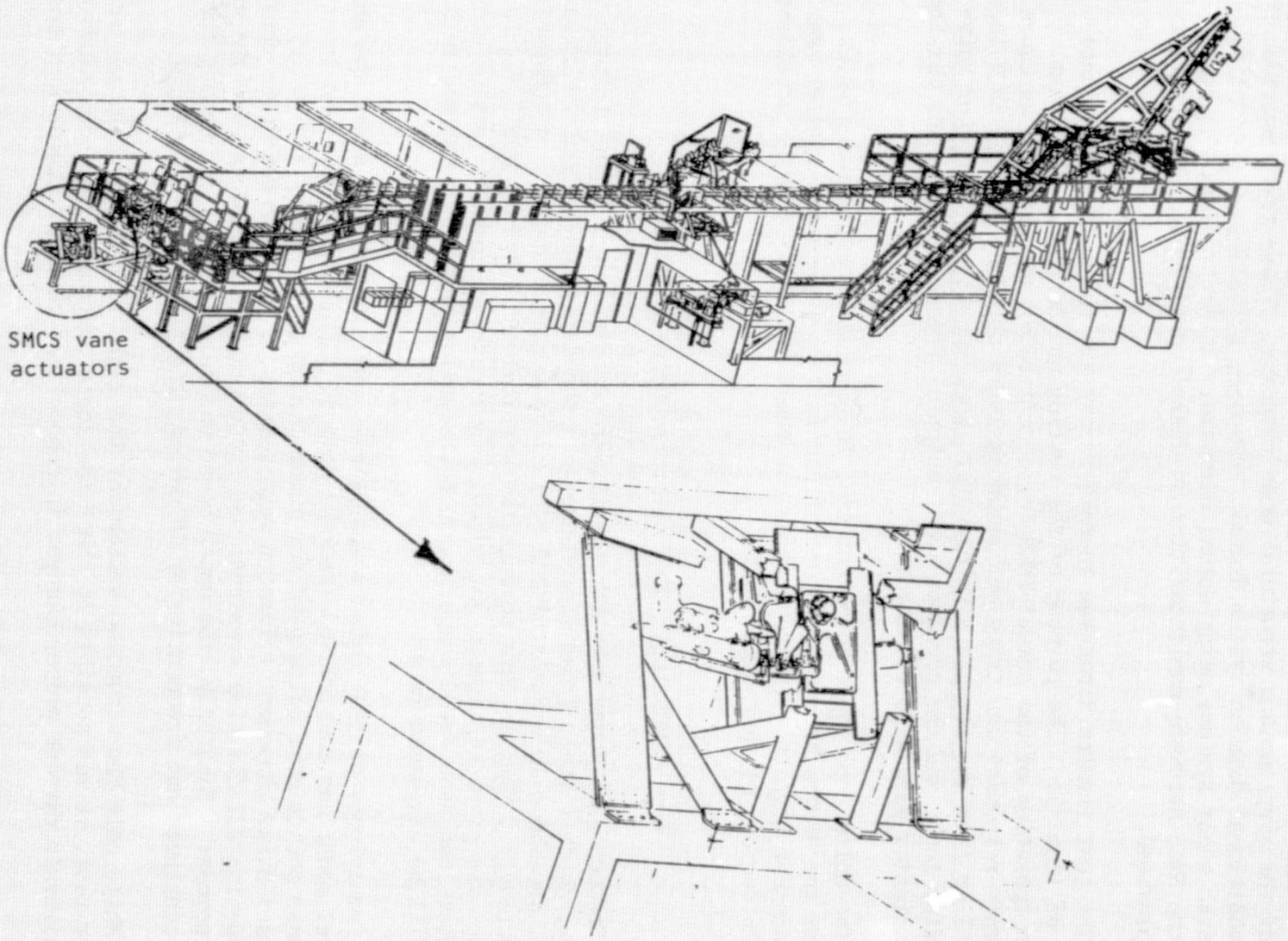

Figure 62. - SMCS right side vane actuators as installed on flight control simulator.

(2) Evaluation of SMCS normal operation and failure mode performance during closed loop tests accomplished using analog computer simulations of the airplane and structural mode response. These tests provide additional data on system dynamic response, stability, and coupling with other systems using actual hardware. In particular, the impact of the SMCS hardware nonlinearities on dynamic performance and stability is provided.

The test results discussed in this report are the design compliance tests of item (1). The purpose of the testing was to verify the dynamic system operation of the actual SMCS logic controller and actuator hardware. Frequency responses and transient responses were obtained for the SMCS logic controller from the forward accelerometer input to both the actuator valve amplifier input and the actuator model output. Frequency responses for the SMCS actuator were also obtained.

The units from input to output used in simulator testing were volts, whereas the system has accelerometer (load factor) inputs and angular vane displacement outputs. The conversion for the B-1 is 3.75 volts/g acceleration and $6/\pi$ degrees of vane angle/volt.

SMCS Logic Controller Frequency Responses

Frequency response data for the forward accelerometer input, through the shaper, notch filter, dynamic pressure gain schedule, and washout to actuator input, are shown in figures 63 and 64 for the vertical and lateral channels, respectively. Similar data through the vertical and lateral model (figure 15) outputs are given in figures 65 and 66. The center-of-gravity located accelerometers and associated shapers were tested using transient response methods and will be discussed later.

Comparisons of test data to analytical results were made where the analytical model was constructed from the data of figure 15. Upper and lower response bounds were calculated for these frequency responses for evaluation purposes using component tolerance requirements. The lower bound was obtained by lowering all the time constants and frequencies by 10 percent and the gain by 8 percent. Similarly, the upper bound was calculated by increasing the time constants and frequencies by 10 percent and the gain by 8 percent.

While only the actuation system for the right side of airplane was set up for test, it was possible to check the logic controller for both sides of the aircraft through proper changes in connections to the actuator hardware.

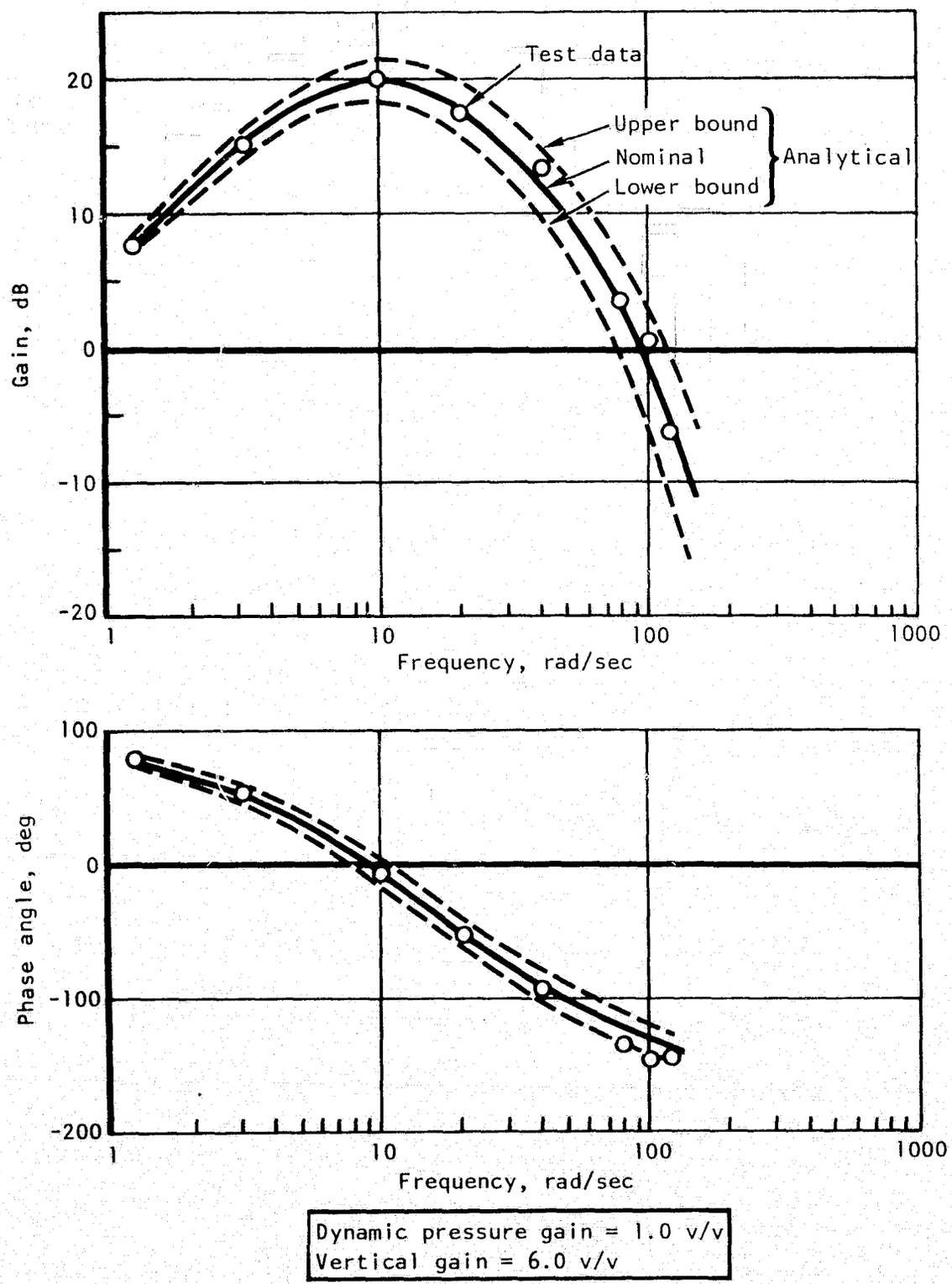

Figure 63. - Frequency response of actuator input to forward vertical SMCS accelerometer input.

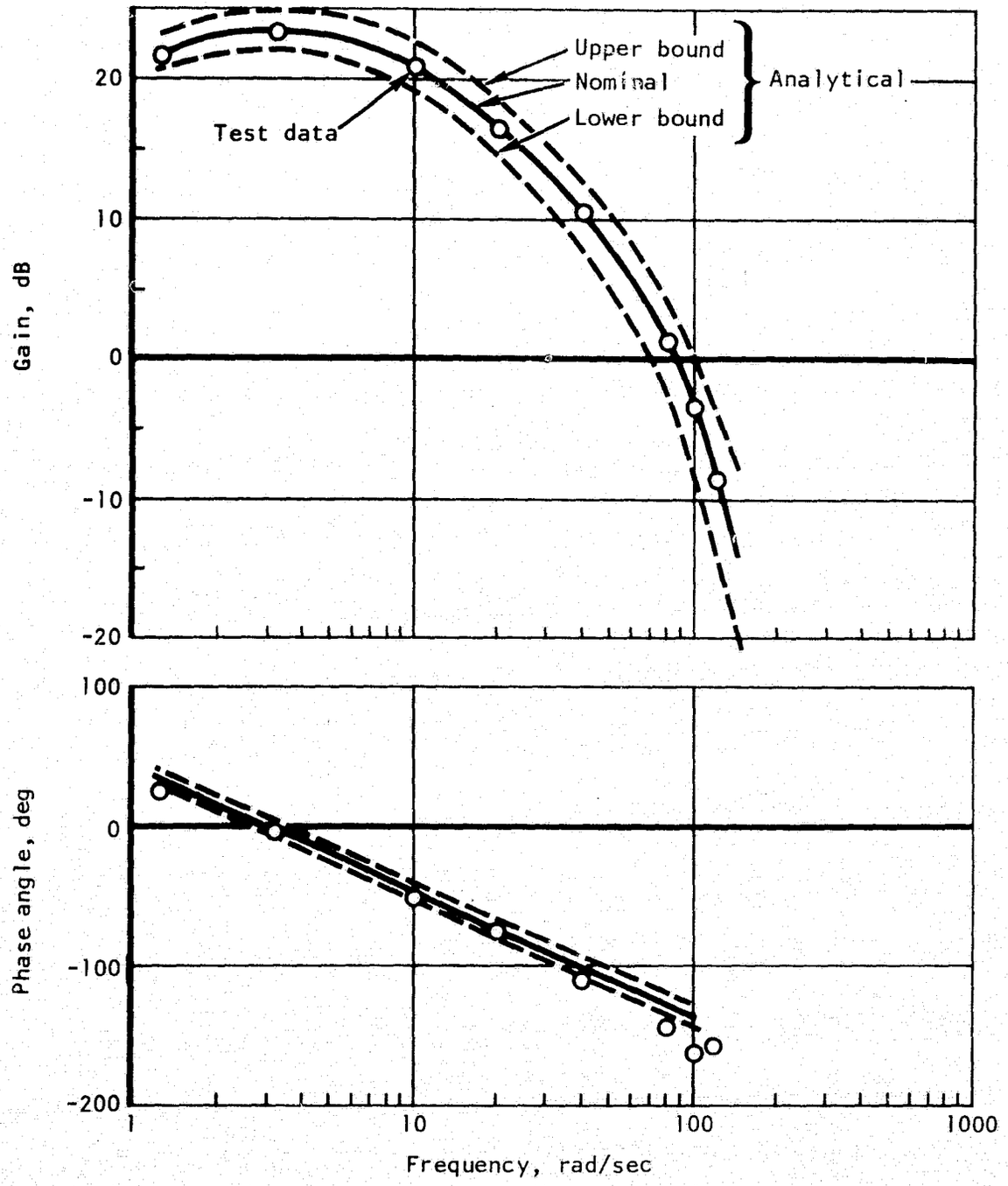

Dynamic pressure gain = 1.0 v/v
Lateral gain = 48.0 v/v

Figure 64. - Frequency response of actuator input to forward lateral SMCS accelerometer input.

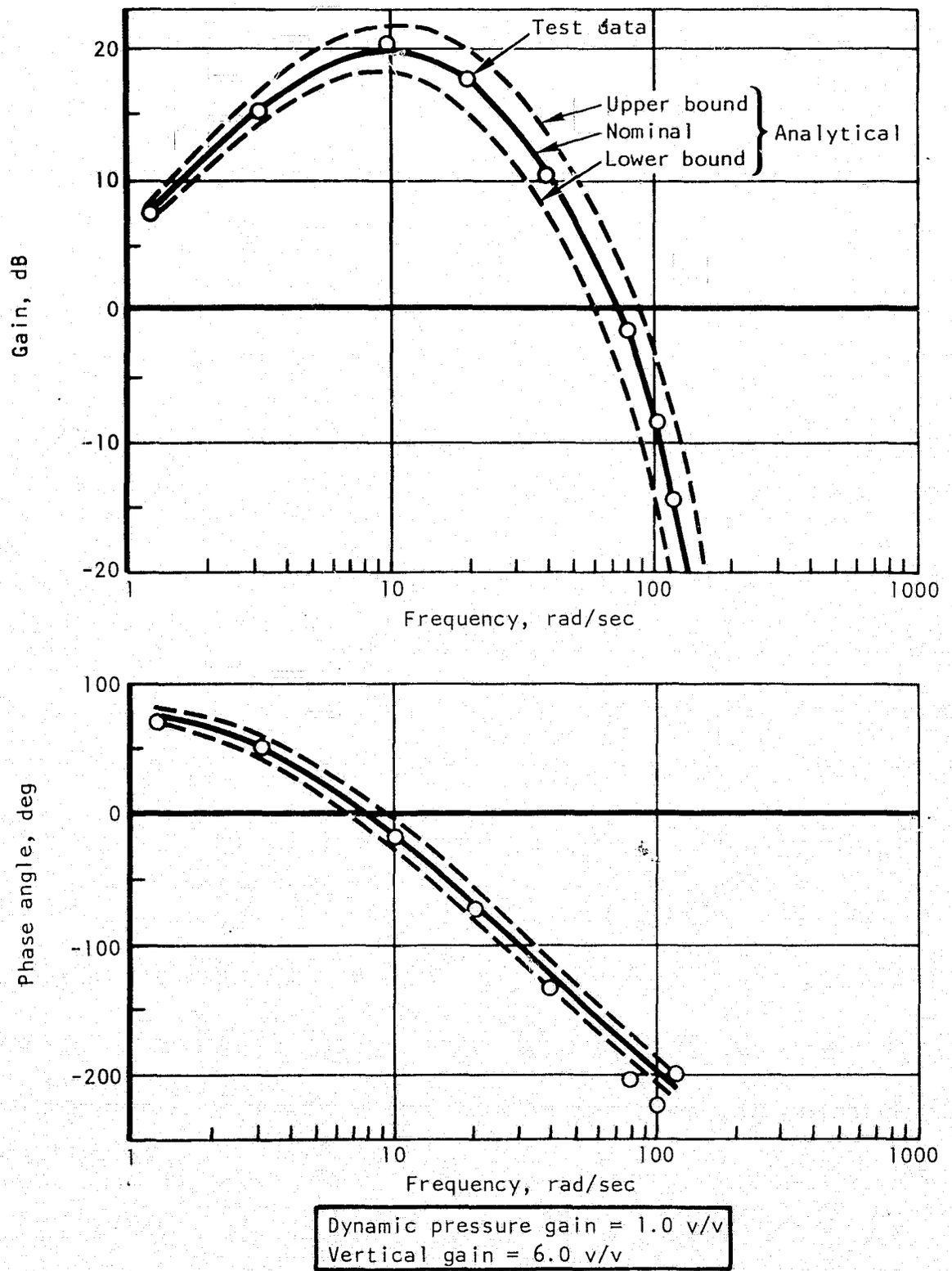

Figure 65. - Frequency response of model output to forward vertical SMCS accelerometer input.

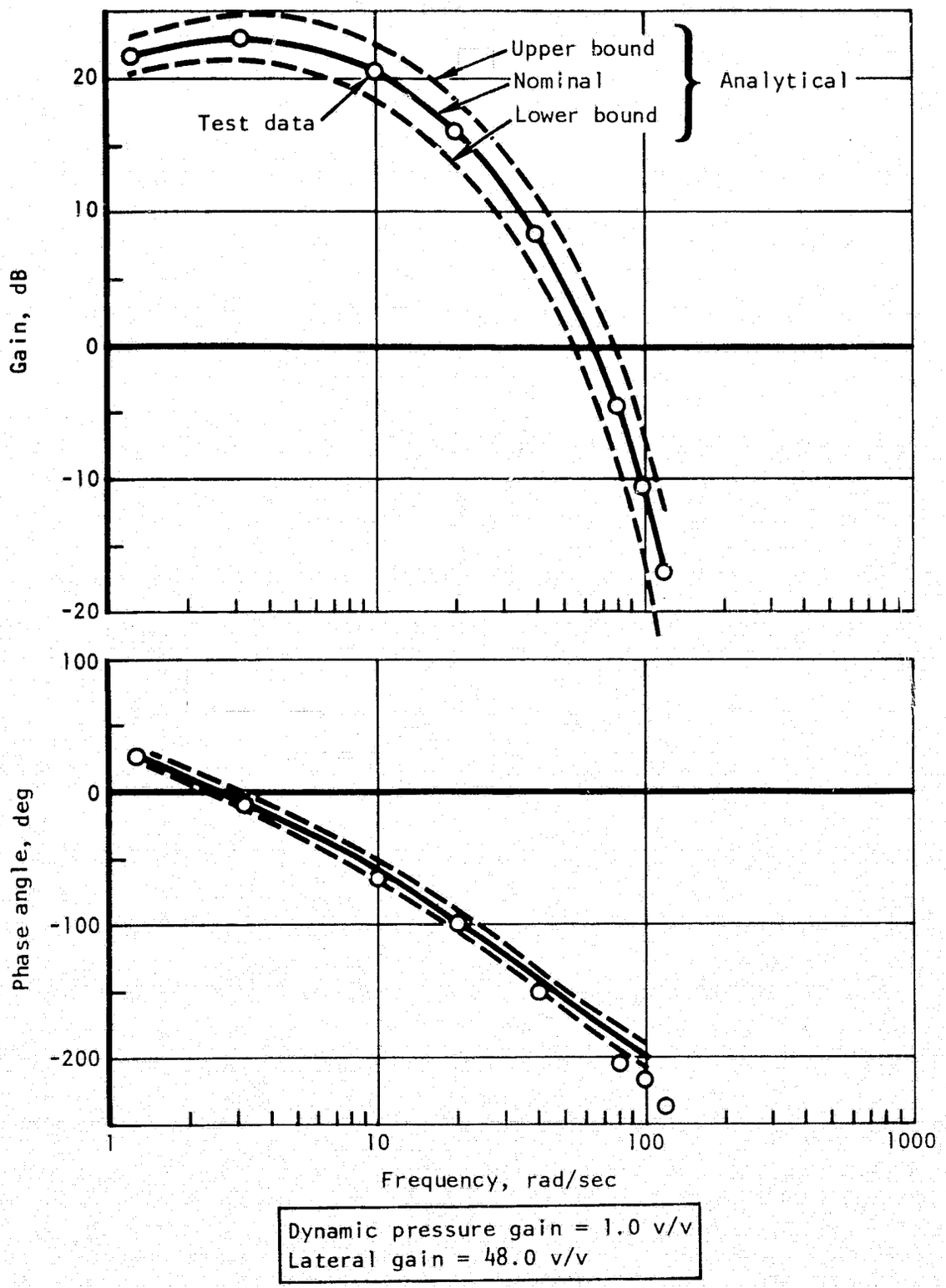

Figure 66. - Frequency response of model output to forward lateral SMCS accelerometer input.

As the data show, the frequency responses for the electronics compare very closely with the analytical data for both the vertical and lateral components of the SMCS. The test-result gains fall on the nominal curve and the phase angles fall within the tolerances of the lower frequencies with some additional phase shift for the higher frequencies. The phase shift at the higher frequencies are the result of graphical accuracy in reading phase angles above 10 Hz with the data recording techniques used.

SMCS Actuator Frequency Response

The SMCS actuator frequency responses were obtained by applying voltage from an external frequency generator to the actuator input and using the position feedback transducer output as the actuator response. These tests revealed a problem in the initial choice of the position feedback LVDT demodulator ripple filter; it degraded the actuator frequency response. During the early checkout of the actuator, it was found that the vane was moving at small amplitudes in the null position and that engagement transients caused the vane to oscillate at high frequencies. To be more specific about this problem, consider the following. The SMCS actuator and the SMCS logic controller are two separate physical devices which are electrically interconnected. The actuator receives a suitable signal at its servovalve from the logic controller and sends a signal about its position from the modulated LVDT to the logic controller. Thus the position feedback around the SMCS actuator includes elements in the logic controller. The 400 Hz-modulated signal from the LVDT is demodulated in the logic controller and is filtered to reduce demodulation ripple. If the corner frequency of this first-order lag filter is too low, it interferes too much with the actuator dynamics. Such an effect is seen in figure 67. This figure shows the SMCS actuator frequency response with a 0.01-second time constant first-order lag in the feedback demodulator. Note that the second-order system response has a gain of +7.5 dB at 12.5 Hz. This high gain at such a low frequency is evaluated as unsatisfactory for SMCS performance. This was a typical frequency response for both the vertical and lateral channels as well as the left and right sides.

The fix for the described difficulty was to change the time constant to 0.001 in the feedback demodulator. As figure 68 demonstrates, the gain is flat out to 20 Hz with only a 3 dB peak at 29 Hz. These actuator dynamics were evaluated as satisfactory for SMCS performance. As a result of these tests, the 0.001-second time constant first-order lag was selected as the demodulator ripple filter for the aircraft.

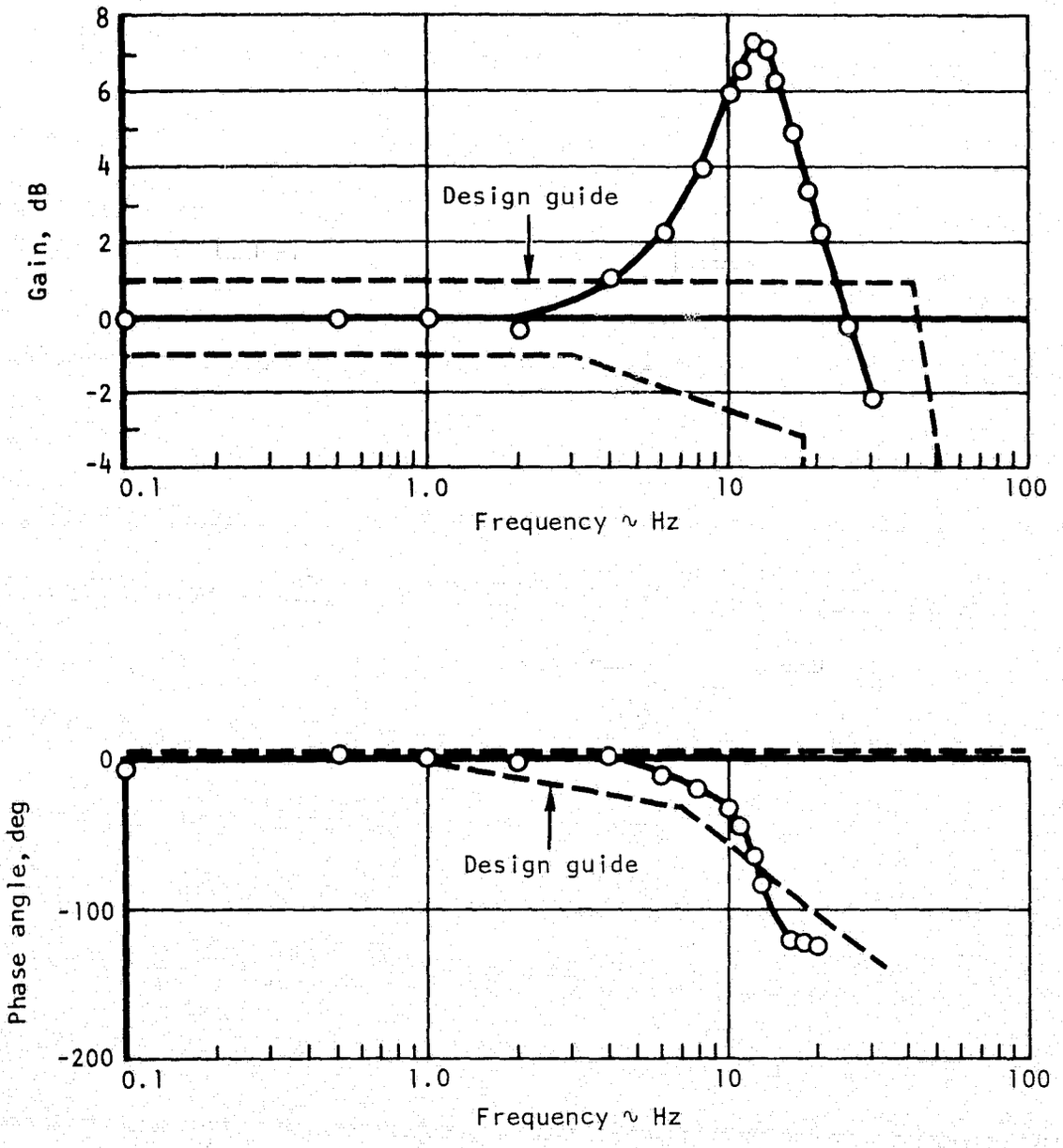

Figure 67. - Frequency response of SMCS actuator with a 0.01-second lag in actuator demodulator ripple filter.

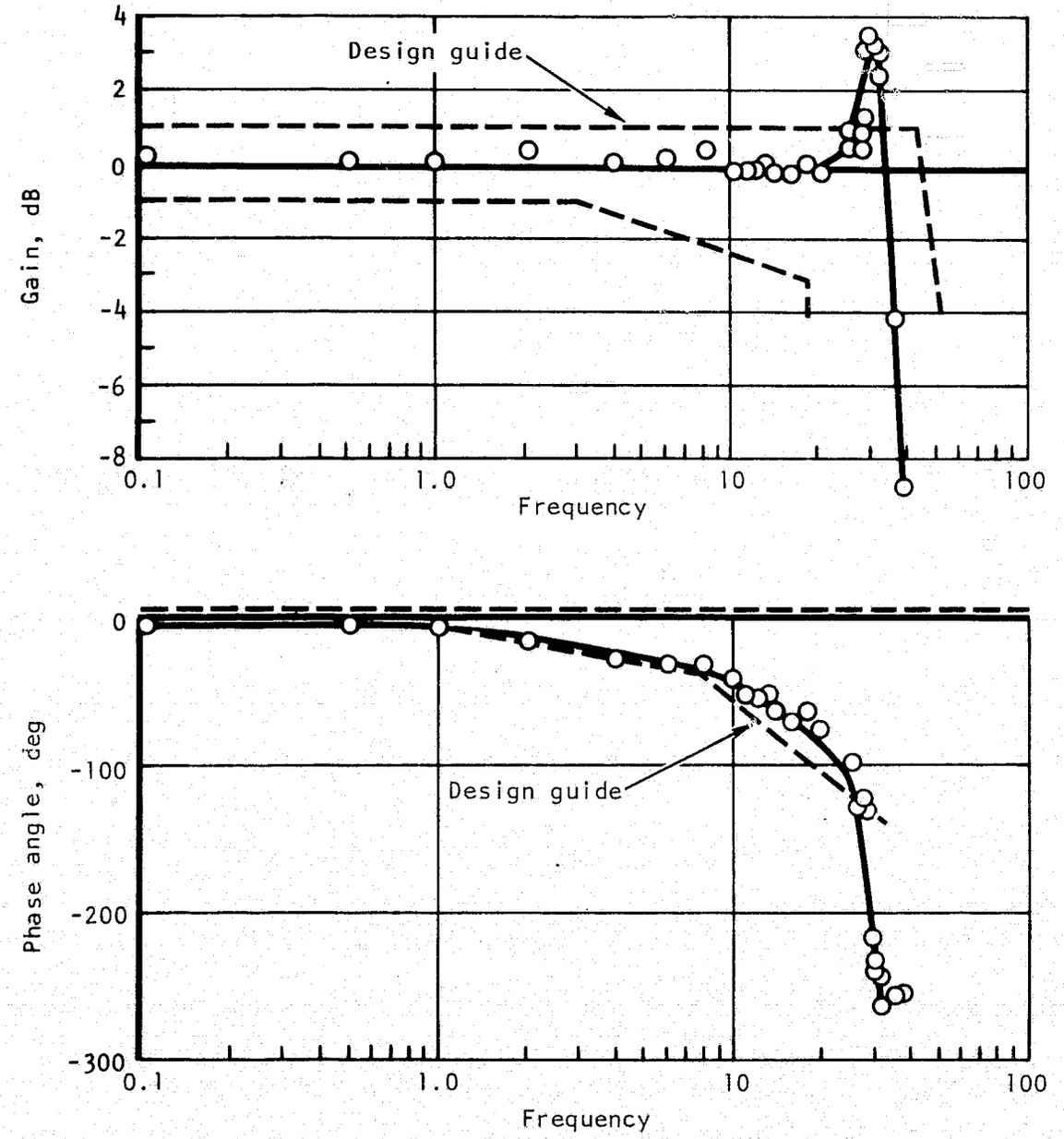

Figure 68. - Frequency response of SMCS actuator with a 0.001-second lag in actuator demodulator ripple filter.

Having solved the demodulator difficulty, frequency responses were obtained for the SMCS actuator for five input amplitudes from 2.5 through 40 percent of the total SMCS actuator excursion capability of ±10 volts. Figure 69 shows the composite normalized gain for these five input amplitudes and the associated phase angles. The larger amplitude frequency responses show attenuation as a result of flow rate saturation at the higher frequencies. These frequency responses show that the actuators are independent of amplitude up to 5 percent of maximum excursion, and are subject to the flow rate limitations for the 10-, 20-, and 40-percent amplitudes. But this has not been a limitation on the aircraft, since even the largest amplitudes will respond for a number of cycles without apparent saturation. The smaller the amplitude is, the more the number of cycles of normal operation that are possible before flow saturation properties become apparent. Flight tests have so far shown that the lower frequencies are stimulated most often and that only three or four cycles of exponentially decayed response reduce the oscillations to a negligible amplitude. Flight tests have not shown flow saturation in the turbulence encounters to date.

Transient Responses

Some of the SMCS characteristics were best checked using transient response techniques. One such test employed a step input to the forward SMCS accelerometer simulating a hardover failure. The vane angle transient response to the step acceleration was a sudden displacement followed by an exponential decay to the null position as shown in figure 70. This decayed response is caused by the washout (a differentiator with a lag) in the system (figure 15). It will also be recalled that the SMCS cannot be operated unless the SCAS is also operating; so any motion imparted to the rigid-body modes by the initial SMCS hardover input would be attenuated by the SCAS.

The SMCS signal sense continuity was also checked using transient inputs. A summary of these tests is given in table VI.

The characteristics of the first-order filters on the vertical and lateral SMCS accelerometers located at the nominal center of gravity were checked using transient techniques. The results are presented in table VII, together with calculated bounds based on ±10 percent of the corner frequency. The test response times fall within the calculated bounds. These tests were run at three different amplitudes to check for linearity, for which the results shown in table VII are typical.

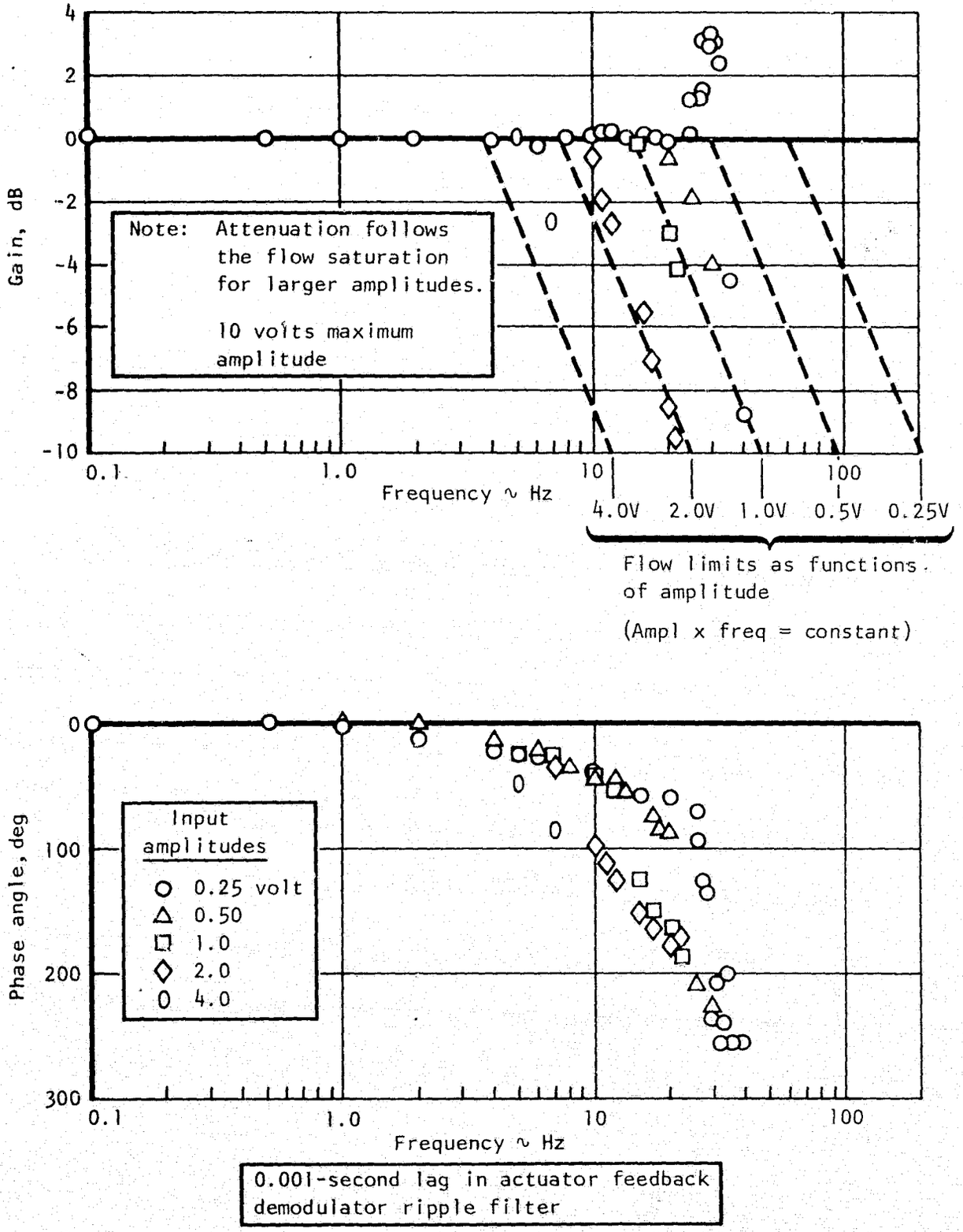

Figure 69. - Frequency response of SMCS actuator as a function of amplitude.

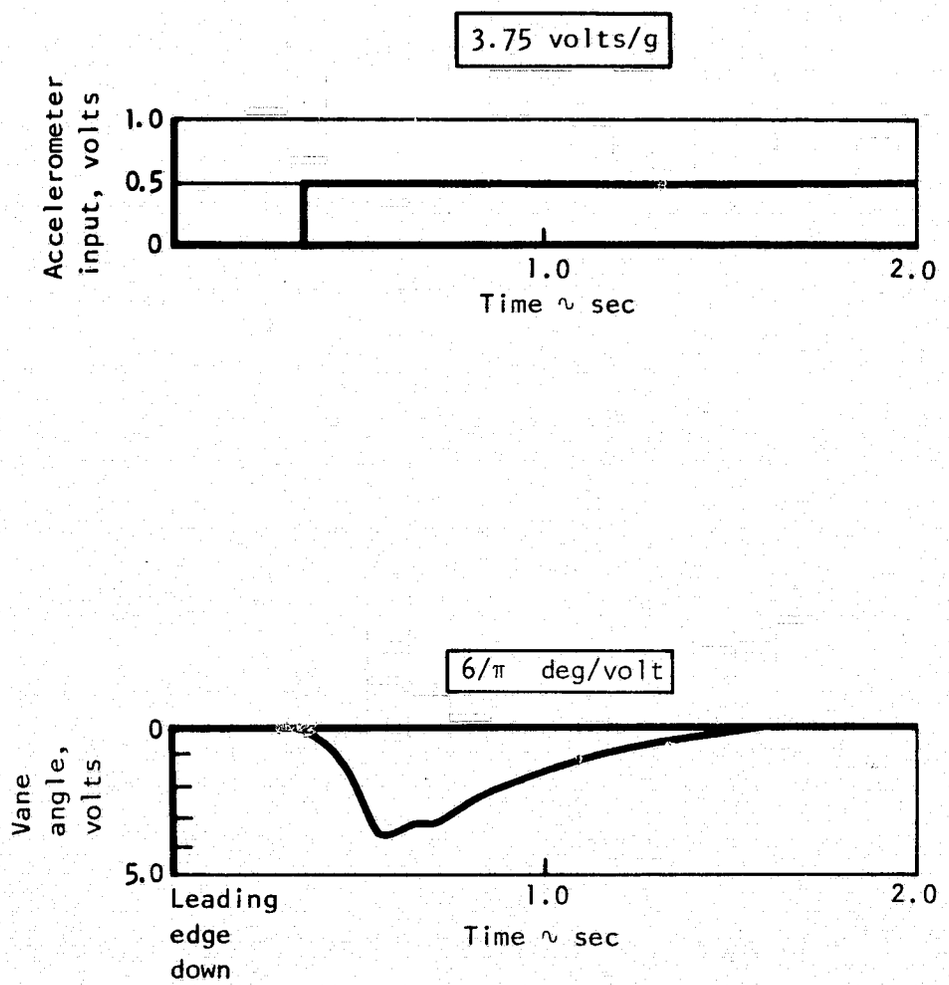

Figure 70. - SMCS response to a step input at forward accelerometer input.

TABLE VI. — CONTINUITY SENSE CHECK

Accelerometer input	Control vane position	
	Left vane	Right vane
$+ n_{Z_{cv}}$ Vertical acceleration at vane	LED	LED
$+ n_{Y_{cv}}$ Lateral acceleration at vane	LEU	LED
Legend: LED = leading edge down LEU = leading edge up		

TABLE VII. — TRANSIENT RESPONSES TO A STEP INPUT TO SHAPER ON SMCS CG ACCELEROMETERS

System	Shaper	(%) steady-state response at various time constants τ		
		τ	2τ	3τ
Vertical	$\frac{10}{S+10}$	62.7	85.0	96.4
Lateral	$\frac{1}{S+1}$	64.0	87.0	96.0
Calculated bounds ±10% of time constants		59.3 to 66.7	83.4 to 88.9	93.3 to 96.3

During the transient responses to large amplitude inputs to the system, an anomaly was found. The vane angle response took a several degree jump as it went into and out of the large amplitudes. The problem source was that the precision operational amplifiers commonly used in notch filters have a discontinuity at the limit as shown in figure 71a. This discontinuity occurs just before the washout filter which emphasizes the signal slope change and causes a kick in the vane response both going into the coming out of the limit as shown in figure 71a. The solution chosen for this difficulty was to limit the input to the notch filter to a level about 15-percent below the saturation amplitude. Satisfactory responses were obtained with this fix as illustrated in figure 71b.

SMCS VANE EFFECT ON INLET/ENGINE CHARACTERISTICS

The object of this section is to briefly describe and summarize B-1 wind tunnel test results that identify effects of ingesting vortices generated by the SMCS vanes into the inlet. Approximately 26 hours of testing in continuous wind tunnels of subscale and full-scale models of the B-1 air induction system were dedicated to investigations of these effects on inlet performance and inlet/engine compatibility. Emphasis was placed on investigations exploring combinations of SMCS vane deflection angles and aircraft maneuvers during operation at mach 0.85. Test procedures and results are summarized to document this B-1 experience as an aid to future programs employing similar systems.

Test Description

The B-1 propulsion system is arranged in two nacelles mounted under the fixed portion of the wing as shown in figure 1. Each nacelle contains two independent two-dimensional (2-D) external compression inlets and two General Electric F101 afterburning turbofan engines. Relative locations between the SMCS vanes and the inlet nacelles are also shown.

The air induction system with its major features is shown in figure 72. One inlet is shown with the ramps in the fully retracted subsonic configuration, while the adjacent inlet is shown in the mach 2.2 supersonic configuration. The movable lip is shown in its normal position and also in its takeoff and landing configuration. Duct flow area distributions for both of these ramp positions are shown in figure 73.

Inlet boundary layer air is removed through porous surfaces on the second movable ramp, the throat panel, and small regions on the upper and lower end plates. The bleed air is collected in two compartments. The air exits from

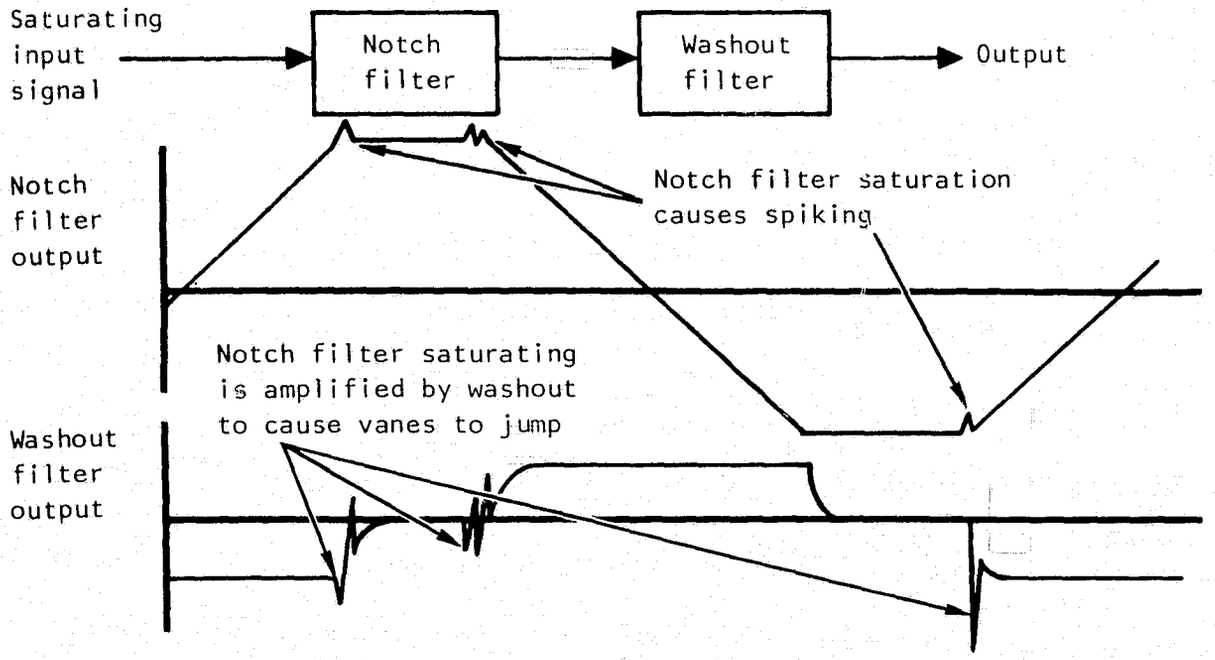

(a) Time history responses before modification, ramp input signals

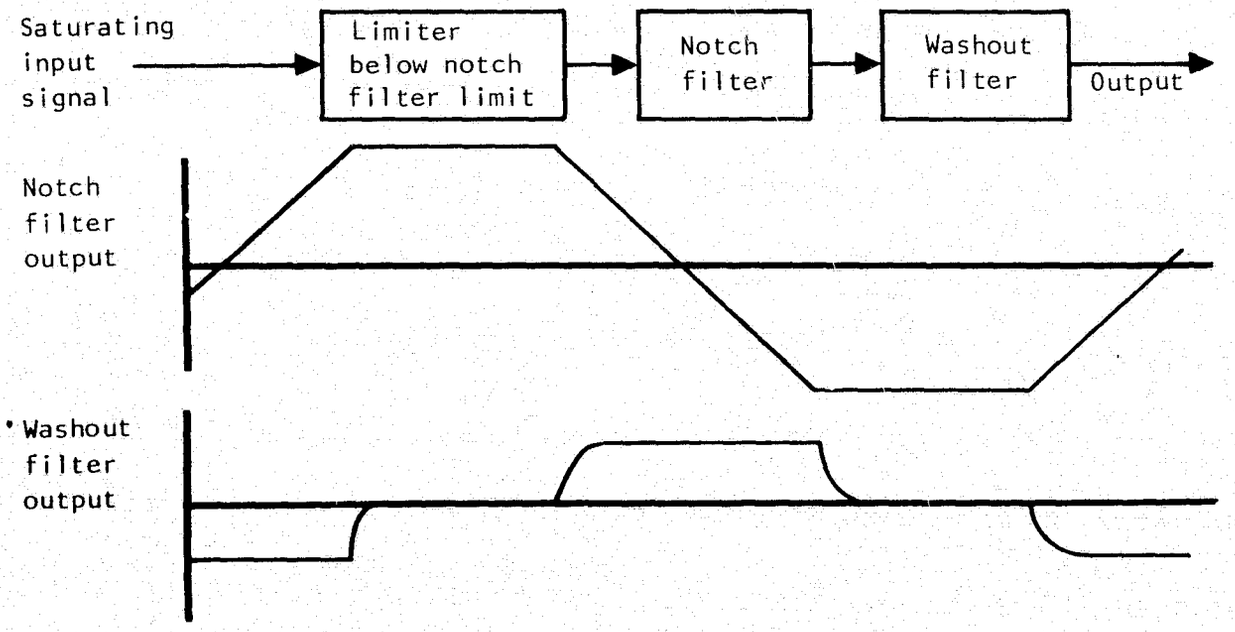

(b) Time history responses after modification, ramp input signals

Figure 71. - SMCS anomaly due to operational amplifier characteristics.

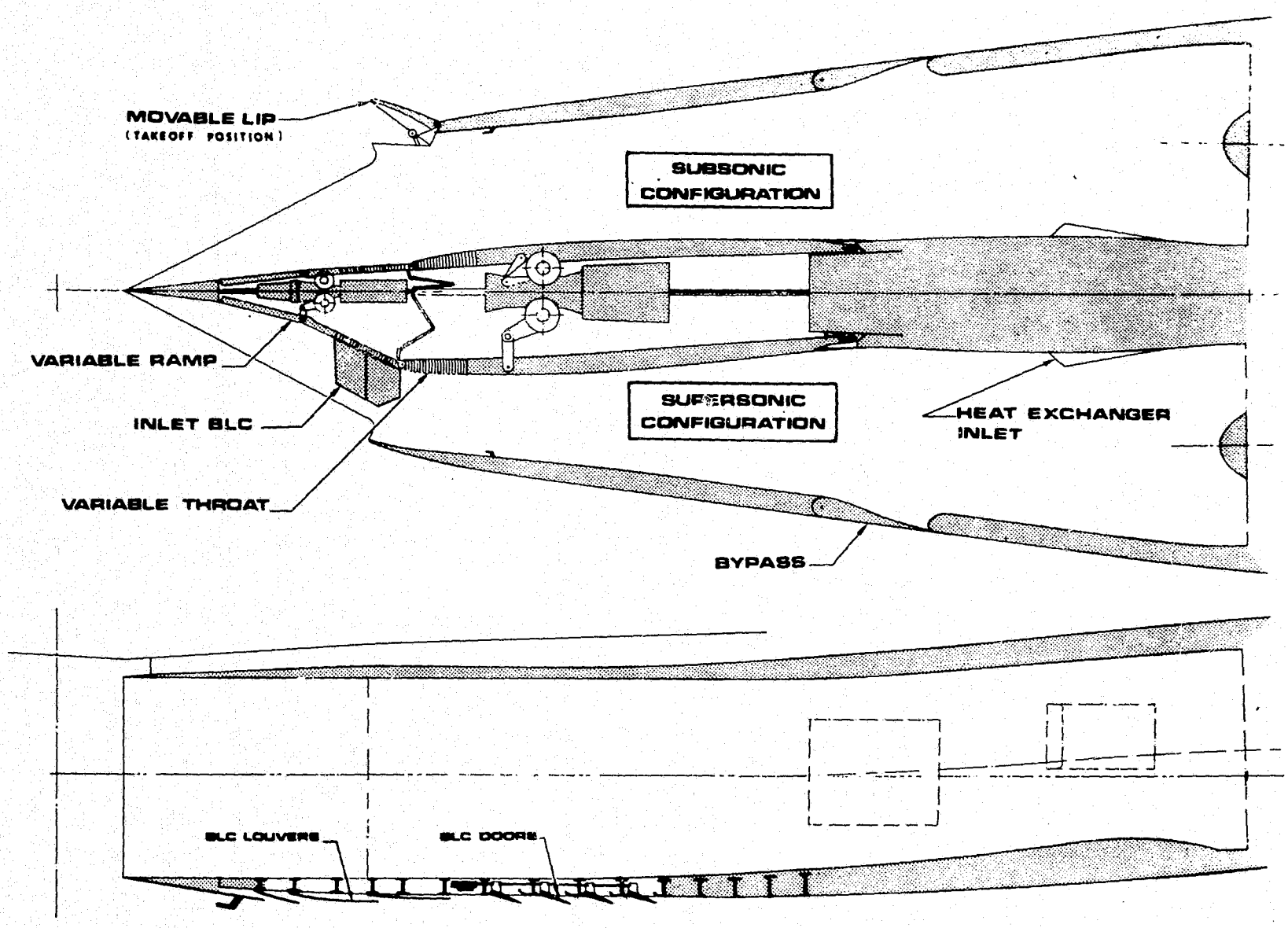

Figure 72. - B-1 air induction system.

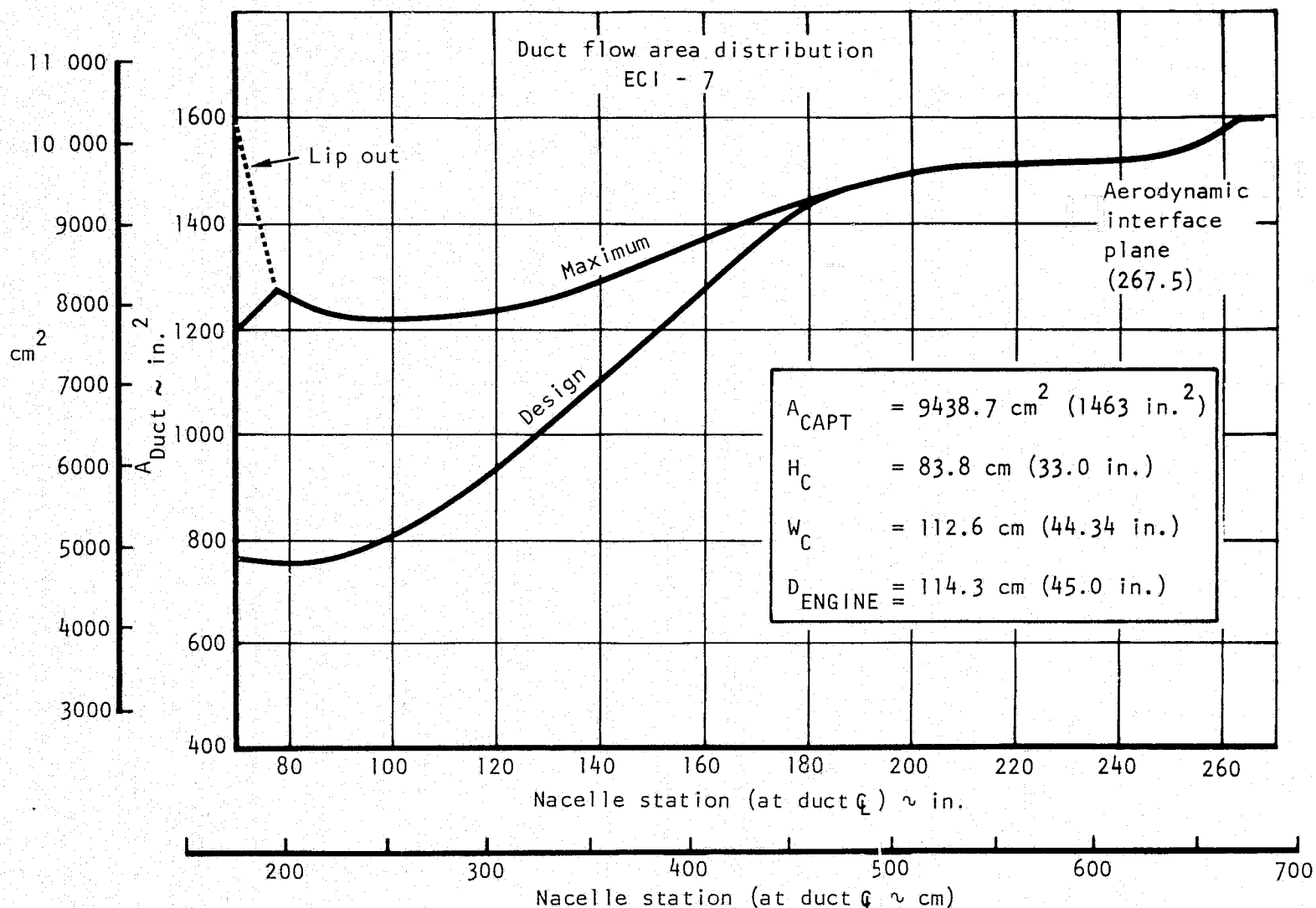

Figure 73. - B-1 duct flow area distribution ECI-7.

the forward compartment through fixed louvers and from the aft compartment (zone II) through two-position doors. The doors are open above mach 1.4 and closed at lower speeds. A sketch of the bleed system is shown in figure 74.

A bypass system operates at supersonic speeds above mach 1.4 to match the inlet supply and the engine demand. The bypass doors open to compensate for reduced engine airflow such as occur on a hot day or during low-power settings.

Wind tunnel tests were conducted with 0.1-, 0.2-, and full-scale models simulating the inlet configuration defined by the previous figures. Subscale models contained a complete fuselage forebody, the portion of the wing influencing the inlet flow field, and the two inlets contained in the left nacelle. The right nacelle was simulated by vertical plates. SMCS vanes were also simulated as shown in the photograph of the 0.2-scale model installed in the supersonic propulsion wind tunnel at AEDC, figure 75.

Airflow control vanes were located as close as possible to the inlet/engine aerodynamic interface plane (AIP) and were generally operated choked to maintain the volume dynamics of the inlet during tests. Instrumentation at the inlet/engine AIP consisted of 40 dual-purpose probes to measure both the steady-state and dynamic components of total pressure. Eight rakes were installed in each inlet, each with five probes at the center of equal areas, as shown in figure 76. Frequency response of the AIP probes in the 0.2 scale model was flat to approximately 8000 Hz.

Full-scale inlet/engine tests were also conducted with a model representing the outboard inlet of the right nacelle. Because of tunnel size restrictions, the model was mounted in a fixed position. A flat plate was used to simulate the entrance flow field. Provisions for the model included the installation of two large vanes just upstream of the inlet. Vortices shed from these variable-position vanes were directly ingested by the inlet/engine combination. A photograph of the full-scale model with the vanes installed is shown in figure 77. Total pressure instrumentation locations at the inlet/engine AIP were similar to those employed on the subscale models. Frequency response of the AIP total pressure probes is flat to 500 Hz. Similar instrumentation is also installed on the No. 1 and 2 B-1 prototype aircraft.

Wind tunnel testing dedicated to investigating SMCS vane effects on inlet/engine performance and compatibility are summarized in table VIII.

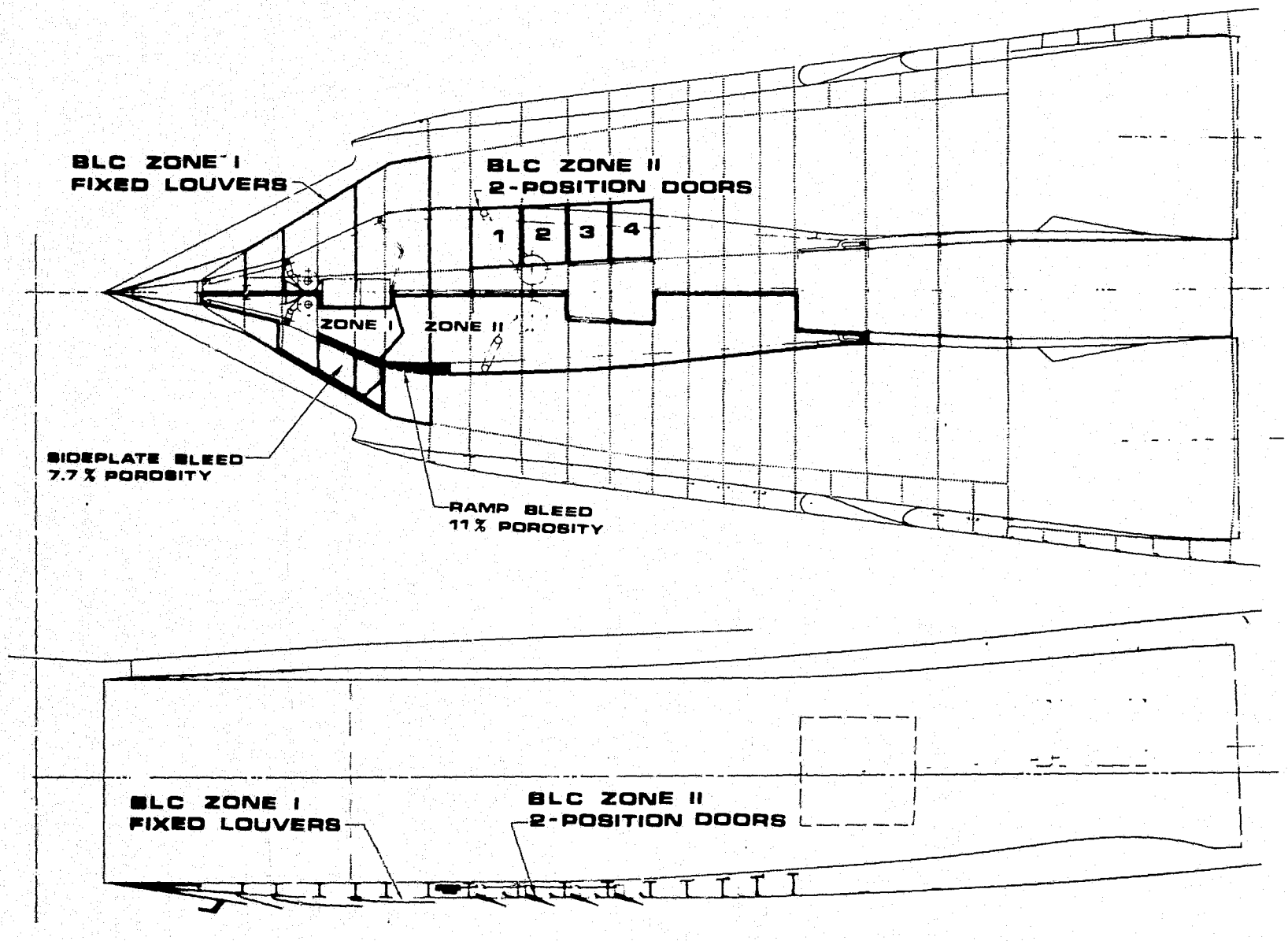

Figure 74. - B-1 air induction system, boundary layer control features.

ORIGINAL PAGE IS
OF POOR QUALITY

Figure 75. - B-1 inlet development wind tunnel model with SMCS vanes.

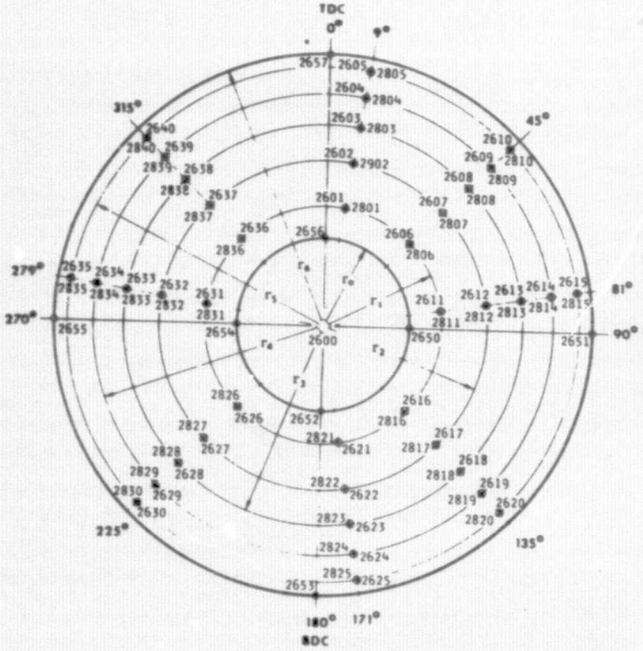

INBOARD

LOOKING DOWNSTREAM

ENGINE FACE RAKES

	MODEL SCALE	FULL SCALE
r_0	1.449	7.245
r_1	1.9785	9.892
r_2	2.7486	13.734
r_3	3.3429	16.714
r_4	3.8477	19.238
r_5	4.2936	21.468
r_6	4.5000	22.500

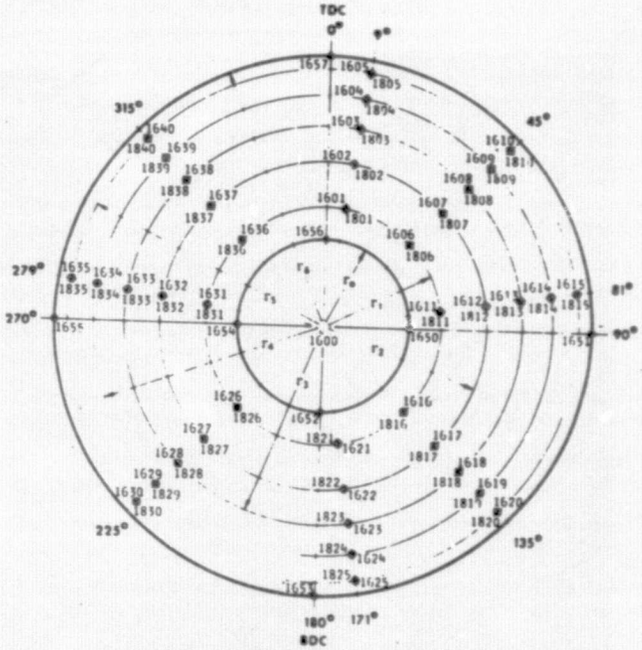

OUTBOARD

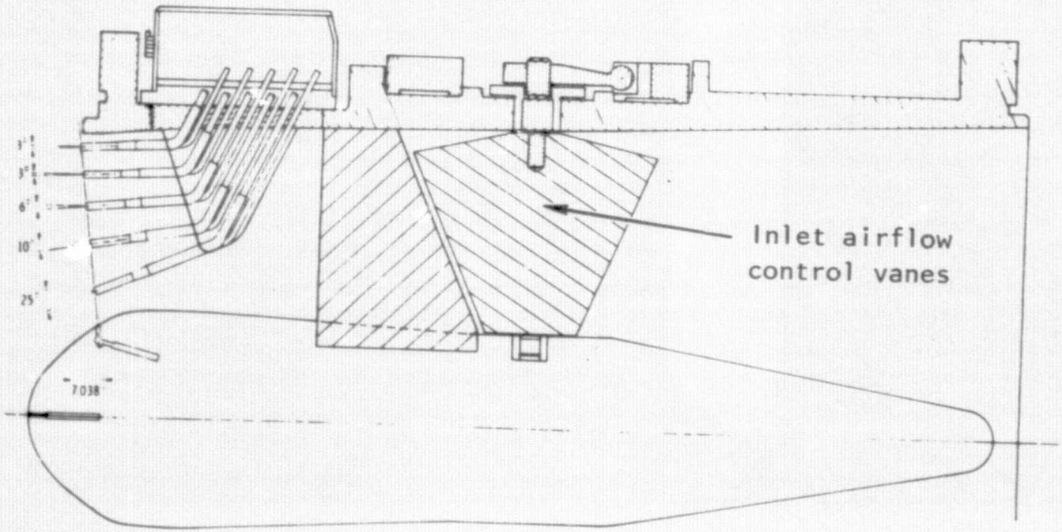

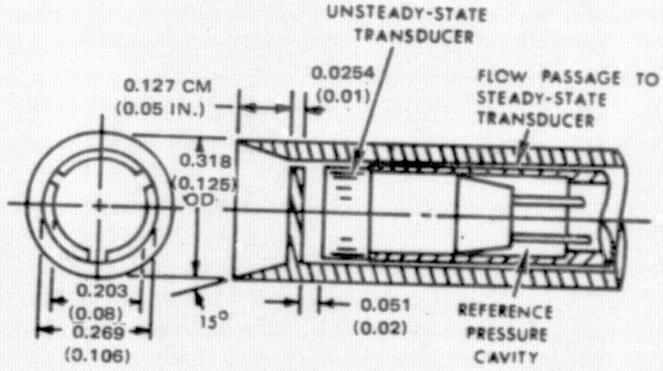

Figure 76. - Engine face instrumentation.

ORIGINAL PAGE IS
OF POOR QUALITY

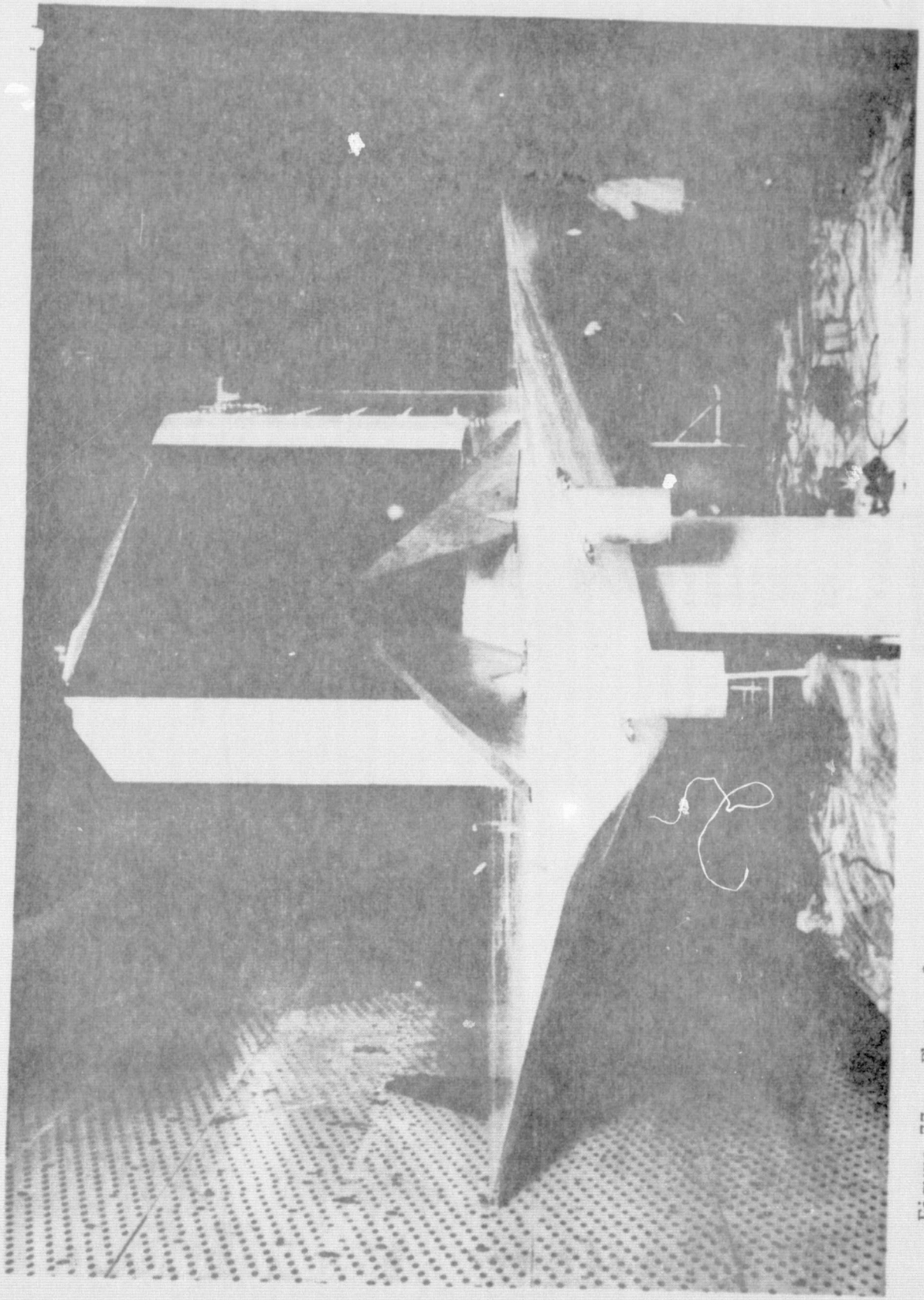

Figure 77. - Photo of vortex generators on B-1 full-scale inlet/engine model installed in Transonic Propulsion Wind Tunnel at AEDC.

TABLE VIII. - SUMMARY OF WIND TUNNEL TESTS INVESTIGATION
SMCS VANE EFFECTS ON ENGINE/INLET CHARACTERISTICS

Model Scale	Test Facility	Test Number	Estimated Test Hours	Date
0.1	Rockwell Trisonic	TWT 275	8	Apr 1973
0.2	AEDC Propulsion Wind Tunnels	TF 316	12	Jul 1973
		SF 164	1	Oct 1973
1.0		TF 329	5	Jan 1974

Test Results

Inlet performance and distortion characteristics are presented as recorded during tests with the SMCS vane operational with the 0.2-scale inlet model and the full-scale inlet/engine model in the propulsion wind tunnels at AEDC. Data from these programs were selected because dynamic distortion characteristics were determined by analog techniques for every data point during the normal conduct of the test.

Several computed parameters from the 40 total-pressure measurements at the inlet/engine AIP are used to present test results. Recovery (PT2/PT0) is the average of the 40 steady-state values. Turbulence levels represent an average of the 40 rms values normalized to recovery. Analog total-pressure signals were filtered to 4000 Hz with 0.2-scale data; to 1000 Hz with full-scale data upstream of rms meters.

Several dynamic distortion indexes are used and were computed with filtered signals from individual AIP total pressure instrumentation. The indexes were calculated using analog techniques with filters corresponding to critical engine frequencies. Signals were filtered to 250 Hz with 0.2-scale data and to 62.5 Hz with full-scale data. The analog distortion analyzer computes both circumferential (IDC) and radial (IDR) distortion components and combines them mathematically to a fan stall margin ratio (IDL). This latter index is normalized to stall margin allocations, and thus values of unity identify distortion levels approaching design limits. Inlet distortion (PTMAX-PTMIN)/PT2 was also computed. Maximum values identified from the approximately 30-second record length for each data point are used to illustrate test results.

Engine-face, total-pressure contours are used to illustrate variations in distortion patterns. High-pressure regions, where the pressure is higher than average, are shaded on the contour plots. Low-pressure regions (pressures lower than average) are unshaded. The magnitude of the difference above or below the average pressure level is defined by the number on the contour. The annular region is formed by protrusion of the engine bullet nose at the AIP.

0.2-scale model test results. - Model scale data with SMCS vanes deflected were recorded over the range of attitudes shown in figure 78. Maximum airflow, corresponding to 156.5 kg/sec (345 lb/sec) full scale, was held constant, and the SMCS vanes were stepped through a range of deflection angles from -20° to $+20^{\circ}$. Outboard inlet performance and distortion characteristics are shown in figure 79 as functions of yaw angle and SMCS vane deflection angle. Angle of attack is constant at 3°.

Combinations of SMCS vane deflection angles and maneuver conditions where vortices are ingested are readily apparent. Losses in total-pressure recovery approaching 5 percent, accompanied by significant increases in turbulence levels and distortion indexes, were recorded when vortices were ingested. Similar data were recorded at all attitudes shown in figure 78, and results were used to identify conditions where SMCS vane vortices could be ingested by the inlet.

Steady-state, total-pressure contours are shown in figure 80 for several vane deflection angles during operation at yaw angles of -6°. Vane deflection angles greater than 15° (leading edge up) increase the size of the low-pressure region producing a larger circumferential distortion component. Similar patterns are derived from dynamic data during scans producing maximum values of stall margin ratio as shown in figure 81, although total-pressure gradients are larger.

Results obtained with the inboard inlet, shown in figure 82, illustrate variations in yaw angle where the vane vortices are swept past the inboard inlet. Losses in recovery with the vane deflected 20° become significant at a yaw angle of -3°, become larger as yaw angle is increased to -5°, and diminish as yaw angle is increased to -6°. Similar trends are evident in the distortion indexes and in total-pressure contours. Effects of varying vane angle during operation at a yaw angle of -5° are shown in figure 83. Effects of varying yaw angle during operation with the SMCS vane deflected 20° are shown in figure 84.

Provisions were also included on the 0.2-scale model for sinusoidal variations of the SMCS vanes at various frequencies. Strip charts of several distortion parameters (analog distortion analyzer output) are shown in figure 85 during peak-to-peak variations in vane deflection angles between zero and 20° at a frequency of 5 Hz. When allowances are made for transport times between

Run/attitude matrix

Mach no. M_o	Fuselage	Wing Sweep (deg)	SMCS VANES (deg)	ECS exit area (%)	Cowl (deg)	Porosity config		Bypass door (deg)
						Outbd	Inbd	
0.85	Long	67.5°	0 & 20°	60%	0°	J1	J1	Closed

BLC bleed exit area cm^2 $(in.^2)$	
Zone I	Zone II
178.7 (21.7)	Closed

Fwd bay door	Mid bay door
Closed	Closed

R_B (deg)	H_L cm (in.)	W2CORR (kg/sec) (lb/sec)
7°	69.34 (27.3)	156.5 (345)

Full scale values

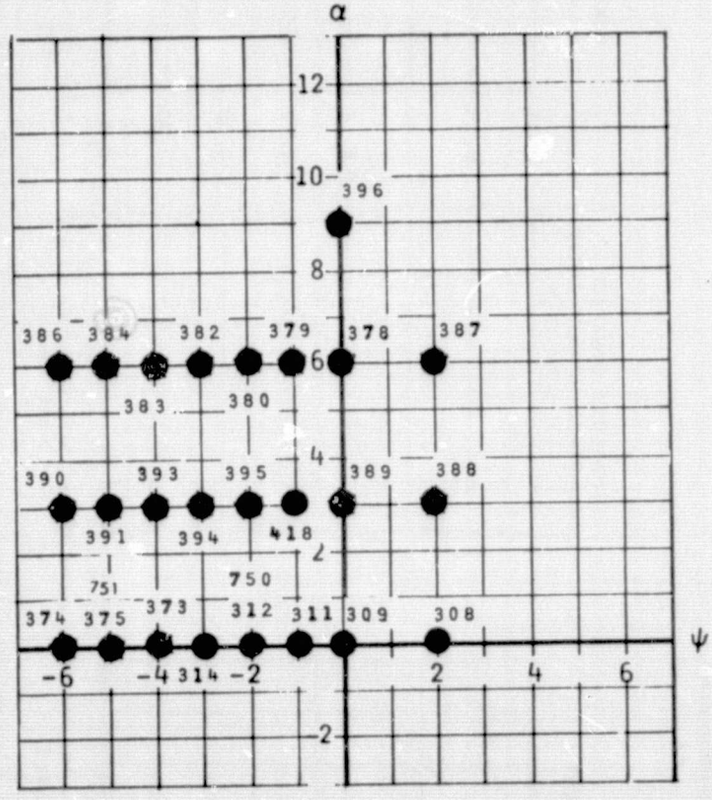

Note:
Vane angle was varied from -20° to +20° during each run. Numbers on grid identify test run.

Figure 78. - Test matrix, 0.2 scale inlet model with SMCS vane deflection.

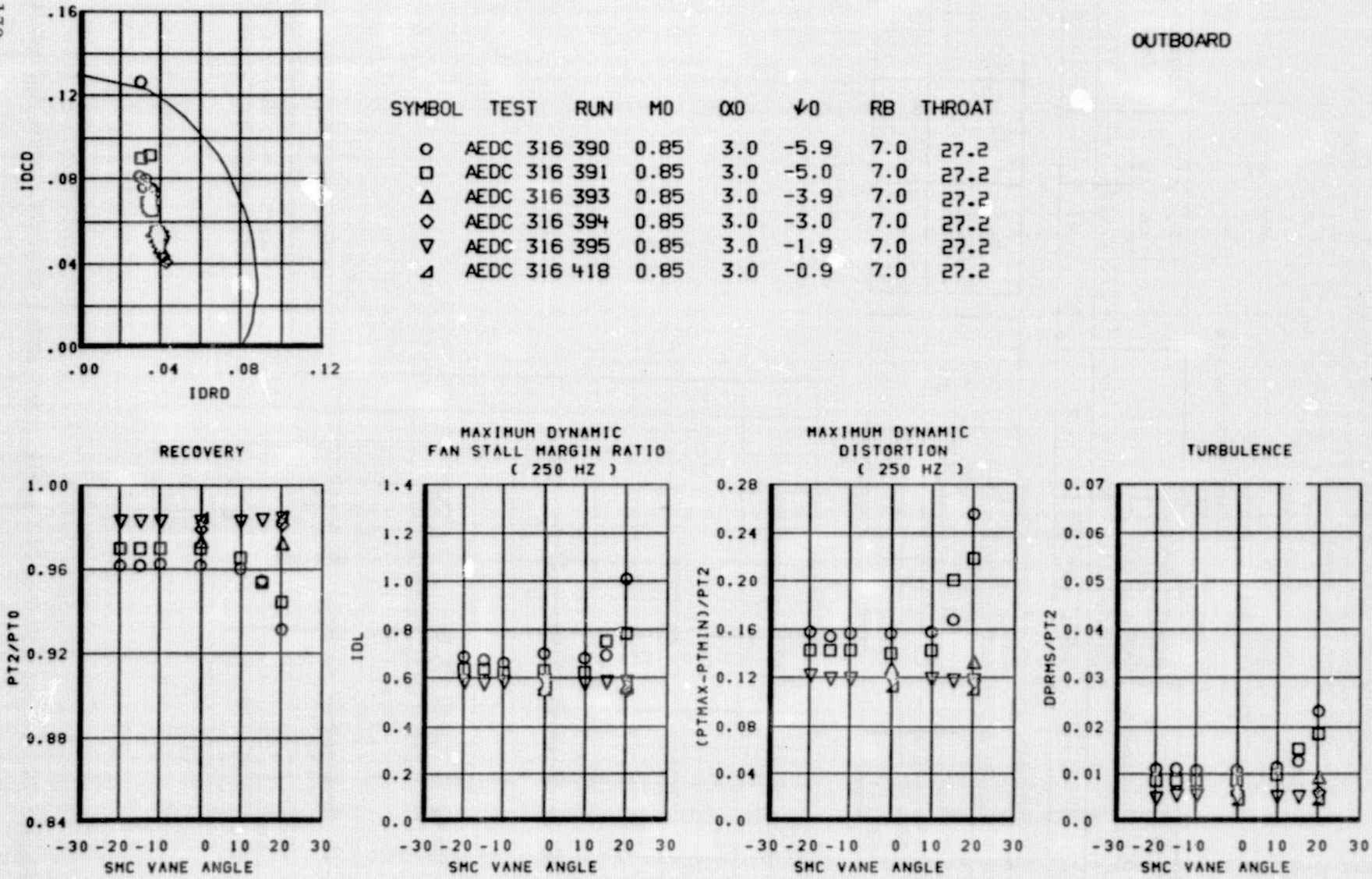

Figure 79. - Yaw angle sweep with constant inlet weight flow and variable SMCS vane angle, outboard inlet, W2CORR = 156.5 kg/sec (345 lb/sec).

0.2 scale model, mach 0.85

W2CORR = 156.5 kg/sec (345 lb/sec), α = 3°, ψ = -6°

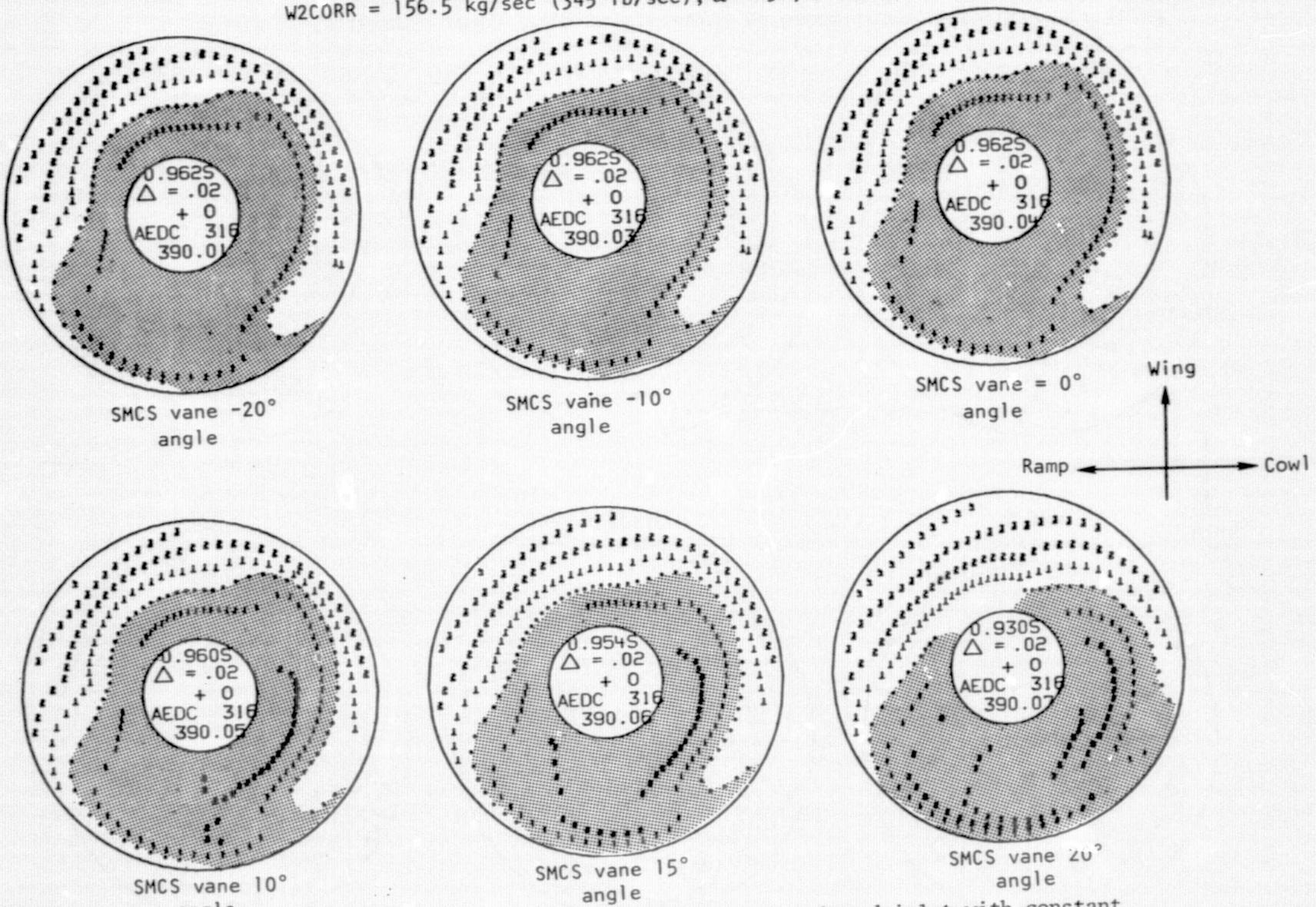

Figure 80. - Steady-state total pressure contours, outboard inlet with constant inlet flow and variable SMCS vane deflection, α = 3°, ψ = -6°.

0.2 scale model, mach 0.85
W2CORR = 156.kg/sec (345 lb/sec), max IDL scans (250 Hz)

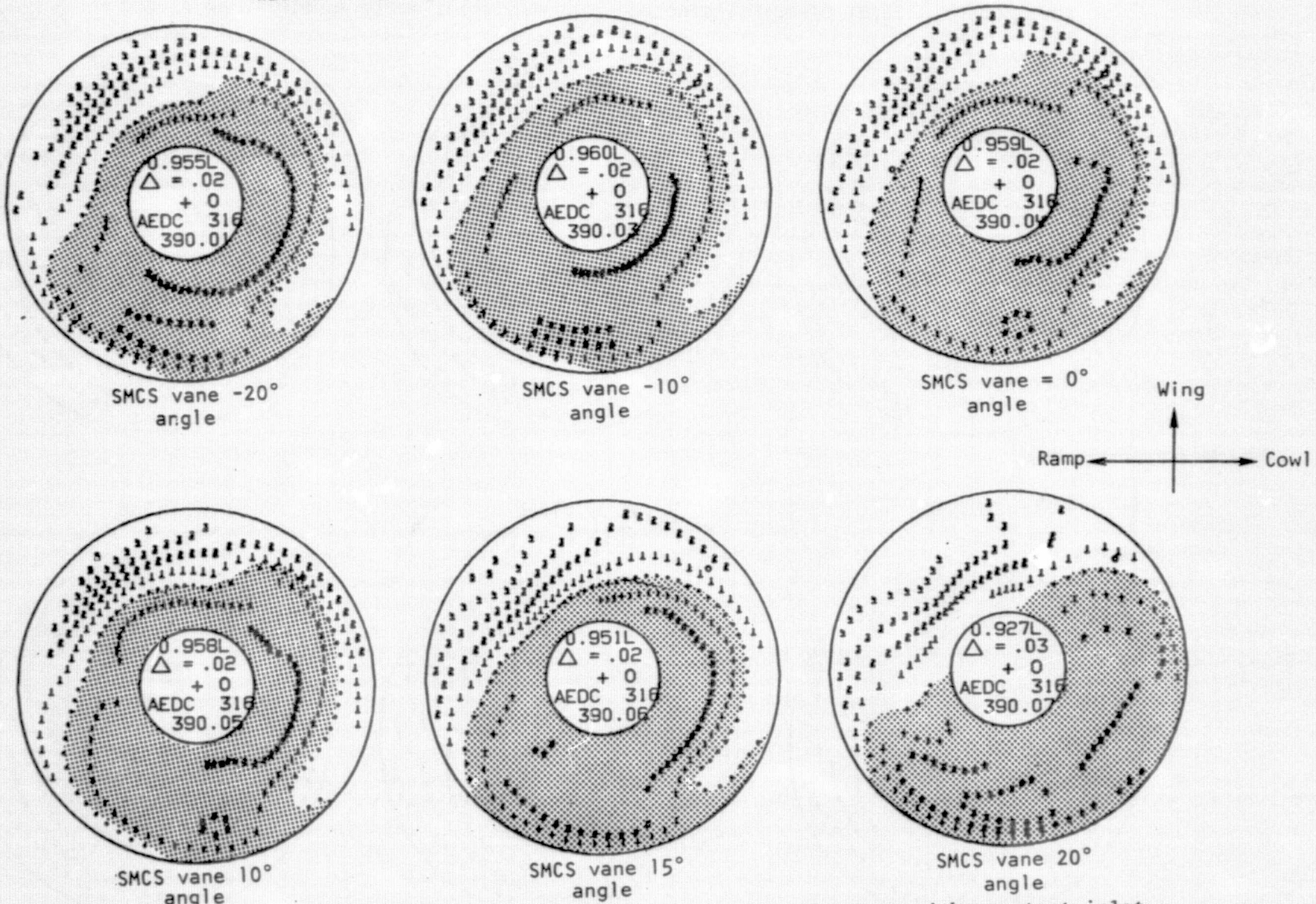

Figure 81. - Dynamic total pressure contours, outboard inlet, with constant inlet flow and variable SMCS vane deflection, $\alpha = 3°$, $\psi = -6°$.

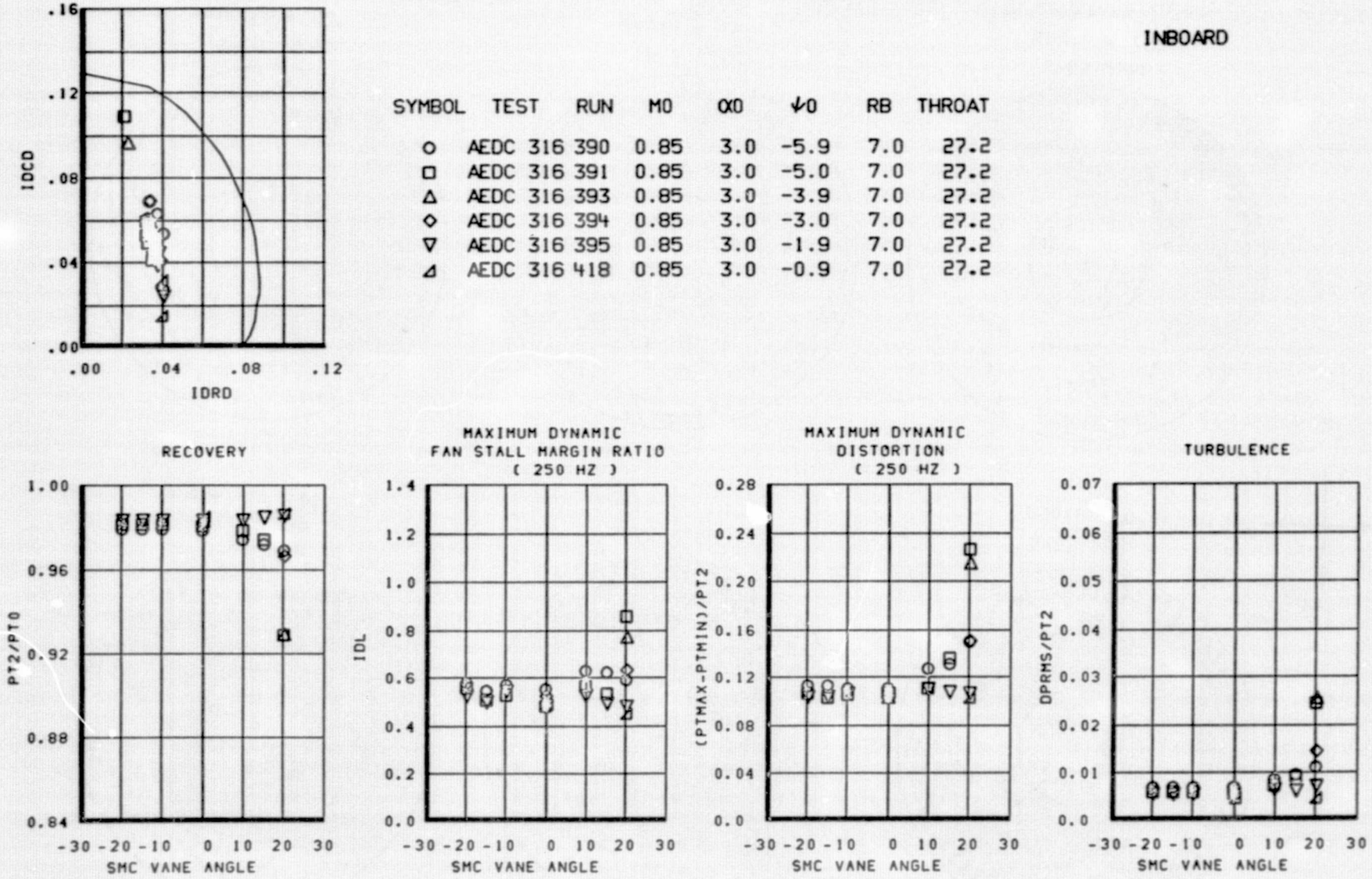

Figure 82. - Yaw angle sweep with constant inlet weight flow and variable SMCS vane angle, inboard inlet, W2CORR = 156.5 kg/sec (345 lb/sec).

0.2 scale model, mach 0.85
W2CORR = 156.5 kg/sec (345 lb/sec), max IDL scans (250 Hz)

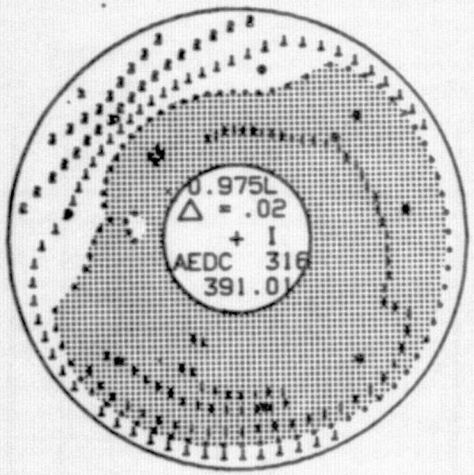

SMCS vane
angle = -20°

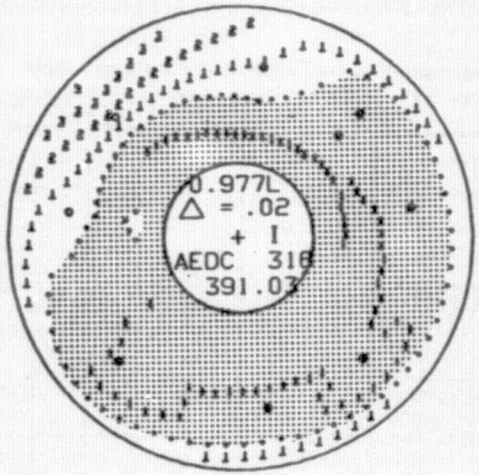

SMCS vane
angle = -10°

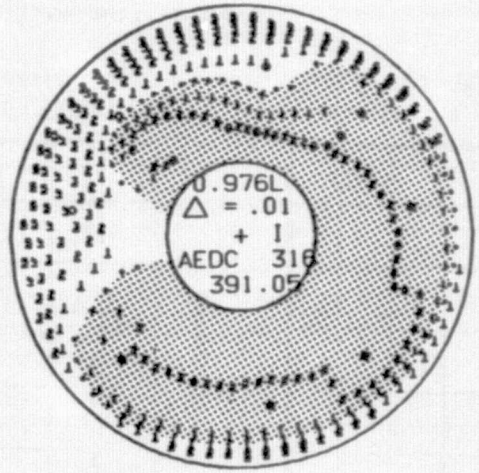

SMCS vane
angle = 0°

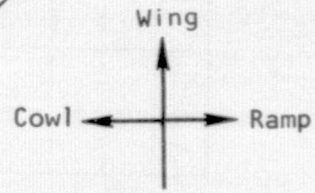

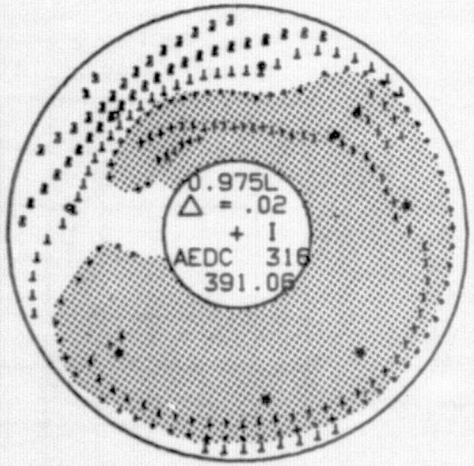

SMCS vane
angle = 10°

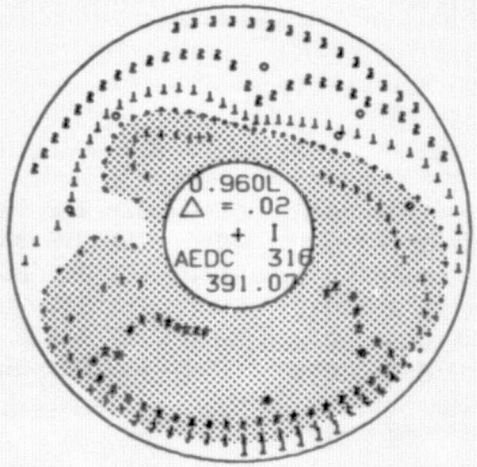

SMCS vane
angle = 15°

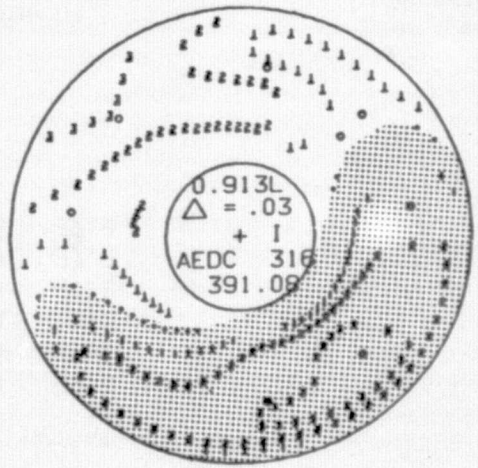

SMCS vane
angle = 20°

Figure 83. - Dynamic total pressure contours, inboard inlet, with constant inlet airflow and variable SMCS vane deflection, $\alpha = 3°$, $\psi = -5°$.

0.2 scale model, mach 0.85, α = 3°
W2CORR = 156.5 kg/sec (345 lb/sec), max IDL scans (250 Hz)

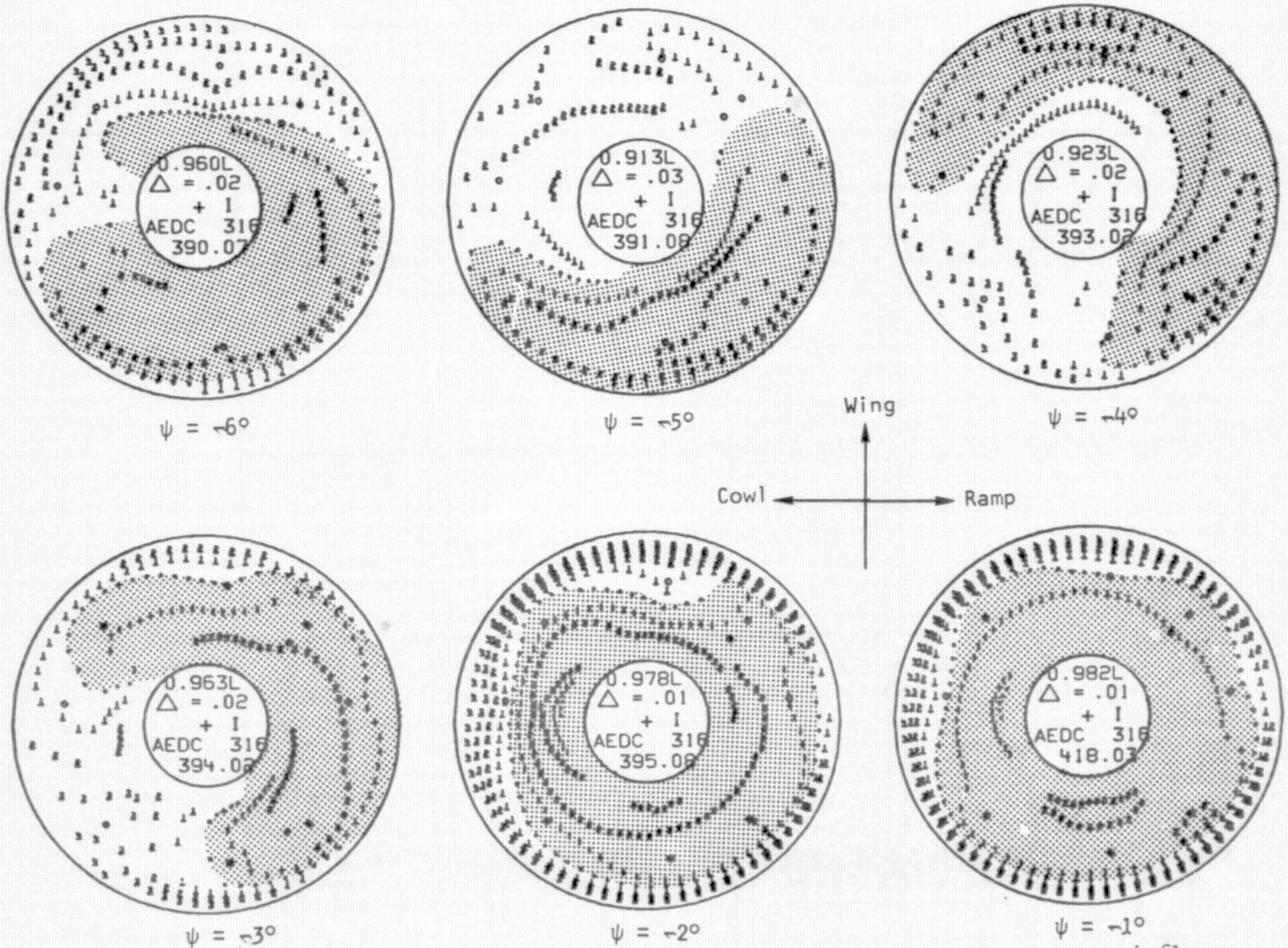

Figure 84. - Dynamic total pressure contours, inboard inlet with constant instant airflow during variations in yaw, SMCS vane deflection = 20°.

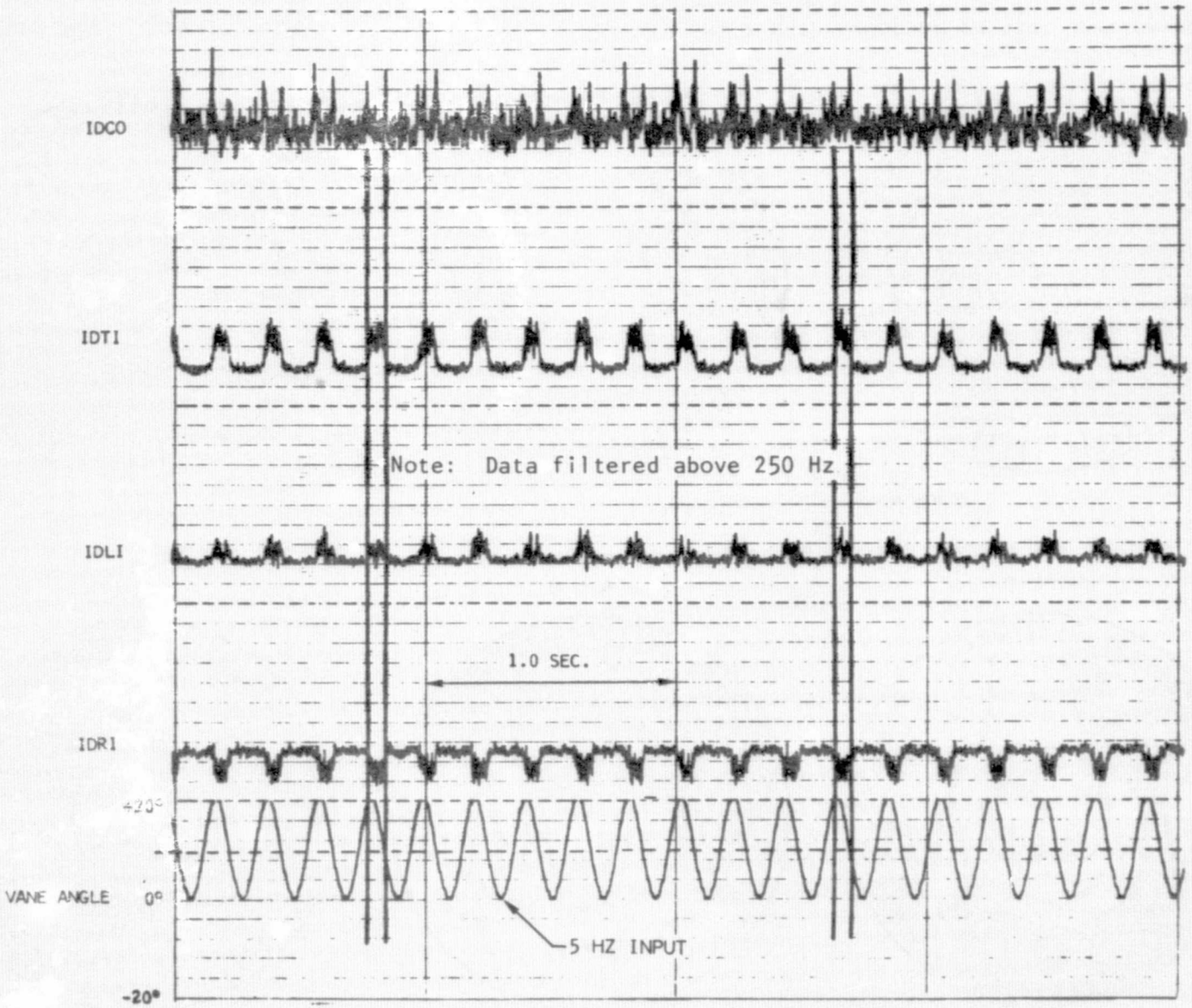

Figure 85. - Dynamic distortion during SMCS vane transient, 0.2 scale model, M = 0.85, α = 3°, ψ=-5°, W2CORR = 156.5 kg/sec (345 lb/sec.)

the disturbance and the measuring station, variations in distortion terms and vane deflection angles greater than 15^{o} correlate well. Distortion trends are characterized by a periodic reduction in the radial distortion component and periodic increases in all other distortion indexes.

Although use of the SMCS vanes is not scheduled during supersonic operation, limited tests were conducted at mach 2.2 with the vanes deflected at fixed angles. No significant effects were identified in total-pressure recovery or distortion levels with vane deflection angles of $\pm 10^{o}$ during operation at normal cruise attitudes. However, as shown in figure 86, a significant loss in inlet stability margin was recorded. Inlet buzz limits are conservatively defined at inlet mass flow ratios where the inlet comes out of buzz. With the SMCS vanes deflected, buzz limits occur at significantly higher mass flow ratios.

Full-scale inlet/engine test results. - One objective of full-scale, inlet/engine testing was to explore the effect of vortex ingestion on the F101 turbofan engine. Large vortex generators (shown in figure 77) were installed on the stubwing of the model to create flow conditions similar to those recorded with the 0.2-scale model when SMCS vane vortices are ingested.

Inlet performance and distortion characteristics resulting during operation at mach 0.85 with both vortex generators deflected through a range of -30^{o} to $+20^{o}$ are shown in figure 87. Engine-face, total-pressure contours representing maximum values of stall margin ratio (IDL) from dynamic data are shown in figure 88. Although recovery losses and distortion increases were not as great as recorded with the 0.2-scale model, it was possible to generate circumferential distortion components and increase turbulence levels. Positive vane angles created cowl side pressure defects, and negative vane angles created ramp side pressure defects. No engine instabilities were detected.

Subsequently, operation with deflected vortex generators was combined with off-scheduled inlet geometry to further reduce recovery and increase distortion levels. Effects of closing the throat and opening the bypass provided levels significantly more severe than those recorded with the 0.2-scale model, as compared in figure 89 as functions of engine corrected airflow. Dynamic, engine-face, total-pressure contours at maximum airflow are compared in figure 90. No engine instabilities were encountered during these runs.

Rapid engine throttle transients between idle and intermediate power settings were also conducted during operation with the vortex generators deflected to -30^{o} and off-scheduled inlet geometry. No engine instabilities were detected. Inlet recovery and distortion levels during these runs are shown in figure 91. Additionally, engine stalls were induced by fuel pulses to determine if vortices produced any shift in the fan stall line. No significant differences were detected.

INBOARD

SYMBOL	TEST	RUN	M_0	α_0	ψ_0	R_b	H_L	VANE
○	AEDC 164	986	2.20	2.5	-0.0	14.0	16.81	+ 10°
□	AEDC 164	987	2.20	2.5	-0.0	14.0	16.81	- 10°
△	AEDC 164	1021	2.20	2.5	-0.0	14.0	16.80	0°

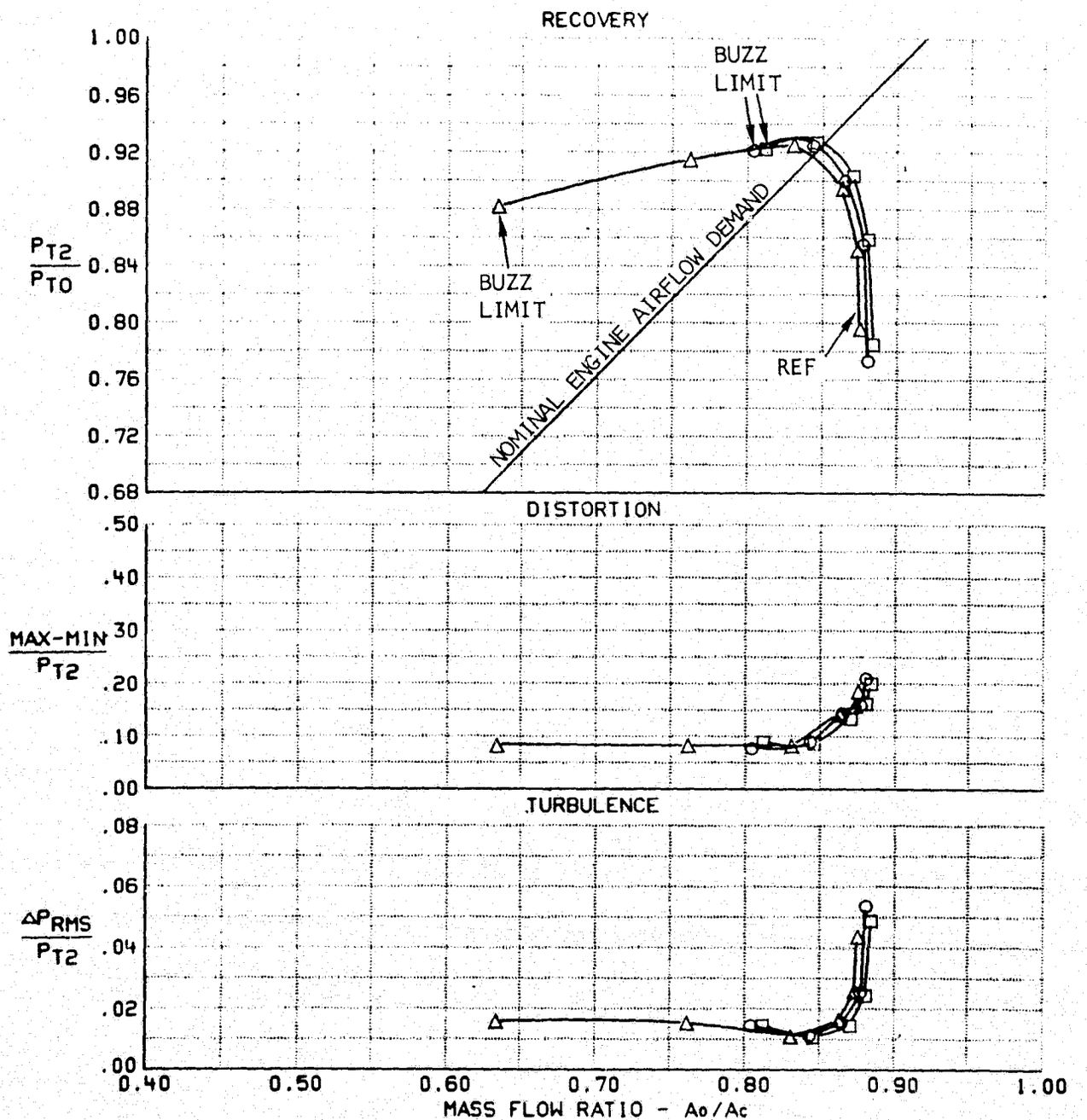

Figure 86. - Influence of SMC vane angle on performance α = 2.5, ψ = -0.0, M = 2.20, inboard inlet.

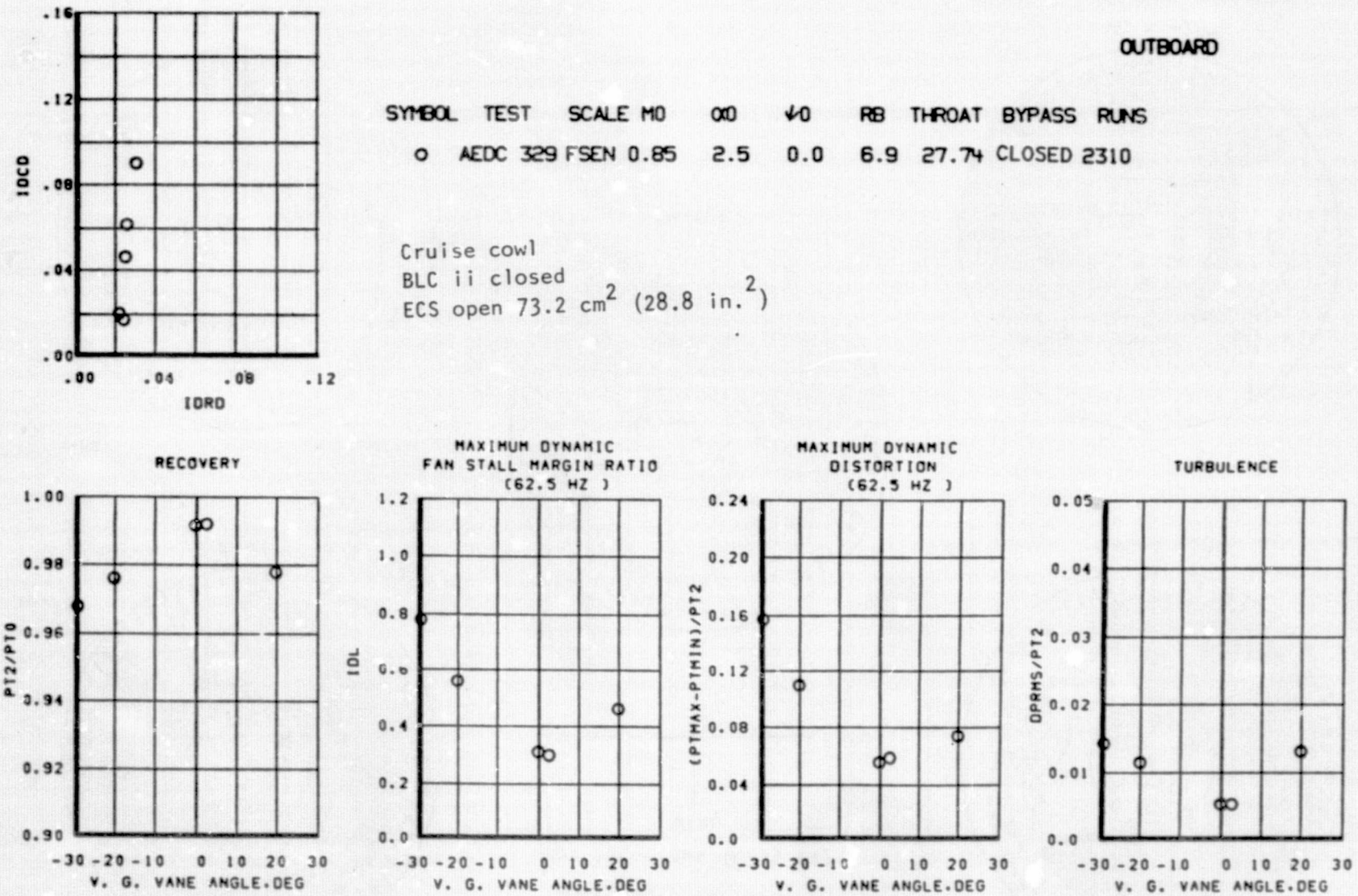

Figure 87. - Effect of vortex generator vane angle on dynamic distortion characteristics, M = 0.85, full scale (engine), W2CORR = 138.3 kg/sec (305 lb/sec).

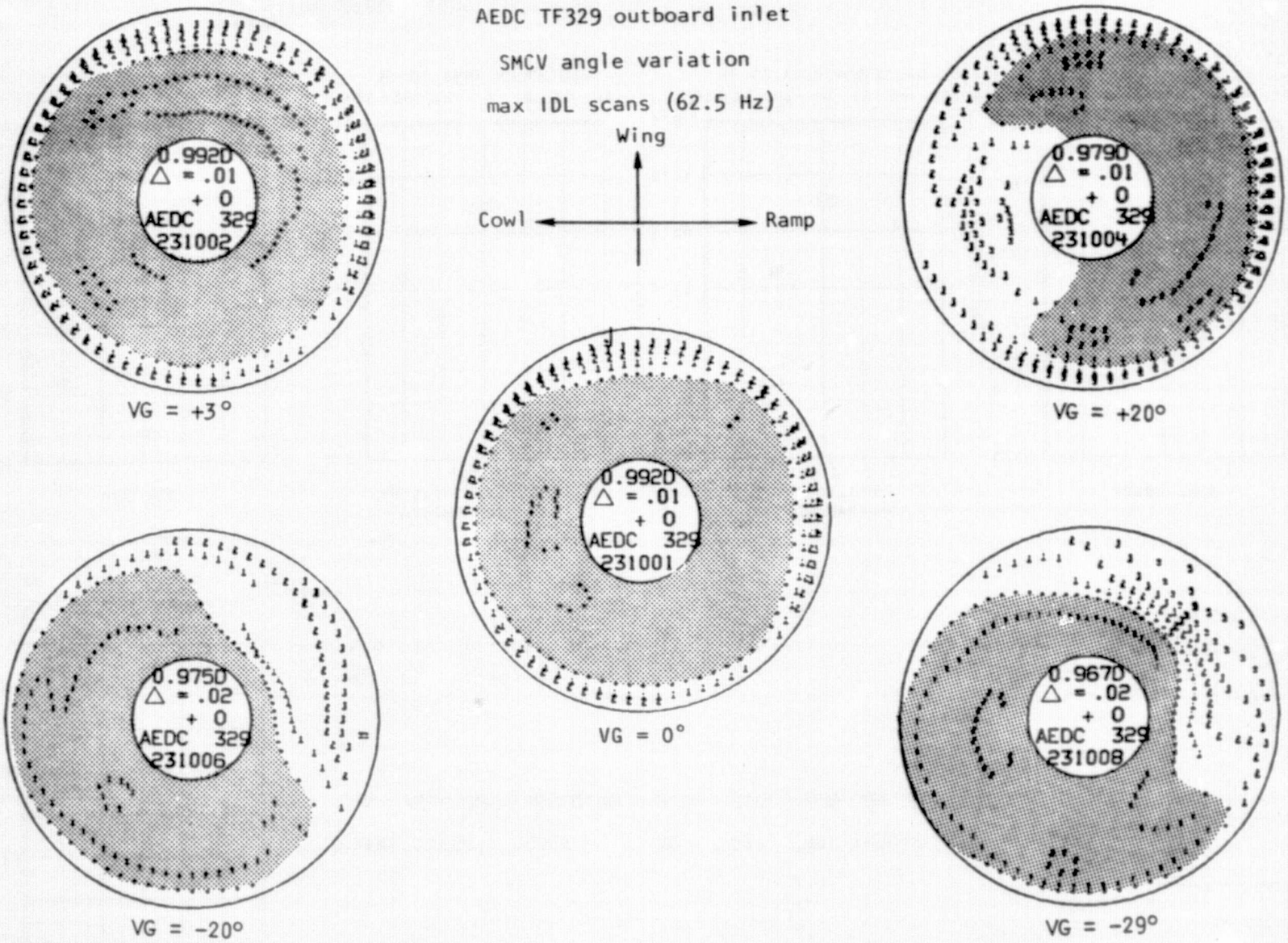

Figure 88. - Effect of vortex generator angle on dynamic engine face total pressure contours, M = 0.85, full scale (engine), W2CORR =138.3 kg/sec (305 lb/sec).

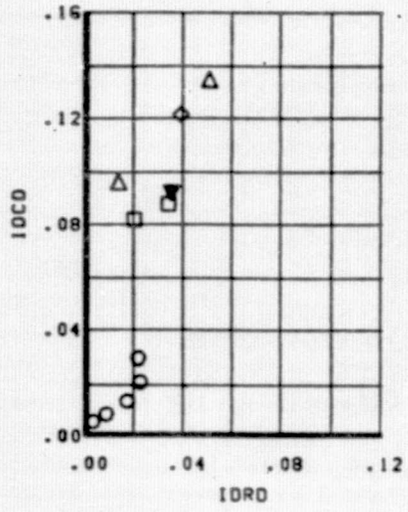

OUTBOARD

SYMBOL	TEST	SCALE	M0	α0	↓0	RB	THROAT	BYPASS	RUNS IN	VG VANE ANGLE	
○	AEDC 329	FSEN	0.85	2.5	0.0	6.9	27.76	0.0	2257	0	0
□	AEDC 329	FSEN	0.85	2.5	0.0	6.9	27.76	0.0	2311	2318	-29
△	AEDC 329	FSEN	0.85	2.5	0.0	6.9	20.14	0.0	2312	0	-29
◇	AEDC 329	FSEN	0.85	2.5	0.0	6.9	27.76	27.6	2316	0	-29
▼	AEDC 316	0.2	0.85	3.0	-5.0	7.0	26.97	0.2	391	0	20 (POINT TO BE SIMULATED)

Cruise cowl
BLC II closed
ECS open 73.2 cm^2 (18.8 $in.^2$)

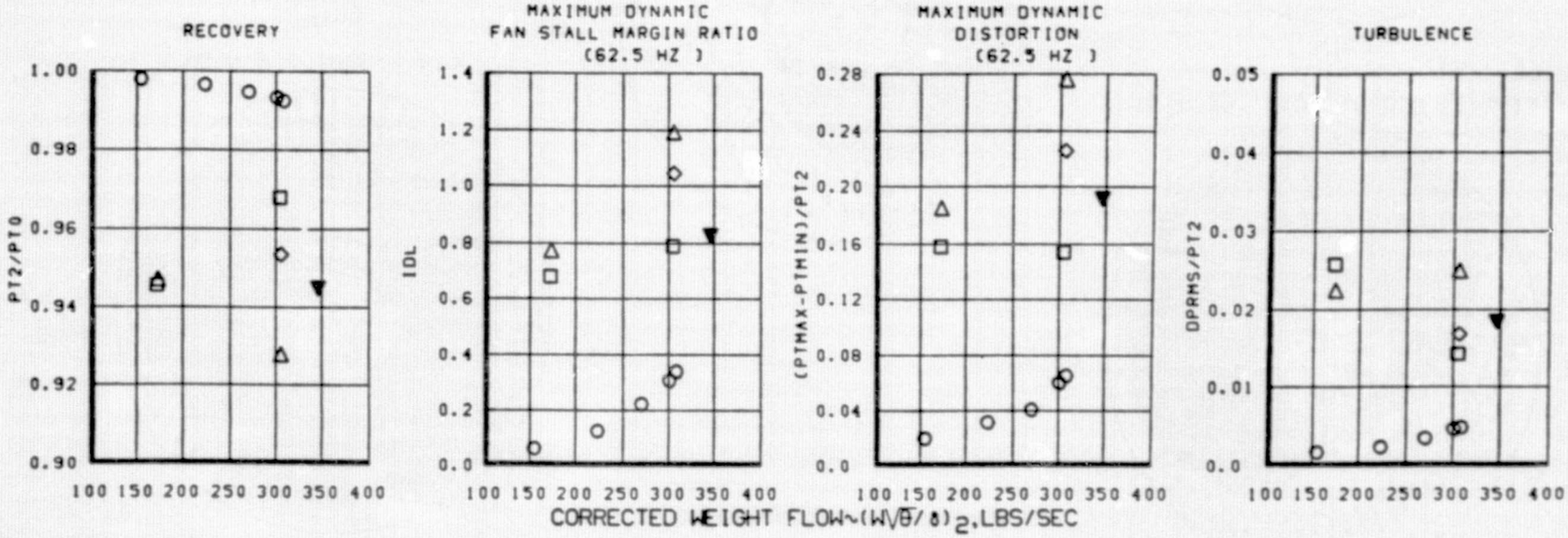

Figure 89. - Effect of vortex generators on dynamic distortion characteristics, M = 0.85, full scale (engine) and 0.2 scale maneuver point.

AEDC TF329 & TF316 outboard inlet

SMCV effects and simulation

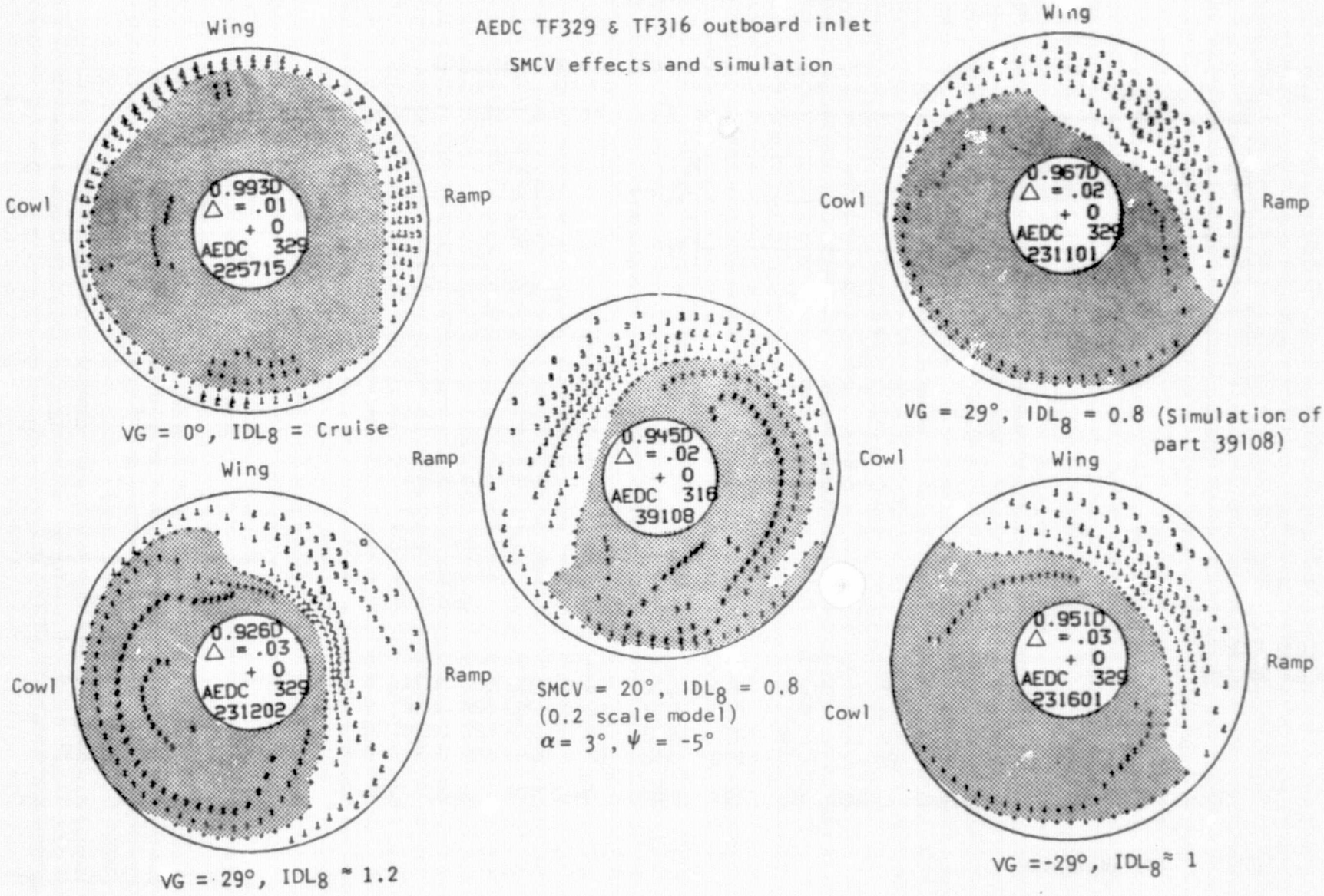

Figure 90. - Effect of SMCS vane on dynamic engine face total pressure contours, M = 0.85, full scale (engine) and 0.2 scale, W2CORR = 138.3 kg/sec (305 lb/sec).

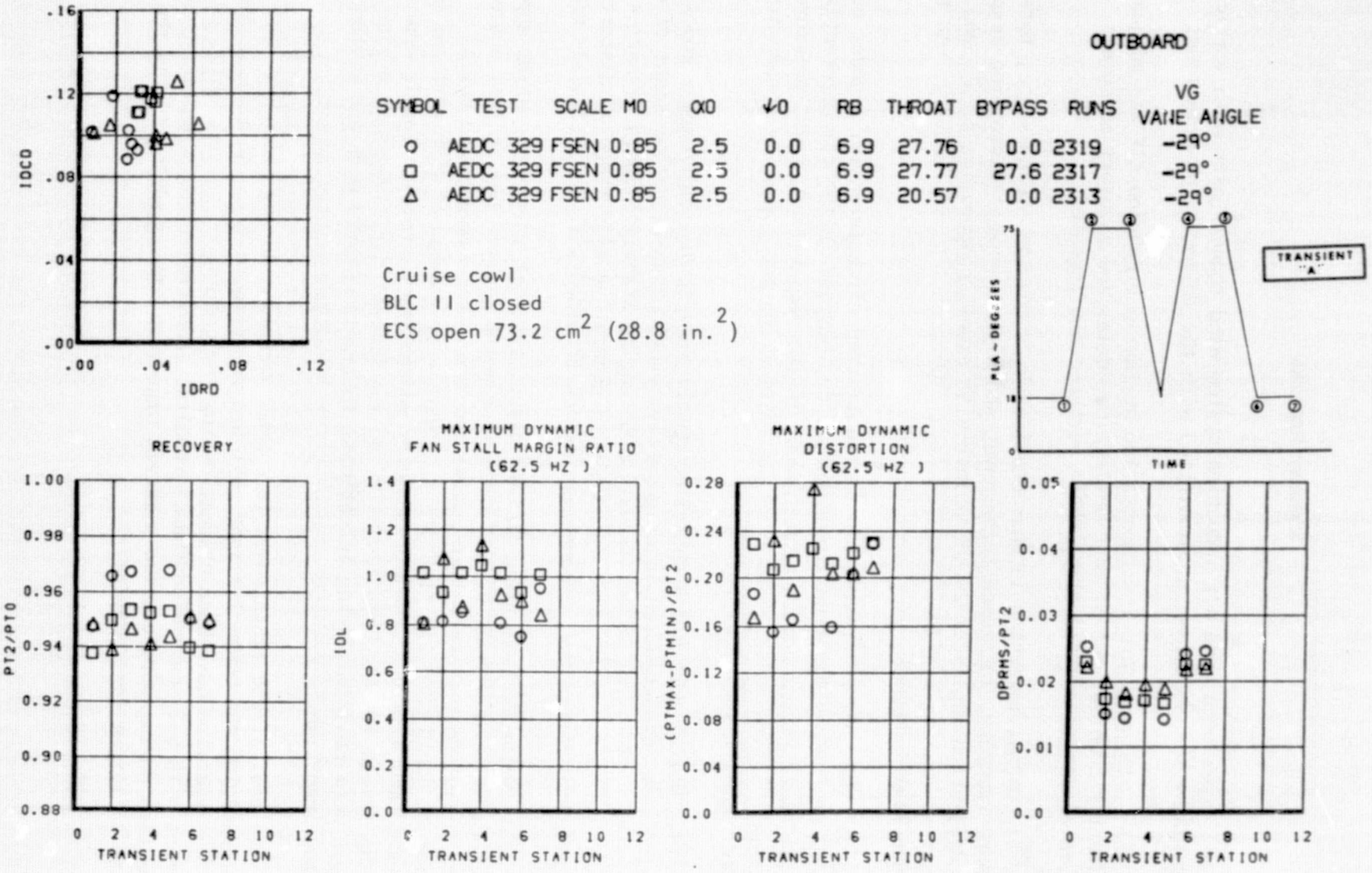

Figure 91. - Dynamic distortion characteristics during engine transient with vortex generators, M = 0.85.

Summary Remarks

B-1 experience from air induction system wind tunnel tests with vortices generated by the SMCS vane is summarized with the following observations:

(1) Total-pressure instrumentation at the inlet/engine AIP was adequate to identify combinations of vane deflection angles and aircraft maneuvers (angles of attack and sideslip) where vortices are ingested.

(2) Vortex ingestion is characterized by a loss in steady-state, total-pressure recovery, increased turbulence, and higher dynamic distortion levels. Vane deflection angles of 20^{o}, combined with sideslip operation at 6^{o}, and engines at maximum airflow, resulted in a 5-percent loss in recovery, and turbulence levels doubled.

(3) The vortex appears to affect a limited circumferential segment of the engine face. This tends to introduce an increase in the circumferential distortion component and is also evident in the engine-face, total-pressure contours. Increases in circumferential distortion are generally accompanied by decreases in radial distortion.

(4) Vortex generators installed on the full-scale inlet/engine model, coupled with off-scheduled inlet geometry, provided an effective means of evaluating the effects of vortex ingestion on engine stability characteristics. With these techniques, it was possible to generate a wide range of distortion patterns and levels that spanned variations recorded with the 0.2-scale model.

(5) Major destabilizing factors associated with vortex ingestion appear to be taken into account by the distortion methodology. During full-scale, inlet/engine tests, stall-free engine operation was demonstrated during a series of rapid throttle transients. Tests were conducted with vortices being ingested and with off-schedule geometry generating distortion levels approximating design limits. Additionally, no significant differences in engine stall margin were recorded during intentional fuel-pulse stalls with and without vortex ingestion.

Initial flight tests to explore SMCS operation during maneuvers were conducted during the phase I flight test program (figure 92). No indications of vortex ingestion have been evident during the conditions tested, which is consistent with 0.2-scale wind tunnel results. Additional tests exploring SMCS operation during more extreme aircraft maneuvers are scheduled during the phase II flight test program.

Notes:

1. Envelope of SMCS vane wake ingestion as determined from wind tunnel data
2. Dark area is more severe area of wake ingestion for vane deflections ≥ 10 degrees

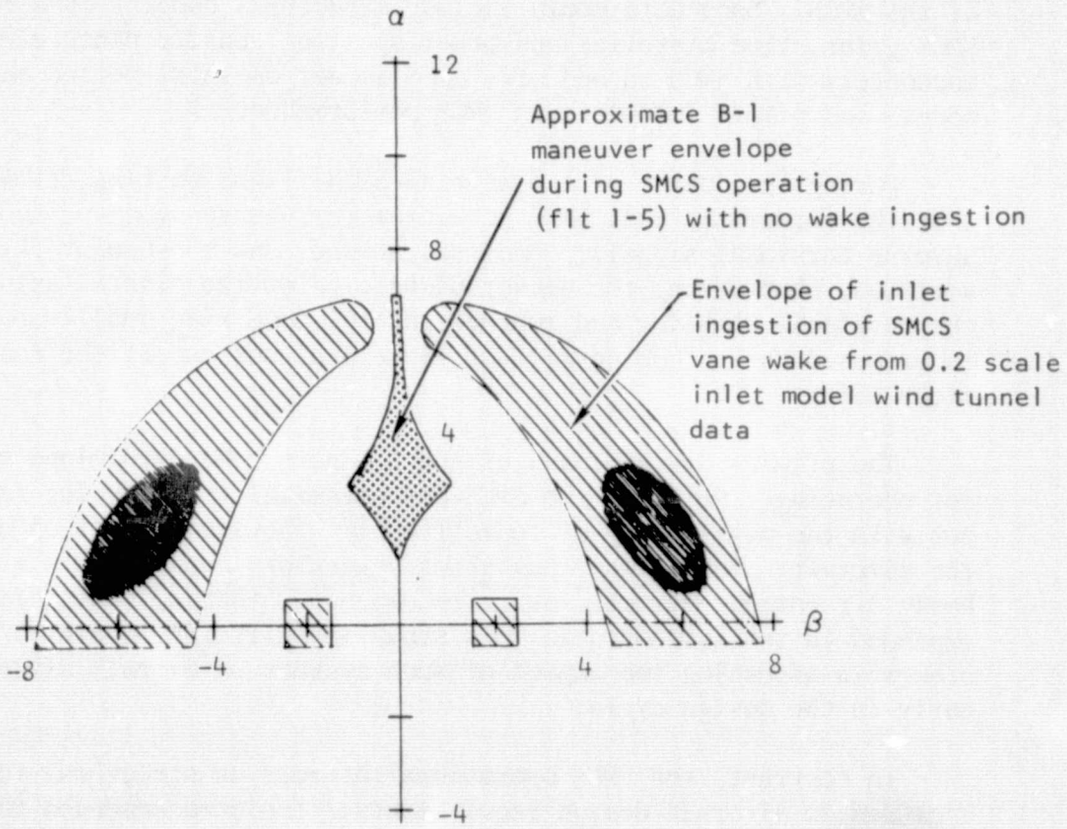

Figure 92. - Predicted envelope of SMCS vane wake ingestion by inlet.

RECOMMENDED FUTURE EFFORT

The study results discussed in the present report have been primarily concerned with tracing the SMCS development and expanding on the key design features and component test results, with little emphasis on the analyses techniques employed. The follow-on effort will permit expanding on these important analyses techniques and analyses conducted in support of the SMCS design, including the analytical modeling of the flexible aircraft and automatic control systems. Flight test data have been obtained to validate the analytical models developed, allowing direct comparisons to be made of analyses and flight test in the form of frequency responses. It is recommended that the highlights from these results be summarized in the follow-on report.

It is also recommended that a summary of the key SMCS flight test results to date, beyond those needed to validate the analyses, be assembled in the next study segment. These data would demonstrate the real-world capability of the SMCS. Such data would include structural damping as a function of SMCS gains, time histories and power spectral density plots of turbulence encounters with SMCS on and off, SMCS impact on short-period and Dutch roll modes, and pilots' comments on SMCS performance.

During the course of the initial SMCS flight testing, it was discovered that the forward lateral SMCS accelerometer was sensing and feeding back adverse torsional signals. Analyses showed, and subsequent flight test verified, that moving the sensor package below the elastic axis could eliminate the torsional coupling and improve lateral SMCS ride quality performance. It is proposed to include details of these analyses and flight tests in the new study effort.

The primary design loads of the B-1 have been determined with the SMCS not operating. However, the SMCS has potential for reducing forebody loads, but with the possibility of redistributing the load impact on other parts of the aircraft. Some effort has already been expended in this area on the basic Air Force contract. It is recommended, though, that this effort be expanded in the follow-on to this study in sufficient depth to be of aid to others in assessing the impact of such systems on overall aircraft loads early in the design cycle.

In contrast, the SMCS operational effects on structural fatigue have been included in aircraft design requirements. It is recommended that the SMCS impact on fatigue be summarized as part of the next study segment.

Moving base simulation has played an important role in the B-1 aircraft design evaluation. The analytical modeling support of this effort has been innovative and of potential general interest. Large analytical models of the rigid-body and structural modes were simplified for simulation, yet were able to retain key dynamic attributes. It is recommended that the unique analytical techniques developed for this task be summarized in the follow-on study.

In the wind tunnel tests conducted and summarized in the present report, the interference effects from the SMCS vane on other parts of the aircraft have been discussed. The true importance of these effects has not been definitively tied down. It is recommended that additional analyses be conducted with the digital computer simulation program capable of accepting the highly nonlinear aerodynamic interference descriptions. These analytical results would be correlated with other analyses and flight test data to determine what elements of the interference effects are most important. Another facet to be evaluated would be the fact that the wind tunnel data were static tests, while the interference effects on the airplane occur in a dynamic environment of fast-moving vanes and a turbulent atmosphere.

As the present report was in the final stages of completion, the initial in-flight SMCS vane/inlet interference tests had been completed. All of the scheduled tests of this nature should be completed in time to include the results in a follow-on study report. It is proposed that these tests be summarized and correlated with data from wind tunnel tests presented herein.

APPENDIX A

NOMENCLATURE

Control System-Related

$\bar{A}_{(\ )}$	Root-mean-square acceleration due to 0.3048 m/sec (1 ft/sec) rms gust intensity; subscript Z denotes vertical axis, Y denotes lateral axis
$\bar{A}_{\delta_{(\ )}}$	Root-mean-square, or vane deflection due to 0.3048 m/sec (1 ft/sec) rms gust intensity; subscript w_g denotes due to vertical gust, v_g denotes due to lateral gust
b_1, b_2, P_1, P_2	Properties of atmospheric turbulence (reference 8)
BP	Butt plane
CADC	Central air data computer
CCV	Control-configured vehicle
C.G.	Center of gravity
cpm	Cycles per minute
deg	Degrees
EI	Bending stiffness
F	Force
ft/sec	Feet per second
fpm	Feet per minute
FS	Fuselage station
g	Gravity constant
GJ	Torsional stiffness
gpm	Gallons per minute

$H_{(\ )}$	Crew sensitivity index; subscript Z denotes vertical axis, Y denotes lateral axis
h_p	Pressure altitude
ILAF	Identical location of accelerometer and force
$I_{(\ )}$	Inertia characteristics; subscripts XX, YY, ZZ denote respective axes; subscripts XZ, XY, YZ denote respective product of inertias
I.D.	Inside diameter
K	System gain
ℓ	Moment arm
L	Turbulence scale length
lb-in.	Pound-inch
LG	Lateral gain
M	Mach number
M__	Mold line
mpm	Meters per minute
$n_{(\ )}$	Load factor; subscript Z indicates vertical axis, subscript Y denotes lateral axis
$N_o\delta_{(\ )}$	Characteristic frequency of vane deflection; i.e., the average number of zero crossings per unit of time
$N(\delta_{CV})$	Number of exceedances of specified magnitude of vane deflection
O.D.	Outside diameter
psi	Pounds per square inch
q_o	Dynamic pressure

$q, \dot{\theta}$	Pitch rate
rad	Radians
rms	Root mean square
S	Laplace operator
sec	Seconds
SAS	Stability augmentation system
SCAS	Stability and control augmentation system
SMCS	Structural mode control system
T_D	Human response weighting function
V_o	Velocity
VG	Vertical gain
v_g	Lateral gust velocity
w_g	Vertical gust velocity
WP	Water plane
$\delta_{(\ )}$, $\delta_{CV_{(\ )}}$	Vane deflection; subscript R denotes right panel, L denotes left panel
$\ddot{\eta}_i$	Acceleration of structural mode i generalized coordinate
ω	Frequency, rad/sec
Ω	Wave number, $\left(\frac{\omega}{V_o}\right)$
$\phi_i^{(\ )}$	Deflection of normalized structural mode i at location designated in superscript
Φ_{gust}	Gust power spectral density
$\Phi_{\tilde{H}}$	Crew sensitivity power spectral density

$\sigma_{(\ )}$	Root-mean-square of subscripted parameter
σ_{w_g}, σ_{v_g}	Vertical and lateral gust intensity, respectively

Aerodynamics-Related

All data are in the airplane body axes unless specifically called out otherwise. The moment data presented in this report are about a center of gravity located at full-scale airplane fuselage station 2509 (987.85) and water plane 50.8 (20.0). Unless stated otherwise, the force coefficient data are referenced to a full-scale wing area S_w = 180.79 m^2 (1946 ft^2); the pitching moment to a reference length $\bar{c}_w$ = 4.67 m (15.32 ft); and the yawing and rolling moments to a reference length b_w = 41.54 m (136.3 ft).

α	Angle of attack of airplane (see figure 93)
α_v	Vane local angle of attack
β	Sideslip angle (see figure 93)
Γ	Dihedral angle of vane (+ if tip chord above root chord)
Λ_v	Sweepback angle of leading edge of vane
Λ_w	Sweepback angle of leading edge of wing
δ	Vane deflection angle about hinge line (see figure 94); subscripts L and R refer to left and right vane panels, respectively, plus deflection produces $+C_N$ or $+C_Y$
ϵ	Downwash angle (sense opposite to that of α)
M	Mach number
q_o	Free-stream dynamic pressure
V_o	Free-stream velocity
V_x, V_y, V_z	Components of V_o along the X, Y, and Z body axes
$\bar{c}$	Mean aerodynamic chord
$\bar{c}_w$	Wing mean aerodynamic chord
b_w	Wing span

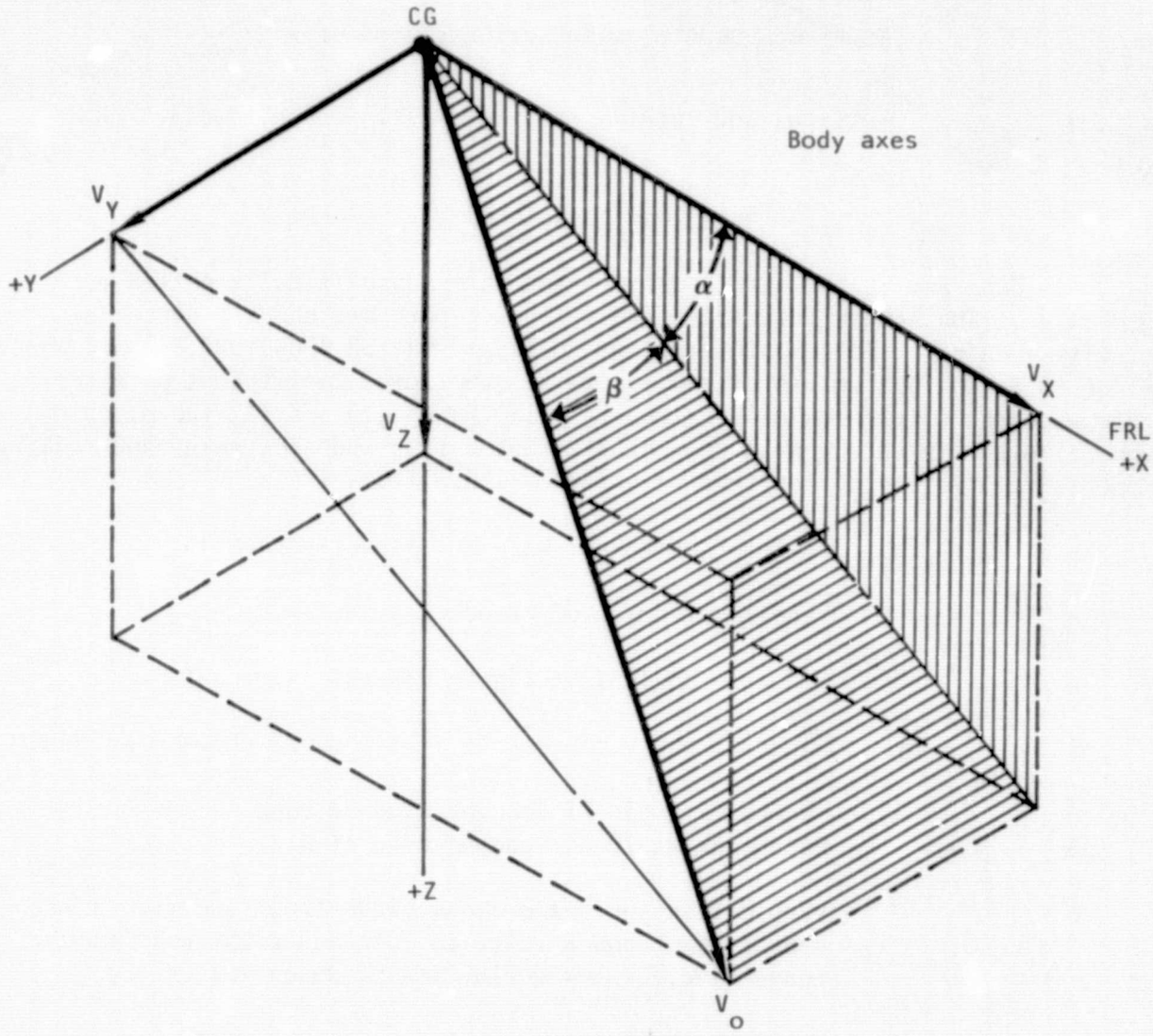

$$V_X = V_o \cos\beta\cos\alpha$$
$$V_Y = V_o \sin\beta$$
$$V_Z = V_o \cos\beta\sin\alpha$$

$$\alpha = \sin^{-1}\frac{V_Z}{V_o\cos\beta} \qquad \beta = \sin^{-1}\frac{V_Y}{V_o}$$

Figure 93.- Angle of attack (α) and sideslip (β) definitions.

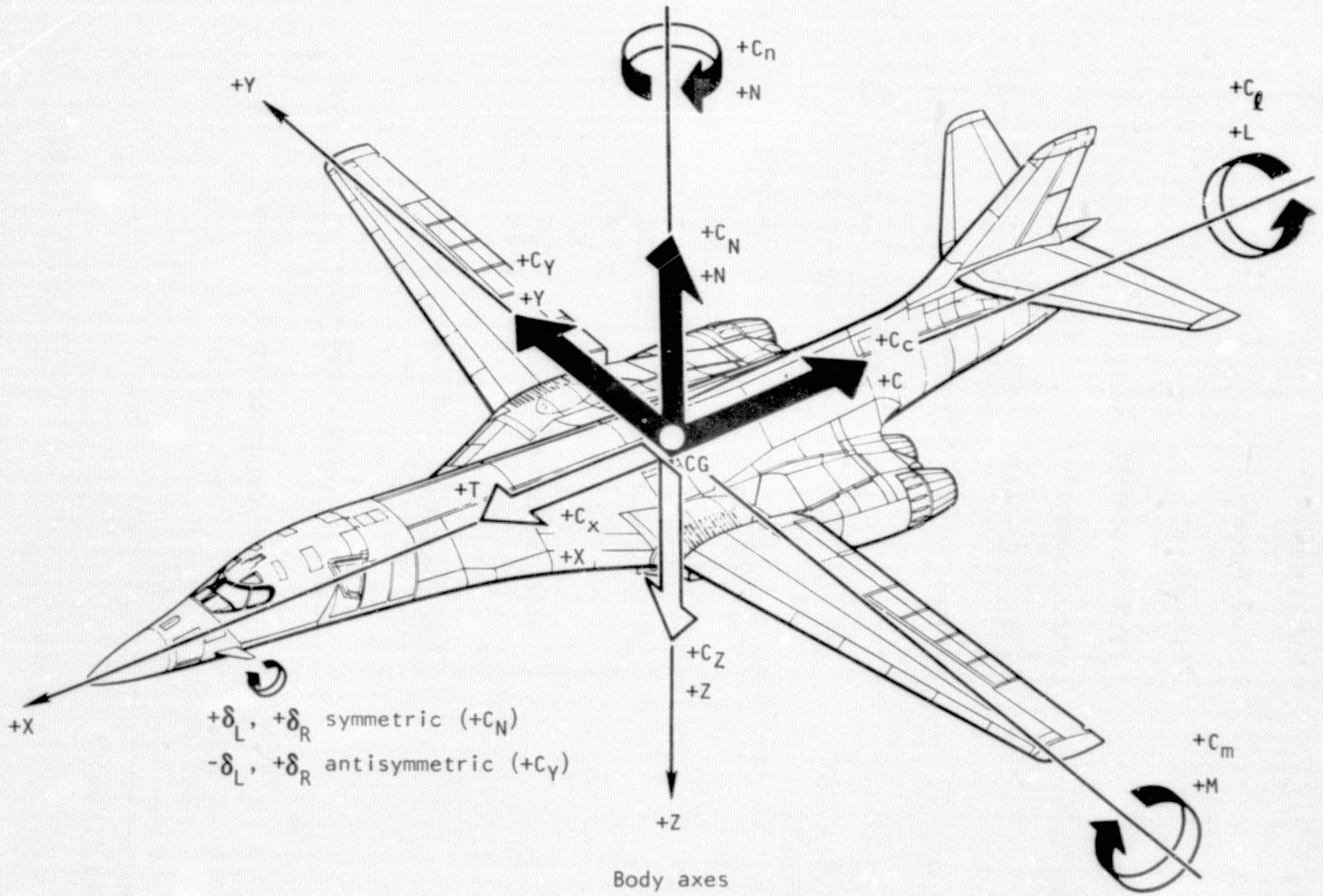

Figure 94. - Sign convention for coefficients and control surface deflections.

S_w	Wing area
N	Normal force*
C	Chord force*
Y	Side force*
M	Pitching moment*
N	Yawing moment*
L	Rolling moment*
C_N	Normal force coefficient, $\frac{N^*}{S_w q_o}$
C_c	Chord force coefficient, $\frac{C^*}{S_w q_o}$
C_y	Side force coefficient, $\frac{Y^*}{S_w q_o}$
C_m	Pitching moment coefficient, $\frac{M^*}{S_w \bar{c}_w q_o}$
C_n	Yawing moment coefficient, $\frac{N^*}{S_w b_w q_o}$
C_l	Rolling moment coefficient, $\frac{L^*}{S_w b_w q_o}$
C_{l_α}	Local lift curve slope; based on local area
$\frac{x}{c}$	Local chordwise center of pressure

*See figure 94

Engine/Inlet-Related

AEDC	Arnold Engineering Development Center
AIP	Inlet/engine aerodynamic interface plane
A_{CAPT}	Inlet capture area
A_{DUCT}	Duct area
Ao/Ac	Engine mass flow ratio
BLC	Inlet boundary layer control
D engine	Engine diameter
DP rms	Root-mean-square pressure differential
ECI	External compression inlet
ECS	Environmental control system
ECI-7	Inlet configuration identification
FSEN	Full-scale wind tunnel test with engine installed
H_c	Inlet capture height
H_L	Relative inlet throat height
IDCD	Dynamic circumferential distortion component
IDCO	Circumferential distortion component, outboard inlet
IDRD	Dynamic radial distortion component
IDRI	Radial distortion component, inboard inlet
IDL	Engine stall margin ratio (function of IDCD and IDRD)
IDLI	Engine stall margin ratio, inboard inlet
IDL8	Dynamic stall margin ratio
IDT	Inlet distortion index, inboard inlet (PTMAX-PTMIN)/PT_2

,1	Inlet porosity configuration identification
M_o, MO	Free-stream mach number
PLA	Engine power lever angle
PT_2, PT2	Average total pressure at inlet/engine AIP
PTMAX	Maximum total pressure at inlet/engine AIP
PTMIN	Minimum total pressure at inlet/engine AIP
P_{TO}, PTO	Free-stream total pressure
R_B, RB	First movable ramp angle
r_i	Rake number i
SF	Supersonic Facility (AEDC)
TF	Transonic Facility (AEDC)
TWT	Trisonic Wind Tunnel (Rockwell)
2D	Two-dimensional
Recovery	Total pressure at AIP referenced to freestream total pressure
Turbulence	Differential pressure average rms value at AIP
V.G.	Vortex generator
W_2CORR, W2CORR	Engine corrected airflow, station 2
αo, α	Trim angle of attack
β	Sideslip angle
ψo, ψ	Yaw angle

APPENDIX B

DESCRIPTION OF DATCOM METHOD AND SMCS VANE PLANFORM OPTIMIZATION STUDY

An empirical method is described in the USAF Stability and Control Handbook (DATCOM) (reference 14) for predicting the characteristics of wings through high angles of attack. The method is based on the results of numerous wind tunnel tests and is valid for planforms with any aspect ratio, taper ratio, sweep angle, and airfoil section. However, it is restricted to wings with straight leading and trailing edges and streamwise tips. The method is described as valid only up to mach 0.6, but was extrapolated to 0.85 in this study.

The basic procedure used may be summarized as follows:

(1) A linear lift curve slope is calculated for the three-dimensional planform as a function of aspect ratio, taper ratio, sweep angle, mach number, and airfoil section lift curve slope, and section maximum lift coefficient.

(2) A nonlinear incremental force is calculated as a function of the previous parameters plus angle of attack. Different equations are used for angles of attack below and above the stall angle.

The described approaches have been employed in a study of vane planforms to determine the "optimum" one for the SMCS at M = 0.85. The "optimum" force characteristics sought for the vane were as high a normal force curve slope as possible and one which did not degrade at high angles of attack up through 30^{o}. The elements of the matrix of planforms studied were aspect ratios of 2, 2.5, and 3.0; taper ratios of 0.1 and 0.2; and leading edge sweep angles of 35^{o}, 40^{o}, 50^{o}, 55^{o}, 60^{o}, and 65^{o}. The normal force characteristics versus angle of attack of these vanes are given in figures 95 through 100. It is to be emphasized that the normal force coefficients shown for these data are based on vane area and are referenced to a body axis system attached to the vane surface.

The "optimum" vane planform selected is the AR = 2.5, $\lambda = 0.20$; $\Lambda_{v} = 60°$; the normal force curve for this surface is shown in figure 95.

The DATCOM method also includes provisions for variation of airfoil thickness ratios by means of varying the section properties. All of the aforementioned studies were conducted with the nominal thickness ratio of 5 percent. Several cases, however, were run with thicknesses of 9 percent. No essential

nange in the results was noted. The Stability and Control Handbook comments that, for low aspect ratios, the high angle-of-attack characteristics are almost completely planform-dependent, with moderate changes in thickness having little or no influence.

Note: C_{N_V} based on vane area and is referenced to vane body axis.

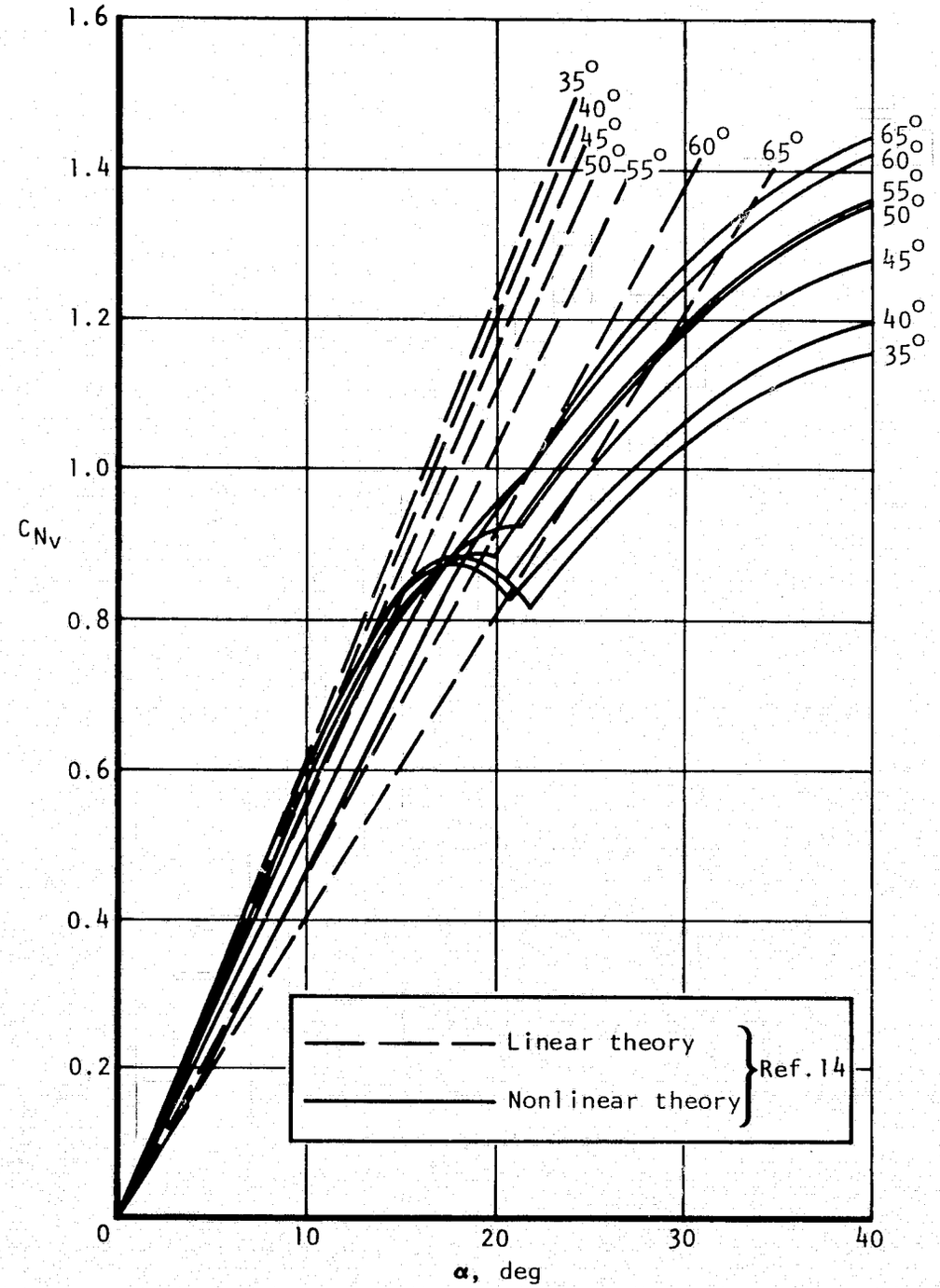

Figure 95. - Vane normal force coefficient versus angle of attack curves for various sweep angles at M = 0.85, AR = 2.5, λ = 0.2.

Note: C_{N_V} based on vane area and is referenced to vane body axis.

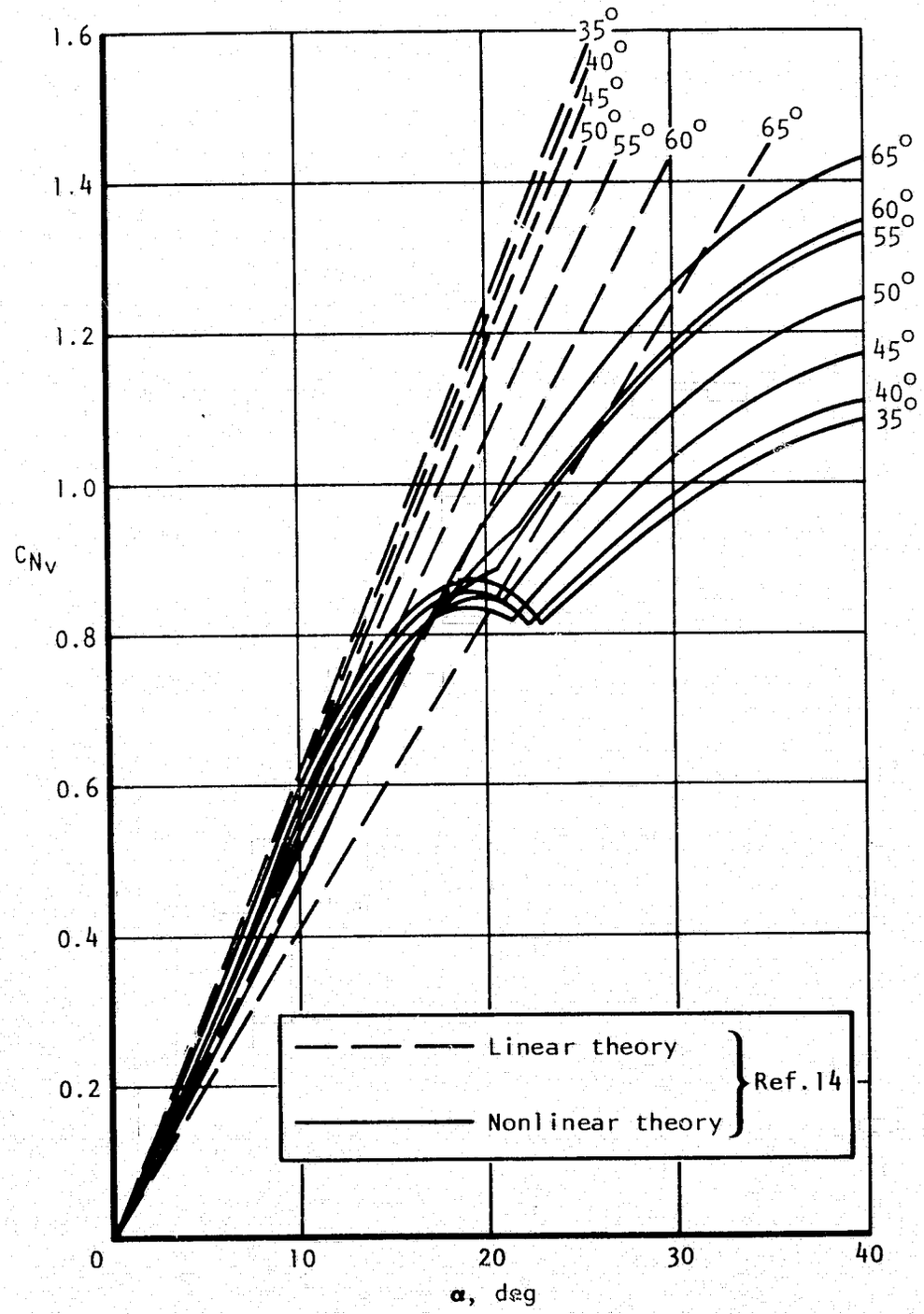

Figure 96. - Vane normal force coefficients versus angle of attack curves for various sweep angles at M = 0.85, AR = 2.5, λ = 0.1.

Note: C_{N_V} based on vane area and is referenced to vane body axis.

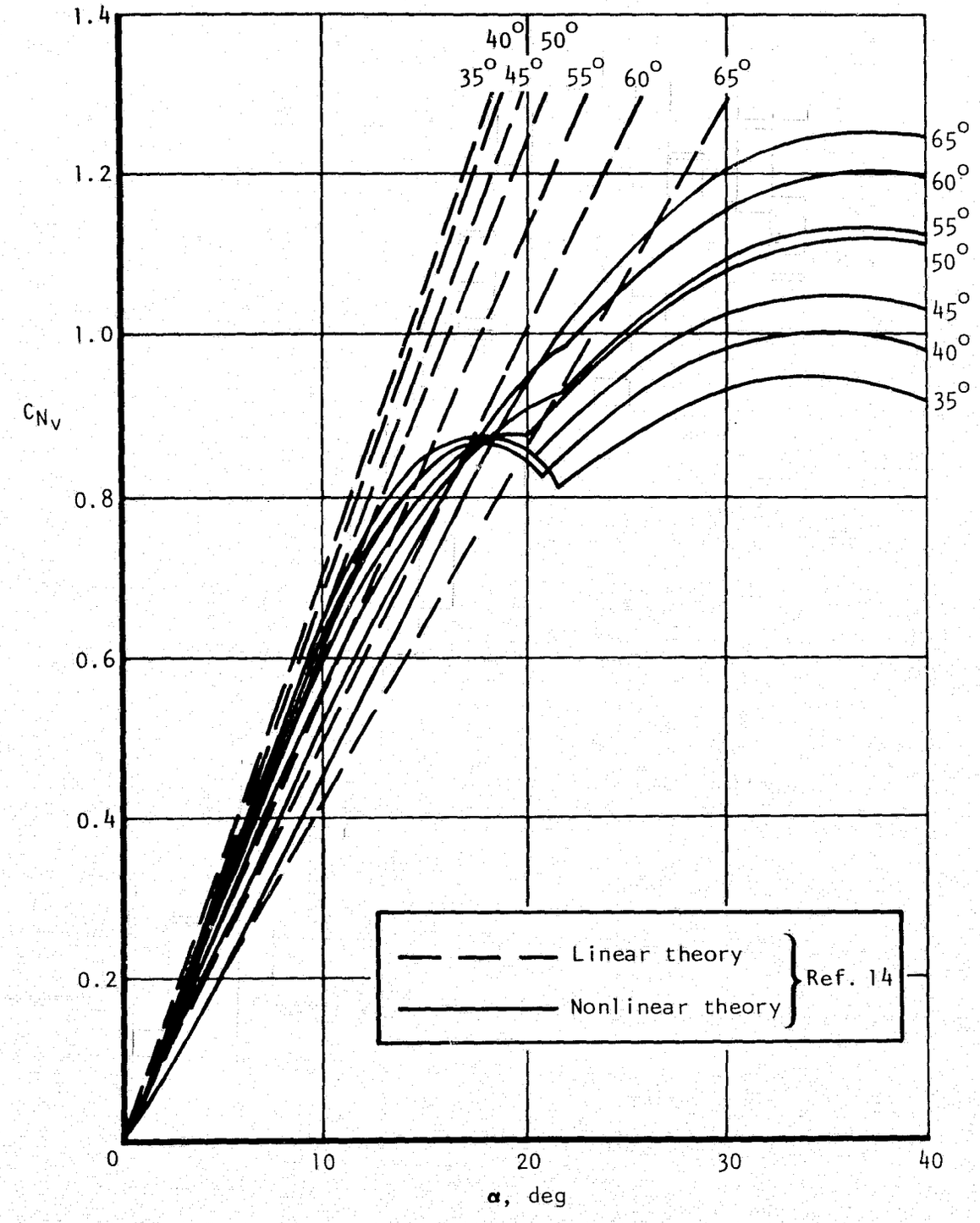

Figure 97. - Vane normal force coefficient versus angle of attack curves for various sweep angles at M = 0.85, AR = 3.0, λ = 0.1.

Note: C_{N_V} based on vane area and is referenced to vane body axis.

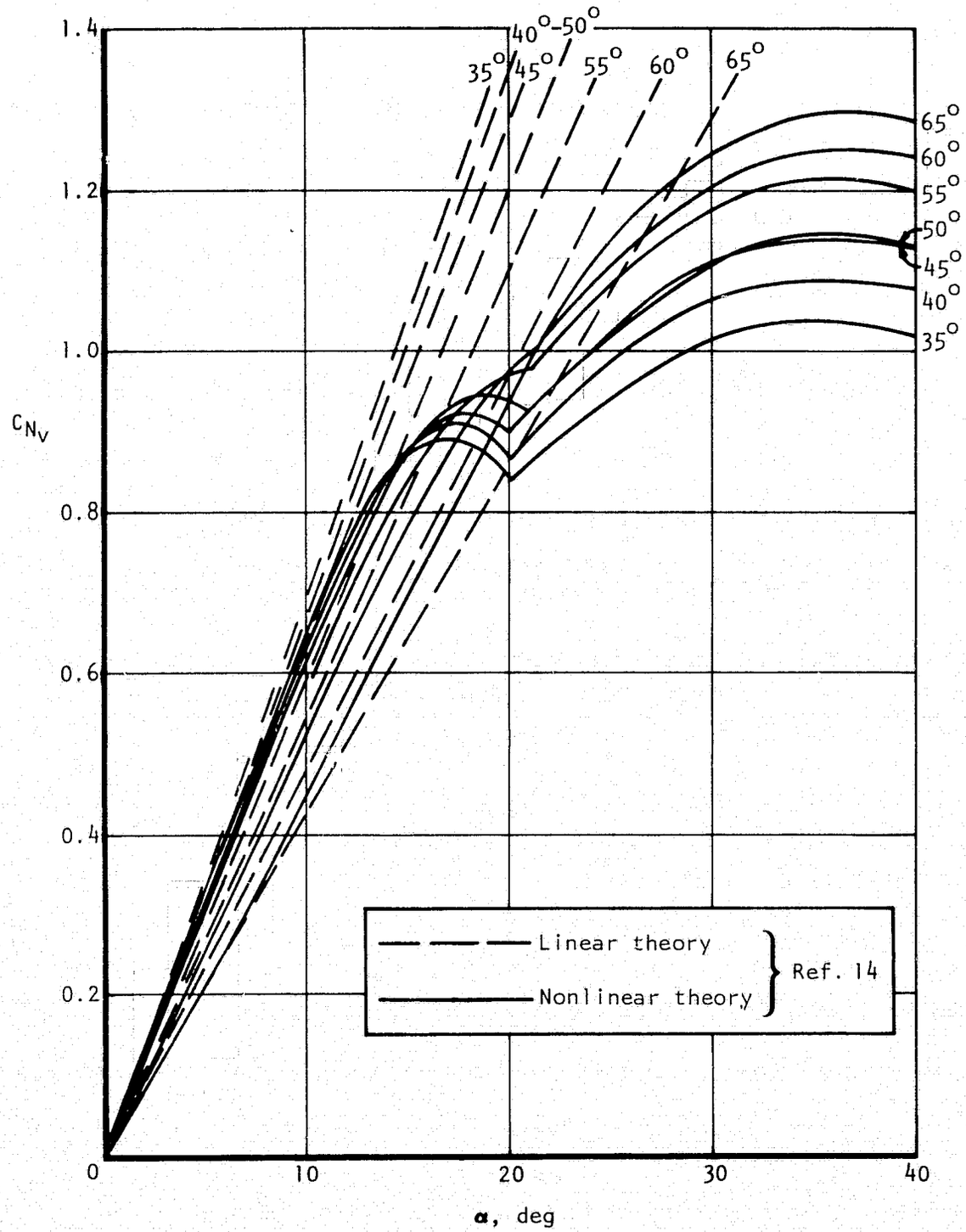

Figure 98. - Vane normal force coefficient versus angle of attack curves for various sweep angles at M = 0.85, AR = 3.0, λ = 0.2.

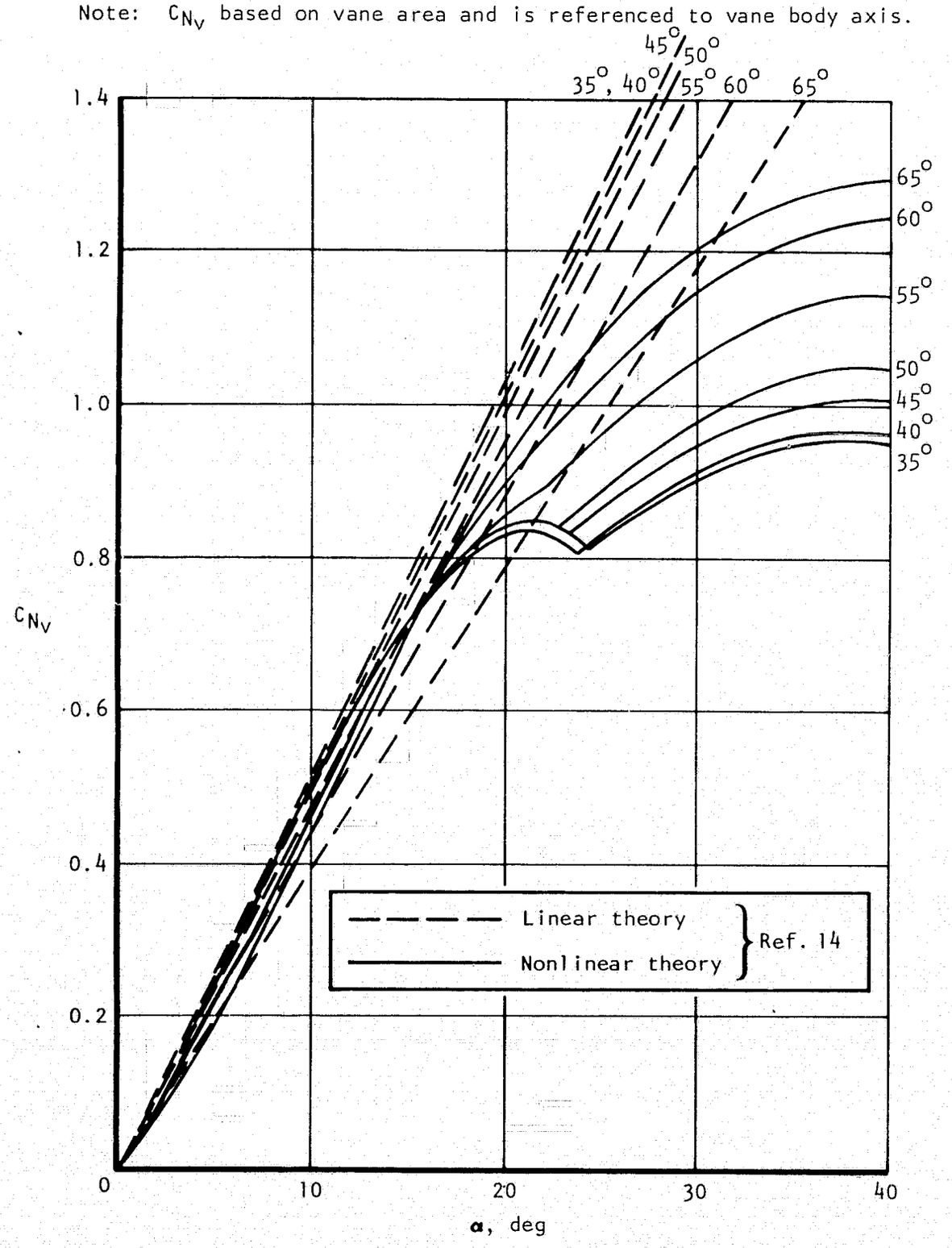

Figure 99. - Vane normal force coefficient versus angle of attack curves for various sweep angles at M = 0.85, AR = 2.0, λ = 0.1.

Note: C_{N_V} based on vane area and is referenced to vane body axis.

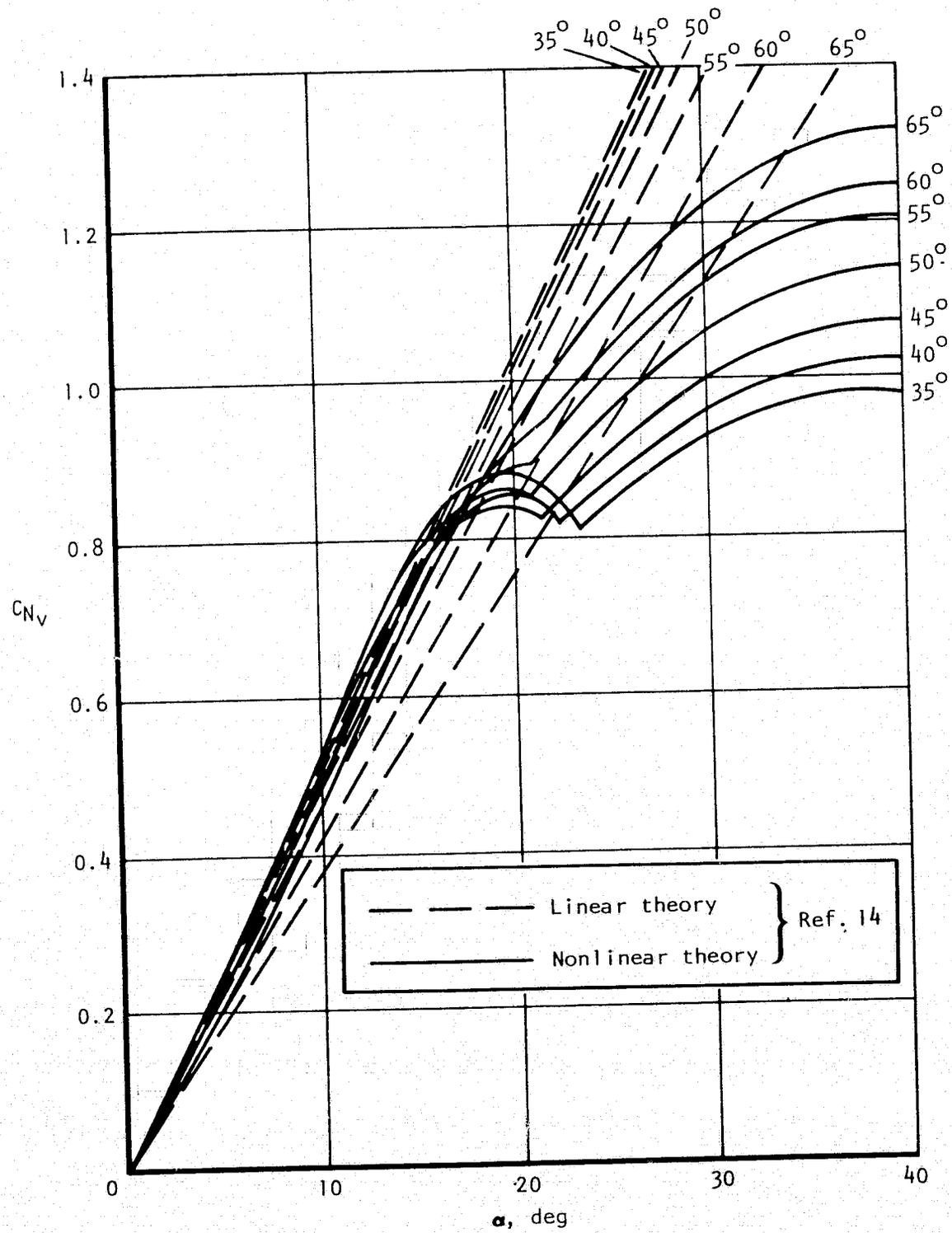

Figure 100. - Vane normal force coefficients versus angle of attack curves for various sweep angles at M = 0.85, AR = 2.0, λ = 0.2.

APPENDIX C

DISTRIBUTED VANE FORCE CHARACTERISTICS

The linear theory total normal force curve slope, local lift curve slope versus spanwise station, and the spanwise variation of the chordwise center of pressure for the modified vane, $\Lambda_v = 60°$, at M = 0.85 are presented in figure 101. These have been calculated using the doublet lattice method of ref. 15.

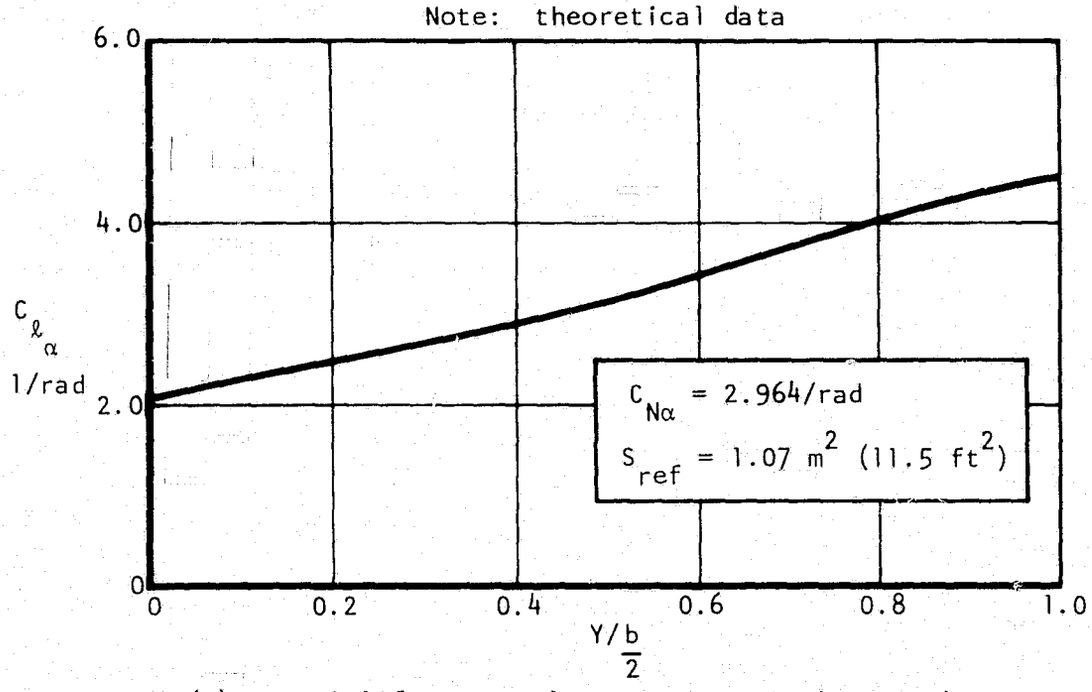

(a) Local lift curve slope versus spanwise station.

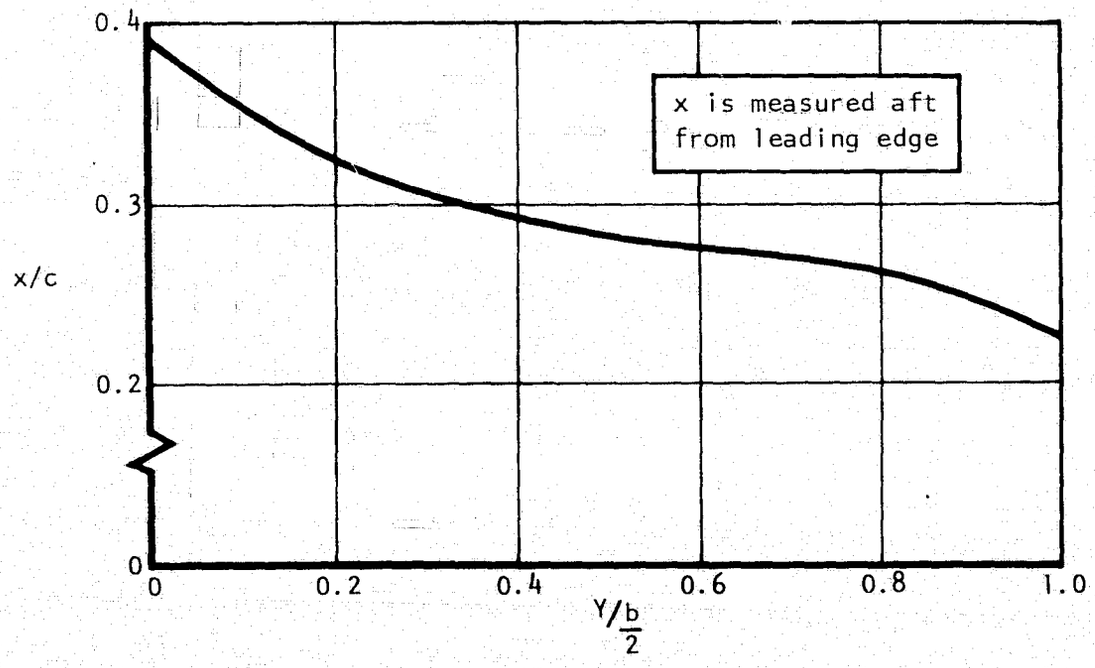

(b) Spanwise variation of chordwise center of pressure.

Figure 101. - Aerodynamic characteristics of $\Lambda_v = 60°$ vane, M = 0.85.

APPENDIX D

SMCS VANE MASS AND STIFFNESS PROPERTIES

The data presented in this appendix reflect the mass and stiffness properties of the vane as finally constructed. Figure 102 shows a vane panel divided into sections for which the mass properties displayed in table IX were determined. Figure 103 presents the spanwise variation of the elastic axis location. The stiffness properties of sections perpendicular to the elastic axis are given in figure 104. The SMCS vane actuators and backup structure flexibility data are presented in figure 105.

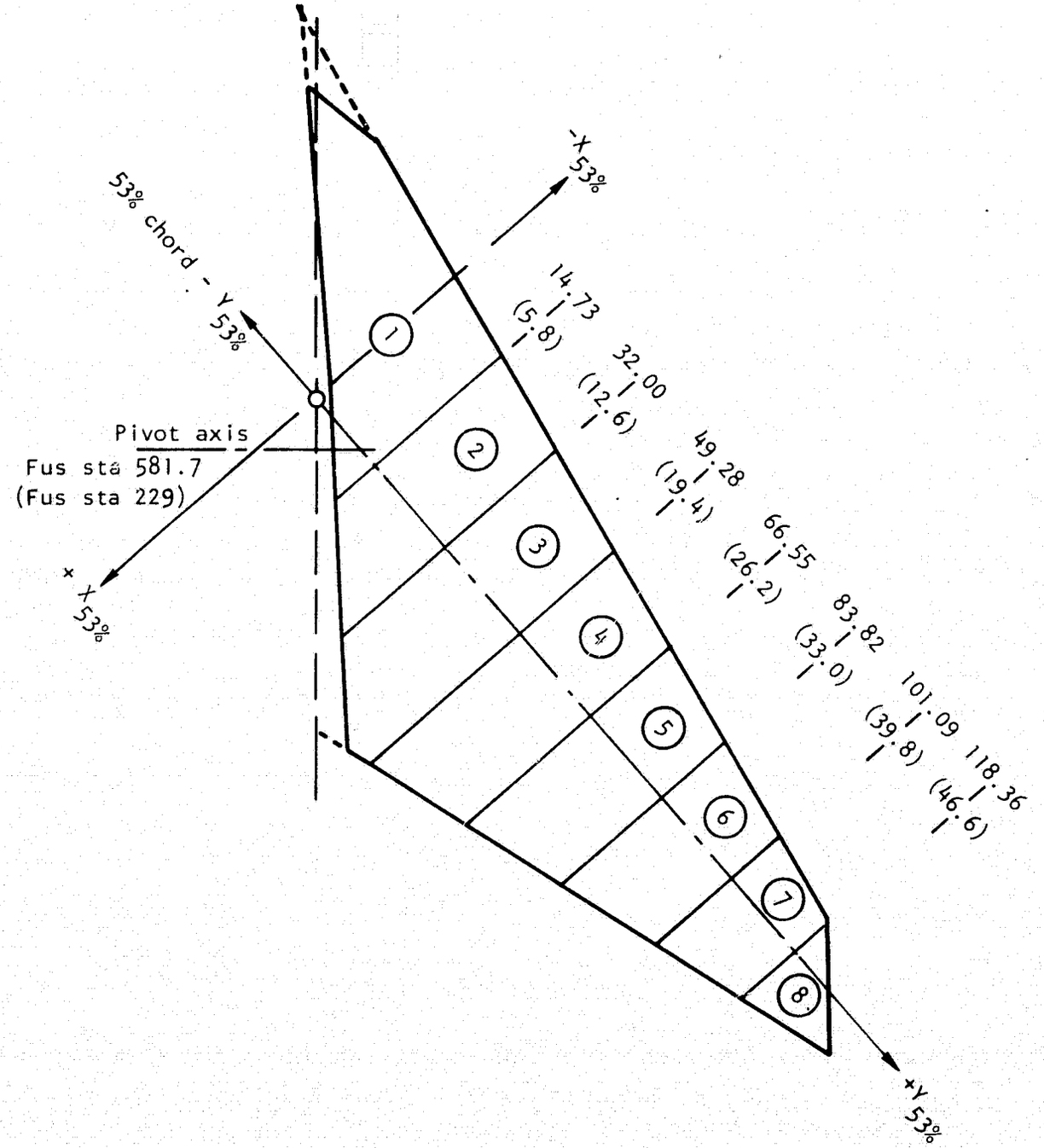

Figure 102. - SMCS vane mass properties sections.

TABLE IX. - SMCS VANE STRIP MASS PROPERTIES - ONE PANEL

Section	Weight kg (lb)	Center-of-gravity, cm (in.)			Moments and products of inertia, kg-cm^2 (lb-in.^{2})		
		x	y	z	I_{XX} I_{XZ}	I_{YY} I_{XY}	I_{ZZ} I_{YZ}
1	15.422 (34.00)	6.274 (2.47)	-1.803 (-.71)	-.584 (-.23)	1 421.05 (485.6) -85.74 (-29.3)	2 806.40 (959.0) 326.00 (111.4)	3 866.04 (1 321.1) 4.68 (1.6)
2	4.273 (9.42)	3.175 (1.25)	22.631 (8.91)	.025 (.01)	115.30 (39.4) 2.05 (.7)	496.05 (169.5) -17.85 (-6.1)	532.94 (199.2) .0 (.0)
3	3.515 (7.75)	1.956) (.77)	40.386 (15.90)	.0	96.28 (32.9) .0 (.0)	401.21 (137.1) 7.02 (2.4)	481.10 (164.4) .0 (.0)
4	2.971 (6.55)	2.743 (1.08)	47.404 (22.60)	.0	73.16 (25.0) .0 (.0)	250.21 (85.5) -2.63 (-9.)	321.24 (106.7) .0 (.0)
5	2.259 (4.98)	2.464 (.97)	75.209 (29.61)	.0	58.53 (20.0) .0 (.0)	152.17 (52.0) 2.34 (.8)	206.90 (70.7) .0 (.0)
6	2.055 (4.53)	2.337 (.92)	92.252 (36.32)	.0	50.33 (17.2) .0 (.0)	82.73 (28.2) -3.22 (-1.1)	129.93 (44.4) .0 (.0)
7	1.615 (3.56)	.965 (.38)	109.576 (43.14)	.0	40.38 (13.8) .0 (.0)	38.63 (13.2) .29 (.1)	77.55 (26.5) .0 (.0)
8	.544 (1.20)	1.981 (.78)	122.174 (48.10)	.0	3.22 (1.1) .0 (.0)	5.56 (1.9) 1.17 (.4)	8.49 (2.9) .0 (.0)
Total	32.654 (71.99)	4.242 (1.67)	30.150 (11.87)	-2.79 (-.11)	47 731.03 (16 310.6) -102.13 (-34.9)	4 363.82 (4 363.2) 1 814.94 (-620.2)	51 663.5 (17 654.4) 291.76 (99.7)

NOTES: 1. I_{PIVOT} = 37 536.7 kg-cm^2 (12 827 lb-in.^{2})

2. Fifty three percent reference system; see figure 103.

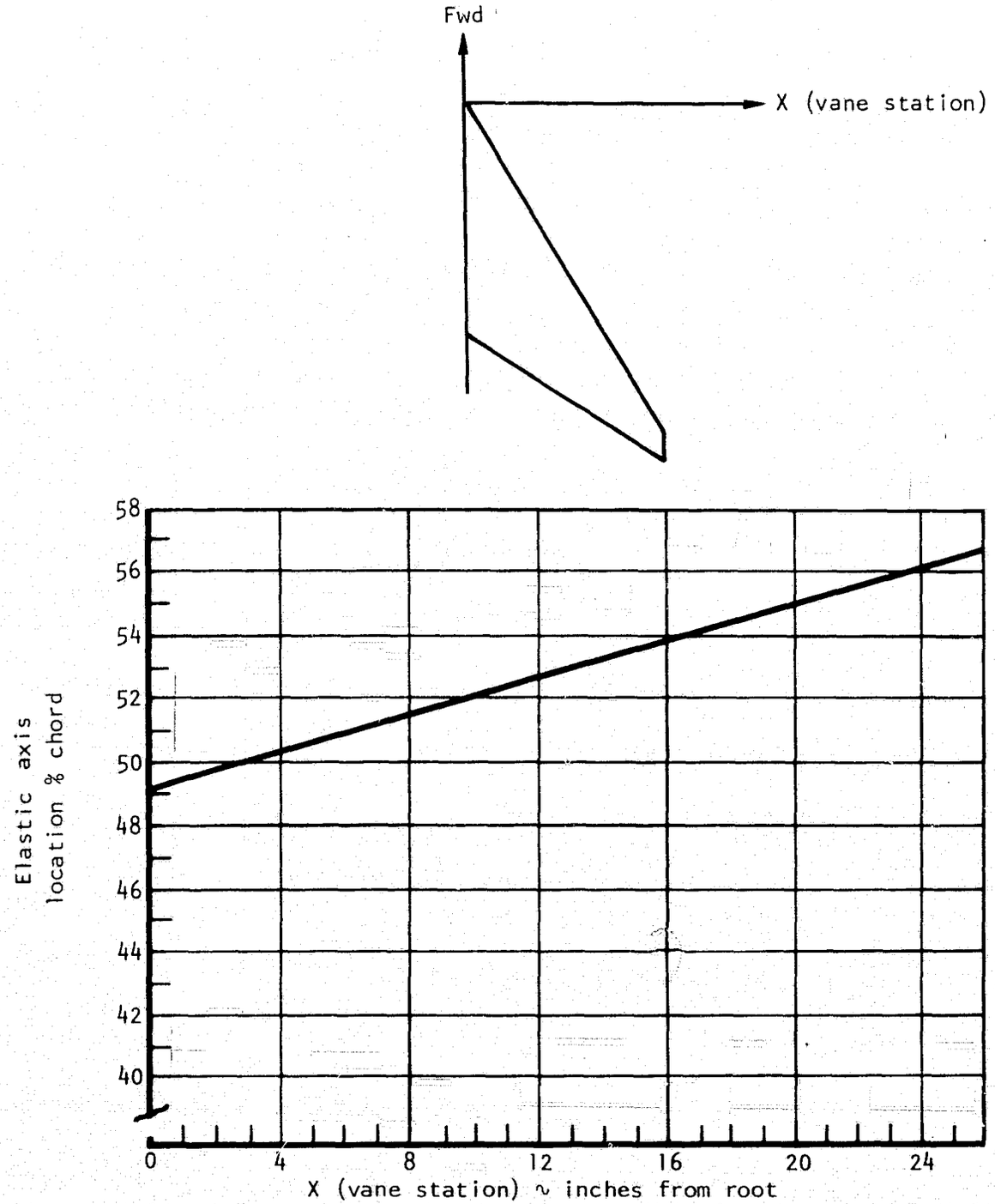

Figure 103. - SMCS vane elastic axis location.

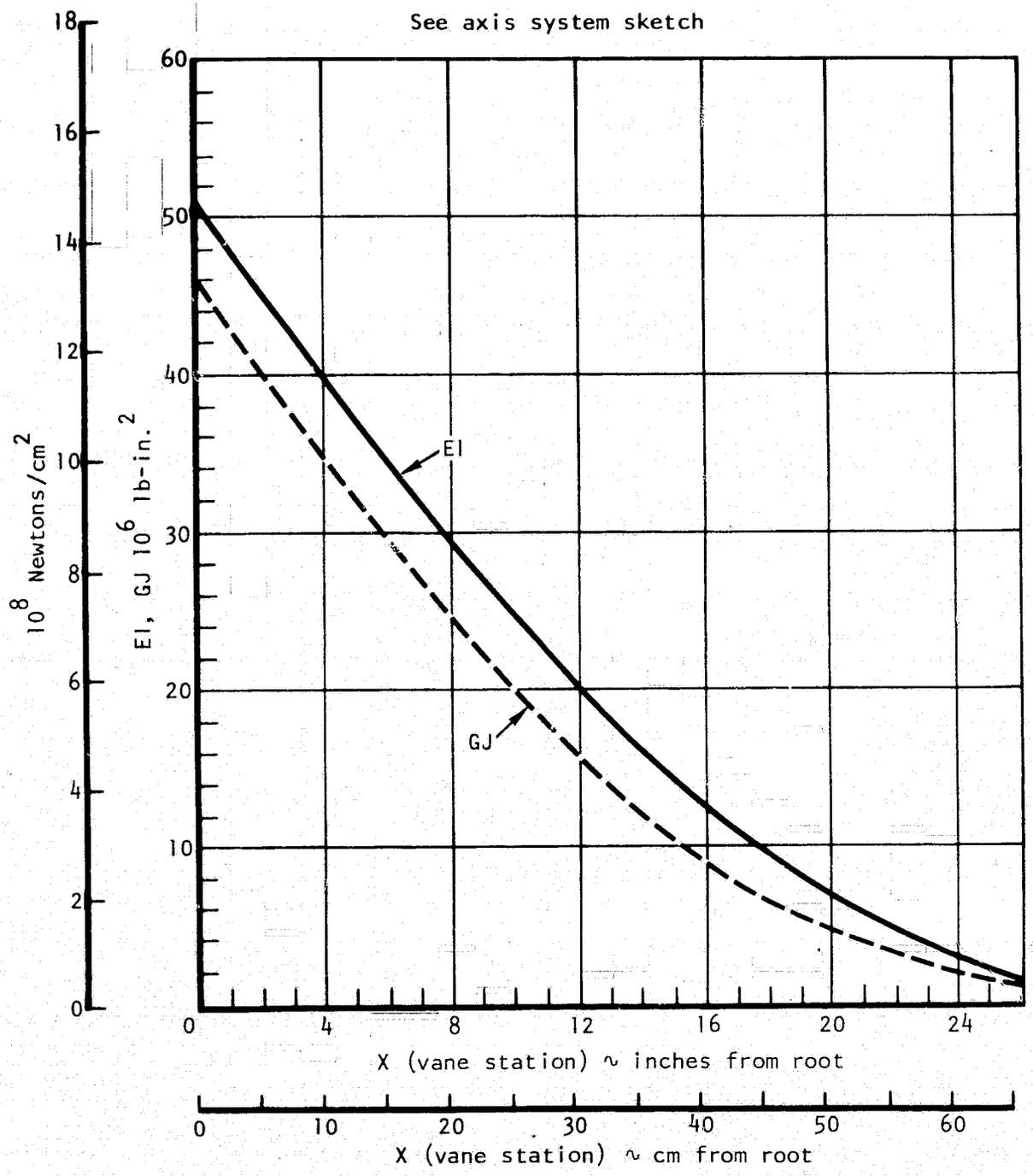

Figure 104. - SMCS vane spanwise variation of EI and GJ.

Normal actuators

$$\begin{bmatrix} Z\ \text{cm} \\ (\text{in.}) \\ \phi\ \text{rad} \\ (\text{rad}) \\ \theta\ \text{rad} \\ (\text{rad}) \end{bmatrix} = \begin{bmatrix} 0.188064 & -0.005354 & 0.0016056 \\ (0.329351) & (-0.009377) & (0.002812) \\ & 0.001187 & -0.000038 \\ & (0.013415) & (-0.000433) \\ & & 0.003497 \\ & & (0.039519) \end{bmatrix} \times 10^{-5} \begin{bmatrix} S\ \text{N} \\ (\text{lb}) \\ M\ \text{cm-N} \\ (\text{in.-lb}) \\ T\ \text{cm-N} \\ (\text{in.-lb}) \end{bmatrix}$$

Fwd actuator failed

$$\begin{bmatrix} 0.188064 & -0.005354 & 0.003868 \\ (0.329351) & (-0.009377) & (0.006774) \\ & 0.001187 & 0.000046 \\ & (0.13415) & (-0.000522) \\ & & 0.003095 \\ & & (0.349713) \end{bmatrix} \times 10^{-5}$$

Aft actuator failed

$$\begin{bmatrix} 0.188064 & -0.005354 & 0.002449 \\ (0.329351) & (-0.009377) & (0.004289) \\ & 0.001187 & -0.000035 \\ & (0.013415) & (-0.000391) \\ & & 0.003634 \\ & & (0.041057) \end{bmatrix} \times 10^{-5}$$

Figure 105. - SMCS vane actuators and backup structure symmetric flexibility influence coefficients.

Fwd actuator failed

Minimum stiffness case

$$\begin{bmatrix} 0.188064 & -0.005354 & 0.003994 \\ (0.329351) & (-0.009377) & (0.006994) \\ & 0.001187 & -0.000057 \\ & (0.013415) & (-0.000639) \\ & & 0.0102334 \\ & & (0.1156229) \end{bmatrix} \times 10^{-5} \quad (\times 10^{-5})$$

Aft actuator failed

Minimum stiffness case

$$\begin{bmatrix} 0.188064 & -0.005354 & 0.002582 \\ (0.329351) & (-0.009377) & (0.004521) \\ & 0.001187 & -0.000041 \\ & (0.013415) & (-0.000458) \\ & & 0.0109571 \\ & & (0.1237987) \end{bmatrix} \times 10^{-5} \quad (\times 10^{-5})$$

S = shear N
(lb)

M = moment cm - N
(in.-lb)

T = torque cm - N
(in.-lb)

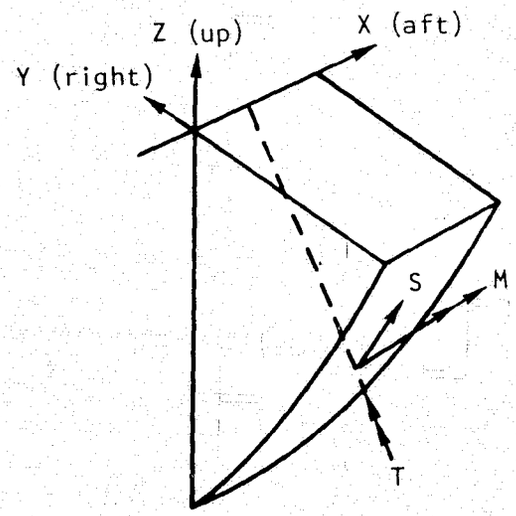

Figure 105. - Concluded.

REFERENCES

1. Rustenburg, John W.: Development of Tracking Error Frequency Response Functions and Aircraft Ride Quality Design Criteria for Vertical and Lateral Vibration. ASD-TR-70-18, January 1971.

2. Wykes, John H.; and Mori, Alva S.: An Analysis of Flexible Aircraft Structural Mode Control. AFFDL-TR-65-190, June 1966.

3. Wykes, John H.; and Knight, Ronald J.: Progress Report on a Gust Alleviation and Structural Dynamic Stability Augmentation System (GASDSAS) Design Study. AIAA Paper No. 66-999, November 29-December 2, 1966.

4. Wykes, John H.: Structural Dynamic Stability Augmentation and Gust Alleviation of Flexible Aircraft. AIAA Paper No. 68-1067, October 21-24, 1968.

5. Wykes, John H.; Nardi, Louis U.; and Mori, Alva S.: XB-70 Structural Mode Control System Design and Performance Analyses. NASA CR-1557, July 1970.

6. Lock, Wilton P.; Kordes, Eldon E.; McKay, James M.; and Wykes, John H.: Flight Investigation of a Structural Mode Control System for the XB-70 Aircraft. NASA TN D-7420, October 1973.

7. McKay, James M.; Kordes, Eldon E.; and Wykes, John H.: Flight Investigation of XB-70 Structural Response to Oscillatory Aerodynamic Shaker Excitation and Correlation with Analytical Results. NASA TN D-7227, April 1973.

8. Austin, W. H., Jr.: Development of Improved Gust Load Criteria for United States Air Force Aircraft. SEG-TR-67-28, September 1967.

9. Calibration System Requirements. MIL-C-45662A, February 6, 1962.

10. Hydraulic Systems, Manned Flight Vehicles, Type III, Design, Installation and Data Requirements for. MIL-H-8891, November 1, 1961.

11. Environmental Test Methods. MIL-STD-810B, 15 June 1969; Notice 1, October 20, 1969; Notice 2, September 29, 1969; Notice 3, September 21, 1972.

12. The Determination of Particulate Contamination in Liquids by Particulate Count Method. ARP 598A, August 1, 1969.

13. Cleanliness Requirements of Part Used in Hydraulic Systems. NAS 1638, January 1964.

14. USAF Stability and Control Methods Handbook (DATCOM).

15. Geising, J. P.; Kalman, T. P.; and Rodden, W. P.: Subsonic Unsteady Aerodynamics for General Configurations: Part I - Direct Application of the Nonplanar Doublet - Lattice Method. Air Force Flight Dynamics Laboratory, TR-71-5, February 1971.

1. Report No.	2. Government Accession No.	3. Recipient's Catalog No.
NASA CR-143846		

4. Title and Subtitle	5. Report Date
DESIGN AND DEVELOPMENT OF A STRUCTURAL MODE CONTROL SYSTEM	October 1977
	6. Performing Organization Code NA-77-296
7. Author(s)	8. Performing Organization Report No.
	10. Work Unit No. 505-02-25
9. Performing Organization Name and Address Rockwell International Corporation 5701 West Imperial Highway Los Angeles, California 90009	11. Contract or Grant No. NAS4-2347
	13. Type of Report and Period Covered Contractor Report - Topical
12. Sponsoring Agency Name and Address National Aeronautics and Space Administration Washington, D. C. 20546	14. Sponsoring Agency Code

15. Supplementary Notes

NASA Technical Monitor: James M. McKay

16. Abstract

A program was conducted to compile and document some of the existing information about the conceptual design, development, and tests of the B-1 structural mode control system (SMCS) and its impact on ride quality. This report covers the following topics:

(1) Rationale of selection of SMCS to meet ride quality criteria versus basic aircraft stiffening.

(2) Key considerations in designing an SMCS, including vane geometry, rate and deflection requirements, power required, compensation network design, and fail-safe requirements.

(3) Summary of key results of SMCS vane wind tunnel tests.

(4) SMCS performance.

(5) SMCS design details, including materials, bearings, and actuators.

(6) Results of qualification testing of SMCS on the "Iron Bird" flight control simulator, and lab qualification testing of the actuators.

(7) Impact of SMCS vanes on engine inlet characteristics from wind tunnel tests.

17. Key Words (Suggested by Author(s))	18. Distribution Statement
Ride quality Structural mode control	U.S. Government Agencies and Contractors Only STAR Category: 05

19. Security Classif. (of this report)	20. Security Classif. (of this page)	21. No. of Pages	22. Price*
Unclassified	Unclassified	185	

*For sale by the Clearinghouse for Federal Scientific and Technical Information Springfield, Virginia 22151